Exploring Mechano-structural Processes in Osteoarthritis



Ying-Chun Chen

Wadham College

University of Oxford

Nuffield Department of Orthopaedics,
Rheumatology, and Musculoskeletal Sciences

A thesis submitted for the degree of

Doctor of Philosophy

Trinity term 2017

In Loving Memory of My Bravest Aunt
Tsui-Ling Hsieh
1959-2014

Acknowledgements

Institutional

I gratefully acknowledge financial support from Orthopaedic Research UK (ref 504), the Taiwan Government Scholarship to Study Abroad (GSSA) and the Oxford NIHR BRU in musculoskeletal disease.

Personal

'The course of a DPhil is a lonely journey.' said my supervisor when we first met during my master after I had told him my future plans. I remember I only smiled, but knew nothing at that time of what he really implied, now I finally understand exactly what he meant.

My DPhil life is like a long, stretched out high tensile wire and I am the tightrope walker who needs to walk from one end of the rope to the other, performing my very own unique show, step by step, sometimes stable, sometimes shaky and sometimes with apprehension, anxiety and frustration. My supervisors are my balancing pole, helping me to maintain my equilibrium and encouraging me to keep walking forward. Support from my loved ones are the safety rope, they make me feel grounded and safe and help keep me enriched.

I would like to thank my supervisors: Professor Cameron Brown and Associate Professor Eamonn Gaffney. Without their patience, expertise and support, I would not have been able to complete my research within these four years. I would also like to thank Dr. Minsi Chen for his support with my computer modelling skills and helping me to resolve many unfathomable problems. Without his help, I would still be sitting in front of my computer, debugging my codes or feeling frustrated with increasing complex tasks. Thanks to Professor Andrew Price and Dr. Abtin Alvand for helping me with human tissue samples and kindly sharing and teaching me clinical knowledge. Thank you also to Associate Professor Philippa Hulley who stood by me whenever I faltered, questioned or doubted my research processes, giving me the support I needed with unending amounts of patience, kindness and empathy. Thank you also to Associate Professor Afsie Sabokbar who always gave me never-ending support throughout many difficulties I faced along the way, and for keeping me focused and determined. Thanks also to Dr. Stephanie Dakin and

Dr. Sarah Snelling who always had time for me, listened to me, and supported and shared their vast amounts of knowledge with me. Without their support, I would still be hopelessly stuck in the middle of the 'rope', being afraid of moving forward or backwards and still struggling with many issues I faced in my life at the time. Thank you also goes to Dr. Stephen Mellon for being my assessor in my confirmation who gave me many ideas and challenges and reassured me in my knowledge base and in how much I have managed to learn and improve. My thanks also go to Dr. Ali Zarei for teaching me about wet lab experiments, checking my design of experiments and for supporting me when I faced many major obstacles along the way. Without his help, I would still be at the very early stages of optimising my experimental protocol and worrying about how I can unravel the problems facing me.

Thanks go to Mrs. Na Wu, doctor-to-be, for not only helping me with my experiments but for always supporting me whenever possible. Her presence and company helped me endure many difficulties and helped brighten and encourage me with my research. Thank you to Ms. Joasia Hewanicka and her lovely daughters, Anna and Kasia, for warming my heart, supporting me and never letting me feel alone in a foreign country. Thanks to Dr. Elise Pegg for listening to me and always standing by me and giving me so much supports. Thanks to Dr. Monica Armengol for cheering me up all the time. Thanks to Dr. Takuya Sekine for being so supportive and never forget sharing his delicious Japanese snacks with me. Thanks to Ms. Zuzana Kalivodova for showing me how strong we can be when tackling the difficulties both in our research and in our lives. Thanks to Dr. Fu-Sheng Chang and Dr. Zhiqiao Wang for encouraging me to stay positive when faced with much anguish and dilemmas with my work. Thanks to Dr. Jennifer Martay for always caring for me and companying with me while we were at Botanr days and nights. Thanks to Dr. Elena Benedetto for always encouraging me and listening to me while I was really down. Thanks to Mr. Yanda Xin, another doctor-to-be, for supporting me through these years and being my supportive group member. Thanks to Mrs. Laura Diment, doctor-to-be, for caring about me all the time, always spending her time listening to and spending her time on helping me before my viva. Thanks also to Ms. Aneka Sowman, doctor-to-be, for listening to me when I was down and whistling her light music to make my gloomy days become brighter. Thanks also to my late night and weekend partners, Mr. Chao Jiang, Mr. Johnny Chan (both doctor-to-be) and Dr. Vikranth Nagaraja for being my companions in the DPhil write-up room, working days and nights and feeding me 'energy' food whenever I was too busy to eat and talking making jokes while we were all tired. Thanks to Mr. Henry Lee, doctors-to-be, for bringing me so many comforting toys during my days of boredom. Thanks to Mr. Nicholas Gee, Mr. Fryad Karim, Mr. Dave Banfield, Mr. Alan Bateman for supporting me whenever

I needed help and being like my wonderful uncles in UK. Thanks to Chirs and Luiz for giving me such warm supports. Thanks to Dr. Srinivasa Rao Rao and Dr. Seint Lwin for always helping me in the lab even they were busy and sharing their precious experiences with me. Thanks to Ms. Lis Ahlstrom, Mrs. Barbara Marks, Dr. Stephanie Smith, Mrs. Louise Appleton and Mrs. Isuara Thomas for giving me such great, happy times during my study.

Thanks to all the doctors-to-be, Mr. Wataru Morita, Ms. Jess Whiburn, Ms. Quitteerie Larrouture, Mr. Akira Wiberg, Mr. Hyungseop (Chris) Han, Mr. Rowan Nicholls, Ms. Chirstina Turner, Mr. Pavel Guzanov, Ms. Floor Timmer, Mr. John Broomfield, Mr. Patrick Garfjeld Roberts and all the people at the Botnar who always looked out for me, helped and supported me in so many ways. Thanks to all my fabulous flat mates, Dr. Alexander Baker, Dr. Simon Leese, Ms. Harriet Topping, Mr. Nils Wilfert, Ms. Jennifer Jo Swinson (doctor-to-be) and Mr. Harry Mason (doctor-to-be) for giving me such a wonderful UK dormitory life and supporting me when I felt low and disheartened with my research.

Thank you also to all my professors during my undergraduate and masters years, Associate Professor Chien-Ming Wu, Professor Chi-Shiun Chiang, Associate Professor Huan-wen Tseng, Associate Professor Zong-Mu Yeh and Associate Professor Chih-Ming Chen, and my line-managers during my work in Taiwan, Associate Professor Chian-Feng Chen, MD-PhD Chi-Chuan Yeh, MD-PhD Ming-Chih Ho and MD-PhD Hsao-Hsun Hsu for always encouraging me to finish my degrees. Thanks to my old mate Mr. Yu-Hsun Lin, whom I've known for more than half of my lifetime, and also thanks to his lovely wife, Mrs. Ming-Jung Hsieh for visiting me in Oxford to encourage me to keep doing and giving me supports whenever I need. Thank you also to my dearest friends, Mrs. Ya-Wen Lin and Dr. Tzu-Wen Yeh, who always showing their support and standing by me through so many years. Thank you to all my former lovely colleagues in room 929 in Department of Medical Research at National Taiwan University Hospital for giving me unstoppable support. Thank you also to my lovely friends in girls' basketball team at National Taiwan Normal University for being so supportive since my undergrad. Thank you also to Dr. Hao-Hsiang Wu for companying with me when I felt down and encouraging me to be positive during my gloomy days. Thanks also to Dr. Cheng-Wei Chang, Mrs. Chung-Hui Chen, Mr. Hsin-Hsiung Lee, Mr. Kai-Hua Shih, Mrs. Ting-Yun Cheng, Ms. Ya-Ting Chang, Mrs. Yu-Fen Huang, Dr. Bo-Shiuan Li and Dr. Yung-Kang Peng and all my lovely friends in Taiwan for always giving me never ending support. But the most important thank you of all has to be to the best parents and sisters in the world, for supporting me financially, mentally and spiritually, giving me the strength to fulfil my DPhil dream, always looking after me and comforting me when I was downhearted.

I am really lucky to have had so many wonderful people around me who encouraged and supported me in so many ways. I shall always remember how fortunate I was during my days in Oxford, how grateful I am for meeting so many kind, supportive, understanding people who helped and encouraged me all the way. I can truly say that I have made many lifelong friends and companions who I hope never to loose contact with. Today, I stand at the last and final step, ready to walk off from my tightrope, leaving behind my completed performance. Again, thank you to all the people who gave me such an unforgettable time here in Oxford; for accompanying me in the path of accomplishing my DPhil dream.

Exploring Mechano-structural Processes in Osteoarthritis

Ying-Chun Chen
University of Oxford, Wadham College
Doctor of Philosophy, Trinity term 2017

Abstract

Articular cartilage is a remarkable tissue with mechanical performance that surpasses engineering standards. Collagen, the most abundant protein in cartilage, plays an important role in this performance. Building on observations of collagen structural changes at the earliest stages of osteoarthritis, we here explore the role of collagen in the disease process. Specifically, we focus on the material properties and organisation of collagen fibrils in the cartilage surface, seeking to answer three key questions:

- What are the physical changes to collagen in early osteoarthritis?
- How do physical changes relate to osteoarthritic progression mechanistically?
- Can we detect early, irreversible changes to cartilage intraoperatively to facilitate early treatment?

Ten human tibial plateaus were characterised by atomic force microscopy and Raman spectroscopy, with clinical and histological scoring used for comparison. Minimal changes were found in the collagen molecules themselves, yet a marked increase in intra-fibrillar crosslinking was observed.

A bottom-up numerical model of the collagen fibril network was then implemented to specifically explore the relationship between fibril interactions and mechanics in osteoarthritis. Simulating two different fibril configurations, we established that high connectivity is critical to the resistance to, and recovery from, loading. Osteoarthritis-like bundled configurations were produced by networks with sparse interactions, and identified as a mechanically irreversible stage in disease progression. Coupling the model with experimental results, we argue that the intra-fibril changes appears to link to disease initiation and it is the inter-fibril interactions that drives the disease.

Finally, a pilot study was conducted to explore the potential for quantitative intraoperative imaging to detect irreversible collagen-related changes in the cartilage surface. Based on spectral analysis of the available light from standard arthroscopic equipment, it may be possible to advance arthroscopy from a qualitative to quantitative assessment tool.

Declaration

In this thesis, some contests have been published in Journal of the Mechanical Behavior of Biomedical Materials and the permissions to reuse the contents and figures from these papers have been granted by Elsevier (Appendix B).

Chapter 1

Ying-chun Chen, Minsi Chen, Eamonn A. Gaffney, Cameron P. Brown, Effect of crosslinking in cartilage-like collagen microstructures, Journal of the Mechanical Behavior of Biomedical Materials, Volume 66, February 2017.

Václav Klika, Eamonn A. Gaffney, **Ying-Chun Chen**, Cameron P. Brown, An overview of multiphase cartilage mechanical modelling and its role in understanding function and pathology, Journal of the Mechanical Behavior of Biomedical Materials, Volume 62, September 2016.

Chapter 3

Ying-chun Chen, Minsi Chen, Eamonn A. Gaffney, Cameron P. Brown, Effect of crosslinking in cartilage-like collagen microstructures, Journal of the Mechanical Behavior of Biomedical Materials, Volume 66, February 2017.

Contents

List of Figures **xiii**

List of Tables **xxv**

List of Abbreviations **xxvi**

1 Introduction **1**
1.1 Background and Motivation 1
1.2 Aims 3
1.3 State of the Art 4
1.3.1 Articular Cartilage and Changes with Osteoarthritis 4
1.3.1.1 Composition of Articular Cartilage 5
1.3.1.2 Structure of Articular Cartilage 7
1.3.1.3 Changes in Osteoarthritis 9
1.3.2 Collagen-specific Changes in Osteoarthritis 11
1.3.3 Intraoperative Diagnostic Techniques in Osteoarthritis . . . 15
1.4 Approach and Chapter Overview 21

2 Characterisation of Osteoarthritis Progression on the Articular Cartilage Surface **22**
2.1 Introduction 23
2.2 Methods 24
2.2.1 Sample Collection 24
2.2.2 Method Development 27
2.2.2.1 Optimisation of Sample Preparation for AFM . . . 27
2.2.2.1.1 Bovine Cartilage Cores 27
2.2.2.1.2 Cryo-sectioned Bovine Cartilage 29
2.2.2.1.3 Enzymatic Treatments - Hyaluronidase (Temperature) 30
2.2.2.1.4 Enzymatic Treatments - Hyaluronidase (Time) 32
2.2.2.1.5 Application to Human Cartilage 34
2.2.2.1.6 Additional Enzymatic Treatment - Chondroitinase 34

2.2.2.1.7 Additional Enzymatic Treatment - Trypsin 35
2.2.2.1.8 Enzymatic Treatment - Hyaluronidase (Increased Concentration and Time) 37
2.2.2.1.9 Final Protocol for Human Cartilage Samples 39
2.2.2.2 System Build for Polarised Raman Spectroscopy . . 41
2.2.2.2.1 Optical System 41
2.2.2.2.2 Basic Raman System Performance 44
2.2.2.2.3 Additional Optical Components 44
2.2.2.2.4 Polarisation Tests on Tissue 47
2.2.2.2.5 Final Raman Set-up 50
2.2.3 AFM - Data Collection and Analysis 51
2.2.3.1 Data Collection 51
2.2.3.2 Stiffness and Young's modulus 51
2.2.3.3 Data Analysis 53
2.2.4 Raman Spectroscopy - Data Collection and Analysis 57
2.2.5 Histology 60
2.2.5.1 Sample Preparation 60
2.2.5.2 Grading 60
2.2.6 Statistical Analysis 64
2.3 Results 65
2.3.1 Histological Analysis 65
2.3.2 Atomic Force Microscopy 67
2.3.2.1 Topography 68
2.3.2.2 Mechanical Properties 72
2.3.3 Raman Spectroscopy 76
2.4 Discussion 80
2.4.1 Topographical Features 80
2.4.2 Mechanical Features 80
2.4.3 Raman Spectral Analysis 82
2.4.4 Scoring Systems 83

3 Development of a 2-D Model of the Collagen Meshwork 84
3.1 Introduction 84
3.2 Zigzag Configuration 87
3.2.1 Materials and Methods 87
3.2.2 Results 92
3.2.2.1 Effect of Crosslink Density 92
3.2.2.2 Effect of Crosslink Stiffness 96
3.3 *Mikado* Configuration 97

3.3.1 Materials and Methods . . . 97
3.3.2 Model Simulation and Analysis . . . 97
3.3.3 Results . . . 99
3.3.3.1 Radial Tensile Force . . . 99
3.3.3.1.1 Anisotropy, Fibril Strain, Bulk Strain and Area Changes . . . 99
3.3.3.1.2 Redundancy and Crosslink Clustering . . . 103
3.3.3.2 Anisotropic Loading . . . 107
3.3.3.2.1 Uniaxial Tensile Force . . . 107
3.3.3.2.2 Uneven 2-D Tensile Force . . . 113
3.3.3.3 Comparison of Loading Conditions . . . 121
3.4 Discussion . . . 124
3.4.1 Zigzag Configuration . . . 124
3.4.2 *Mikado* Configuration . . . 125

4 Potential for Intraoperative Assessment of Initiation and Progression of Osteoarthritis 128
4.1 Introduction . . . 128
4.2 UV-VIS-NIR Spectroscopy . . . 130
4.2.1 System Set-up . . . 130
4.2.2 Data Collection and Data Analysis . . . 131
4.2.3 Results . . . 133
4.2.3.1 Absorbance Peaks . . . 135
4.2.3.2 Colour . . . 138
4.2.3.3 Slope Between the Wavelengths of 600 and 980 nm 140
4.3 Mie Scattering Model . . . 141
4.3.1 Mie Theory and the Scattering Model . . . 141
4.3.2 Results . . . 142
4.3.2.1 Polar Scattering Profiles . . . 142
4.3.2.2 Cylinder Diameter and 600-980 nm Slope . . . 148
4.4 Discussion . . . 152

5 Discussion and Future Work 156
5.1 Limitations . . . 157
5.2 Discussion and Conclusion . . . 159
5.3 Future Work and Future Directions . . . 167
5.3.1 Opportunities to Improve Current Work . . . 167
5.3.2 Future Directions . . . 169

Appendices

A Publications **172**

B Copyright Clearance **175**

C Safranin-O Staining Protocol for Cartilage **180**

D Training and Skills **181**

References **185**

List of Figures

1.1 Hierarchical structure of articular cartilage, showing the organisation of collagen at different length scales from millimetre (left) to micrometre (right). On the left, the 'Benninghoff' arcades of collagen fibre orientation, which represent the predominant orientation of collagen fibrils on the mesoscale within a given region, are illustrated with bone at the bottom of the diagram. The typical distribution of aggrecan to form the functional unit of load carriage is illustrated for healthy tissue in red (left), and its entanglement within the collagen meshwork, which is pseudo-random at lower level of scale (centreand right) [23]. 4

1.2 The structure of aggrecan. HA - hyaluronan; KS - keratan sulphate; CS - chondroitin sulphate; GAGs - glycosaminoglycans. 6

1.3 A schematic diagram showing the four zones of articular cartilage and the orientation of collagen fibrils (left) and chondrocyte organisation (right) in the different zones. The collagen fibrils are shown in blue, the yellow region shows the calcified zone, and the line between yellow and red colour shows the tide mark. From top to bottom, chondrocytes are flattened and smaller in the superficial zone and become spherical in the middle zone. In the deep zone, chondrocytes are typically aligned along the collagen fibrils and perpendicular to the joint line. 7

1.4 Second harmonic generation microscopy shows the surface structure change from (A) a normal collagen configuration (intact meshwork) to (B) sub-micron changes (alignment and minor bundling), (C) micron-scale bundles and (D) finally macroscopic degradation with proximity to a focal defect in bovine cartilage [21]. (image A is 500 $\times$ 500 μm, B-D are 200 $\times$ 200 μm) (permissions to reuse the contents and figures of these papers have been granted by Elsevier (Appendix B)) 12

1.5 Schematic diagram of the general OCT design. Red line: broad band light. 16

1.6 Schematic diagram of the general SHG design. H: half wave plate; P: polariser; G: galvo mirror; D: dichroic beamsplitter; PMT: photomultiplier tube; OBJ: objective; red line: laser; light red line: reflected light; light blue: reflected light passes filter. 17
1.7 Schematic diagram of the general NIR design. D: dichroic beamsplitter; OBJ: objective; dark red line: laser; light red line: reflected and transmitted light pass filter. 18
1.8 Schematic diagram of the general Raman design. D: dichroic beamsplitter; OBJ: objective; dark red line: laser; light red line: reflected light passes filter. 19

2.1 Representative photograph showing the measuring points (red points for Raman, AFM and histological measurements; black dotted circle for UV-VIS-NIR measurement) on a sample of human articular cartilage. The red arrow shows disease progression. The blue dashed line shows the cutting line after optical measurement. 25
2.2 Schematic diagram of the sample preparation process. Red arrow: disease progression determined by a clinician. Black dashed lines: cutting line. dia.: diameter. 26
2.3 Decision paths of the strategy for optimisation of sample preparation on bovine cartilage. Optimisation began with fresh bovine cartilage cores, testing whether collagen could be observed by AFM after a number of sample processing steps, including sectioning and enzymatic treatments. Preparation was continued until collagen fibrils were well exposed, after which the changes in mechanical properties were measured. An iterative process was followed to balance the exposure of fibrils with the minimisation of mechanical effects, before application to human tissues. 28
2.4 Representative AFM amplitude images of 5 × 5 μm samples of bovine cartilage following different pre-wash treatments: (A) PBS pre-wash (control), (B) ethanol pre-wash and (C) 30% isopropanol pre-wash. . 30
2.5 Flow chart of hyaluronidase treatment of the samples after a 30% isopropanol pre-wash at different temperatures for 30 minutes. The dotted line indicates the process of OCT removal. 31
2.6 Representative AFM amplitude images of a 1 × 1 μm area of bovine cartilage with 30% isopropanol pre-wash with and without hyaluronidase treatment at 25°C and at 37°C for 30 minutes: (A) samples without hyaluronidase treatment; (B) samples with hyaluronidase treatment at 25°C; (C) samples with hyaluronidase treatment at 37°C. 32

2.7 Representative AFM amplitude images of a 5 × 5 μm area of bovine cartilage pre-washed with 30% isopropanol and treated with 1 mg/ml hyaluronidase at 37°C for different time periods: (A) before treatment (control), (B) 30 minutes treatment, (C) 60 minutes treatment and (D) 90 minutes treatment. (E) Young's modulus of collagen fibrils increased slightly but insignificantly after hyaluronidase treatment for 90 minutes. 33
2.8 Decision path for the optimisation of sample preparation for human cartilage. 34
2.9 Representative AFM amplitude images of a 4 × 4 μm area on a human tissue sample (A) before and (B) after trypsin treatment for 60 s. 36
2.10 Young's modulus of 12 collagen fibrils within regions A, B, C, D, and E with and without trypsin treatment. Data are shown as mean ± standard deviation. ***:$P < 0.0001$. 36
2.11 AFM amplitude images of a 3 × 3 μm area of human cartilage surface after treatment with different concentrations of hyaluronidase for one hour: (A) PBS (control), (B) 1 mg/ml hyaluronidase, (C) 5 mg/ml hyaluronidase, (D) 10 mg/ml hyaluronidase, (E) 20 mg/ml hyaluronidase and (F) 40 mg/ml hyaluronidase. 37
2.12 Young's moduli of collagen fibrils after treatment with different concentrations of hyaluronidase for 3 hours. Hyaluronidase treatment had little effect on mechanical properties, despite increase in both time and concentration.cntr.: control. 38
2.13 Flow chart of AFM sample preparation after washing with 30% isopropanol. Hemi-cylinders of cartilage were washed with 30% isopropanol, snap-frozen in liquid nitrogen and stored at −80°C before sectioning at 10 μm, mounting on glass slides, and removal of OCT. Samples were then treated with 40 mg/ml hyaluronidase in a 37°C incubator for 3 hours, washed with distilled water for 3 × 10 minutes and dried at room temperature (25°C) for a minimum of 30 minutes. 40
2.14 (A) Schematic diagram of the Raman spectroscopy set-up. (B) Photograph showing the Raman spectroscopy set-up. L: lens; M: mirror; Pol: Glan-Thompson polariser; HWP: half-wave plates; Di-BS: dichroic beamsplitter; N: notch filter; Red line: incident light; green line: scattered light. 42
2.15 Flow chart of the system testing process during set-up of the polarised Raman spectroscopy system. 43

2.16 Raman spectra of (A) chondroitin sulphate, (B) hydroxyapatite and (C) collagen. 44
2.17 Components affecting testing and laser polarisation profile. (A) Changes in laser power with rotation of the half-wave plate. (B) Polarisation profile of the laser after passing through the Glan-Thompson polariser. 45
2.18 Laser stability test after passing the half-wave plate. (A) Teflon^{TM} spectrum with increasing time. (B) Intensity changes at 748 cm^{-1}. . 46
2.19 Raman spectra of porcine tendon. (A) Spectra allowing dehydration during the experiment, showing the resultant drift of signal intensity. (B) Spectra with the addition of distilled water during the measurements, showing more consistent results. 47
2.20 Raman spectra of porcine tendon at different laser polarisation angles, in 15 degree increments. (A) Full spectra at different polarisation settings. Polar plots of (B) 937 cm^{-1}, (C) 1251 cm^{-1}, and (D) 1663 cm^{-1}. 48
2.21 Raman spectra of porcine tendon at different polarisation angles with a 0.45 NA objective. (A) Spectra at different polarisation directions. (B) Polar plot of 937 cm^{-1} spectra at different polarisation angles. (C) Polar plot of 1251 cm^{-1} spectra at different polarisation angles. (D) Polar plot of 1663 cm^{-1} at different polarisation angles. 49
2.22 Modified Raman spectroscopy. (A) Schematic diagram of the Raman spectroscopy set-up. (B) Photograph showing the Raman spectroscopy set-up where the white dotted circle shows the location of the removed polariser and half-wave plate. (C) Representative photograph showing the Raman spectroscopy measuring points (red points) on a sample of human articular cartilage where the red arrow shows disease progression. The blue dotted line shows the cutting line after optical measurement. L: lens; M: mirror; Pol: Glan-Thompson polariser; Di-BS: dichroic beamsplitter; N: notch filter; red line: incident light; green line: scattered light; white dotted circle showed the location of the removed half wave plate and polariser. 50
2.23 Representative figure showing the formation and analysis of D-periods. (A) Height, (B) amplitude and (C) phase images showing D-periods of collagen fibrils. (D) The D-period patterns from the red rectangle in the amplitude image (B). (E) Schematic diagram showing the formation of D-periodic gaps. 55

2.24 Representative figure showing the difference in the Young's modulus across the D-periods: calculations from a single fibril. One D-period of a collagen fibril is observed as a major peak and adjacent valley (the red arrow). Blue arrows indicate the peaks along one collagen fibril. The differences between major peak and valley values (shown in d_1, d_2 and d_3) were calculated. 56
2.25 Representative figure of Raman spectrum processing. (A) Raw spectra. (B) Spectra after processing. 57
2.26 Representative image of a safranin-O stained section showing the positions used for histological scoring. Each section was divided into five regions at 1 mm intervals (magnification 2.5×). 61
2.27 The cumulative probability of the Outerbridge and OARSI scoring systems. 66
2.28 Representative AFM images of 3 × 3 μm areas on the human articular cartilage surface. (A) and (B) show the topography of the cartilage surface by height and amplitude respectively. (C) and (D) show the mechanical properties of the cartilage surface by Young's modulus and loss tangent. 67
2.29 AFM amplitude images of 3 × 3 μm areas of the human cartilage surface at different disease stages: (A) grade 0, (B) grade 1, (C) grade 2, (D) grade 3 and (E) grade 4. 69
2.30 AFM images of thin fibrils from the human articular cartilage surface: amplitude image (A, C) and height image (B, D) of 4 × 4 μm and 3 × 3 μm areas on human articular cartilage samples. Red arrows indicate thin fibrils. 70
2.31 Knotting formation shown in an AFM amplitude image of a 3 × 3 μm area on the cartilage surface. 70
2.32 Granules on the surface of human cartilage: (A) amplitude images of a 3 × 3 μm area on the surface of human cartilage and (B) deflection images of a 5 × 5 μm area on human femoral cartilage in PBS [167]. (permissions to reuse the contents and figures of these papers have been granted by Springer (Appendix B)) 71
2.33 Mechanical properties within each collagen fibril at different disease stages: (A) Young's modulus and (B) loss tangent. *:P<0.05, **:P<0.01 and ***:P<0.001. 72
2.34 Mechanical properties of collagen fibrils grouped by patient at different disease stages: (A) Young's modulus and (B) loss tangent. **:P<0.01. 73
2.35 Distribution of mechanical properties of collagen fibrils at different disease stages. 74

2.36 The D-period of collagen fibrils at different disease stages: (A) changes in Young's modulus across each D-period on a single fibril and (B) the variance of the changes in Young's modulus. *:P<0.05, **:P<0.01 and ***:P<0.001. 75
2.37 Raman spectra at different disease stages (mean ± SEM). 76
2.38 The areas under collagen type II bands at different disease stages: (A) phenylalanine ring (995-1015 cm^{-1}), (B) CH_2/CH_3 scissoring (1450-1460 cm^{-1}), (C) amide III (1209-1332 cm^{-1}); (D) CH_2/CH_3 scissoring (1429-1469 cm^{-1}); (E) proline (848-868 cm^{-1}) and (F) hydroxyproline (872-881 cm^{-1}). 77
2.39 Collagen helix stability, given by the ratio of proline (856 cm^{-1}) to hydroxyproline (872 cm^{-1}). **:P<0.01. 77
2.40 Ratios of random coil to alpha-helix (1240/1272 cm^{-1}) at different disease stages. 78
2.41 The relative concentration of (A) sulphate and (B) hyaluronic acid in cartilage ECM and (C) the ratio of the sulphate to hyaluronic acid at different disease stages. 79

3.1 The material property of a fibril was calculated by fitting experimental data from a single fibril tensile test [197] (inset figure) to give a linear force-strain relationship of 4 μN/unit strain (the black dashed line). The red dots show the fitting nodes from the stress-strain experimental data after conversion to a force-strain relationship. . 88
3.2 Representative collagen network model. Spring segments are shown in green, nodes shown in yellow and crosslinks shown in red. 90
3.3 A representative structure (A) before stretching, (B) after stretching and (C) after relaxation. White arrows show the force direction. Springs are shown in green, nodes in yellow and crosslinks in red. . 92
3.4 Representative structure with (A) 314 crosslinks and (B) with 81 crosslinks after stretching. (C) Transmission electron micrograph of collagen fibril organisation in osteoarthritic cartilage, reproduced from [120]. Scale bar 1.5μm. (permissions to reuse the contents and figures of these papers have been granted by John Wiley and Sons (Appendix B)) 92
3.5 Relationship between crosslink density and angular anisotropy (r_{mean}) of the pre-loaded structure. Each line represents data from a single crosslink threshold. Black represents 0.3 μm, blue represents 0.5 μm and green represents 0.8 μm crosslink proximity thresholds. 93

3.6 Structural anisotropy as defined by r_{mean} under loading and recovery. (A) Greater isotropy was maintained, and (B, C) recovered, in highly-crosslinked microstructures. Dashed lines plot the trends within the same structure at different crosslink thresholds. Different crosslink proximity thresholds are presented in different colours where 0.3 μm is black, 0.5 μm is blue and 0.8 μm is green. 94

3.7 Bulk mechanical strain under loading and recovery. (A, B) Bulk strain decreased with increasing crosslink density, (C) with greater recovery in highly crosslinked microstructures. Dashed lines plot the trends within the same structure at different crosslink proximity thresholds. Different crosslink proximity thresholds are presented in different colours where 0.3 μm is black, 0.5 μm is blue and 0.8 μm is green. 94

3.8 Fibril strain at equilibrium at different crosslink densities. Dashed lines link the same structure with different crosslink thresholds. Different crosslink thresholds are shown in different colours where 0.3 μm is black, 0.5 μm is blue and 0.8 μm is green. 95

3.9 Representative boundary detection from one structure with a crosslinking threshold of 0.9 μm. Black dots represent the boundary nodes of the structure before stretching. Blue dots represent the boundary nodes of the structure at equilibrium and red dots show the boundary nodes of the structure after recovery. The boundary of the structure before stretching is shown in blue, after stretching is shown in red and after recovery is shown in yellow. 98

3.10 Configuration of a representative surface specific simulation with a 0.9 μm crosslink threshold (A) before stretching, (B) after stretching and (C) after relaxation. Fibrils are shown in green, nodes are shown in yellow and crosslinks are shown in red. 99

3.11 Relationship between crosslink density and angular anisotropy (A) at equilibrium and (B) after relaxation. Different crosslink thresholds are shown in different colours where 0.5 μm is black, 0.7 μm is blue, 0.9 μm is green, 1.1 μm is red, 1.3 μm is cyan and 1.5 μm is magenta. 100

3.12 Area changes (A) after stretching, (B) after relaxation and (C) recovery. Dashed lines link the same structure with different crosslink thresholds. Different crosslink thresholds are shown in different colours where 0.5 μm is black, 0.7 μm is blue, 0.9 μm is green, 1.1 μm is red, 1.3 μm is cyan and 1.5 μm is magenta. 100

3.13 Fibril strain at equilibrium at different crosslink densities. Dashed lines link the same structure with different crosslink thresholds. Different crosslink thresholds are shown in different colours where 0.5 μm is black, 0.7 μm is blue, 0.9 μm is green, 1.1 μm is red, 1.3 μm is cyan and 1.5 μm is magenta. 101
3.14 A representative structure highlighting fibrils under high strain (over 7.5%) with crosslink thresholds of (A) 7 μm and (B) 15 μm. The fibrils in white indicates those with strain of over 7.5%. The yellow dashed ellipse shows a region of local strain reduction due to the high density of crosslinks. 102
3.15 Variance of fibril strain at equilibrium at different crosslink densities. Dashed lines link the same structure with different crosslink thresholds. Different crosslink thresholds are shown in different colours where 0.5 μm is black, 0.7 μm is blue, 0.9 μm is green, 1.1 μm is red, 1.3 μm is cyan and 1.5 μm is magenta. 102
3.16 Number of lengths shorter than the original lengths after stretching. Different crosslink thresholds are shown by different colour dots where 0.5 μm is black, 0.7 μm is blue, 0.9 μm is green, 1.1 μm is red, 1.3 μm is cyan and 1.5 μm is magenta. 103
3.17 Schematic diagram showing crosslinking in the *Mikado* spring structure. (Left) each node (grey circle) except the top and bottom nodes has two neighbours (N1 and N2). (Right) when forming a crosslink (red) with other fibrils, the neighbouring nodes increased. 104
3.18 Example of the structure showing the high density of crosslinks in a specific area. A structure with a 1.1 μm crosslink threshold (left) and with a 1.3 μm crosslink threshold. The red dotted rectangle indicates the formation of the region with a high density of crosslinks when the crosslink threshold increased. The lower half of the figures shows this formation at higher magnification. Nodes are shown in yellow, springs in green and crosslinks in red. 104
3.19 The relationship between the number of crosslinks and the number of nodes with $\geqslant$ 2 neighbouring nodes (red dots) and with $\geqslant$ 4 neighbouring nodes (blue dots). 105
3.20 Fifty fibril strains of ten representative structures with 0.7 μm and 1.5 μm. Red crosses indicate the outliers (whisker lengths are defined as $\pm$ 2.7σ and 99.3% coverage if data are normally distributed). . . 106
3.21 Histogram of a total of 500 fibril strains from ten representative structures with crosslink thresholds of 0.7 μm (blue) and 1.5 μm (light grey). 106

3.22 A representative surface specific simulation with a 1.1 μm crosslink threshold (A) before stretching, (B) after stretching and (C) after relaxation. Fibrils are shown in green, nodes in yellow and crosslinks in red. 107
3.23 Relationship between crosslink density and angular anisotropy at (A) equilibrium and (B) after relaxation. Different crosslink thresholds are shown in different colours where 0.5 μm is black, 0.7 μm is blue, 0.9 μm is green, 1.1 μm is red, 1.3 μm is cyan and 1.5 μm is magenta. 108
3.24 Area changes (A) after stretching, (B) after relaxation and (C) after recovery. Dashed lines link the same structure with different crosslink thresholds. Different crosslink thresholds are shown in different colours where 0.5 μm is black, 0.7 μm is blue, 0.9 μm is green, 1.1 μm is red, 1.3 μm is cyan and 1.5 μm is magenta. 109
3.25 Fibril strain at equilibrium at different crosslink densities. Dashed lines link the same structure with different crosslink thresholds. Different crosslink thresholds are shown in different colours where 0.5 μm is black, 0.7 μm is blue, 0.9 μm isgreen, 1.1 μm is red, 1.3 μm is cyan and 1.5 μm is magenta. 110
3.26 Variance of fibril strain at equilibrium at different crosslink densities. Dashed lines link the same structure with different crosslink thresholds. Different crosslink thresholds are shown in different colours where 0.5 μm is shown in black, 0.7 μm in blue, 0.9 μm in green, 1.1 μm in red, 1.3 μm in cyan and 1.5 μm in magenta. 111
3.27 Fifty fibril strains of ten representative structures with 0.7 μm and 1.5 μm. Red crosses indicate the outliers (whisker lengths are defined as $\pm$ 2.7σ and 99.3% coverage if data are normally distributed). . . 112
3.28 Histogram of a total of 500 fibril strains from ten representative structures with crosslink thresholds of 0.7 μm (blue) and 1.5 μm (light grey). 112
3.29 A representative anisotropic 2-D simulation with a 1.1 μm crosslink threshold (A) before stretching, (B) after stretching (0.5 μN in the x-direction and 0.1 μN in the y-direction) and (C) after relaxation. Fibrils are shown in green, nodes in yellow and crosslinks in red. . . 113
3.30 A representative structure with 139 crosslinks (A) before and (B) after application of anisotropic force. The red dashed rectangle indicates the knots formed and the yellow dashed rectangle indicates bundle formation. 114
3.31 A representative structure with (A) 94 crosslinks and (B) 820 crosslinks after loading. Bundle formation is indicated by the yellow rectangle. 114

3.32 A representative structure with (A) 129 crosslinks and (B) 916 crosslinks after loading. Bundle formation is indicated by the yellow rectangle. 114
3.33 Relationship between crosslink density and angular anisotropy at (A) equilibrium and (B) after relaxation. Different crosslink thresholds are shown in different colours where 0.5 μm is shown in black, 0.7 μm in blue, 0.9 μm in green, 1.1 μm in red, 1.3 μm in cyan and 1.5 μm in magenta. 115
3.34 Area changes (A) after stretching, (B) after relaxation and (C) after recovery. Dashed lines link the same structure with different crosslink thresholds. Different crosslink thresholds are shown in different colours where 0.5 μm is shown in black, 0.7 μm in blue, 0.9 μm in green, 1.1 μm in red, 1.3 μm in cyan and 1.5 μm in magenta. 116
3.35 Fibril strain at equilibrium at different crosslink densities. Dashed lines link the same structure with different crosslink thresholds. Different crosslink thresholds are shown in different colours where 0.5 μm is shown in black, 0.7 μm in blue, 0.9 μm in green, 1.1 μm in red, 1.3 μm in cyan and 1.5 μm in magenta. 117
3.36 Variance of fibril strain at equilibrium at different crosslink densities. Dashed lines link the same structure with different crosslink thresholds. Different crosslink thresholds are shown in different colours where 0.5 μm is shown in black, 0.7 μm is blue, 0.9 μm is green, 1.1 μm is red, 1.3 μm is cyan and 1.5 μm is magenta. 118
3.37 Fifty fibril strains of ten representative structures with 0.7 μm and 1.5 μm. Red crosses indicate the outliers (whisker lengths are defined as $\pm$ 2.7σ and 99.3% coverage if data are normally distributed). . . 119
3.38 Histogram of a total of 500 fibril strains from ten representative structures with crosslink thresholds of 0.7 μm (blue) and 1.5 μm (light grey). 120
3.39 Relationship between crosslink density and angular anisotropy at (A) equilibrium and (B) after relaxation with different types of tensile force. Different crosslink thresholds are shown in different colours where 0.5 μm is shown in black, 0.7 μm is blue, 0.9 μm is green, 1.1 μm is red, 1.3 μm is cyan and 1.5 μm is magenta. 121
3.40 Area changes (A) after stretching, (B) after relaxation and (C) after recovery with different types of tensile force. Different crosslink thresholds are shown in different colours where 0.5 μm is shown in black, 0.7 μm is blue, 0.9 μm is green, 1.1 μm is red, 1.3 μm is cyan and 1.5 μm is magenta. 122

3.41 Summary of the (A) fibril strain and (B) variance of fibril strain at equilibrium with different types of tensile force. Dashed lines link the same structure with different crosslink thresholds. Different crosslink thresholds are shown in different colours where 0.5 μm is shown in black, 0.7 μm is blue, 0.9 μm is green, 1.1 μm is red, 1.3 μm is cyan and 1.5 μm is magenta. 123

4.1 Schematic diagram of the (A) UV-VIS-NIR spectroscopy setup and (B) measurement from the probe. (A) Light from the deuterium-halogen light source (UV-VIS-NIR) was delivered to the probe head through six 400 μm optical fibres. The probe was held in a position by a probe holder to maintain the correct distance between sample and probe head. Scattered light from the sample was collected by the probe and delivered to the spectrometer. D: distance from the probe head to the core. (B) Probe is composed of six illumination fibres (light gray circle) around one read fibre (red circle). 131

4.2 The measuring point used for UV-VIS-NIR spectroscopy (black dotted circle). The blue dotted line shows the cutting line after optical measurement. The cut edge shows the mark of disease progression. 132

4.3 The UV-VIS-NIR spectrum between the wavelengths of 250-980 nm at grade 0 and grade 1. Grade 0: green straight line and grade 1: red dashed line. Shaded areas show the standard deviation. 133

4.4 The mean UV-VIS-NIR spectrum between the wavelengths of 250-980 nm at different stages of disease. Grade 0: black straight line; grade 1: green dashed line; grade 2: blue short-dotted line; grade 3 line: yellow dash-dotted line and grade 4: red dash-dot-doted line. 134

4.5 Areas under the main peaks at different stages of disease at (A) 320 nm, (B) 405 nm, (D) 455 nm, (E) 531 nm and (F) 566 nm. *:$P <$ 0.05. cntr.:control. 136

4.6 Comparison of the under areas of the five peaks at different stages of disease: (A) 320/531, (B) 320/566, (C) 405/531, (D) 405/566, (E) 455/531, (F) 455/566, (G) 320/405, (H) 320/455, (I) 405/455 and (J) 531/566. *:$P < 0.05$ and **:$P < 0.01$. 137

4.7 RGB profile of a generic detector [209]. 139

4.8 The intensity of RGB reflectance at different disease stages: (A) changes in RGB profile and (B) resulting artificial colour. cntr.:control. 139

4.9 Slopes of UV-VIS-NIR absorbance spectra between the wavelengths of 600 and 980 nm at different stages of disease. *:$P < 0.05$. 140

4.10 Angular scattering intensity. σ: cross section; N_s: number of scattering particles. 142

4.11 Calculated scattering profiles with different diameters of cylinders (5-400 nm) at wavelengths of 600, 650, 700, 750, 800, 850, 900, 950 and 980 nm. Dia.:diameter. 143
4.12 Calculated scattering profiles with different diameters of cylinders (200-1600 nm) at 600-980 nm. Profiles for 50-310 degree scattering angles are included below each figure. Cylinder diameters were (A) 200 nm, (B) 600 nm, (C) 1000 nm, (D) 1200 nm, (E) 1400 nm, and (F) 1600 nm. Dia.:diameter. 144
4.13 Differential scattering cross-sections as a function of scattering angle with different diameters of cylinders at a wavelength of 600 nm. . . 145
4.14 Differential scattering cross-sections as a function of scattering angle with different diameters of cylinder at a wavelength of 980 nm. . . . 146
4.15 Differential scattering cross-section of single and multiple cylinders at wavelengths of 600 and 980 nm. The diameters of cylinders were 100, 200 and 600 nm. Scattering profiles showed more noisy from multiple cylinders. 147
4.16 Differential scattering cross sections at (A and B) a 0 degree scattering angle, (C and D) between 0 ± 90 degree scattering angles and (E and F) total cross-sections with different diameters of cylinder at wavelengths of 600 and 980 nm from Mie simulation. 149
4.17 Differential scattering cross sections at (A and B) a 180 degree scattering angle, (C and D) between 90-270 degree scattering angles and (E and F) total cross-sections with different diameters of cylinder at wavelengths of 600 and 980 nm from Mie simulation. 150
4.18 The ratio of 980 and 600 nm comparison from Mie scattering model and experimental data. (A) Ratio of the proportional backscattering between 980 and 600 nm with cylinder diameter ranging from 5-800 nm (inset figure shows the slope of proportional backscattering between 980 and 600 nmwith cylinder diameter ranging from 5-1600nm. (B) Slope changes from experimental data (reflectance). . 151
4.19 Safranin-O stained sections at different stages of disease: (A) grade 1, (B) grade 2 and (C) grade 3. Cracks/fissures from the surface of the cartilage appeared at grade 2 and grade 3 (magnification 10×). 154

5.1 Summary of the characterisation of OA progression and potential methods for detection of OA structural features. 160

List of Tables

2.1 Raman bands of collagen and range selection [109, 112, 160, 161] . . 58
2.2 Raman bands of hydroxyproline, hyaluronic acid and sulphate and their selected ranges 59
2.3 OARSI scoring methodology and histological staining [163]. 62
2.4 Outerbridge classification system [165, 166]. 63
2.5 Number of regions with each histological score (OARSI). 65
2.6 Number of regions with each clinical score (Outerbridge). 65
2.7 Numbers of fibrils measured at each OARSI score. 67

3.1 Numerical spring length error under one-dimensional tensile test load for an isolated spring segment (single spring) and a single, 20-segment spring (single fibril). 89
3.2 Mechanical behaviour of a representative structure (293 crosslinks) with different crosslink stiffness. 96

4.1 Numbers of samples with each histological score. 133
4.2 The wavelengths of the peaks and range selection 134

List of Abbreviations

OA . . . . . Osteoarthritis.

ECM . . . . . Extracellular matrix.

PCM . . . . . Pericellular matrix.

RVE . . . . . Representative volume element.

AFM . . . . . Atomic Force Microscopy.

IFOP . . . . . Infra-red fibre optic probe.

OCT . . . . . Optical coherence tomography.

SHG . . . . . Second harmonic generation.

NIR . . . . . Near infra-red.

UV-VIS . . . . Ultraviolet–visible.

PCA . . . . . Principal component analysis.

UV-VIS-NIR Ultraviolet–visible-near infra-red.

TKA . . . . . Total knee arthroplasty.

UKA . . . . . Unicompartmanetal knee arthroplasty.

PBS . . . . . Phosphate-buffered saline.

OARSI . . . . Osteoarthritis research society international.

AM . . . . . Amplitude modulation.

FM . . . . . Frequency modulation.

PCL . . . . . Polycaprolactone.

NA . . . . . Numerical aperture.

BSA . . . . . Bovine serum albumin.

SEM . . . . . Standard error of the mean.

1-D, 2-D . . . One- or two-dimensions, referring in this thesis to spatial dimensions in an image.

EM . . . . . Electromagnetic.

RGB . . . . . Red, green and blue.

1 Introduction

Contents

1.1 Background and Motivation 1
1.2 Aims 3
1.3 State of the Art 4
1.3.1 Articular Cartilage and Changes with Osteoarthritis . . 4
1.3.1.1 Composition of Articular Cartilage 5
1.3.1.2 Structure of Articular Cartilage 7
1.3.1.3 Changes in Osteoarthritis 9
1.3.2 Collagen-specific Changes in Osteoarthritis 11
1.3.3 Intraoperative Diagnostic Techniques in Osteoarthritis . 15
1.4 Approach and Chapter Overview 21

1.1 Background and Motivation

In terms of disability burden [1,2], related pain and loss of function [1], and the strong causal link with other major diseases (e.g. depression [3] and cardiovascular disease [4]), musculoskeletal diseases are a major issue for UK health. Musculoskeletal conditions are the largest single cause of years lived with disability, and the third-largest cause of disability adjusted life years [2]. Foremost among musculoskeletal disorders is joint disease, and osteoarthritis (OA) in particular [1]. Data from Arthritis Research UK in 2013 [1] show that one-third of people aged 45 years and

over, a total of 8.75 million people in the UK have sought treatment for OA. OA is also prevalent on the global stage, presenting a significant burden to an ageing population. In Singapore, for example, OA is one of the five leading causes of disability [5]. In the United States, about 10% of adults over the age of 50 suffer from the disease [6]. Beyond its direct impact, pain and lack of mobility associated with the disease have considerable social, psychological and economic impacts [7–9].

Of particular importance to this research is the 'treatment gap'. Approximately 13% of osteoarthritis sufferers are unresponsive to conservative care, yet are unsuitable for the surgical procedures that can successfully treat end-stage disease [10]. This manifests in a protracted period in which the patient experiences debilitating pain, reduced quality of life, and a significant financial burden. The typical knee osteoarthritis treatment gap extends 20 years [10]. Based on Arthritis Research UK data [1], this equates to approximately 630,000 people in the UK, and is predicted to rise to over 1,000,000 people by 2035. Consequently, increased attention is being given to treatment procedures with the potential to arrest the degradation process in its earliest stages to narrow this treatment gap [11, 12]. Many attempts have been made to treat early OA [13–16], mainly using 'local' approaches that aim to treat a defect in a specific region of a joint, preserving the majority of tissue in the joint. These can include, for example, tissue-engineered replacement, cell implantation or load modification procedures such as osteotomy. Such treatment, however, has met with limited success.

For any of these 'localised' approaches to work effectively, we require both a better understanding of what constitutes functionally-viable tissue, and a way to distinguish the non-viable tissue from the surrounding viable tissue in the joint that can be used during early-stage treatments. Currently, the surgeon has no accurate or objective way of judging, short of his or her visual and tactile impression, the integrity of the articular cartilage encountered at surgery. This visual impression is important, but it is now widely accepted that the visually normal tissue in a damaged/diseased joint is not necessarily healthy [17–19]. Although arthroscopic grading systems can be used to classify the stage of osteoarthritis or the

severity of a focalised defect, they cannot on their own facilitate treatment [20] or provide information about the tissue surrounding the defect. As a result, localised treatments are arguably poorly informed and the current arthroscopic scoring and other assessment/diagnostic tools may not be adequate for informing clinical decisions. In this thesis, we examine cartilage viability from a mechano-structural viewpoint, with a focus on the role of collagen in OA progression.

1.2 Aims

This focus on collagen raises three main questions which will be addressed in the thesis:

1. *What physical changes occur in collagen during early disease progression?*
   The importance of collagen to cartilage integrity is well known (see Section 1.3.1.3 for discussion). The changes to collagen with disease, however, are not. This thesis first aims to examine and define the physical changes to the collagen fibril itself, in terms of mechanical properties, underlying structural properties, and organisation, during the early stages of OA.

2. *How do collagen changes relate mechanistically to disease progression?*
   Advancing from the knowledge base in the literature, which associates collagen meshwork breakdown with early irreversible damage [15,21,22], the thesis then aims to examine the processes by which a functional network can change to a dysfunctional, OA-like network. Specifically, we focus on fibril organisation and interactions.

3. *How can we detect these changes during surgery?*
   Having established the physical features of early disease, and an indicator of irreversible damage, the thesis finally explores approaches to detecting these features during keyhole surgery. Aiming towards a low-cost, simple technology, this focuses on the quantitative examination of light reflected from the cartilage surface during arthroscopy.

1.3 State of the Art

1.3.1 Articular Cartilage and Changes with Osteoarthritis

Articular cartilage, being devoid of blood vessels, lymphatics or nerves, is a remarkable tissue which surpasses engineering standards but has limited potential for healing and repair. As it experiences extremes of performance and loading during an individual's lifetime, it is no surprise to find that the function of articular cartilage is mechanically complex and that it is prone to degeneration and pathological changes. The mechanical performance of cartilage is based on its underlying structure, illustrated in Figure 1.1 [23], which has been well documented (e.g. [24]). Several studies have addressed the importance of the integrity of the solid cartilage matrix and its role in mechanical performance [25, 26]. Therefore, it is important to understand each constituent of cartilage and how these components relate to disease progression.

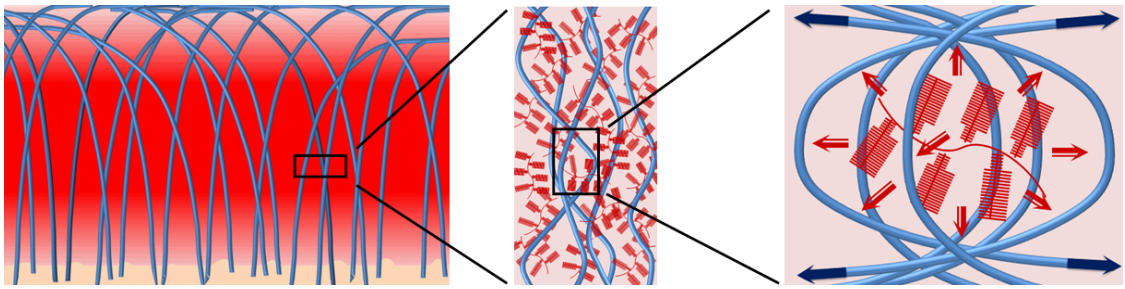


Figure 1.1: Hierarchical structure of articular cartilage, showing the organisation of collagen at different length scales from millimetre (left) to micrometre (right). On the left, the 'Benninghoff' arcades of collagen fibre orientation, which represent the predominant orientation of collagen fibrils on the mesoscale within a given region, are illustrated with bone at the bottom of the diagram. The typical distribution of aggrecan to form the functional unit of load carriage is illustrated for healthy tissue in red (left), and its entanglement within the collagen meshwork, which is pseudo-random at lower level of scale (centreand right) [23].

1.3.1.1 Composition of Articular Cartilage

In general, 60-80% of the total wet weight of cartilage is fluid such as interstitial water and electrolytes [25, 27]. The remaining 20-40% of the tissue is composed of solid extracellular matrix (ECM) and chondrocytes [27]. Each component has its own role in maintaining cartilage function under external forces.

Chondrocytes, a specialised cell type, comprise approximately 4% of the net weight of the tissue [27]. They vary in shape, number and size, depending on the anatomical region of the articular cartilage where they are found. Although they do not directly contribute to the mechanical properties of cartilage, the mechanosensitive chondrocytes proliferate and secrete ECM in response to mechanical stimuli within the individual microenvironment [28]. Chondrocytes are mesenchymal cells that differentiate during development; however cell division does not occur in healthy adult articular cartilage [29], thereby limiting the regenerative capacity of cartilage after injury.

Articular cartilage ECM includes various constituents such as collagen, proteoglycans and other noncollagenous proteins. The ECM and its interplay with the interstitial fluid play a pivotal role in dictating the mechanical performance of cartilage. Collagen with its triple helical structure comprises 15-20% of the net weight of cartilage and is responsible for its tensile strength as well as determining tissue anisotropy [6, 30, 31]. Different types of collagen such as collagen type II, VI, IX, X, and XI are the main constituents of articular cartilage, with type II being the predominant type of collagen in adult cartilage [31, 32]. At a few micrometres in length, the orientation of collagen fibres is pseudorandom, easily forming an inter-connected network which provides effective entanglement of aggrecans [33–35]. These are the major proteoglycan constituents of articular cartilage, providing tensile stiffness and maintaining cartilage volume [36]. The strength of the matrix thus arises from both collagen-collagen and collagen-proteoglycan interactions [37, 38].

Aggrecan (Figure 1.2), with a bottle brush structure, is composed of a core protein with negatively-charged chondroitin sulphate and keratan sulphate side chains. Three globular domains (G1, G2 and G3) and three interglobular domains

form the core protein of aggrecan [39]. The G1 domain at the N-terminus interacts with a link protein to attach aggrecan to the hyaluronan backbone and the G3 domain is located at the C-terminus of the glycoprotein. G2 and G3 domains link the keratan sulphate and chondroitin sulphate side chains to the core protein [40]. The fixed charge density of aggrecan attracts water and positively-charged ions from the synovial fluid, producing osmotic pressure which is counteracted by the tense collagen meshwork (Figure 1.1, right). When constrained by the collagen network, the large aggrecan macromolecules are deformed and compressed, together forming a low-permeability structure which retains fluid pressure. This water-swollen property plays an important role in cartilage, resisting compression under loading [41].

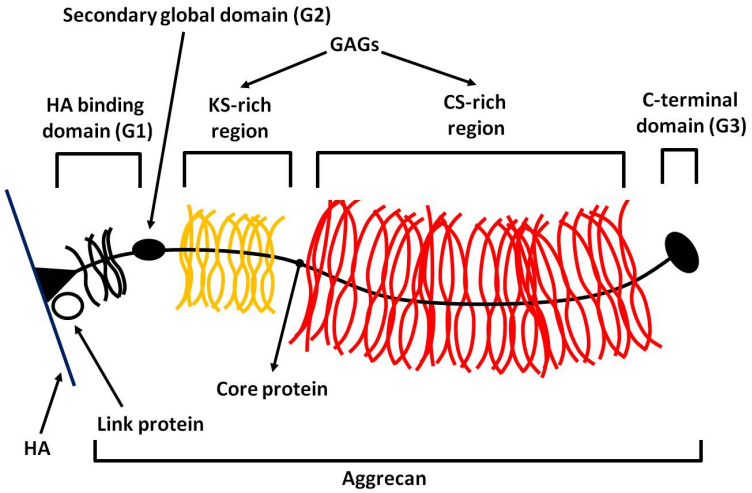


Figure 1.2: The structure of aggrecan. HA - hyaluronan; KS - keratan sulphate; CS - chondroitin sulphate; GAGs - glycosaminoglycans.

1.3.1.2 Structure of Articular Cartilage

Cartilage can generally be divided into four different zones, each with different matrix compositions, mechanical, metabolic and morphological properties [28]. From top to bottom (Figure 1.3, left), these are the superficial, middle (or transitional), deep (or radial) and calcified zones. The alignment of the collagen is different in each zone and chondrocytes also vary in shape, number and size (Figure 1.3, right). When cartilage is examined from the superficial to the deep zone, the water content and the collagen gradually decrease. Each zone plays a different role in contributing to the functional properties of articular cartilage.

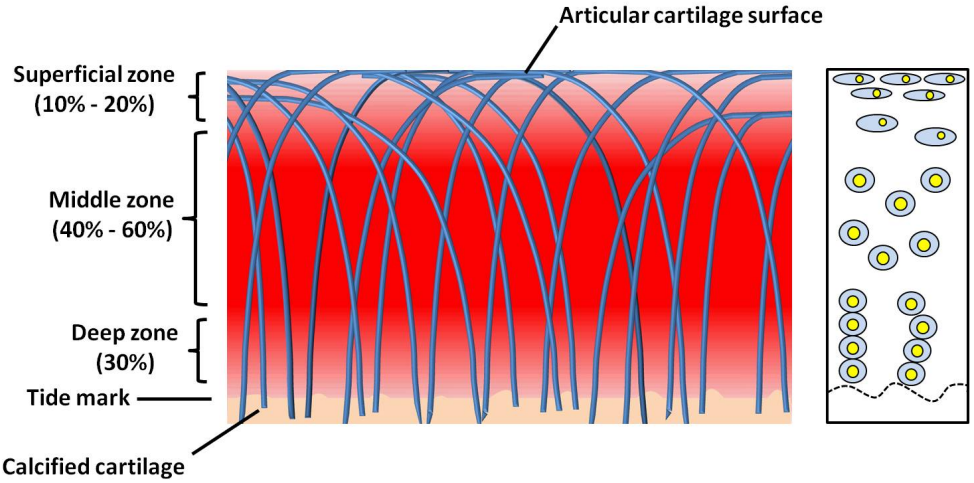


Figure 1.3: A schematic diagram showing the four zones of articular cartilage and the orientation of collagen fibrils (left) and chondrocyte organisation (right) in the different zones. The collagen fibrils are shown in blue, the yellow region shows the calcified zone, and the line between yellow and red colour shows the tide mark. From top to bottom, chondrocytes are flattened and smaller in the superficial zone and become spherical in the middle zone. In the deep zone, chondrocytes are typically aligned along the collagen fibrils and perpendicular to the joint line.

The calcified zone forms the transitional region between articular cartilage and subchondral bone. In the deep calcified zone, few chondrocytes are present [27]. Collagen type X is only found in this zone, aiding cartilage mineralisation and maintaining structural integrity [42].

In the deep zone, collagen fibrils are the largest in diameter. They are predominantly oriented perpendicular to the surface and are well organised. The main function of these collagen fibrils is to strengthen the bond between cartilage and bone [42, 43]. Chondrocytes in this zone are packed and align along the collagen fibrils. Although deep zone chondrocytes have twice as much surface area and volume as cells in the superficial zone, yet they show around 10-fold higher synthetic activities [44].

The middle zone is a transitional zone between the superficial and deep zones. The collagen fibrils change from a perpendicular orientation to a random orientation. Chondrocytes are rounded at low density and contain synthetic organelles.

The last zone is the superficial zone which accounts for 10-20% of the total articular cartilage thickness. The superficial zone contains the highest density of collagen organised into the thinnest fibrils, while chondrocytes are flattened and smaller and are oriented parallel to the surface. In both the superficial and middle zones, the main function of chondrocytes is to synthesise ECM composed of collagen type II, IX and XI and proteoglycans [45]. Meanwhile, the content of aggrecan is lower than in other zones. The composition and organisation of this zone contribute to tensile strength, resit shear during articulation and adjust fluid permeability [46].

Among all the constituents, collagen, a dominant molecule in cartilage, plays an important role in maintaining structural integrity. The architecture of the collagen meshwork is intriguing (Figure 1.3, left). This arcade-like macro-architecture is known as ‘Benninghoff’ arcades and is widely accepted as a model of the collagen fibril arrangement in cartilage [47–50]. The material strength of the tissue relies on the complex architecture of this collagen meshwork. A theoretical study also showed that this architecture acts to reduce stresses under load [51].

1.3.1.3 Changes in Osteoarthritis

OA is a metabolically-active and dynamic process that includes both destruction and repair processes which may be triggered by a variety of biochemical as well as mechanical insults [7]. Once the balance between destruction and repair has been overcome and a lesion develops, the cartilage will not heal, or will heal only partially under certain biological conditions, and will usually progress to more severe OA [16]. The key features of OA include cartilage degradation, joint stiffening and osteophyte formation [45]. These changes are thought to result from cellular and constituent-level changes in the cartilage layer. Therefore, an improved understanding of the relationships between the mechanical behaviour, composition and structure of cartilage, and their changes associated with disease could lead to the development of better procedures for disease intervention and treatment that can arrest such processes at their earliest stages.

Changes to collagen fibrils and aggrecans are routinely observed in early OA [52]. A loss of tensile strength of the tissue has been found in osteoarthritic cartilage [53, 54]. Collagen breakdown is considerable, constituting a critical and perhaps irreversible step in disease progression [15, 21, 22]. A quantitative immunoassay study has shown that there is increased denaturation of type II collagen at the articular surface in osteoarthritic cartilage [26, 55]. Due to the damaged collagen, the proteoglycans decorin, biglycan and aggrecan are lost from the surface while their contents increase deeper within the cartilage as if to compensate for the superficial loss [56].

In addition to these extracellular matrix changes, it has been found that chondrocyte metabolism also changes [57], exhibiting a decline in proliferative and synthetic capacity [58]. As a result, the mechanics of cartilage are necessarily altered with disease progression [25, 25, 59]. Although the mechanisms of this initiation remain to be determined, it has been found that these changes in structure, composition, and metabolism alter the mechanical behaviours of the tissue.

Direct experimental measurement of such phenomena and relationships, however, is infeasible. Computational models of articular cartilage have therefore been

developed to investigate the mechanical properties of articular cartilage and the effect of changes in cartilage constituents on mechanical properties in OA progression. In addition to describing bulk behaviour, this allows prediction or assessment of the individual constituent responses and properties. Wilson *et al.* developed a fibril-reinforced poroviscoelastic swelling model to predict the equilibrium and transient response of articular cartilage during mechanical stimulation. This model allows the mechanical consequence of compositional changes during OA to be assessed [60]. A viscoelastic model coupled with experimental data was developed to show that the viscoelastic properties of different zones of the cartilage were lower in osteoarthritic cartilage than in normal tissue, suggesting that changes in constituents would affect the mechanical behaviours of cartilage [61]. A further model combining collagen, proteoglycan, fluid and chondrocytes was developed to understand the influence of the pericellur matrix (PCM) composition on the deformation of chondrocytes. Results showed that the PCM plays a significant role in the deformation behaviour of chondrocytes, implying that the PCM may modulate cartilage development, adaptation and degeneration [62]. Through these models, the importance of each component, their functions in cartilage and how they affect the mechanical behaviours of cartilage were shown.

1.3.2 Collagen-specific Changes in Osteoarthritis

Although constituents change during disease progression, collagen remains the most abundant structural molecule in the ECM, resisting tensile deformations and loads. Its architecture provides the material strength of the tissue and reduces stress under load. Macroscopically, fibrillation is the first sign observed at the articular surface in early OA [25, 26]. The disruption or loosening of the collagen network in the superficial zone is closely involved in the initiation of OA [38, 63, 64]. It is also suggested that collagen breakdown is considerable, constituting a critical and perhaps irreversible step in disease progression [15, 21, 22]. Hence, changes to collagen are important during disease progression.

Restructuring of collagen [16, 19, 21, 65], particularly the formation of collagen bundles (e.g. Figure 1.4) has been observed in the OA cartilage surface. Further study also revealed localised regions of collagen meshwork disruption and reconfiguration at early stages of disease before the appearance of histological changes [34]. A recent study also suggested that the bundling of fibrils at the surface is likely to be a mechanically-irreversible step in the damage process [21]. An early simple structural model of collagen was developed to investigate the possible mechanism of this bundling formation. This revealed that it was the entwinement of the collagen fibrils that causes the changes in fibril alignment and bundle formation under load which correspond to images of the osteoarthritic cartilage surface obtained by scanning electron microscopy [65]. This entwinement of the collagen fibrils indicated the importance of their interaction. Later, instead of entwinement, a representative volume element (RVE) model of the collagen fibre network implemented crosslinks between fibrils and found that increased crosslink density within a fibril network has a great impact on material stiffening and further, that fibre alignment affects the strain stiffening of the fibre network [66]. On the other hand, it also implies that decreasing the density of crosslinks between fibrils may result in loss of tensile strength of the tissue corresponding to findings in osteoarthritic cartilage [53, 54]. Therefore, it is believed that changes in fibril interactions are crucial in disease progression [15, 21, 67, 68].

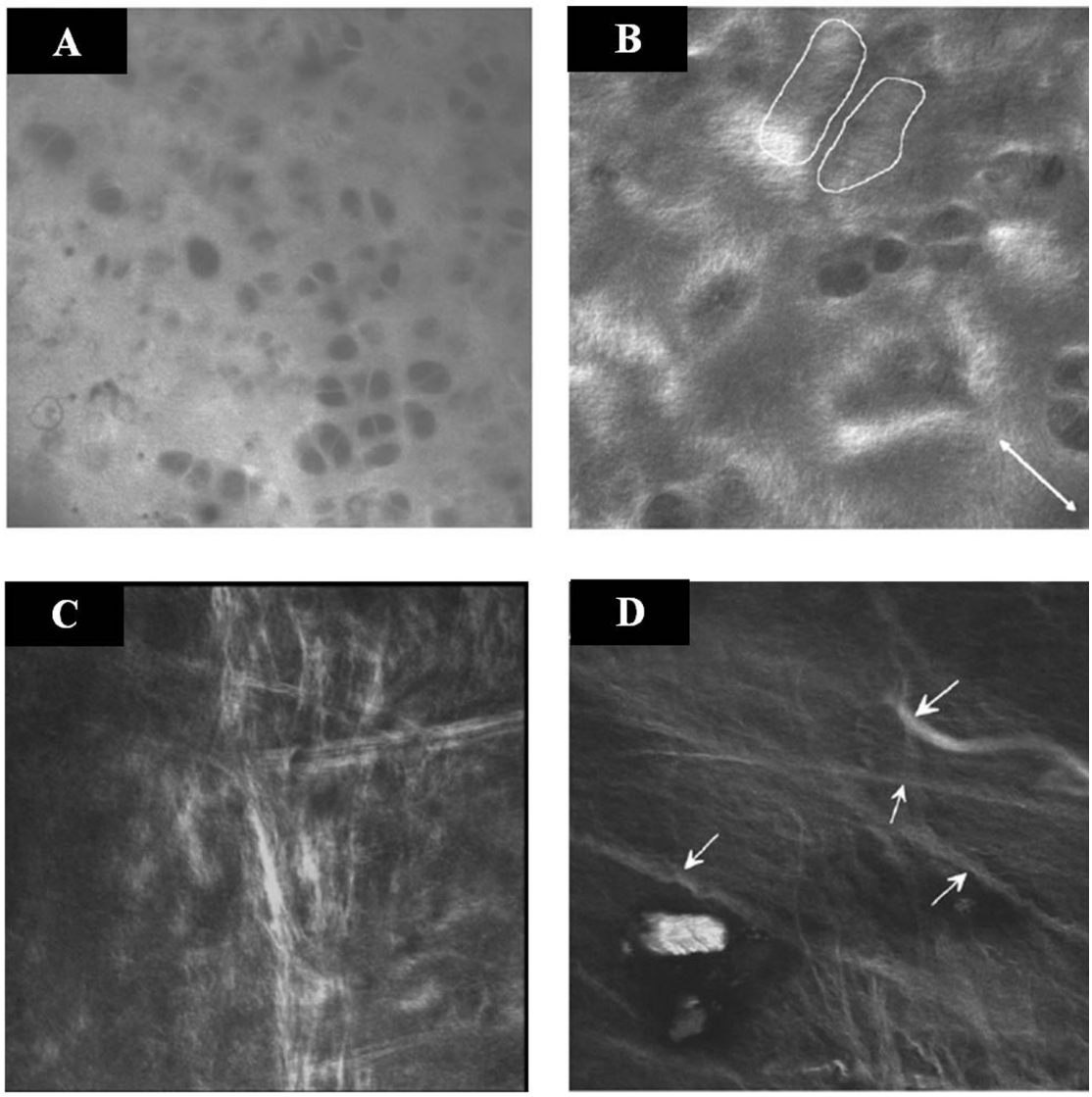


Figure 1.4: Second harmonic generation microscopy shows the surface structure change from (A) a normal collagen configuration (intact meshwork) to (B) sub-micron changes (alignment and minor bundling), (C) micron-scale bundles and (D) finally macroscopic degradation with proximity to a focal defect in bovine cartilage [21]. (image A is 500 × 500 μm, B-D are 200 × 200 μm) (permissions to reuse the contents and figures of these papers have been granted by Elsevier (Appendix B))

Before forming a bundle, rearrangement and reorientation of the collagen fibrils are required. Initial disorganisation and altered orientation of the collagen fibrils has been found to appear while the cartilage surface is still intact and smooth following experimental anterior cruciate ligament section [63]. Since collagen is a birefringent material, this characteristic allows the use of optical-based techniques to observe the orientation of the collagen fibrils by measuring the optical path differences

(retardation, Γ) of the light [59]. The birefringence of a fibril in linearly-polarised light is dependent on the angle between the axis of polarisation and the axis of the fibril, on the thickness of the specimen or the structure, and the organisational pattern of collagen fibres or the density of collagen structures [69]. Birefringence of articular cartilage has been shown to be reduced in the superficial zone, indicating either disorganisation or orientation of the collagen network in the superficial zone in OA cartilage [69]. Later, it was suggested that this reduction in birefringence is due to the derangement of the collagen meshwork in the superficial zone and also that this change occurred before fibrillation was observed [59]. A current collagen-like computational model suggested that the underlying cause of this orientation of the collagen fibrils is related to changes in inter-connectivity between the fibrils [70]. This again demonstrates the importance of the inter-connectivity of the collagen fibrils in cartilage and suggests ways in which it may affect the collagen meshwork during disease progression.

In recent years, with improvements in nano-biotechnology, it has become possible to observe OA prior to the onset of micro- or macro- structural damage to articular cartilage [71]. Atomic force microscopy (AFM) has been widely used for imaging and testing of mechanical properties in biological tissue because of its high spatial resolution, fine force sensitivity and versatility [68, 72, 73]. In 2009, Soltz *et al.* used indentation-type AFM for early detection of OA in both animal models and human specimens [68]. They observed changes in fibril thickness and in nanostiffness of cartilage specimens with disease progression. From their animal model, they even found a transient increase in the nanostiffness of the collagen fibril meshwork at the cartilage surface before the loss of cartilage integrity. Further studies measured a single collagen fibril extracted from osteoarthritic cartilage and found that the collagen fibrils stiffened with disease progression [74, 75]. These measurements suggested that changes at the molecular level lead to changes in nanostiffness of collagen fibrils. Although AFM is not suitable to directly measure collagen changes in collagen molecules, yet in combination with other techniques, it could provide an insight into collagen fibril changes. An example of such an application was

reported by Wallace *et al.* who found structural changes in collagen fibrils in bone from wild type mice and from genetically-modified mice whose collagen protein structure had been altered by changing the *colα1* allele [76]. Their observations provide insight into the structural basis for changes in bone composition, geometry and mechanical integrity in bone. Therefore, investigation of the nanomechanical properties of collagen fibrils is also important for understanding the disease.

Overall, changes in the mechanical properties of collagen fibrils at the nano- or micro- scale and arrangement of the collagen fibril meshwork with disease progression seems to be an inevitable process during OA. However, the mechanism underlying these alterations in collagen fibrils still remains to be elucidated. Computer modelling provides a platform to understand the possible mechanism of changes in the collagen meshwork, but the findings of these models suggest correlation rather than a causation. Therefore, to increase understanding of changes in the mechanics of the collagen meshwork, the way in which it changes, and how these changes affect the mechanical behaviour of the tissue still need to be explored.

1.3.3 Intraoperative Diagnostic Techniques in Osteoarthritis

Early cartilage disruption occurs at the biomolecular level but without noticeable visible changes to the tissue surface and macro-structure [26]. Arthroscopic evaluation is a current clinical technique to evaluate pre-OA chondral lesions which do not involve bone and generally are not visible by radiography [77]. However, this evaluation is more qualitative based on clinicians' experiences of evaluating softness, roughness and other features on the cartilage surface; therefore, access to such quantitative information could both improve the accuracy of the cartilage assessment and benefit clinicians' decision making regarding early treatment.

Currently, a number of intra-articular probes have been proposed and are being studied such as ARTSCAN - an indentation-based device [78], infra-red fibre optic probe (IFOP) [79] and arthroscopic optical coherence tomography (OCT) probe [80]. Optical-based techniques have emerged in recent decades because of their characteristics of high sensitivity and ability to measure at the molecular scale. This allows increased accuracy of intra-cartilage assessment. In this section, we will mainly discuss these techniques which include OCT, second harmonic generation (SHG), near infra-red (NIR) spectroscopy, Raman spectroscopy and ultraviolet-visible (UV-VIS) spectroscopy.

OCT (i.e. Figure 1.5) is sensitive to OA-associated changes in cartilage birefringence [81]. It has been shown to be feasible for articular cartilage assessment in OA [77, 82–84]. Further study showed that combining polarisation controllers can render OCT sensitive to birefringence detection and improve OCT for early OA assessment [84]. In 2010, Chu *et al.* demonstrated that OCT may become a potential tool to complement arthroscopy for clinical use by providing quantifiable, microscopic-resolution cross-sectional information on cartilage [77]. However, OCT has its limitations including heavy dependence on operator-use and image post processing [85].

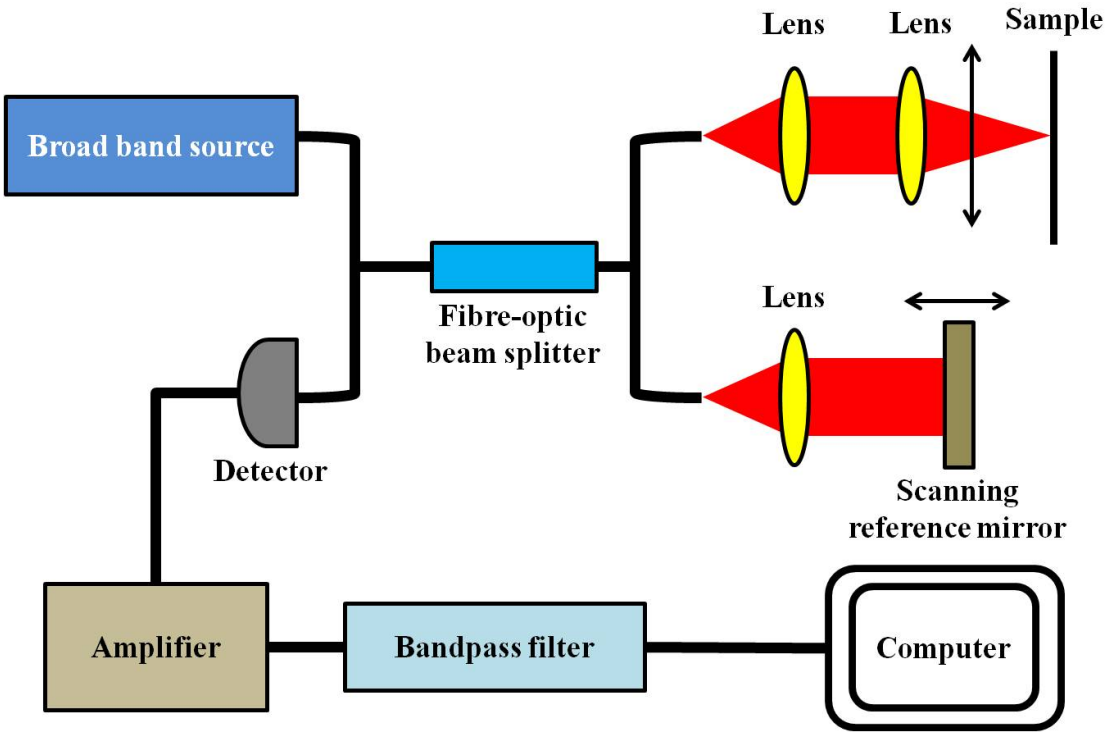


Figure 1.5: Schematic diagram of the general OCT design. Red line: broad band light.

SHG microscopy (i.e. Figure 1.6), because of its high sensitivity to collagen organisation, shows promise of becoming a powerful diagnostic tool. It is often used for collagen imaging in biological and medical science. Owing to the important role of collagen in cartilage, SHG microscopy could have profound implications for cartilage research. With SHG images, changes in orientation and organisation of collagen in the different zones could be observed [86]. At the early stage of OA, collagen content is maintained, but its organisation is perturbed [6]. Therefore, developing an SHG arthroscope would benefit early OA detection by detecting changes in the SHG signals of collagen organisation. SHG, coupled with a two-dimensional spring-mass network model, has been used to image and investigate architectural changes in the collagen meshwork at the osteoarthritic cartilage surface, providing more information about early OA detection [21]. SHG microscopy has also been suggested to show potential to precisely identify the stages of disease, which would improve the accuracy of cartilage assessment [87]. In addition, SHG could distinguish different types of collagen through use of polarisation settings [88,89]. Since different types of

collagen are present in the different cartilage zones, this could provide information regarding which zones of the cartilage were assessed. However, challenges remain to be overcome before SHG arthroscopy can be developed. One of the challenges is collection of the SHG signal, since both the excitation and emission wavelengths travel the same path, although this can be overcome by applying filters or using two different fibres. At the same time, it may be necessary to introduce several magnifications to obtain information at different levels. The biggest challenge could be minimisation of SHG microscopy. To develop SHG arthroscopy, the device should be movable and have a small, long and thin probe instead of a set of objectives, which challenge the effectiveness of laser generation and the cooling system.

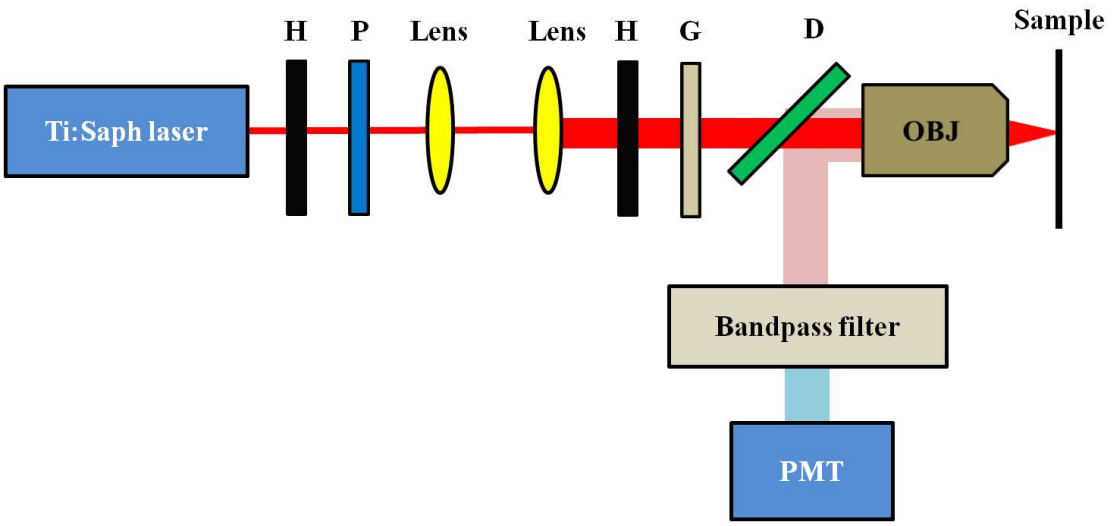


Figure 1.6: Schematic diagram of the general SHG design. H: half wave plate; P: polariser; G: galvo mirror; D: dichroic beamsplitter; PMT: photomultiplier tube; OBJ: objective; red line: laser; light red line: reflected light; light blue: reflected light passes filter.

NIR spectroscopy (i.e. Figure 1.7) has also been proposed as a potential tool. This is mainly because NIR penetrates deeper into the tissue [90] and its typical spectral regions correspond to C-H, O-H, N-H and S-H bonds, which fundamentally make up the cartilage matrix. The potential of this technique for articular cartilage evaluation has been investigated in a number of applications such as measurement of the thickness of cartilage and structural changes [91–97]. These studies showed that NIR spectra can be used to monitor disease progression in OA and provide better

cartilage evaluation [98–101]. However, absorbances in NIR spectra are very low and generally arise from a combination of molecular species which makes it difficult to analyse specific peaks. Therefore, further methods to analyse the spectrum are required. Recently, a study showed that using principal component analysis (PCA) techniques can overcome this signal overlap to evaluate the composition of cartilage tissue [102]. Brown *et al.* applied Beer's Law dimensionality reduction method to resolve spectral measurements from NIR into chemical concentration [103]. Since compositional changes are also a sign of OA, this information could improve assessment of OA cartilage.

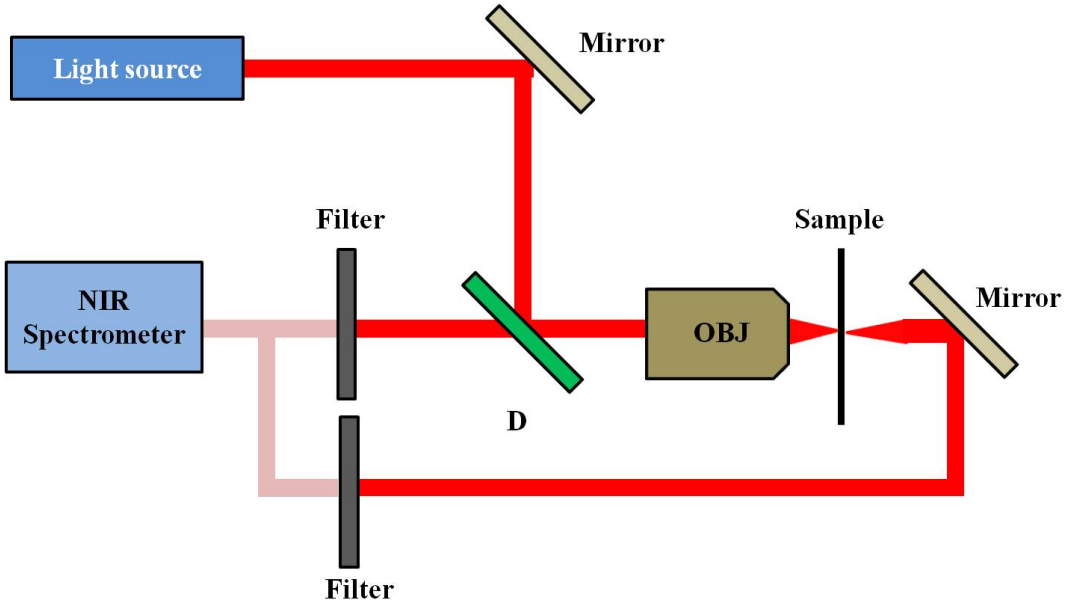


Figure 1.7: Schematic diagram of the general NIR design. D: dichroic beamsplitter; OBJ: objective; dark red line: laser; light red line: reflected and transmitted light pass filter.

Unlike NIR spectroscopy, Raman spectroscopy (i.e. Figure 1.8) encounters less interference from water in the tissue, producing better spectra and also eliminating the necessity to process or dehydrate the samples before analysis [104], enabling characterisation of biomolecular changes in living cartilage tissue. Recently, Raman spectroscopy has been used to study microstructual alterations in cartilage [105], molecular changes in osteoarthritic tissue [106], the ability to distinguish between various cartilage tissues [107] and molecular changes in strained collagen tendon fibres [108]. Raman spectroscopy has been successfully used with a custom-built optical fibre probe to assess joint tissue, demonstrating the proof of principle for Raman arthroscopic measurement of joint tissue. [109]. Like SHG microscopy, polarised Raman spectroscopy has also been shown to optimise the assessment of tissue and can be used to investigate the orientation of collagen fibrils at early stages of disease [110–113]. Polarised Raman has been demonstrated to effectively detect a wide spectrum of biomolecular changes associated with cartilage damage prior to visible histological changes, including a decrease in glycosaminoglycans and changes in amide III (collagen) Raman bands [112]. In addition to measurement of biomolecular changes, detection of the orientation of collagen fibrils has been demonstrated [113–115]. These results suggest that Raman spectroscopy could be a powerful tool for diagnosis and detection of early disruption to cartilage at the molecular level.

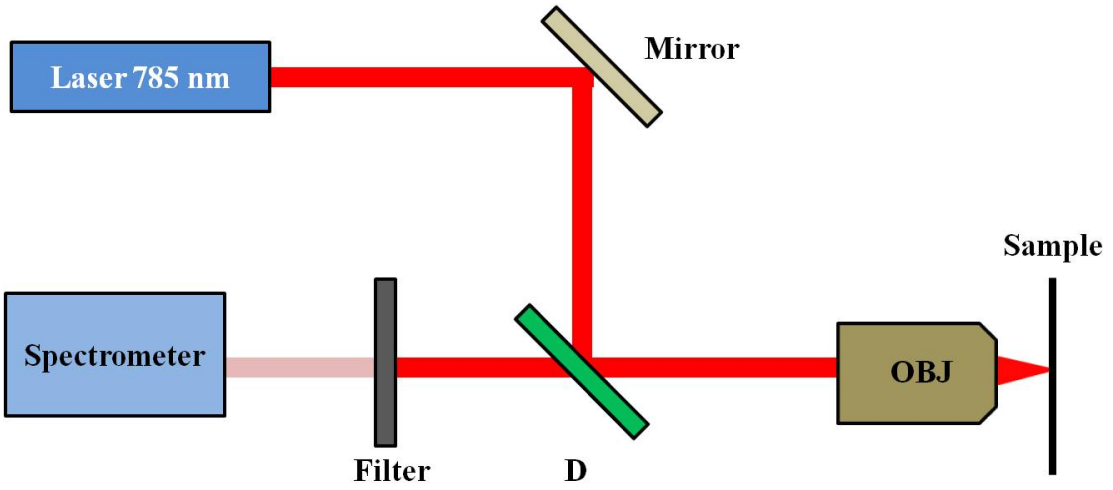


Figure 1.8: Schematic diagram of the general Raman design. D: dichroic beamsplitter; OBJ: objective; dark red line: laser; light red line: reflected light passes filter.

These optical-based techniques show great promise for the development of new diagnostic tools. However, addition of a laser light source, together with heavy dependence on image processing or further design is required in diagnostic tool development. Ultraviolet-visible-near infra-red (UV-VIS-NIR) spectroscopy provides an easier and simpler option because the scattering profile of UV-VIS-NIR spectroscopy from the articular surface occurs over a wavelength range approximately available to the arthroscope camera. Additionally, the wide spectral range encompasses several wavelengths including ultraviolet, visible, and near-infra-red laser wavelengths currently used in the clinic as well as some potential laser wavelengths which may be considered for clinical application. Therefore, without coupling with other devices, the only thing that is required is to develop a method to analyse the spectra which could provide appropriate information for assessment of the cartilage. Kinnuen *et al.* analysed visible light spectral imaging (420 to 720 nm) with sophisticated spectral analysis and also transformed the colour coordinates to evaluate the integrity of cartilage [116]. Cartilage thickness could also be assessed and visualised over the joint tissue by analysing specific wavelengths of the visible or near-infrared wavelength range [117, 118]. It has also been found that the spectra of cartilage in the visible and NIR range could correlate with biomechanical properties, biochemical composition, histological score of cartilage, and the thickness of non-calcified cartilage [119].

In short, optical-based techniques could provide improved accuracy of measurement compared to current techniques, and have been shown to have the ability to assess cartilage properties such as roughness and thickness. Either combining these approaches with current techniques or developing a new arthroscopy technique based on this principle would improve the quality of diagnosis. However, among these techniques, knowledge of the relationship between spectra and collagen structural features is still incomplete. Therefore, there is a need to fill this gap to provide more information about OA.

1.4 Approach and Chapter Overview

This thesis combines experimental and computational approaches to address the questions and aims outlined in Section 1.2, in light of the state of knowledge/state of the art outlined in Section 1.3.

Chapter 2 first examines the physical properties of collagen fibrils in the articular cartilage surface, and their changes with disease. Following an extensive sample optimisation and equipment build, AFM and Raman spectroscopy measurements are applied to probe structural and mechanical properties at the nanometre to micrometre scales. Topographical, elastic and viscoelastic properties probed by AFM are supplemented by measurements of the protein secondary structure by Raman spectroscopy, specifically focussed on quality.

Having established physical changes to the fibrils themselves, Chapter 3 examines the role of fibril organisation and interactions in the degradation process. Here, bottom-up models of the collagen meshwork are developed, representing a range of fibril organisations and simulating their response to applied load in terms of mesoscale mechanical resistance, local restructuring and susceptibility to failure to establish key indicators of irreversible damage.

Finally, a UV-VIS-NIR approach is proposed as a method by which arthroscopic imaging can be supplemented with a quantitative view of early surface damage. Patterns in absorbance bands are explored as potential diagnostic markers, and scattering-related features analysed via a Mie simulation. Taking advantage of the light source, probe and fibreoptics already used in standard arthroscopy, this offers an opportunity to provide key information to the surgeon without changing the radiation or instrumentation to which the patient is exposed.

2

Characterisation of Osteoarthritis Progression on the Articular Cartilage Surface

Contents

2.1 Introduction 23
2.2 Methods 24
2.2.1 Sample Collection 24
2.2.2 Method Development 27
2.2.2.1 Optimisation of Sample Preparation for AFM 27
2.2.2.2 System Build for Polarised Raman Spectroscopy 41
2.2.3 AFM - Data Collection and Analysis 51
2.2.3.1 Data Collection 51
2.2.3.2 Stiffness and Young's modulus 51
2.2.3.3 Data Analysis 53
2.2.4 Raman Spectroscopy - Data Collection and Analysis . . 57
2.2.5 Histology 60
2.2.5.1 Sample Preparation 60
2.2.5.2 Grading 60
2.2.6 Statistical Analysis 64
2.3 Results 65
2.3.1 Histological Analysis 65
2.3.2 Atomic Force Microscopy 67
2.3.2.1 Topography 68
2.3.2.2 Mechanical Properties 72
2.3.3 Raman Spectroscopy 76
2.4 Discussion 80
2.4.1 Topographical Features 80
2.4.2 Mechanical Features 80

2.4.3 Raman Spectral Analysis 82
2.4.4 Scoring Systems 83

2.1 Introduction

The collagen meshwork is one of the main components of articular cartilage and is central to its function. As described in Section 1.3.2, disruption of the collagen meshwork is strongly linked to OA progression [15, 21, 68, 120]. These studies, through a range of experimental approaches, have identified the bundling of collagen fibrils as an important step in the disease process, although the precise role of this restructuring is yet to be established. The physical changes to collagen itself, i.e. at and below the fibril level, are less clear.

One of the best known changes is in crosslinking. Intra-fibrillar crosslinking (in particular via advanced glycation endproducts, AGEs) has been observed to increase in osteoarthritic cartilage [121–124]. These crosslinks have been found to alter the mechanical properties of collagen, specifically by stiffening the fibril [125–127]. Numerical modelling studies suggest that increased crosslinking may also act to reduce tissue viscoelasticity by limiting inter-molecular sliding [128]. This has the effect of reducing the energy that can be dissipated during fibril deformation, restricting a major mechanism of collagen load carriage. The accumulation of AGEs crosslinks may therefore stiffen the wider cartilage collagen network, potentially making it more brittle and susceptible to mechanical failure [123, 124, 129].

In this chapter we aim to characterise the physical changes to collagen during OA initiation and progression using a well-phenotyped manifestation of the disease: anteromedial OA of the knee. Specifically, we probe the structural and mechanical properties of collagen at the articular surface, using AFM and Raman spectroscopy. Following an extensive optimisation of sample preparation for AFM, and a system build for Raman spectroscopy, AFM was used to measure structural and mechanical properties (Young's modulus, loss tangent), and Raman spectroscopy to assess fibril-level organisation, measures of collagen quality, and the relative concentration

of collagen to other key matrix components. Finally, these properties are related to histological grading to assess changes with disease progression.

2.2 Methods

2.2.1 Sample Collection

Human articular cartilage was obtained from the tibial plateaus of knee joints (n = 10, three males and seven females, aged 61 ± 9 years, six left knees and four right knees) after total knee arthroplasty (TKA) or unicompartmental knee arthroplasty (UKA). Sample collection was managed by the Oxford Musculoskeletal Biobank, with informed donor consent in compliance with national and institutional ethical requirements, the United Kingdom Human Tissue Act, and the Declaration of Helsinki (HTA Licence 12217 and Oxford REC C 09/H0606/11).

After extraction, samples were quickly frozen at −80°C and thawed immediately prior to their use in experiments in order to minimise the number of freeze-thaw cycles, which is known to affect the integrity of cartilage samples [130, 131]. A pictorial overview of the sample preparation protocol is given in Figure 2.2. Cylindrical osteochondral cores (ϕ = 6 mm) were punched out from the tibial plateaus under the guidance of an orthopaedic registrar, who also provided clinical assessment of the excised tissue (Figure 2.2A). All cores were immersed in ice-cold-phosphate-buffered saline (PBS) after punching to minimise further degradation. The edge of each core was cut with a surgical scalpel to mark the direction of disease progression and each core was mounted onto a glass slide. Images of the whole core and the middle of the core were taken using a digital microscope (VHX-600, Keyence Corp., Osaka, Japan) with a high-performance zoom lens (VH-Z20W) (Figure 2.2B). Subsequently, samples were immersed in ice-cold-distilled-water and subjected to Raman and UV-VIS-NIR spectroscopy measurement (Figure 2.2C). Each core could therefore be measured at a single position for UV-VIS-NIR spectroscopy and at five positions at 1 mm intervals for Raman spectroscopy, AFM and histology (Figure 2.1).

After measurement, cartilage from each core was removed with a scalpel and the top edge of each core was cut to mark the surface of the cartilage (Figure 2.2D).

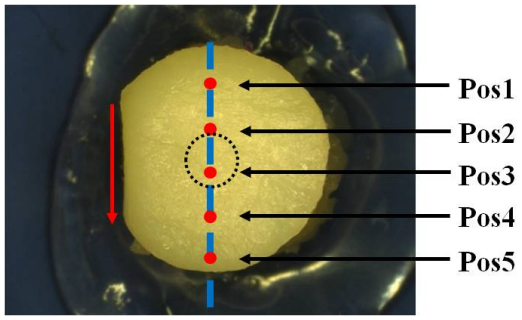


Figure 2.1: Representative photograph showing the measuring points (red points for Raman, AFM and histological measurements; black dotted circle for UV-VIS-NIR measurement) on a sample of human articular cartilage. The red arrow shows disease progression. The blue dashed line shows the cutting line after optical measurement.

Each core was then cut in half along the direction of OA progression, and processed for AFM and histology (Figure 2.2E-G). Details of sample processing for AFM and histological staining are provided in Section 2.2.2.1 and Section 2.2.5.1 respectively.

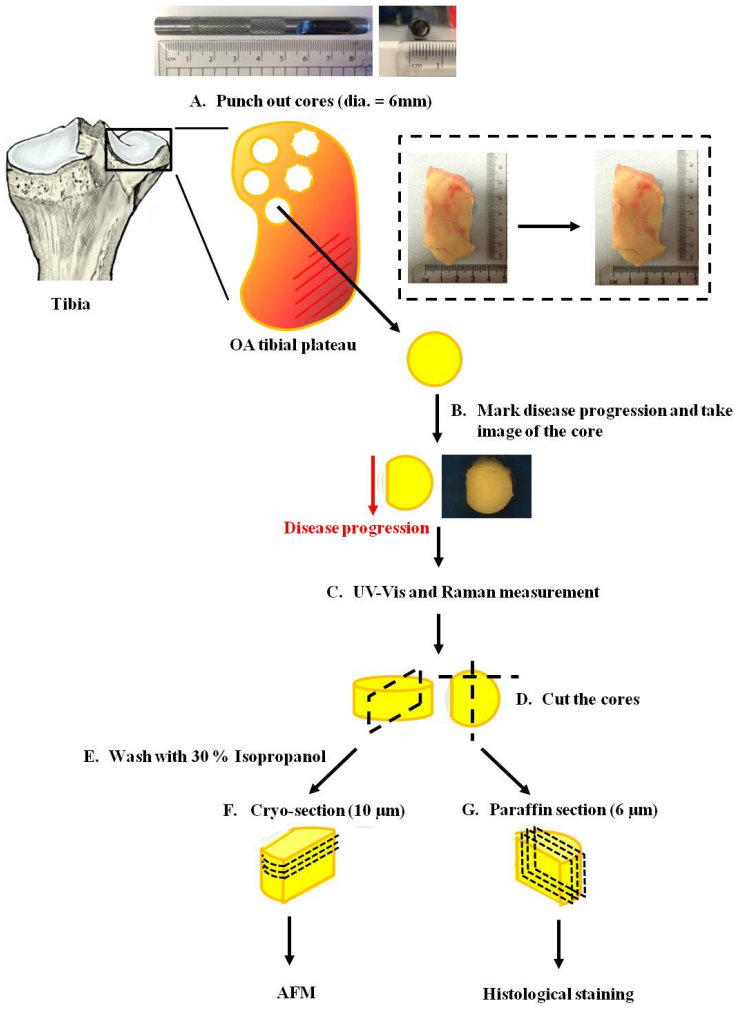


Figure 2.2: Schematic diagram of the sample preparation process. Red arrow: disease progression determined by a clinician. Black dashed lines: cutting line. dia.: diameter.

2.2.2 Method Development

The experimental methods used in this chapter required development and optimisation for application in cartilage. The following section describes the development of an appropriate sample preparation protocol for scanning probe measurements of cartilage, and the set-up and testing of a polarised Raman spectroscopy system.

2.2.2.1 Optimisation of Sample Preparation for AFM

Sample preparation is critical for AFM due to its high sensitivity to surface properties. It was therefore necessary to develop a protocol to produce consistent, high-quality measurements of collagen in the cartilage surface. Using bovine cartilage, we tested and optimised a number of preparation steps (sample presentation, washing, enzymatic treatment, temperatures and treatment times) to expose the collagen meshwork with minimal changes to its properties. Figure 2.3 illustrates the decision paths for the optimisation on bovine cartilage samples. This optimisation was based on two parameters: (qualitative) clarity of fibrils in topographic imaging; and (quantitative) Young's modulus. As a clean and clearly-exposed collagen fibril is a prerequisite for measurement of its material properties, the image quality was the first criterion used to assess the protocol. Young's modulus was chosen as a representative property to describe the mechanical integrity of the collagen.

The optimisation process tested the effects of washing to remove debris and lipids, sectioning to reduce sample drift, and enzymatic treatment to remove ground substance. Finally, enzyme combinations and treatment times were optimised for best exposure without compromising mechanical properties.

2.2.2.1.1 Bovine Cartilage Cores

To avoid the possibility of damage to the collagen from tissue processing, measurements were first attempted on the surface of fresh, 6-mm cores of cartilage. After extraction, each core was first washed with PBS, trimmed to a thickness of approximately 1 mm and glued to a glass slide for measurement, however meaningful data (i.e. reliable tip-surface contact) could not be obtained. It was

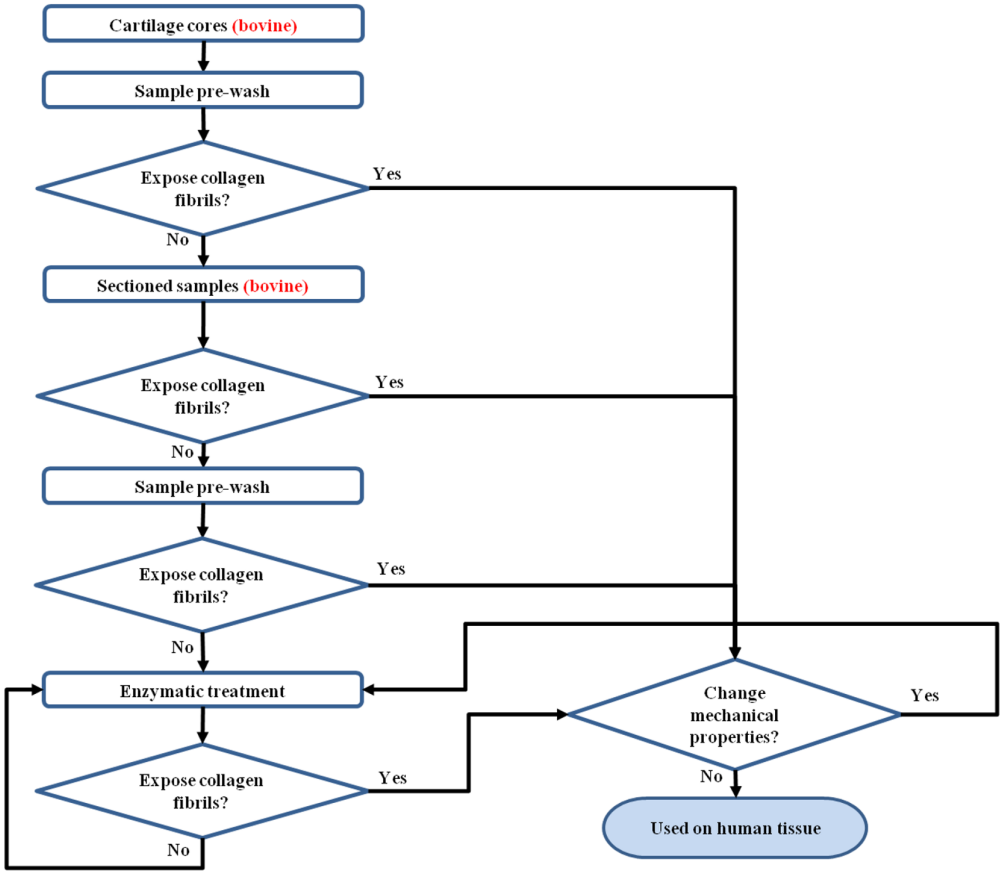


Figure 2.3: Decision paths of the strategy for optimisation of sample preparation on bovine cartilage. Optimisation began with fresh bovine cartilage cores, testing whether collagen could be observed by AFM after a number of sample processing steps, including sectioning and enzymatic treatments. Preparation was continued until collagen fibrils were well exposed, after which the changes in mechanical properties were measured. An iterative process was followed to balance the exposure of fibrils with the minimisation of mechanical effects, before application to human tissues.

first hypothesised that this problem was due to debris and lipids on the cartilage surface. Cores were therefore washed with PBS (control), 30% isopropanol [132], or absolute ethanol to remove debris and lipids and re-tested. Meaningful data still could not be obtained. This failure was due to a combination of the microscopically uneven surface of the cartilage preventing imaging within the 7 μm z-range of the instrument, and rapid dehydration of the sample causing drift. Drift and sample roughness were addressed by cryo-sectioning parallel to the surface to produce thin samples that could be imaged within the z-range of the instrument, with drift

minimised by reducing the bulk water content of the tissue.

2.2.2.1.2 Cryo-sectioned Bovine Cartilage

Hemi-cylinders of fresh cartilage were washed in PBS (control), 30% isopropanol, or absolute ethanol, then snap-frozen in liquid nitrogen and stored at $-80°C$ for cryo-sectioning. All frozen tissues were embedded in water-soluble OCT mounting medium (Thermo Fisher Scientific, Waltham, MA, USA), cryosectioned (cryostat 2800 Frigocut, Reichert Jung, Depew, NY,USA) at a thickness of 10 μm parallel with the articular surface (Figure 2.2F), and mounted on glass slides. The first cut section from each sample was considered to be the surface of the cartilage. Up to five to six sequential sections were taken to represent the remainder of the superficial zone (considered to be up to $\approx$200 μm [133, 134]). In each case, OCT mounting medium was removed after sectioning by immersion in distilled water for 10 minutes with three changes.

First, the effects of washing on image quality were observed. Figure 2.4 shows that pre-washing samples with either absolute ethanol or 30% isopropanol improved the image quality compared to PBS, with 30% isopropanol being the most effective at removing debris from the surface. These results helped us to develop an initial step for sample preparation and presentation. However, collagen remained embedded in 'ground substance', thought to be proteoglycans (Figure 2.4) and in many samples the fibrils were not sufficiently exposed for reliable mechanical measurements. Enzymatic treatments were then implemented to better-expose the collagen fibrils.

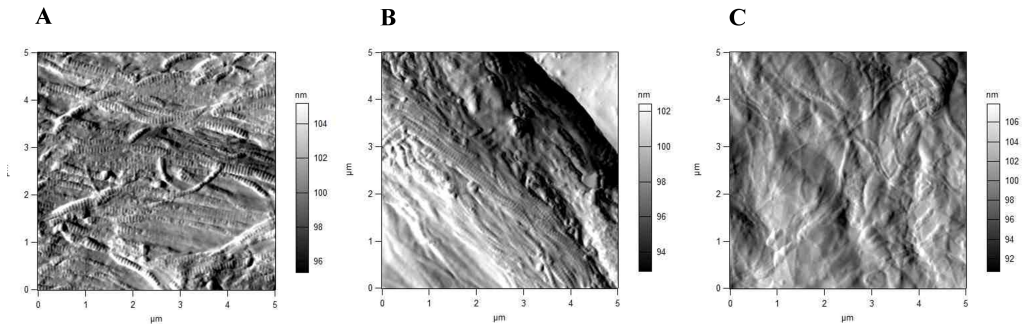


Figure 2.4: Representative AFM amplitude images of 5 × 5 μm samples of bovine cartilage following different pre-wash treatments: (A) PBS pre-wash (control), (B) ethanol pre-wash and (C) 30% isopropanol pre-wash.

2.2.2.1.3 Enzymatic Treatments - Hyaluronidase (Temperature)

The first enzymatic treatment used hyaluronidase (Sigma-Aldrich, St Louis, MO, USA) [65], which attacks the hyaluronic acid backbone of the aggrecan macromolecule. Figure 2.5 shows the enzymatic treatment protocol. After OCT removal, samples were treated with 1 mg/ml hyaluronidase in PBS at 25°C (room temperature) or in a 37°C incubator for 30 minutes. Following the enzymatic treatment, the samples were washed in three changes of distilled water for 10 minutes each time and then dried at room temperature for at least 30 minutes. Finally, samples were analysed by AFM and the effect on image quality recorded. As shown in Figure 2.6, samples treated with hyaluronidase showed better results than without treatment and we found that samples incubated at 37°C showed the best results, as expected due to the temperature dependence of enzyme activity.

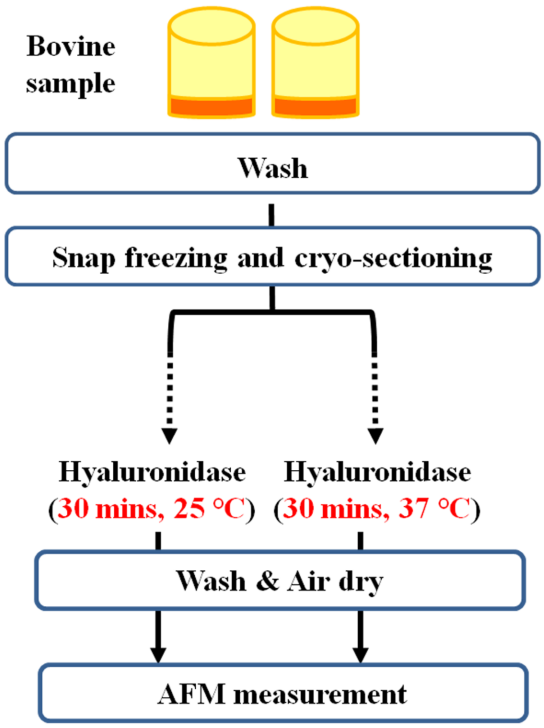


Figure 2.5: Flow chart of hyaluronidase treatment of the samples after a 30% isopropanol pre-wash at different temperatures for 30 minutes. The dotted line indicates the process of OCT removal.

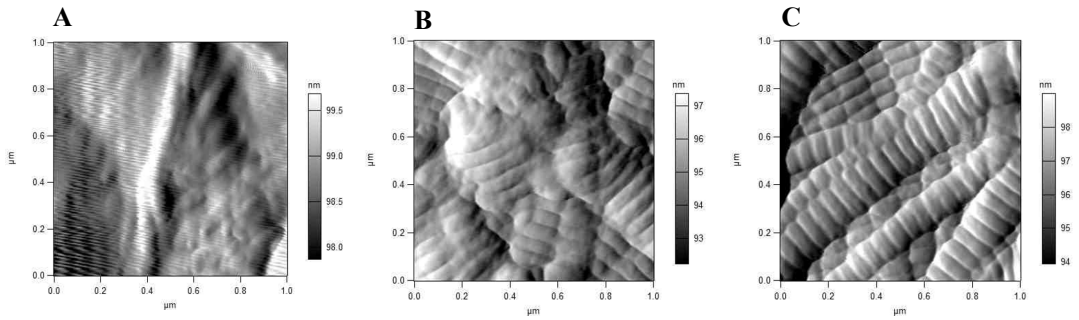


Figure 2.6: Representative AFM amplitude images of a 1 × 1 μm area of bovine cartilage with 30% isopropanol pre-wash with and without hyaluronidase treatment at 25°C and at 37°C for 30 minutes: (A) samples without hyaluronidase treatment; (B) samples with hyaluronidase treatment at 25°C; (C) samples with hyaluronidase treatment at 37°C.

Treatment with 1 mg/ml hyaluronidase successfully exposed fibrils in approximately 80% of samples. To improve fibril exposure, additional treatments were applied using alternative enzymes, or extending the incubation time with hyaluronidase. Again, the effects of treatment on image quality and material properties were examined.

2.2.2.1.4 Enzymatic Treatments - Hyaluronidase (Time)

To determine the effect of treatment time on fibril exposure and mechanical properties, samples were immersed in 1 mg/ml hyaluronidase at 30 minute increments after each analysis, resulting in time periods of 30, 60 and 90 minutes. The sample treated for 90 minutes exhibited the best fibril exposure (Figure 2.7A-D). For mechanical measurements, four fibrils in three random regions from the sample were measured, resulting in a total 12 fibrils. Mean values of Young's modulus from these fibrils were compared (Figure 2.7E). One-way ANOVA revealed that there were no significant differences ($P > 0.005$) between treated and untreated samples (after washing), or between treatment times, indicating that extending the incubation time has no effect on material properties.

Based on the above results for bovine cartilage samples, the following protocol used for application to human samples: pre-washing the samples with 30% isopropanol; cryo-sectioning; and treating sectioned samples with 1 mg/ml hyaluronidase in a 37°C incubator for 90 minutes.

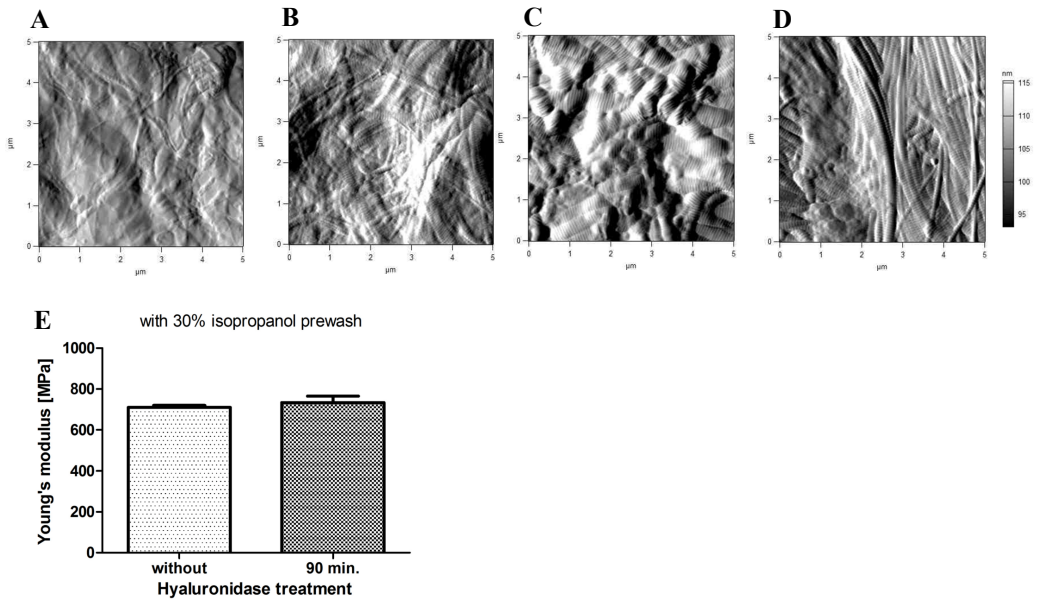


Figure 2.7: Representative AFM amplitude images of a 5 × 5 μm area of bovine cartilage pre-washed with 30% isopropanol and treated with 1 mg/ml hyaluronidase at 37°C for different time periods: (A) before treatment (control), (B) 30 minutes treatment, (C) 60 minutes treatment and (D) 90 minutes treatment. (E) Young's modulus of collagen fibrils increased slightly but insignificantly after hyaluronidase treatment for 90 minutes.

2.2.2.1.5 Application to Human Cartilage

Application of the above protocol on human samples produced poor results, with limited exposure of collagen fibrils. The optimisation strategy was therefore extended to test the effects of additional enzymes, as well as increased concentrations. Additional enzymes included chondroitinase (Sigma-Aldrich) [135, 136] and trypsin (TrypLE, Gibco, Thermo Fisher Scientific, Waltham, MA, USA) [137].

Figure 2.8 summarises the decision paths for the optimisation of human cartilage. Similar to bovine samples, treatment was increased until the collagen fibrils were sufficiently exposed, after which mechanical properties were measured and compared to pre-treatment values. Once the appropriate combination of collagen fibril exposure and unchanged mechanical properties was observed, the modified protocol was applied to the remaining tissue samples.

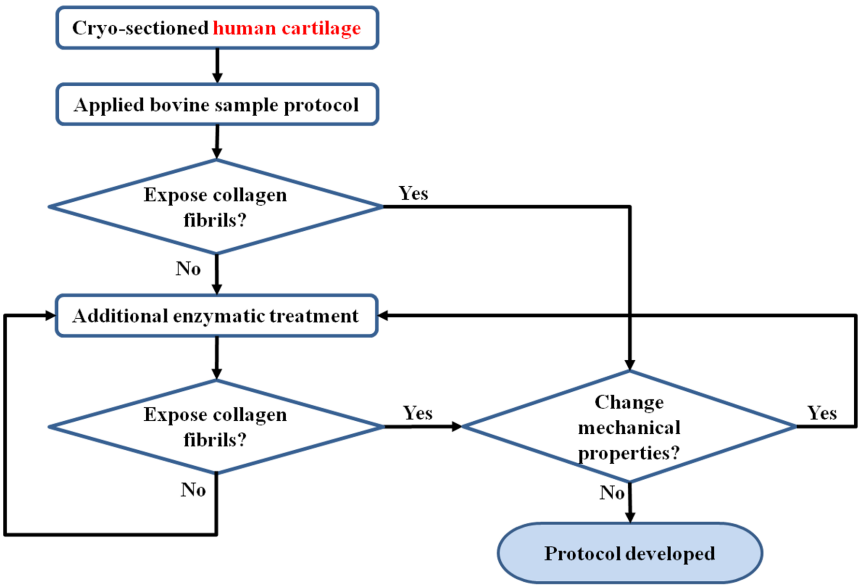


Figure 2.8: Decision path for the optimisation of sample preparation for human cartilage.

2.2.2.1.6 Additional Enzymatic Treatment - Chondroitinase

Following treatment with hyaluronidase, samples were immersed in 0.1 U/ml or 0.5 U/ml of chondroitinase ABC in 0.01% bovine serum albumin (BSA) at 37°C for 30 minutes. This was expected to enhance removal of proteoglycans while maintaining

the collagen network [138], however no improvement was observed (data not shown). Both concentration and time were increased to 1U/ml of chondroitinase ABC in 0.01% BSA at 37°C at 30 minutes and one hour, yet the results were not improved (data not shown). Based on these results, chondroitinase was not considered further.

2.2.2.1.7 Additional Enzymatic Treatment - Trypsin

Trypsin has a broader spectrum of efficacy than hyaluronidase or chondroitinase. It is known to attack collagen with existing damage, however there is no guideline on either the concentration or exposure time to which a sample can be treated without this effect. Samples were therefore exposed to trypsin with increasing incubation times (<5 s, 30 s and 60 s) at room temperature to observe the differences in its effect on exposure and mechanical properties. Treatment for 5 or 30 s had a minimal effect on collagen exposure (data not shown). Trypsin treatment for 60 s in contrast resulted in a substantial improvement in collagen exposure (Figure 2.9), and samples were therefore subjected to mechanical testing.

For mechanical measurements on human samples, each core was divided into five regions (regions A-E), each with three 4×4 μm sub-regions. Within each sub-region, the material properties of four randomly-selected fibrils were measured, resulting in a total of 12 fibrils per region. Mean values of Young's modulus from these fibrils were taken to compare the difference between samples before and after treatments. Figure 2.10 shows the Young's modulus of five regions of the same tissue before and after treatment. A two-way ANOVA revealed that no statistically-significant difference was found in either region A or B between before and after trypsin treatment, but there was a significant decrease in Young's modulus in regions C, D and E after treatment ($P < 0.0001$), indicating collagen damage. Again, since mechanical properties are important in this study, the use of trypsin was abandoned, and alternative treatment was considered.

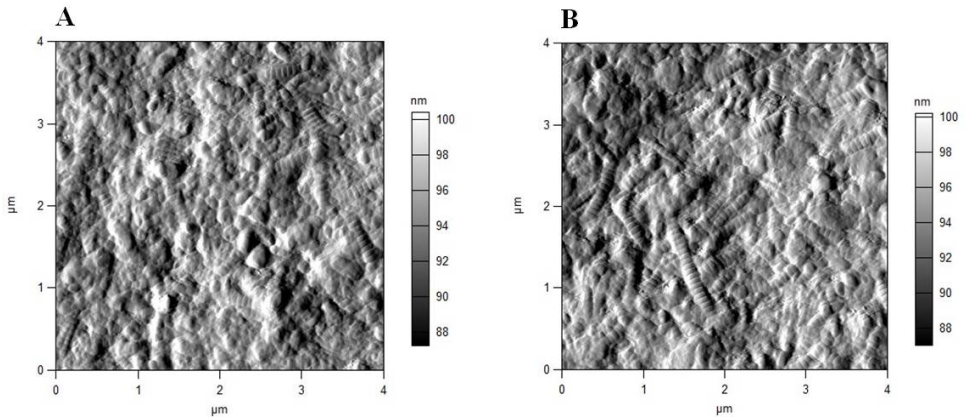


Figure 2.9: Representative AFM amplitude images of a 4 × 4 μm area on a human tissue sample (A) before and (B) after trypsin treatment for 60 s.

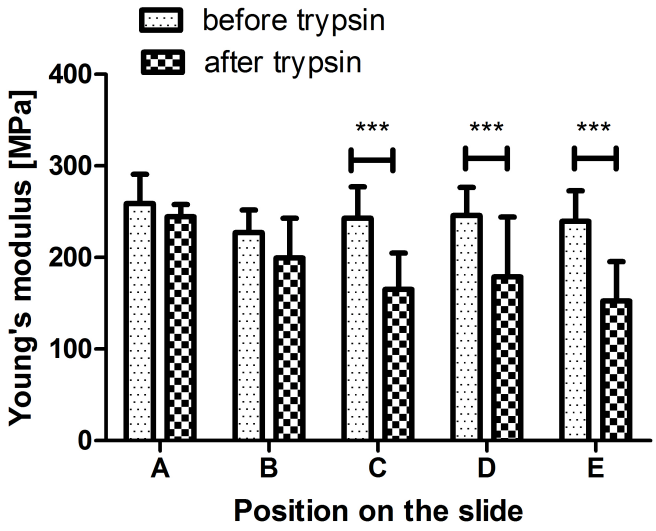


Figure 2.10: Young's modulus of 12 collagen fibrils within regions A, B, C, D, and E with and without trypsin treatment. Data are shown as mean ± standard deviation. ***:$P < 0.0001$.

2.2.2.1.8 Enzymatic Treatment - Hyaluronidase (Increased Concentration and Time)

With the failure of alternative enzymes to expose collagen fibrils, or to achieve exposure at the expense of changes in mechanical properties, modification to the hyaluronidase protocol was considered. Here, concentrations of 1 to 40 mg/ml hyaluronidase and incubation times of 90 minutes to 3 hours at 37°C were applied and tested. Both increased time (Figure 2.11) and increased concentration (Figure 2.12) improved exposure, with little effect on mechanical properties ($P > 0.05$ compared to control). The small increase in Young's moduli are indicative of removal of soft non-collagenous ground substance rather than an increase in the modulus of collagen itself.

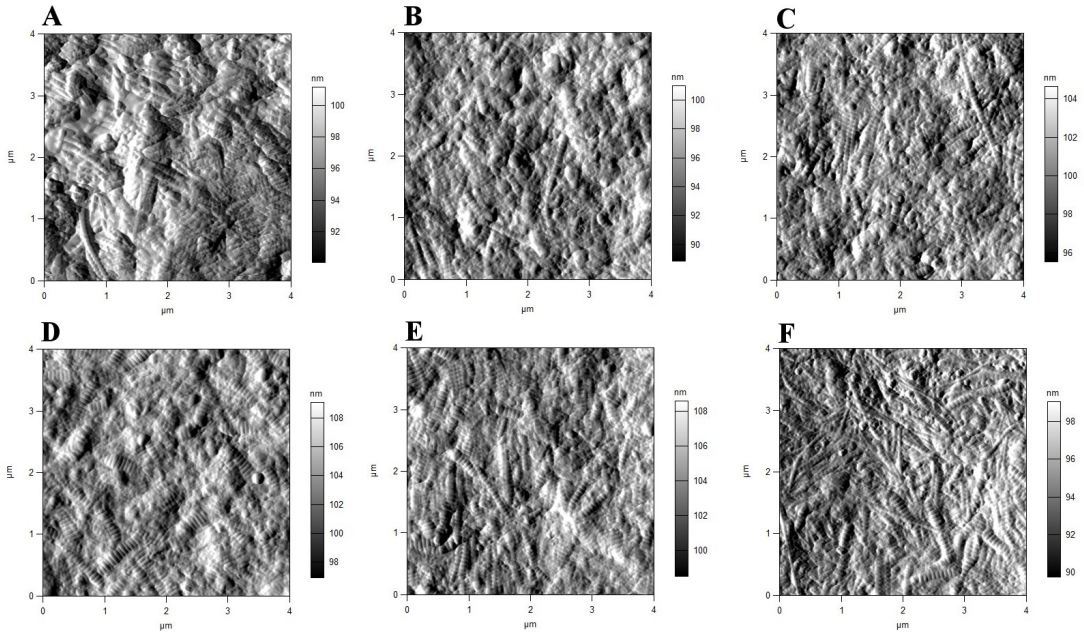


Figure 2.11: AFM amplitude images of a 3 × 3 μm area of human cartilage surface after treatment with different concentrations of hyaluronidase for one hour: (A) PBS (control), (B) 1 mg/ml hyaluronidase, (C) 5 mg/ml hyaluronidase, (D) 10 mg/ml hyaluronidase, (E) 20 mg/ml hyaluronidase and (F) 40 mg/ml hyaluronidase.

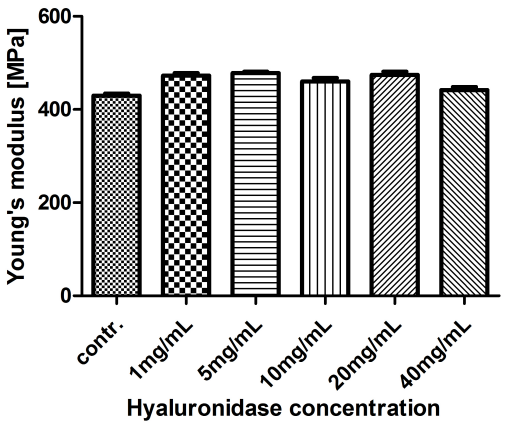


Figure 2.12: Young's moduli of collagen fibrils after treatment with different concentrations of hyaluronidase for 3 hours. Hyaluronidase treatment had little effect on mechanical properties, despite increase in both time and concentration.cntr.: control.

2.2.2.1.9 Final Protocol for Human Cartilage Samples

Figure 2.13 shows the final protocol for sample preparation for AFM. Hemi-cylinders of cartilage were immersed and gently shaken 10 times in 30% isopropanol after extraction (Figure 2.2E). All samples were then snap-frozen in liquid nitrogen and stored at −80°C before cryo-section. All frozen tissues were embedded in water-soluble OCT mounting medium and were sectioned at a thickness of 10 μm parallel to the articular surface and mounted on glass slides. Before AFM measurement, samples were immersed in distilled water for 10 minutes with three changes at room temperature (25°C) to remove OCT and were then treated with 40 mg/ml hyaluronidase in a 37°C incubator for three hours. After enzyme treatment, all samples were washed with distilled water for 10 minutes with three changes and dried at room temperature (25°C) for a minimum of 30 minutes.

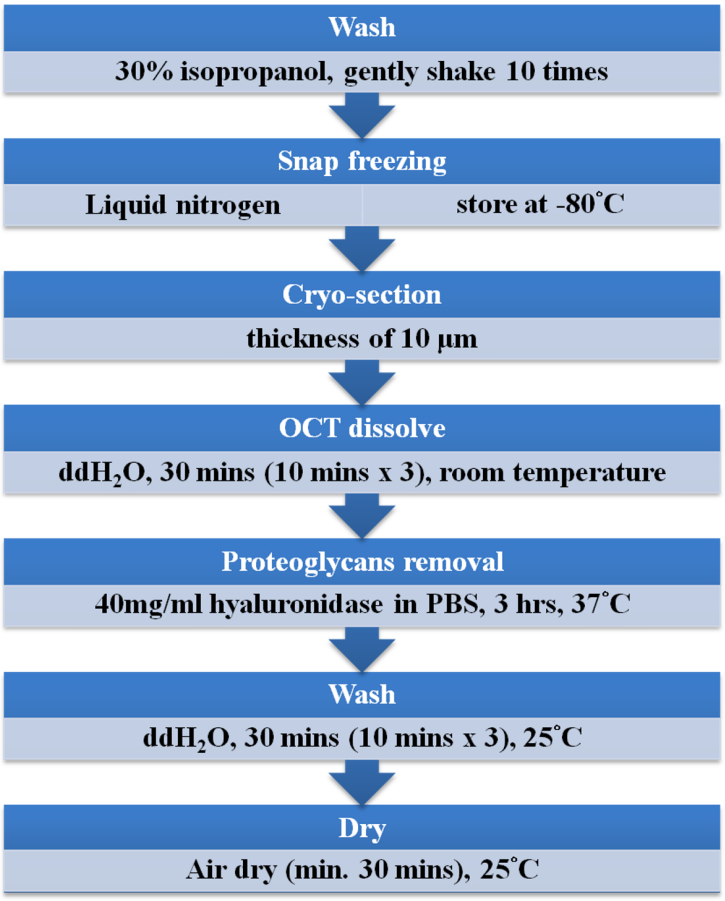


Figure 2.13: Flow chart of AFM sample preparation after washing with 30% isopropanol. Hemi-cylinders of cartilage were washed with 30% isopropanol, snap-frozen in liquid nitrogen and stored at −80°C before sectioning at 10 μm, mounting on glass slides, and removal of OCT. Samples were then treated with 40 mg/ml hyaluronidase in a 37°C incubator for 3 hours, washed with distilled water for 3×10 minutes and dried at room temperature (25°C) for a minimum of 30 minutes.

2.2.2.2 System Build for Polarised Raman Spectroscopy

2.2.2.2.1 Optical System

The Raman spectroscopy system used for this study was built in-house. We aimed to develop a polarised Raman system to assess the alignment and organisation of collagen fibrils as well as the quantity and quality of collagen fibrils at different stages of disease. Figure 2.14 shows the set-up of the polarised Raman system. One end of an optical fibre (600 μm, 0.22 NA, Ocean Optics, Dunedin, FL, USA) was connected to a 785 nm diode laser to excite the samples and the other end connected to a collimator (f = 7.5 mm, 600-1050 nm, Thorlabs Inc., Newton, NJ, USA) to generate a parallel laser beam. Lens 1 (f = 50 mm, 650-1050 nm, Thorlabs Inc.) and Lens 2 (f=175 mm, 650-1050 nm, Thorlabs Inc.) expanded the laser beam to fill the back aperture of the objective. Iris 1 (Thorlabs Inc.) cut the remaining non-collimated light and iris 2 (Thorlabs Inc.) cut the laser beam to a diameter of around 1 cm. The laser passed through a clean up filter (785 nm, Semrock Inc., Rochester, NY, USA) and reflected off a broadband dielectric mirror (750-1100 nm, Thorlabs Inc.) at 45 degrees. After reflection, the laser passed through a Glan-Thompson polariser with extinction ratio of 10000:1 (650-1050 nm, Thorlabs Inc.) to provide polarised output. A half-wave plate (690-1200 nm, Thorlabs Inc.) was used to rotate the polarised laser beam. The polarised laser then reflected off a dichroic beamsplitter (Semrock Inc.) which reflects wavelengths shorter than 804 nm, transmitting wavelengths longer than 804 nm (> 301 cm^{-1} for a 785 nm pump). After reflecting off the dichroic beamsplitter, the laser passed through an objective (Olympus Plan Fluorite Objective 10×, 0.3 NA, VIS-NIR, Thorlabs Inc.) to reach the sample which was held in a slide holder (Thorlabs Inc.). The reflected Raman signal, which was longer than 785 nm, was then collected by an objective and passed through a notch filter (Semrock Inc.) to filter out the laser light. Lens 3 (f = 175 mm, 650-1050 nm, Thorlabs Inc.) converged the light into a collimator then into a spectrometer (QE Pro-Raman, Ocean Optics).

The spectrometer uses a 900 lines/mm grating and a 50 μm slit with a 2-D detector (1044 horizontal × 64 vertical pixels) which is responsive from a wavelength

of 185 nm to 1100 nm. This gives a spectral resolution of 7-8 cm^{-1}, and coupled with a 16-bit A/D converter delivered a dynamic range of 85,000:1 with a signal-to-noise ratio of $>$ 1000:1.

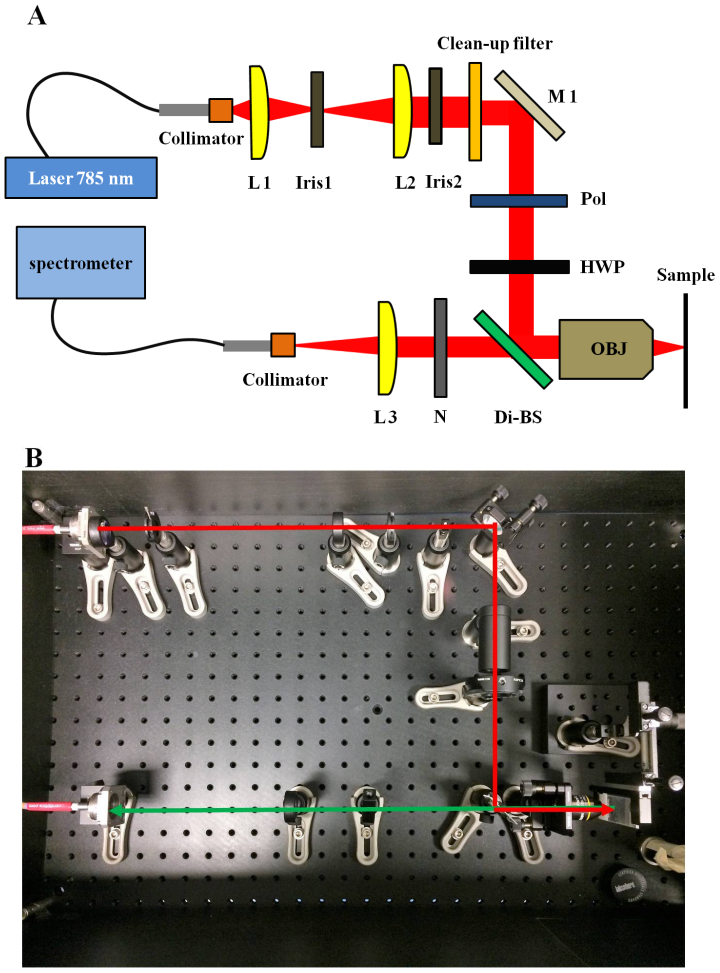


Figure 2.14: (A) Schematic diagram of the Raman spectroscopy set-up. (B) Photograph showing the Raman spectroscopy set-up. L: lens; M: mirror; Pol: Glan-Thompson polariser; HWP: half-wave plates; Di-BS: dichroic beamsplitter; N: notch filter; Red line: incident light; green line: scattered light.

As the system was built in-house, testing was required to characterise the sensitivity and reliability of the system (Figure 2.15). In brief, prior to mounting the polarisation components (half-wave plate and polariser), the system set-up was tested for basic performance by measuring samples with a known Raman spectrum. After the system performance test, polarisation components were included incrementally to observe their effect on both system performance and laser profile. At completion of system testing, samples with a known polarisation profile were tested to examine the polar sensitivity of the system, with modifications applied as required.

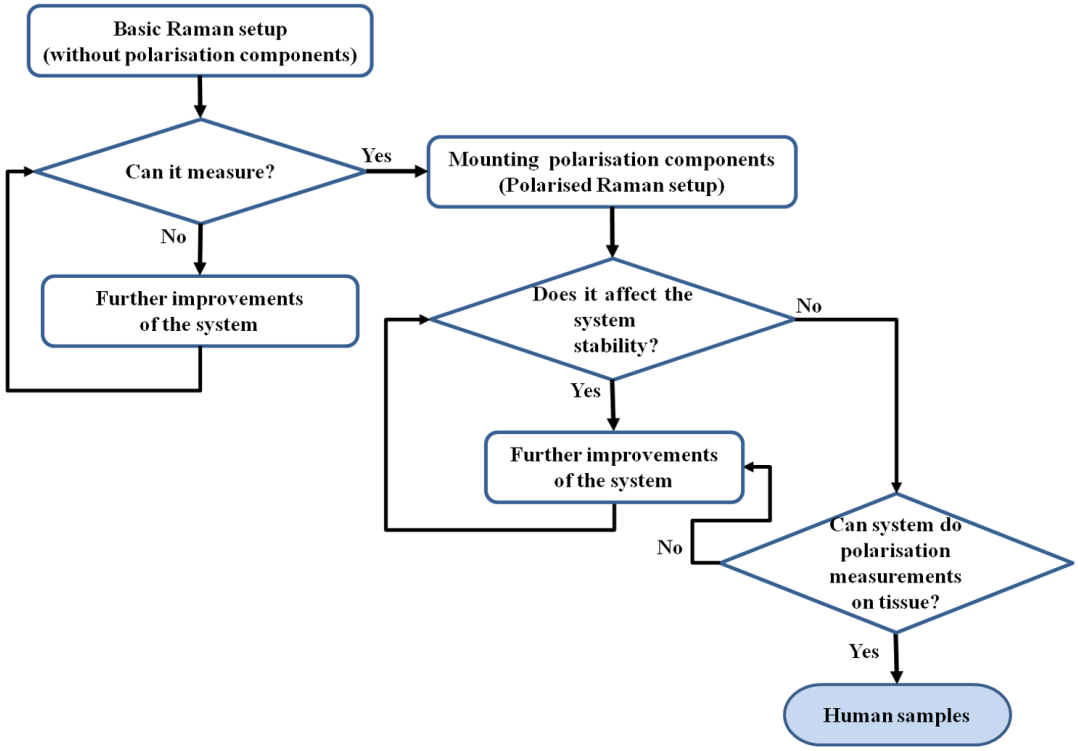


Figure 2.15: Flow chart of the system testing process during set-up of the polarised Raman spectroscopy system.

2.2.2.2.2 Basic Raman System Performance

Before mounting the polariser and half-wave plate (the polarisation set-up), chondroitin sulphate, hydroxyapatite and collagen (all from Sigma-Aldrich) were measured to test system performance for matrix components of interest. Spectra were compared and matched with data in the literature [139–141] (Figure 2.16).

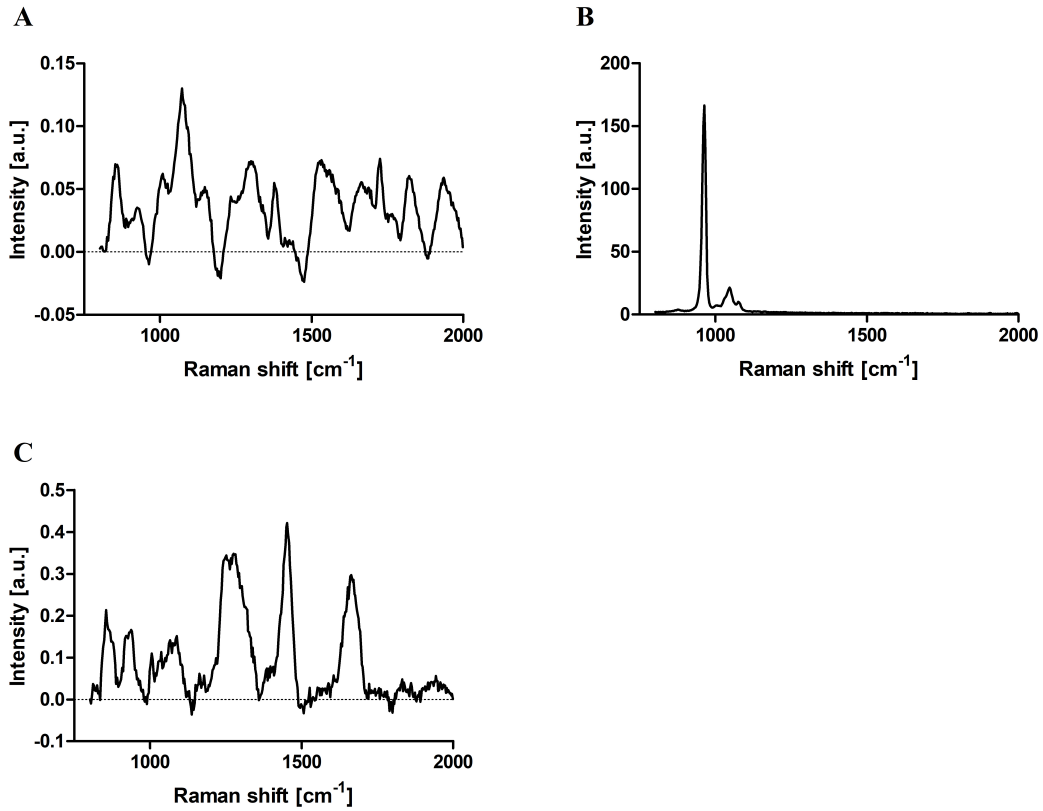


Figure 2.16: Raman spectra of (A) chondroitin sulphate, (B) hydroxyapatite and (C) collagen.

2.2.2.2.3 Additional Optical Components

Following successful initial testing, the system was tested for polarisation control and stability. The half-wave plate and Glan-Thompson polariser were sequentially mounted and their effect on laser power was measured at different angles of rotation. As shown in Figure 2.17A, the half-wave plate maintained total laser power at all orientations (variation up to 0.8%). Figure 2.17B shows laser polarisation when the

initially circular polarised beam was cut by the Glan-Thompson polariser, evaluated by measuring laser power changes at 15-degree increments.

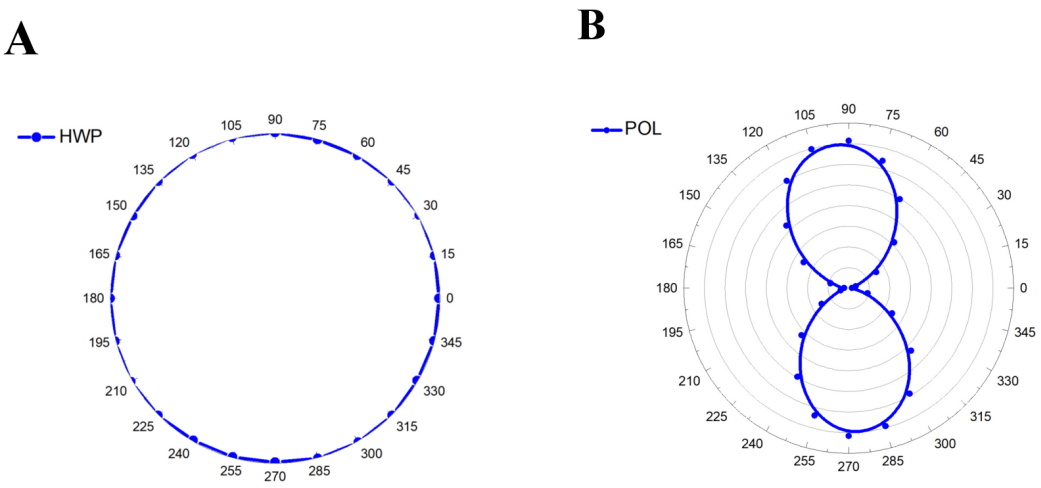


Figure 2.17: Components affecting testing and laser polarisation profile. (A) Changes in laser power with rotation of the half-wave plate. (B) Polarisation profile of the laser after passing through the Glan-Thompson polariser.

The spectrum of a diffuse reflecting Teflon^{TM} sample was then measured with increasing time to test laser stability. Figure 2.18A shows the spectrum of Teflon^{TM} over time, with the intensity of the main peak at 748 cm^{-1} plotted against the increasing time (Figure 2.18B). The system was thus considered stable over time (variation up to 0.6% of the mean value).

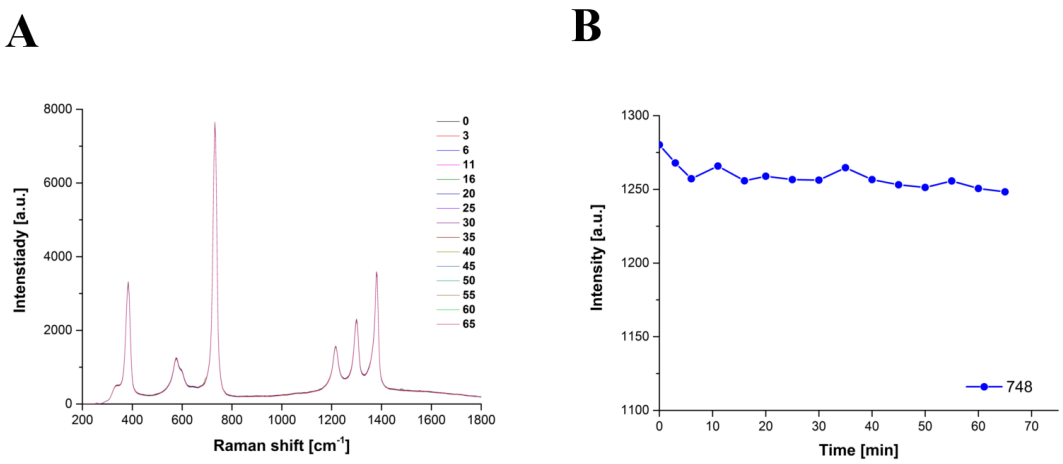


Figure 2.18: Laser stability test after passing the half-wave plate. (A) Teflon^{TM} spectrum with increasing time. (B) Intensity changes at 748 cm^{-1}.

2.2.2.2.4 Polarisation Tests on Tissue

To test the ability to extract usable polarisation information from the system, initial measurements were performed on porcine tendon due to its alignment characteristics [114]. This study first considered the effects of sample dehydration, using distilled water to avoid the possibility of salts from PBS having an effect on the spectra. Spectra were therefore acquired both without and with the addition of distilled water during measurements for 180 minutes at 15 minutes intervals. Figure 2.19 shows that allowing dehydration during measurement created fluctuations that would affect the results of the polarisation measurement by adding substantial drift in intensity superimposed on the polarisation effect. It was thus seemed critical to maintain hydration during measurements to acquire reproducible spectra.

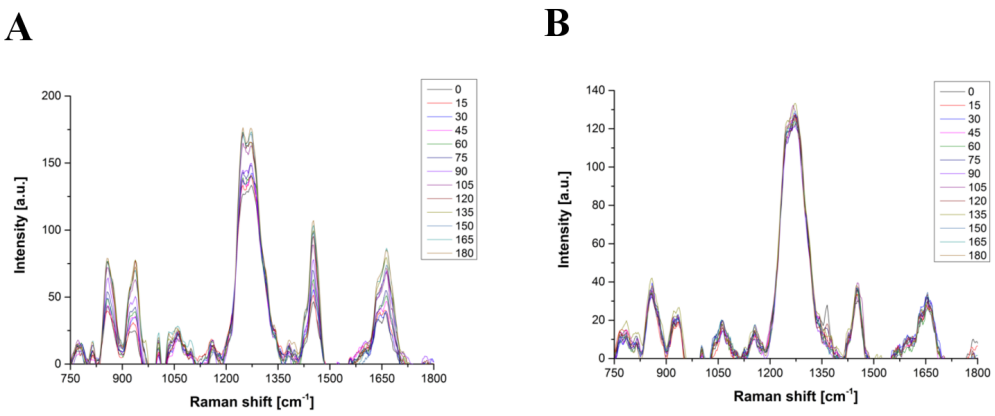


Figure 2.19: Raman spectra of porcine tendon. (A) Spectra allowing dehydration during the experiment, showing the resultant drift of signal intensity. (B) Spectra with the addition of distilled water during the measurements, showing more consistent results.

The polarisation dependence of porcine tendon spectra at 15 degree increments was then measured while maintaining hydration. Peaks at 937, 1251 and 1663 cm^{-1} (type II collagen bands) at different polarisation angles were observed (Figure 2.20). Results showed that the patterns were close to circular in each Raman band, with no clear polarisation profile. Substantial drift was also observed, seen in the difference between intensities at 0 degrees, despite maintaining sample hydration.

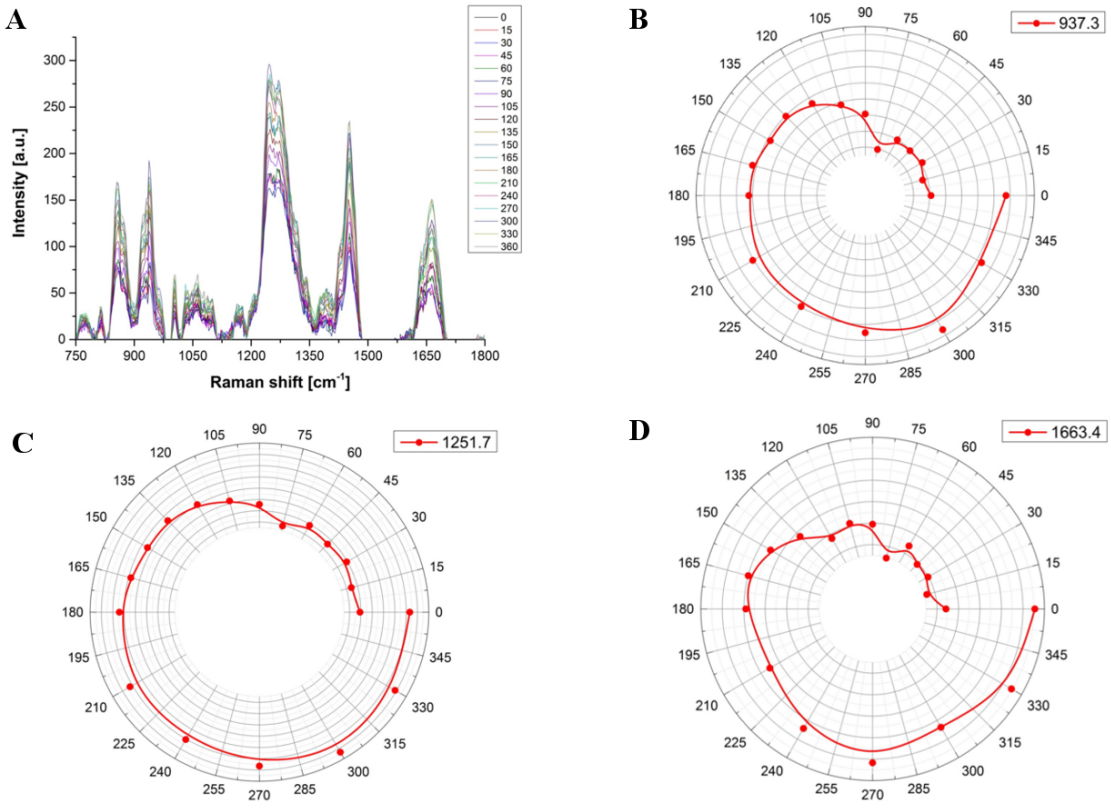


Figure 2.20: Raman spectra of porcine tendon at different laser polarisation angles, in 15 degree increments. (A) Full spectra at different polarisation settings. Polar plots of (B) 937 cm^{-1}, (C) 1251 cm^{-1}, and (D) 1663 cm^{-1}.

The above experiment was repeated with a higher NA objective, to determine whether a usable polarisation profile could be extracted from the drift signal when probing a smaller focal volume and thus tighter alignment. Previous work on bone showed that higher NA objectives (i.e. 0.9 NA) provided improved resolution of the polarisation profile against low NA objectives [142], despite the deleterious effects of polarisation mixing in the focal volume due to tight focus. This project had a limited number of objectives available to it: the highest NA usable objective was 0.45 the

Olympus Plan Fluorite Objectives 20×, with a working distance of 6.6 to 7.8 mm in air, UV-NIR (Olympus, Tokyo, Japan). This 0.45 NA objective was installed and polarisation tests repeated. As shown in Figure 2.21A, improved spectral details were seen when using the higher NA objective, and stronger polarisation effects were observed at 937 and 1663 cm^{-1} (Figure 2.21B and 2.21D), although problems with drift persisted. These data suggest that a higher NA objective indeed provides better results, yet the drift from the sample rendered measurements inconsistent.

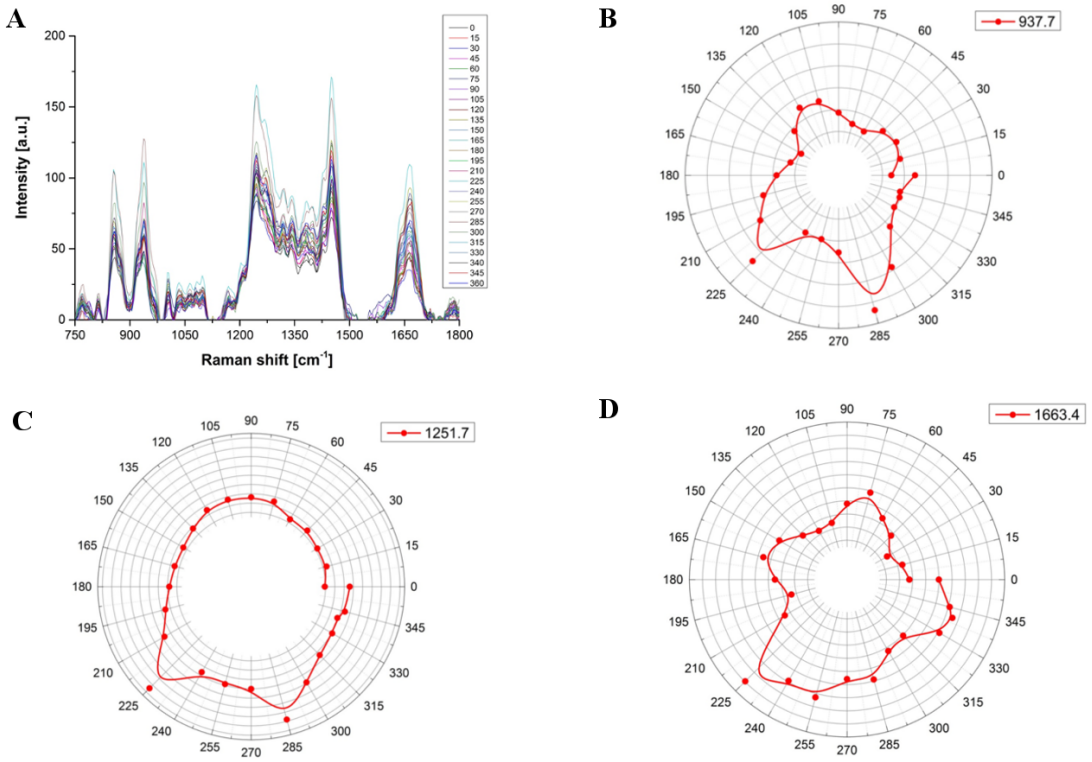


Figure 2.21: Raman spectra of porcine tendon at different polarisation angles with a 0.45 NA objective. (A) Spectra at different polarisation directions. (B) Polar plot of 937 cm^{-1} spectra at different polarisation angles. (C) Polar plot of 1251 cm^{-1} spectra at different polarisation angles. (D) Polar plot of 1663 cm^{-1} at different polarisation angles.

2.2.2.2.5 Final Raman Set-up

As an appropriate objective (high NA, long working distance) was unavailable for this study, compounded by persistent issues with drift, polarised Raman was unable to be realised within the time and financial constraints of the project. It was therefore abandoned in favour of standard Raman measurements from a scanning spectroscopy system (Figure 2.22), which could be applied after removal of polarisation components to scan the surface of cartilage cores.

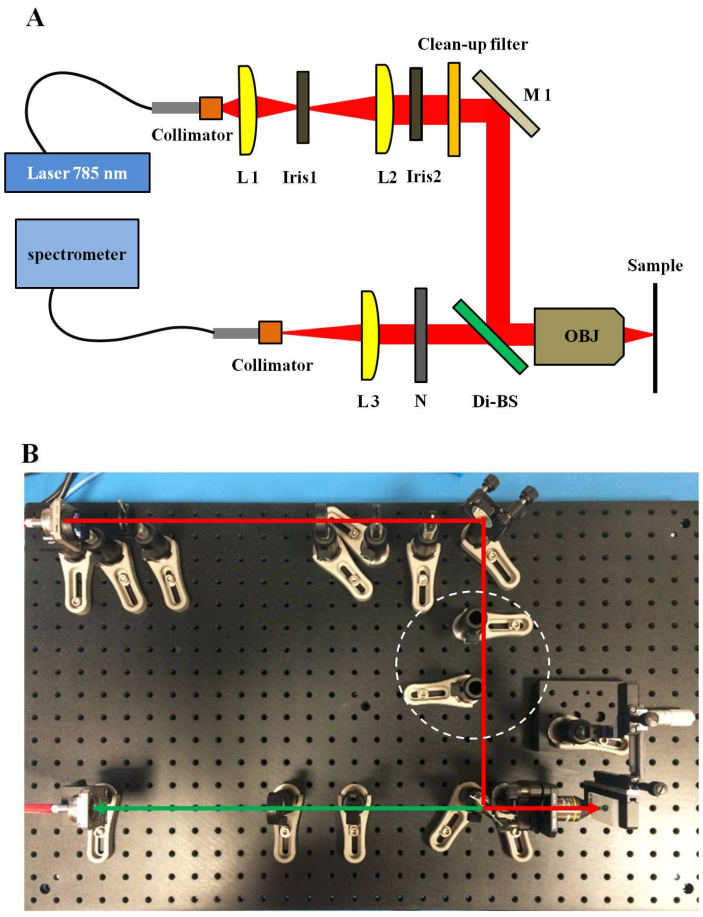


Figure 2.22: Modified Raman spectroscopy. (A) Schematic diagram of the Raman spectroscopy set-up. (B) Photograph showing the Raman spectroscopy set-up where the white dotted circle shows the location of the removed polariser and half-wave plate. (C) Representative photograph showing the Raman spectroscopy measuring points (red points) on a sample of human articular cartilage where the red arrow shows disease progression. The blue dotted line shows the cutting line after optical measurement. L: lens; M: mirror; Pol: Glan-Thompson polariser; Di-BS: dichroic beamsplitter; N: notch filter; red line: incident light; green line: scattered light; white dotted circle showed the location of the removed half wave plate and polariser.

2.2.3 AFM - Data Collection and Analysis

2.2.3.1 Data Collection

Scanning probe microscopy was performed on an MFP-3D AFM (Asylum Research, High Wycombe, UK). AC240 AFM tips (spring constant $1.1 \leqq k \leqq 1.6$ N/m, nominal tip radius 9 nm, Asylum Research) were employed for each measurement. Measurements were performed using intermittent-contact (tapping) mode [143], applying AM-FM nanomechanical mapping [144] and loss tangent (tan δ) mapping [145]. AM-FM mode is a multifrequency and bimodal AFM which operates at two cantilever resonances simultaneously. The lower resonance (first mode) is used for amplitude modulation (AM) and the higher resonance (second mode) is operated in frequency modulation (FM) mode. Surface tracking in repulsive mode was optimised by manipulating gains and set points. The lower resonance acts in standard tapping mode by adjusting the cantilever's vertical position to keep the amplitude at the setpoint value to obtain the topographic data and meanwhile, the amplitude and phase at a fixed frequency are measured by a lock-in amplifier to determine the loss tangent. At the second mode (higher resonance), phase and amplitude were monitored to keep the phase lag of the cantilever at 90 degrees. The interaction of an AFM probe with a surface produces a shift in the probe's resonant frequencies that is dependent on the strength of the interaction, or tip-sample contact force [146]. Considerations of the contact geometry (after Sneddon [147]) result in simple scaling laws relating frequency shift to the tip-sample contact stiffness and Young's modulus.

2.2.3.2 Stiffness and Young's modulus

The concept of stiffness in Young's modulus conversion is based on the theory of Heinrich Hertz [148] and a simple harmonic oscillation formula. Heinrich Hertz theory has been derived to extrapolate elastic modulus by

$$k_{t-s} = 2aE, \tag{2.1}$$

where k_{t-s} is the tip-sample contact stiffness, a is the contact radius and E is the effective elastic modulus. By expanding the simple harmonic oscillation formula

which is common in non-contact AFM, the relationship between stiffness and frequency can be derived from

$$\Delta f_2 = \frac{f_{0,2}}{2}\frac{k_{t-s}}{k_2}, k_2 = (\frac{\omega_2}{\omega_1})^2 k_1, \tag{2.2}$$

where k_{t-s} is the tip-sample contact stiffness, k_2 is the calibrated cantilever stiffness at the second mode, k_1 is the calibrated cantilever stiffness at the first mode, ω_1 and ω_2 are the angular frequency at the first and second mode respectively, Δf_2 is the frequency shift when the cantilever is moved near the substrate and $f_{0,2}$ is the second mode frequency of the AFM cantilever oscillating far from the substrate. Combing E.q. 2.1 and E.q. 2.2, Young's modulus could then be calculated by

$$E = \frac{\Delta f_2}{f_{0,2}}\frac{k_2}{a}. \tag{2.3}$$

As shown in E.q.2.3, the Young's modulus depends on the contact radius which is unknown a-priori, the stiffness of the sample, and the second mode frequency of the AFM cantilever which is known. To simplify the equation, this expression can be rewritten in terms of

$$E = C(A_{sp}, A_{free})\Delta f_2, \tag{2.4}$$

where $C(A_{sp}, A_{free})$ is a calibration factor including factors such as setpoint (A_{sp}), free amplitude (A_{free}), resonance frequency ($f_{0,2}$) and stiffness (k_2) which result in a relationship between Young's modulus and frequency shift. Here, the calibration factor C was determined by assuming a uniform indentation depth with a punch indentation geometry, and adjusting the prefactor to calibrate against a known sample, polycaprolactone (PCL) with Young's modulus of 300 MPa [109]. To maintain the accuracy of the Young's modulus after several measurements and potential changes in tip shape, recalibration was performed between samples.

The second mechanical property of interest is the loss tangent (tanδ). The loss tangent is the ratio of a material's dissipated energy to stored energy in response to cyclic excitation and is defined as

$$\tan\delta = \frac{E''}{E'}, \tag{2.5}$$

where E' is the storage modulus and E'' is the loss modulus. Earlier studies described the relationship between loss modulus (E'') and phase angle [149] and the relationship between storage modulus (E') and phase angle [150] in AFM respectively as

$$\langle F_{ts} \cdot \dot{z} \rangle \sim \sin\varphi - \frac{A}{A_0} \tag{2.6}$$

and

$$\omega \langle F_{ts} \cdot z \rangle \sim \cos\varphi \tag{2.7}$$

where F_{ts} is the tip-sample interaction force, z is the tip motion, $\dot{z}$ is the tip velocity, A is the cantilever operating amplitude, A_0 is the reference measurement, ω is the angular frequency at which the cantilever is driven, and $\langle\rangle$ represents a time-average. A recent study took the ratio of these two equations (E.q. 2.6 and E.q. 2.7) to express the loss tangent of the material [145] and found that it agrees well with numerical solutions. Therefore, the expression of the loss tangent can be simplified to

$$\tan\delta = \frac{E''}{E'} = \frac{\langle F_{ts} \cdot \dot{z} \rangle}{\omega \langle F_{ts} \cdot z \rangle} = \frac{\sin\varphi - \frac{A}{A_0}}{\cos\varphi}. \tag{2.8}$$

This loss tangent measurement provides a simple, almost calibration free method and unlike the Young's modulus, it does not consider the tip shape.

2.2.3.3 Data Analysis

At each measurement site (five positions per core, at 1 mm intervals in the direction of disease progression. Figure 2.1), three regions were randomly selected and scanned at a size of 3 × 3 μm with 512 × 512 pixel resolution and a scan rate of 1 Hz. Within each region, four exposed fibrils were chosen for measurement of their material properties, resulting in a total of 12 fibrils per measurement site. Mean values of Young's modulus and loss tangent in each region were then calculated.

The material properties across the D-period [151–153] were also measured. The formation of the D-period is caused by the combination of collagen molecule overlap and lengthwise spacing [154](Fig 2.23E). This produces a periodic pattern in both topographic and material property measurements along the length of the fibril

(Figure 2.23A-C). As shown in Figure 2.23D, each D-period was characterised by a prominent peak (between gaps) and valley (at a gap site). The secondary peak, attributed to quasi-hexagonal packing, was not used. Relative material properties across the single fibril were processed by MATLAB (2015a, MathWorks Inc., Natick, MA, USA), calculating the difference in Young's modulus across the D-period (the value at the major peak minus the valley value, e.g. Figure 2.24, d_1 - d_3). The mean value and the variance of this difference were recorded and compared.

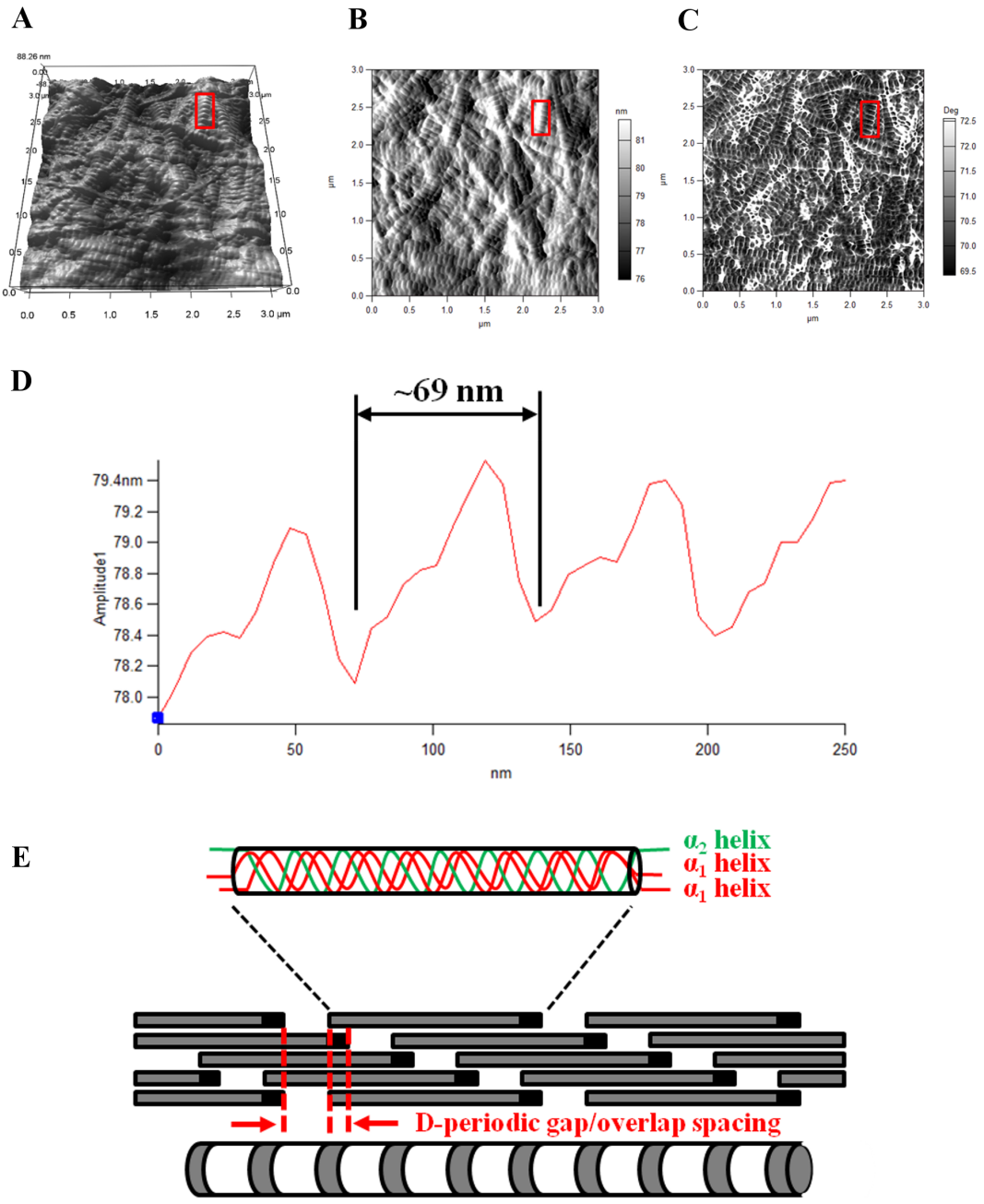


Figure 2.23: Representative figure showing the formation and analysis of D-periods. (A) Height, (B) amplitude and (C) phase images showing D-periods of collagen fibrils. (D) The D-period patterns from the red rectangle in the amplitude image (B). (E) Schematic diagram showing the formation of D-periodic gaps.

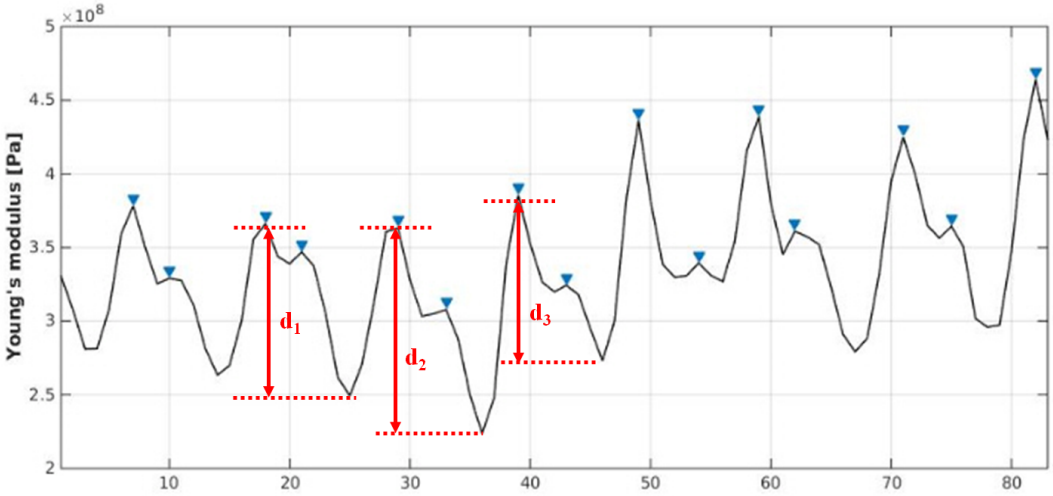


Figure 2.24: Representative figure showing the difference in the Young's modulus across the D-periods: calculations from a single fibril. One D-period of a collagen fibril is observed as a major peak and adjacent valley (the red arrow). Blue arrows indicate the peaks along one collagen fibril. The differences between major peak and valley values (shown in d_1, d_2 and d_3) were calculated.

2.2.4 Raman Spectroscopy - Data Collection and Analysis

Spectra were collected at 7-8 cm^{-1} resolution from 150 to 2100 cm^{-1}. A background spectrum was acquired prior to scanning and was subtracted from each subsequent Raman spectrum from the sample. Each Raman spectrum, taken at 1 mm intervals in the direction of disease progression was acquired with a 30 second integration time, with three continuous spectra averaged. Acquisition was repeated three times and averaged a second time for each sample point on the cartilage surface (a total of 9 scans). Between each measuring point, drops of distilled water were added to avoid tissue dehydration.

The measured tissue spectra contained a combination of Raman scattering, autofluorescence and noise. Following averaging, each spectrum was smoothed by a 10-point, third-order Savitzky-Golay filter to reduce noise [112]. A fifth-order polynomial [155] was then fitted to the autofluorescence background from 750 to 2,000 cm^{-1} (Origin 9.1, OriginLab, Northapmton, MA, USA), and subtracted. Finally, each spectrum was normalised to its total area under the curve between 750 and 2,000 cm^{-1} (Origin 9.1), enabling comparison of spectral patterns (Figure 2.25).

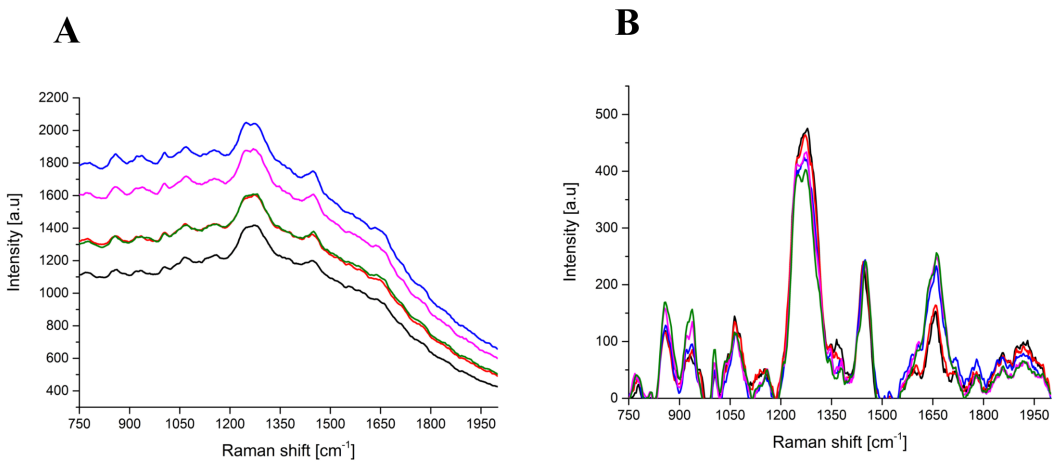


Figure 2.25: Representative figure of Raman spectrum processing. (A) Raw spectra. (B) Spectra after processing.

Following collection, Raman bands of collagen were measured and compared. As mentioned above, the tropocollagen molecule is formed by three α-helical domains. Each α-chain is composed of multiple triplet sequences of Gly-X-Y where X and Y can be any amino acid. The glycine (Gly) residue ensures the proper folding of each of these chains. X is commonly proline and Y is usually present as hydroxyproline, with phenylalanine also found in the position X [156, 157]. The presence of hydroxyproline in the Y position is thought to contribute to stabilisation of the helical form [158]. Therefore, helix stability was analysed by calculating the ratio of proline to hydroxyproline [106, 112], providing a measure of quality. The CH_2 and CH_3 from the amino acid side chains were also observed.

Amide III was used to characterise order in collagen secondary structure [159]. In the amide III region (1209-1332 cm^{-1}), 1241 and 1269 cm^{-1} represent random coil (disordered) and alpha-helix (ordered) formations respectively [105]. Peak values at 1240 and 1272 cm^{-1} were calculated in this study to provide further information about the quality of the collagen fibrils. Both peak heights and areas under collagen-related bands were calculated, with wavenumbers of interest and ranges used for area calculations given in Table 2.1.

Table 2.1: Raman bands of collagen and range selection [109, 112, 160, 161]

Raman shift (cm^{-1})	**Spectral assignment**	**Range selection**
855	Type II collagen, proline	848-868
869	Type II collagen, hydroxyproline	868-875
1002	Type II collagen, phenylalanine	995-1015
1209-1332	Type II collagen, Amide III	1209-1332
1429-1469	Type II collagen, CH_2/CH_3 scissoring	1429-1469
1453	Type II collagen, CH_2/CH_3 scissoring	1450-1460

Areas under the peaks of sulphate and hyaluronic acid bands were also calculated to provide relative concentration data in relation to aggrecan. Table 2.2 shows the Raman band assignments and selected regions.

Table 2.2: Raman bands of hydroxyproline, hyaluronic acid and sulphate and their selected ranges

Raman shift (cm^{-1})	**Spectral assignment**	**Range of Raman bands**
1063	SO_{3-} (chondroitin sulphate)	1059-1069
1135-1175	Hyaluronic acid	1135-1175

2.2.5 Histology

2.2.5.1 Sample Preparation

Hemi-cylinders of cartilage for histological staining (Figure 2.2) were fixed in 4% paraformaldehyde and rotated at 4°C overnight. After fixation, samples were washed with PBS for 2 hours with one change and then re-fixed in a tissue processor (Leica ASP300 S, Leica Microsystems Ltd, Wetzlar, Germany). Tissue samples were then embedded in paraffin and sectioned perpendicular to the surface at a thickness of 6 μm by microtome (Leica RM2125 RTS, Figure 2.2G). Specimens were transferred to glass slides and incubated at 70°C overnight. Safranin-O (Sigma-Aldrich) was used to stain the tissue for histological grading (protocol is provided in Appendix C).

2.2.5.2 Grading

The integrity of cartilage specimens was evaluated using the histology-based OARSI (Osteoarthritis Research Society International) scoring system due to its sensitivity to early or mild OA [162]. Three serial sections were prepared from each sample and stained with Safranin-O. The slide with the best staining from each sample was selected for histological scoring. In the OARSI scoring system, there are a total of 6 scores with a low score indicating normal tissue and increasing scores reflecting advancing disease stage. Because disease progression was often observed within the 6 mm wide sections, scores were recorded from 5 positions at 1 mm intervals, matching AFM and Raman measurement positions, as shown in Figure 2.26. Each region was analysed by light microscopy with a 10× objective (Zeiss Upright Microscope, Carl Zeiss Microscopy GmbH, Jena, Germany). Images were randomised and scored by an independent researcher based on reference images and scoring criteria from Pritzker *et al.* [163]. Table 2.3 describes the OARSI scoring methodology and its related Safranin-O staining.[1]

[1]Black: nuclei, bluish green: cytoplasm, and orange to red: cartilage, mucin (proteoglycan), and mast cell granules

Histological grading was supplemented by clinical grading using the Outerbridge classification system (Table 2.4 [164–166]), performed by an independent orthopaedic registrar.

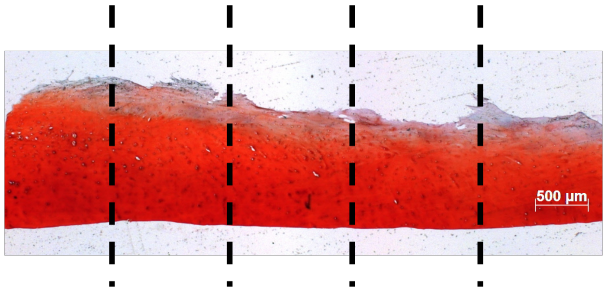


Figure 2.26: Representative image of a safranin-O stained section showing the positions used for histological scoring. Each section was divided into five regions at 1 mm intervals (magnification 2.5×).

Table 2.3: OARSI scoring methodology and histological staining [163].

Score	Description	Safranin-O
0	Surface intact and the cartilage morphology intact	
1	Articular surface is uneven and demonstrate superficial fibrillation	
2	Focally fibrillation extends through superficial to the superficial zone to mid zone	
3	The matrix fibrillation extends vertically downward into mid zone	
4	Cartilage matrix loss	
5	Cartilage is completely eroded	
6	Fibrocartilage has grown along the eroded and denuded surface	

Table 2.4: Outerbridge classification system [165, 166].

Score	Description
0	Normal cartilage, shining intact surface
1	Softening of the cartilage, less shiny surface
2	Fissures or fragments on the surface
3	Deep fissures or fragments of the surface without exposed bone
4	Erosion of cartilage, exposure of bone

2.2.6 Statistical Analysis

All statistical analyses utilised GraphPad Prism (Version 5, GraphPad Software, Inc., La Jolla, CA, USA), and a value of $P < 0.05$ was considered significant. The Grubbs' test (also called extreme studentised deviate) was applied to determine whether the most extreme value in the data was a significant outlier from the rest. Data were then tested for normality using the Pearson omnibus normality and Shaprio-Wilk normality test before comparison analysis. The mean fibril mechanical properties before and after trypsin treatment in different regions were compared using two-way ANOVA with Bonferroni post-hoc tests. The mean fibril mechanical properties before and after treatment with different concentrations of hyaluronidase, Young's modulus of the fibrils, and Raman spectra at different disease stages were compared using one-way ANOVA with Tukey's multiple comparison test. Loss tangent of fibrils, changes in Young's modulus of the D-period and variance of the changes in Young's modulus of the D-period in a fibril at different disease stages were compared using the Kruskal-Wallis test with Dunn's Multiple comparison test. All results are presented as mean ± standard error of the mean (SEM) unless indicated otherwise.

2.3 Results

2.3.1 Histological Analysis

A total of 172 regions from 35 cores were histologically scored in this study. Due to failures in some sections, three regions could not be scored. The table below (Table 2.5) shows the numbers of regions with each score. As only one region was scored 5 and the aim of the thesis is to explore early rather than late disease processes, the results from AFM and Raman from that region were excluded from this study.

Table 2.5: Number of regions with each histological score (OARSI).

OARSI score	**0**	**1**	**2**	**3**	**4**	**5**
Number of samples	10	36	48	55	22	1

Clinical scoring, using the Outerbridge system, assessed whole cores rather than specific regions, giving a total of 35 scores (Table 2.6). Where variable levels of degradation were observed over the surface or where the observed cartilage characteristics did not conform to a single category, cores were assigned transitional scores, such as 'grade 1 $\rightarrow$ 2'. These transitional scores were taken as individual categories.

Table 2.6: Number of regions with each clinical score (Outerbridge).

Score	**0**	**1**	**1 $\rightarrow$ 2**	**2**	**2 $\rightarrow$ 3**	**3**	**3 $\rightarrow$ 4**	**4**
Number of samples	0	7	5	14	4	4	1	0

Although the direct comparison of histological and clinical grading is inappropriate (clinical scoring 'averages' the core, and considers different features to histological scoring), yet their agreement on the study's representation of disease state can still be tested. The transition scores from the Outerbridge system were allocated to integer scores, for example, grade 1 $\rightarrow$ 2 was allocated to both grade 1 and grade 2. As cores were divided into 5 regions for OARSI scoring, the mode score from each core was taken as the combined score of the core. Finally, as the scoring range

of each system was different, we rescaled the OARSI scores to range from 0 to 4, matching that of the Outerbridge system. The Kolmogorov–Smirnov test (MATLAB, 2015a) was then implemented to compare the two systems. Figure 2.27 shows the cumulative probability of the Outerbridge and OARSI system. Results from the Kolmogorov–Smirnov test indicated that the study's representation of disease state is similar ($P > 0.05$) for clinical and histological scoring. Analysis therefore continued using histological scoring as the basis for comparing disease states.

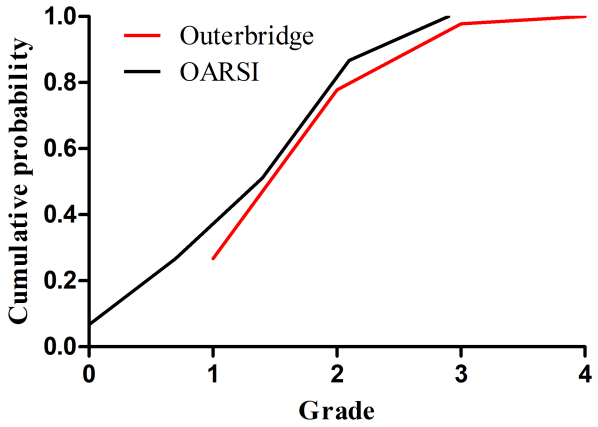


Figure 2.27: The cumulative probability of the Outerbridge and OARSI scoring systems.

2.3.2 Atomic Force Microscopy

Topography (height and amplitude), Young's modulus and loss tangent images were captured from each region of the cartilage surface, with mechanical measurements taken from individual fibrils within these regions. Representative images are shown in Figure 2.28. A total of 1,360 fibrils were measured, with Table 2.7 describing the breakdown by disease stage.

Table 2.7: Numbers of fibrils measured at each OARSI score.

OARSI score	**0**	**1**	**2**	**3**	**4**
Number of fibrils	96	336	424	468	36

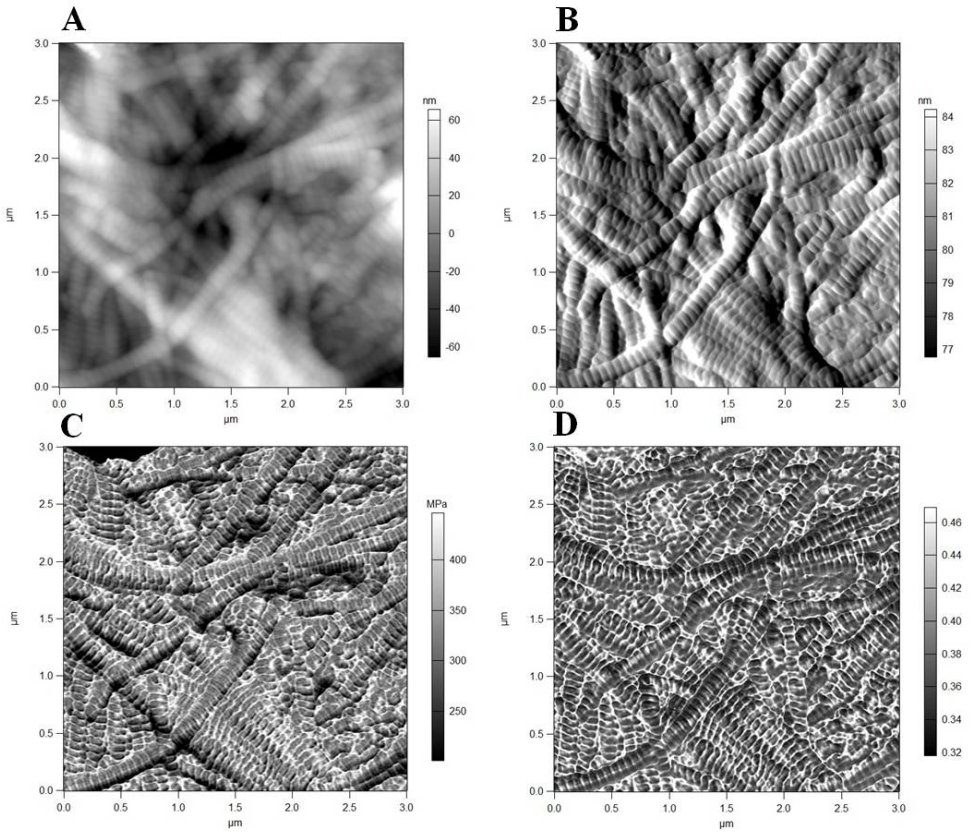


Figure 2.28: Representative AFM images of 3 × 3 μm areas on the human articular cartilage surface. (A) and (B) show the topography of the cartilage surface by height and amplitude respectively. (C) and (D) show the mechanical properties of the cartilage surface by Young's modulus and loss tangent.

2.3.2.1 Topography

Figure 2.29 shows typical fibril organisation at different disease stages. Generally, fibrils are in the order of 80-100 nm in diameter and randomly aligned. No clear pattern of fibril morphology was observed with disease progression at this scale, however, a number of morphological features were noted. Regions of local alignment, consistent with nonlinear optical measures of early OA cartilage [21] were observed at low OARSI grades (Figure 2.29A-C) but less commonly in higher grades. Other features included the presence of thin fibrils (Figure 2.30, red arrows); knotted fibril formations (Figure 2.31, OARSI grade 3); and collagen-bound granules (Figure 2.32A) which have also been observed from in another study [167] (Figure 2.32B).

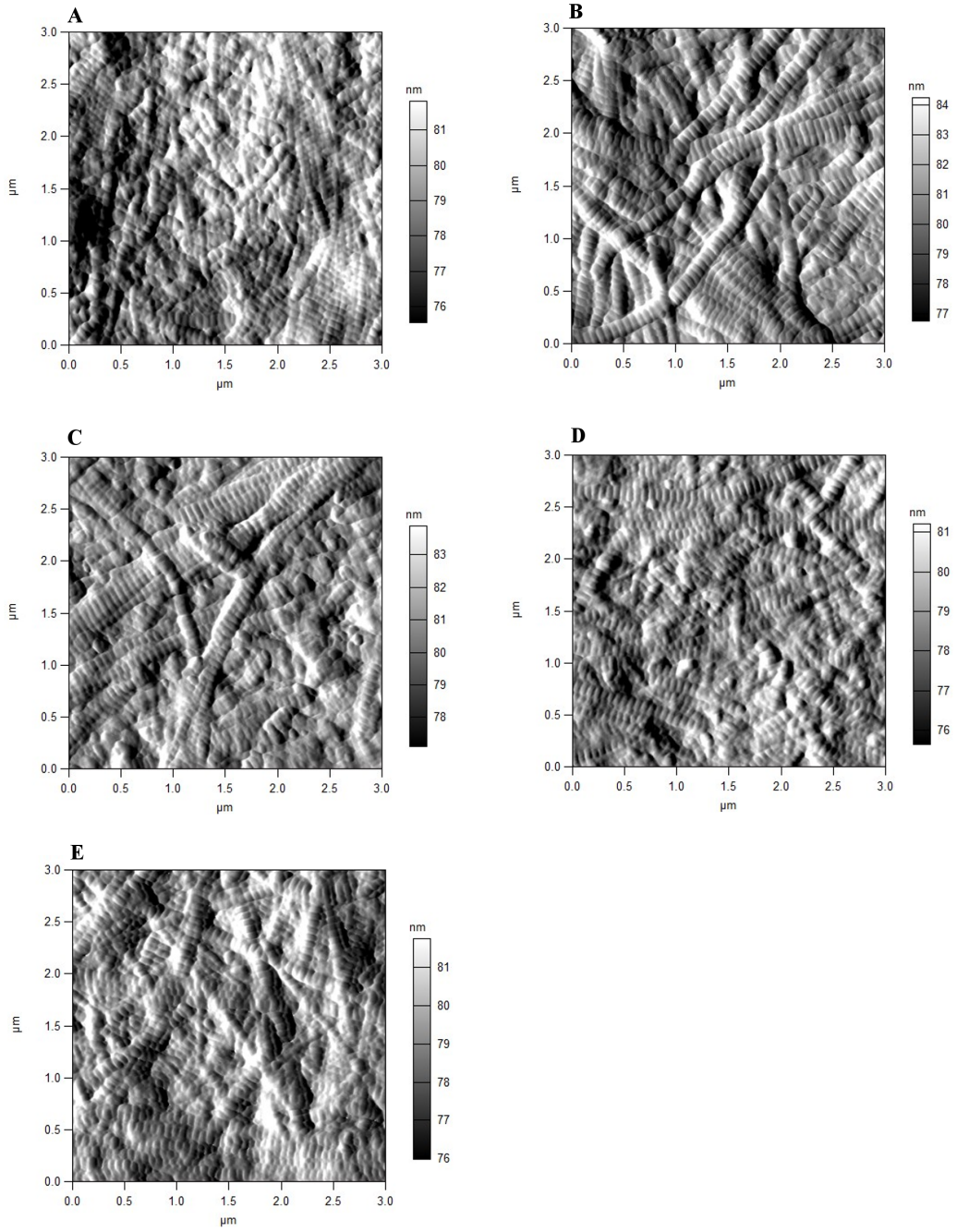


Figure 2.29: AFM amplitude images of 3 × 3 μm areas of the human cartilage surface at different disease stages: (A) grade 0, (B) grade 1, (C) grade 2, (D) grade 3 and (E) grade 4.

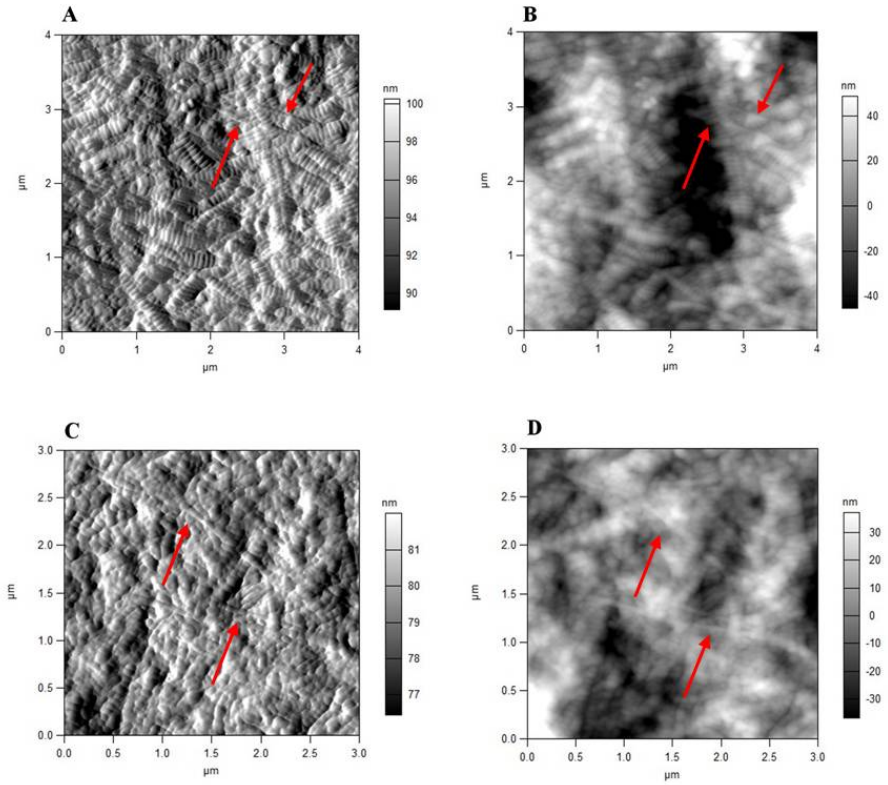


Figure 2.30: AFM images of thin fibrils from the human articular cartilage surface: amplitude image (A, C) and height image (B, D) of 4 × 4 μm and 3 × 3 μm areas on human articular cartilage samples. Red arrows indicate thin fibrils.

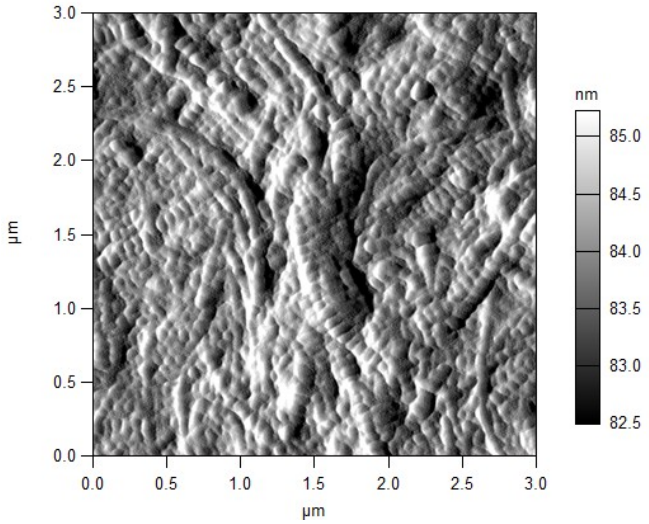


Figure 2.31: Knotting formation shown in an AFM amplitude image of a 3 × 3 μm area on the cartilage surface.

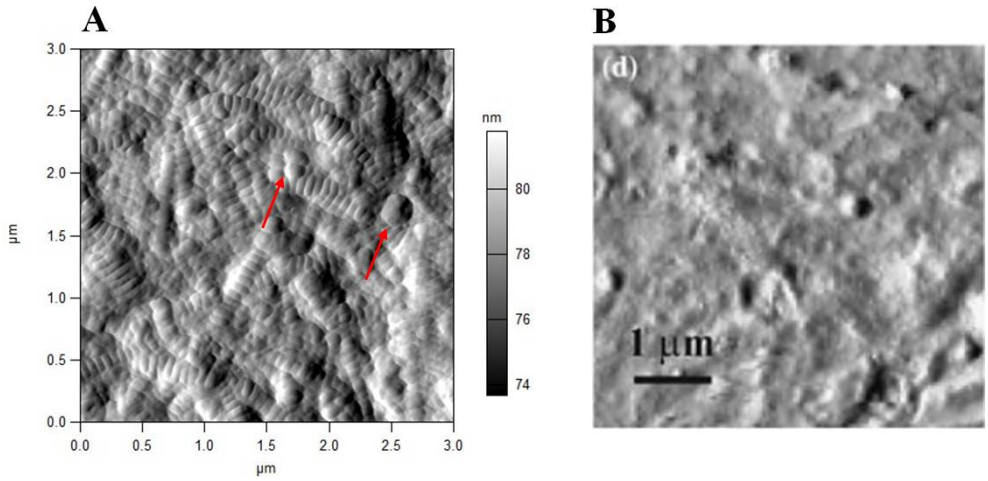


Figure 2.32: Granules on the surface of human cartilage: (A) amplitude images of a 3 $\times$ 3 μm area on the surface of human cartilage and (B) deflection images of a 5 $\times$ 5 μm area on human femoral cartilage in PBS [167]. (permissions to reuse the contents and figures of these papers have been granted by Springer (Appendix B))

2.3.2.2 Mechanical Properties

Figure 2.33A and B shows the mechanical properties of the collagen fibrils at different disease stages. Grade 2 appears to be an inflection point at which the trends of Young's modulus and loss tangent reverse with disease progression. Collagen fibrils became slightly softer from grade 0 to grade 1 (≈0.006%) and slightly stiffer with increasing disease stage from grade 0 to grade 2 (≈6% increase from grade 0) after which they soften again. The loss tangent, a measure of the mechanical contribution from viscosity of the collagen fibrils, showed considerably larger changes. Here, the reduction in loss tangent was 21% and 60% from grade 0 to grade 1 and 2 respectively, with statistically significant changes at each stage.

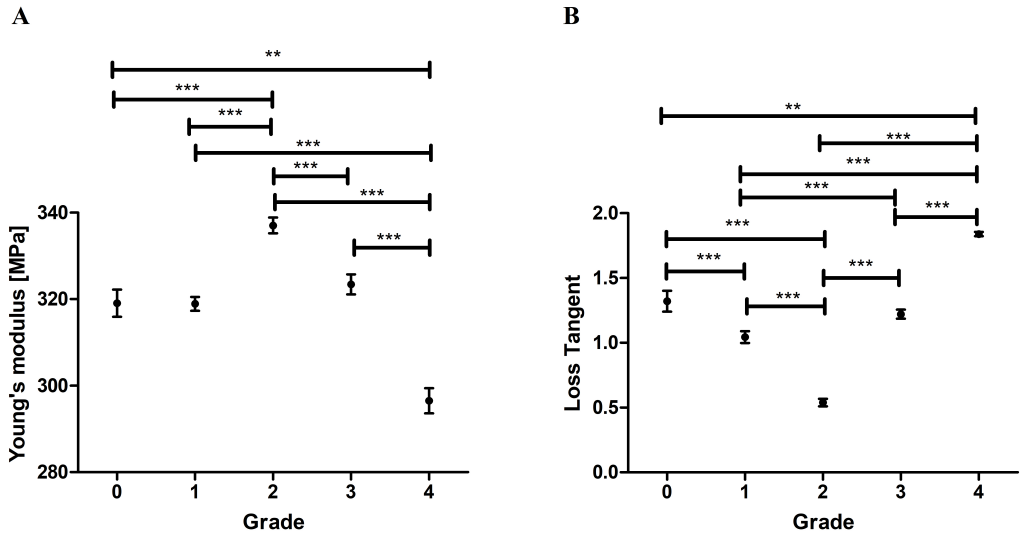


Figure 2.33: Mechanical properties within each collagen fibril at different disease stages: (A) Young's modulus and (B) loss tangent. *:$P<0.05$, **:$P<0.01$ and ***:$P<0.001$.

To investigate whether the observed pattern of variance was caused by potential issues of independence (all measurements were considered independent in the above), the analysis was re-run with measurements grouped by patient. Both Young's modulus and loss tangent (Figure 2.34A and B) showed similar trends to those shown in Figure 2.33A and B. Therefore, we argue that the observed patterns of mechanical properties can be attributed to disease stage.

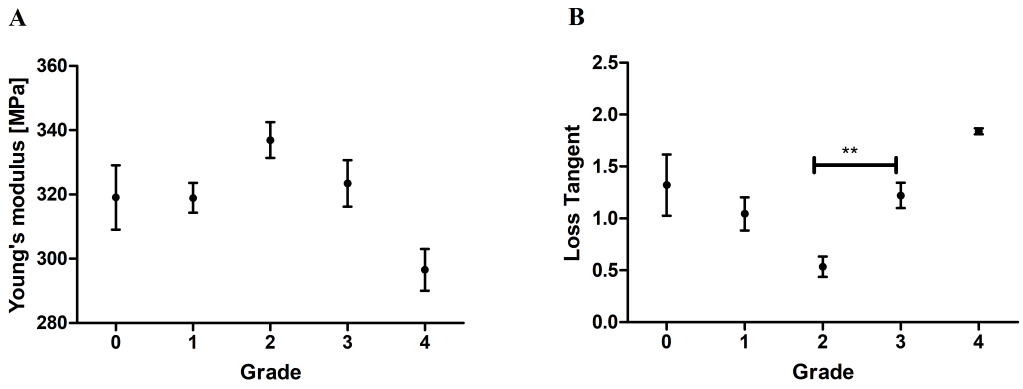


Figure 2.34: Mechanical properties of collagen fibrils grouped by patient at different disease stages: (A) Young's modulus and (B) loss tangent. **:P<0.01.

Figure 2.35 shows the distribution of Young's modulus of collagen at different disease stages. At grade 0, the Young's modulus appeared distributed between 260-380 MPa. Interestingly, at grade 1 and grade 2, some fibrils with high Young's modulus were detected (above 400 MPa). At grade 3, we could still observe some fibrils with high Young's modulus but at grade 4, there were no fibrils with high Young's modulus above 400 MPa and most were rated between 280-320 MPa.

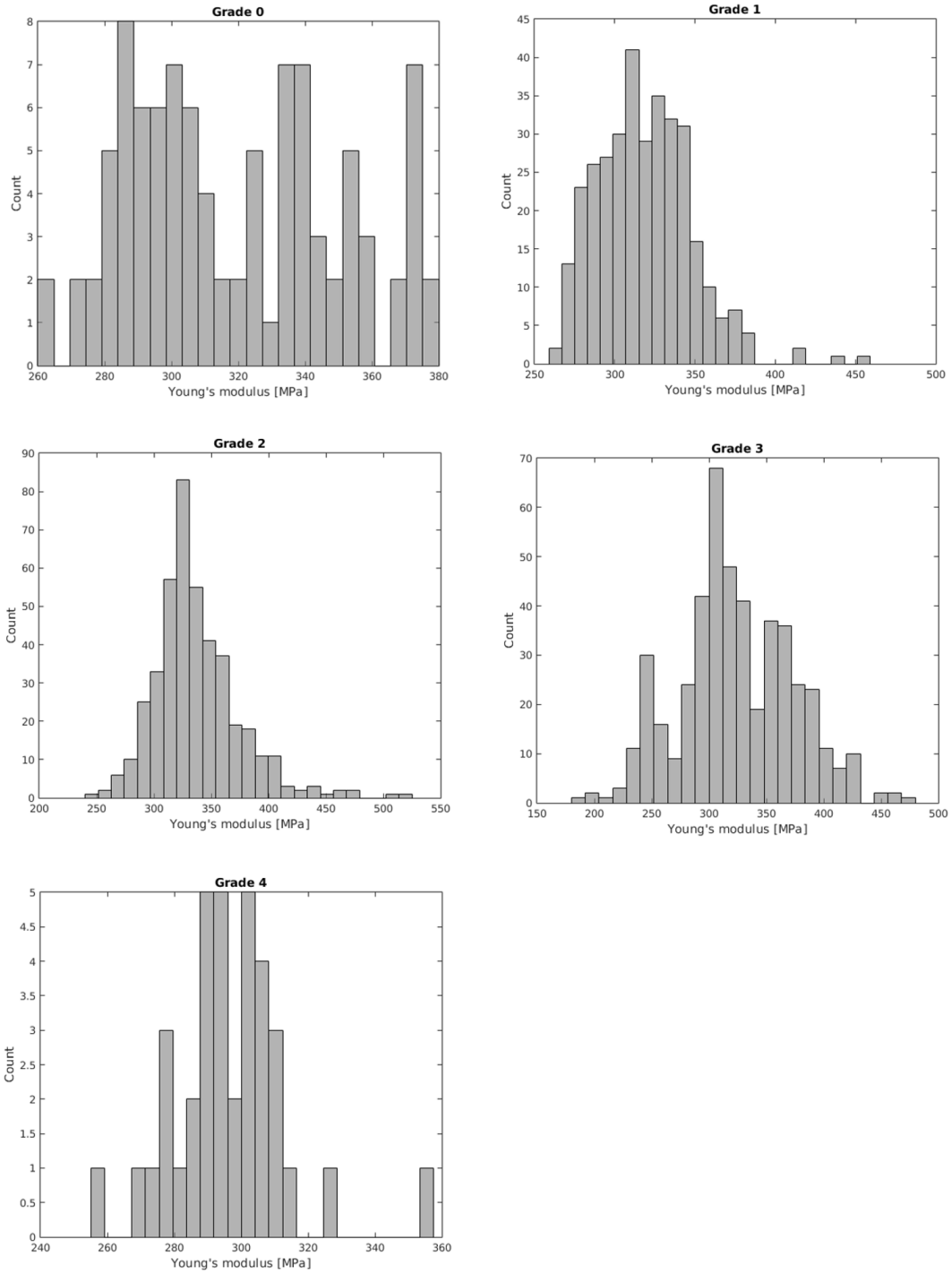


Figure 2.35: Distribution of mechanical properties of collagen fibrils at different disease stages.

Patterns of mechanical properties along fibrils were also considered. Figure 2.36A shows that the changes in Young's modulus across each D-period on a single fibril were largest in samples of grade 0, with a reduction of ≈24% with the onset of histologically detectable disease. The variance of the changes in Young's modulus (Figure 2.36B) along the fibrils showed a similar trend.

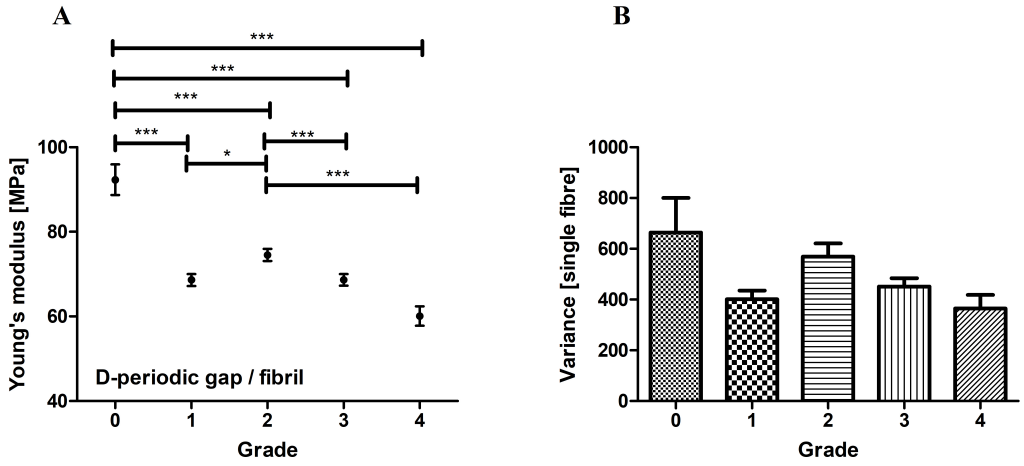


Figure 2.36: The D-period of collagen fibrils at different disease stages: (A) changes in Young's modulus across each D-period on a single fibril and (B) the variance of the changes in Young's modulus. *:$P<0.05$, **:$P<0.01$ and ***:$P<0.001$.

2.3.3 Raman Spectroscopy

Raman spectra at each OARSI grade are shown in Figure 2.37.

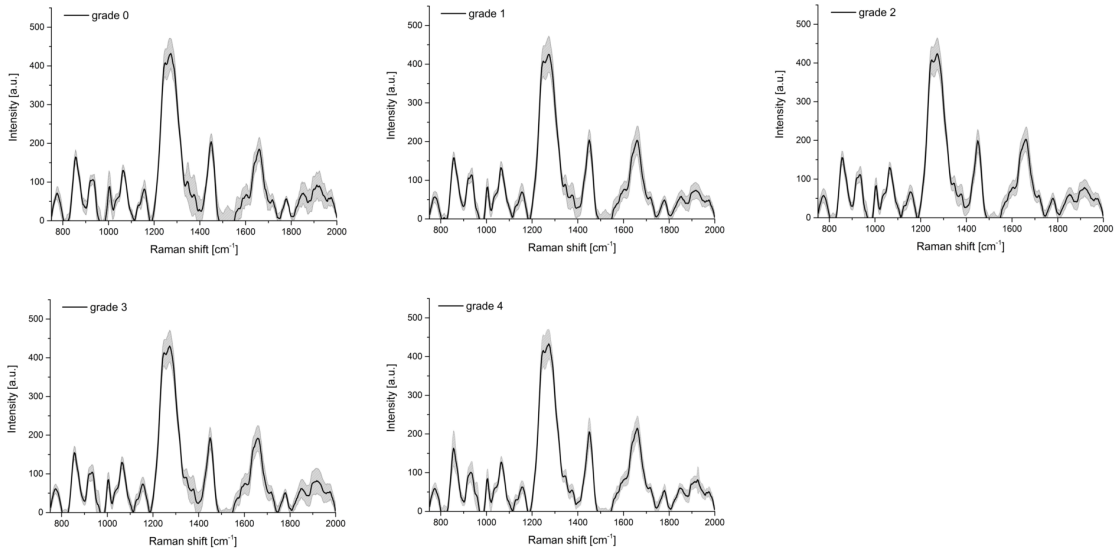


Figure 2.37: Raman spectra at different disease stages (mean ± SEM).

Areas under the Raman bands associated with collagen (Table 2.1) were analysed to assess the relative quality/quantity of the protein at different disease stages (Figure 2.38). No significant differences were observed between disease stages for any individual band. A general trend of decreased area, however, was observed from normal to diseased samples in the early stages (grade 0 to grade 1) with the exception of CH_2/CH_3 scissoring (Figure 2.38B).

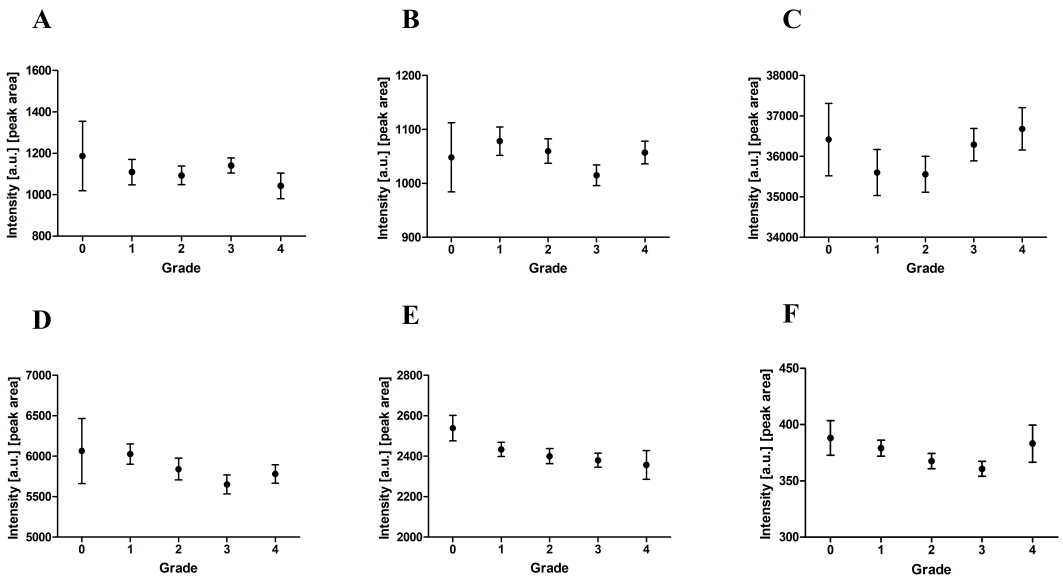


Figure 2.38: The areas under collagen type II bands at different disease stages: (A) phenylalanine ring (995-1015 cm^{-1}), (B) CH_2/CH_3 scissoring (1450-1460 cm^{-1}), (C) amide III (1209-1332 cm^{-1}); (D) CH_2/CH_3 scissoring (1429-1469 cm^{-1}); (E) proline (848-868 cm^{-1}) and (F) hydroxyproline (872-881 cm^{-1}).

Ratios of Raman bands were used as measures of quality. These measurements included helix stability and the level of order in the helix secondary structure. Helix stability, given by the ratio of proline to hydroxyproline, was similar at each disease stage (Figure 2.39), decreasing slightly from grade 0 to grade 1 (≈0.5%), increasing to grade 2 (≈1.2% from grade 0) and grade 3 (≈2.4% from grade 0) and decreasing again at grade 4 (≈3% from grade 0).

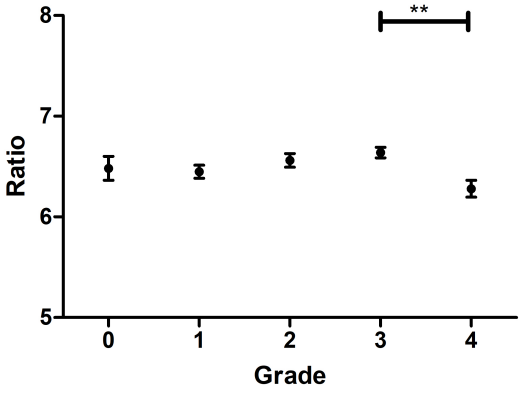


Figure 2.39: Collagen helix stability, given by the ratio of proline (856 cm^{-1}) to hydroxyproline (872 cm^{-1}). **:$P<0.01$.

The peak height ratio of 1240/1272 cm^{-1} was calculated to assess the order of the collagen [105]. Figure 2.40 shows that secondary structure within the collagen fibrils became less ordered with disease progression. Order decreased by 0.08% to grade 1 and 1.6% to grade 2 relative to grade 0, decreasing by ≈2% to grade 4. There were, however, no significant differences between the different disease stages.

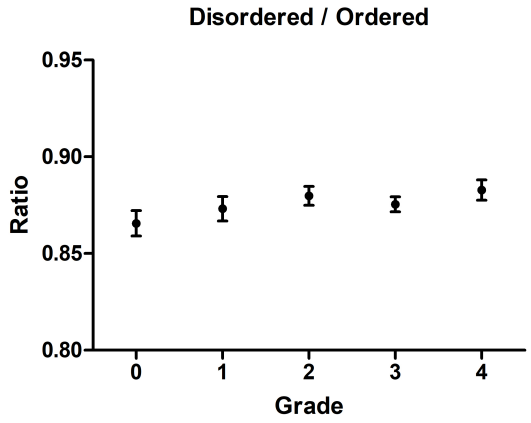


Figure 2.40: Ratios of random coil to alpha-helix (1240/1272 cm^{-1}) at different disease stages.

The relative concentrations of sulphate and hyaluronic acid in the ECM of cartilage were also considered. The Raman peak at 1002 cm^{-1} (collagen, phenylalanine ring) is generally assumed to be the most stable collagen peak against any changes in the local tissue environment [168, 169]. Therefore, the ratios of sulphate to collagen (I_{1062}/I_{1002}) and hyaluronic acid to collagen ($I_{1135-1175}/I_{1002}$) were calculated to provide an indication of proteoglycan content and hyaluronic acid content in the ECM of cartilage. Figure 2.41A shows that the sulphate content slightly increased from grade 0 to grade 1 (≈0.6%), decreased from grade 1 to grade 3 (≈8%) and increased from grade 3 to grade 4 (≈0.5%). Figure 2.41B shows that the hyaluronic acid slightly decreased with disease progression from grade 0 to grade 3 (≈1.5% decrease from grade 0 to grade 1, ≈3% decrease from grade 0 to grade 2 and ≈9% decrease from grade 0 to grade 3) but with a 5% increase from grade 3 to grade 4. However, there were no significant differences ($P > 0.05$) in the content of either in cartilage with disease progression. Figure

2.41C shows their ratio (sulphate to hyaluronic acid) at different stages of disease, together providing measures of aggrecan concentration and quality. We found that there was no significant difference, yet, generally, the ratio increased slightly with disease progression but with a small fluctuation (≈6% increase from grade 0 to grade 1, ≈5% increase from grade 0 to grade 2, ≈6% from grade 0 to grade 3 and ≈2% increase from grade 0 to grade 4).

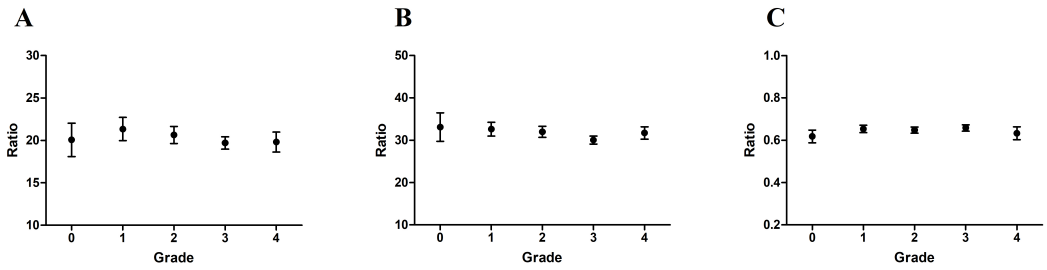


Figure 2.41: The relative concentration of (A) sulphate and (B) hyaluronic acid in cartilage ECM and (C) the ratio of the sulphate to hyaluronic acid at different disease stages.

2.4 Discussion

In this chapter, a sample preparation protocol was developed for AFM and a Raman spectroscopy system built. Using AFM and Raman spectroscopy, the physical characteristics of collagen fibrils, and their changes with OA progression were then investigated. Within the time and financial constraints of the project, the Raman system was unable to be extended for robust polarisation measurements. Hence, we focus on measures of quality and concentration rather than organisation. Other limitations are discussed in Chapter 5.

The low-level physical characterisation of cartilage surfaces revealed a number of features that could be associated with disease progression. The first, and perhaps most critical, observation was that physical changes with disease are nonlinear, reinforcing the concept of OA as a dynamic process. For this reason, and to ensure that comparisons between disease states are fair (the original surface is no longer present in OARSI grades > 2) we therefore focus our discussion on early-stage changes.

2.4.1 Topographical Features

Qualitative topographical information at the few-micron scale may further provide insight into the physical aspects of the disease process. Regions of local alignment were observed at early stages (Figure 2.29A-C) but less commonly in higher grades. The diameter of collagen fibrils was around 100 nm but some fibrils appeared thinner (e.g. Figure 2.30, red arrows). This may be because of the formation of new collagen fibrils, or alternatively the presence of fibrils of a different collagen type. Although bundling is strongly associated with disease progression before histological changes [21], such bundling is typically on the same or larger, size scales as the 3×3 μm image areas used here, rendering them unsuitable for this purpose.

2.4.2 Mechanical Features

The Young's modulus (Figure 2.33A) of collagen fibrils increased at early disease stages. While interesting and statistically significant, this is unlikely to be meaningful

in itself with just a 6% change from grade 0 to 2. The decrease in loss tangent (21% and 60% for grades 1 and 2 respectively), however, was more substantial (Figure 2.33B). The loss tangent provides a measure of a material's ability to dissipate rather than store mechanical energy. A substantial decrease in loss tangent with disease thus indicates a change from a dissipative, ductile deformation and fracture mechanism to one which is brittle, releasing substantial stored energy with fracture and undermining the controlled fracture propagation [170] that characterises high toughness biological materials.

In this context, the small increase in Young's modulus becomes more revealing. During AFM indentation, localised bending on the collagen fibril is resisted by tropocollagen tension and shear in the intermolecular bonds, similar to the application of bulk tensile loading. In both situations, molecular stretching competes with intermolecular sliding and breaking of weak and strong bonds.This mechanism protects the integrity of the structure by allowing localised failure through energy dissipation. With disease progression, studies have found increasing cross-link densities such as through AGEs which stiffens the fibrils [121–124]. A theoretical model [171] showed that excessive cross-link densities would lead to stronger fibrils, yet display a brittle deformation and smaller yield strains. Therefore, the decreased loss tangent we observed in this study is likely due to increasing density of crosslinks within fibrils with disease progression: the deformation mechanism is then characterised by fracture, instead of sliding, slip initiation or bond disruption within fibrils, resulting in less dissipated energy and thus lower damage resistance. These changes in the patterns of mechanical properties along fibrils (Figure 2.36) with the onset of disease add weight to the argument that major changes occur in the interactions between molecules rather than in the molecules themselves.

The distributions of Young's modulus are also interesting. Although grade 0 samples were of insufficient number to clearly distinguish a distribution, results for grades 1 and 2 showed a number of isolated, stiffer fibrils within the matrix (Figure 2.35). Such isolated fibrils create sharp deformation gradients in a loaded network, potentially creating stress concentrations at their periphery. Combined

with the decrease in loss tangent, the higher stresses these fibrils experience for a given deformation, and the related increased probability of failure, may act to embrittle the network due to the high elastic energy released upon fracture.

2.4.3 Raman Spectral Analysis

Analysis of Raman spectra was hampered by insufficient numbers, yet patterns of spectral change were observed. Probing the secondary structure (at the level of the tropocollagen molecule) directly, most collagen-related bands decreased in intensity with disease progression (Figure 2.38) indicating a potential loss of this protein with disease. Measures of tropocollagen quality, however, showed little change with disease. Helix stability (ratio of hydroxyproline to proline, Figure 2.39), remained stable in early disease, indicating little effect of OA processes on the fundamental helical structure of the molecule itself. This conclusion is supported by measures of order. Order appeared to decrease slightly with disease (Figure 2.40), although this trend was not statistically significant.

Later stages of disease did, however, show significant changes, such as the 5% decrease in helix stability from grade 3 to 4. This correlates with a previous study using the N-H stretching intensity (3310 cm^{-1}), which is associated with the triple-helical conformation [172]. These authors observed a peak shift to higher wave number at later stages of OA, indicating molecular disorder and a decrease in the concentration and stability of crosslinks [173].

It is interesting to note that no correlation was observed between mechanical and Raman results. The lack of a relationship between the properties of the tropocollagen molecules and those of tropocollagen assemblies suggests that disease related changes are specific to interactions between molecules. This further implicates intra-fibrillar crosslinking, and the potential for subsequent embrittlement to initiate and more easily propagate network damage.

2.4.4 Scoring Systems

Finally, it is interesting to note that, despite histological grading revealing 'normal' samples, no sample was graded as normal by the clinician. This is related to differences in spatial resolution. Clinical assessment is performed at the macro-scale, providing a single score for each core, with histological scoring performed on a 1 mm wide 2-D section. It should also be noted that no core was scored as histologically normal at more than three of the five measurement positions (only 2 out of 35 samples).

The relationships between scoring systems, and between such scores and the properties measured, raises the issue of their true relation to tissue viability. This is particularly important for the treatment gap in early OA that forms the main motivation of this thesis. Where, for example, non-viable tissue is to be replaced by a tissue engineered construct, terminally dysfunctional tissue must be defined and demarcated from surrounding viable, or at least recoverable, tissue. The work described in this chapter has established the physical changes to collagen in early OA, and provided a mechanistic link between these changes and an increased susceptibility to damage initiation and progression, yet it cannot on its own define an irreversible loss of integrity. This definition requires insight into the function of collagen in a network, and the *inter*-fibril interactions at this higher hierarchical level.

3

Development of a 2-D Model of the Collagen Meshwork

Contents

3.1 Introduction 84
3.2 Zigzag Configuration 87
3.2.1 Materials and Methods 87
3.2.2 Results 92
3.2.2.1 Effect of Crosslink Density 92
3.2.2.2 Effect of Crosslink Stiffness 96
3.3 *Mikado* Configuration 97
3.3.1 Materials and Methods 97
3.3.2 Model Simulation and Analysis 97
3.3.3 Results 99
3.3.3.1 Radial Tensile Force 99
3.3.3.2 Anisotropic Loading 107
3.3.3.3 Comparison of Loading Conditions 121
3.4 Discussion 124
3.4.1 Zigzag Configuration 124
3.4.2 *Mikado* Configuration 125

3.1 Introduction

In Chapter 2, we established changes in the physical properties of collagen fibrils with disease progression, and argued that the change in interactions between

tropocollagen molecules leads to embrittlement and susceptibility to damage. It is unclear from these results, however, how this increased susceptibility to structural damage fits with the function and dysfunction of collagen as a network, or with the reversibility of damage. We here propose that the process of collagen network restructuring observed in early disease is principally related to the interactions between fibrils rather than within them.

Computational modelling has become a popular method to explore the mechanics of diseases such as OA due to its tractability, flexibility (simulation of different situations) and predictability (predicting mechanical behaviour). It has been widely used to advance the understanding of cartilage/bone response to load and is becoming increasingly capable of representing cartilage structure [70, 174]. The earliest constitutive models of cartilage were single phase in which only the solid part of the tissue was considered [175, 176]. As such, these models, and subsequent viscoelastic models [177, 178], were incapable of capturing the controlled fluid exudation that we now understand dominates macroscale function. In addition, the scope of such models in parameter space is limited by the extent to which the hard-wired single phase constitutive relations retain validity as the ratios of the constituents change. Furthermore, single-phase frameworks do not track the constituents, and thereby do not allow for the way in which a change in constituents would impact the constitutive relations. A second generation of cartilage models (poroelastic or biphasic models), which considered both solid and fluid phases, were proposed. Poroelasticity represents a porous elastic material saturated with fluid, as initially developed by Biot in the context of soil consolidation [179] and later adapted for cartilage [180, 181]. A biphasic model was first proposed for articular cartilage in 1980 [180] and then further developed to include permeability [182] and large deformation [183]. However, such models fail to capture important aspects of cartilage behaviour such as microstructure and the influence of changes in osmotic pressure. Further, both models were limited in describing the short-term and time-dependent response when the compressive strain-rate was high. Consequently, fibril-reinforced models were then proposed to account for not only high fluid pressurisation

[184, 185] in the tissue but also to predict stresses in the cartilage under fast compression [186]. Wilson *et al.*, for example, integrated the relationship between permeability and tissue composition with a viscoelastic constitutive relationship within a fibril-reinforced model to predict the equilibrium and transient response of articular cartilage during compression, indentation and swelling tests [60]. Ateshian *et al.* applied continuous fibril angular distributions to model the solid matrix of cartilage, and successfully predicted experimental observations of the tissue's equilibrium response to mechanical and osmotic loading [187].

Triphasic models have been developed generalising biphasic models by incorporating an ionic phase in the proteoglycan matrix in addition to fluid and solid phases [188]. This yields complex models that allow for a tighter link between the actual observed process and the modelling representation. Nonetheless triphasic treatments, with the solid phase of tissue simplified to a homogeneous, isotropic, linearly-elastic material undergoing infinitesimal strain, could be related to biphasic models *a posteriori* in contexts where the properties of the aggrecans do not change extensively [189]. Later these models were extended to account for multi-electrolytes and polyvalent ions [190]. Further generalisation appeared with quadriphasic description of cartilage, with cations and anions treated separately in order to capture swelling more accurately [191]. A recent review article has documented these advances in multiphase cartilage modelling and their challenges [23].

Such models provide excellent representation of bulk properties yet are unable to represent damage processes as they average fibril properties and orientations on the scale of a continuum, and thus cannot access the scale of early matrix damage. In particular, while there have been advances in the theoretical mechanics of upscaling (e.g. [192–194]), whereby material properties at the sub-continuum scale are systematically incorporated into the constitutive relation of continuum models with controlled accuracy, such approaches are generally not tractable for collagen networks and cartilage [23, 170]. Hence, it is currently not feasible to assess the impact of fibril-scale changes and individual crosslinks in a continuum model. Thus one must instead adopt a bottom-up approach and represent collagen fibrils

individually; furthermore elastic-dominated constitutive relationships are indicated for fibrils [170] in contrast to entropic-dominated models at lower scales. There has been relatively little study below the scale of the continuum approximation until recently. An exemplar of such a model has been explored by Lee *et al.* [195], who concentrated on elucidating the stress-strain relationship of materials made from networks of collagen fibrils. They found that fibril network geometry is a key determinant of the mechanical properties of the fibre network. A recent study also developed a representative volume element (RVE) model of the collagen fibre network to investigate the tensile behaviour under different crosslink densities and stiffnesses at the microscale, and found that increased crosslink density within a fibril network has a much greater impact on the material stiffening than the crosslink stiffness [66].

Here, a bottom-up two-dimensional (2-D) model of the cartilage collagen meshwork was developed to explore the relationship between the fibril interactions in the collagen meshwork and the consequent mechanical performance and restructuring under load. To test these fibril interactions, different numbers of crosslinks within each structure were used to represent inter-connectivity between fibrils, with structural changes related to fibril alignment as it is a known characteristic of cartilage pathology [21, 196]. Two different collagen fibril configurations were developed to investigate the mechanical behaviours under load. In Section 3.2, a 'zigzag' network configuration is considered, with initially aligned fibrils perturbed to produce a kinked, interlocking microstructure capturing the mesoscale alignment and microscale randomness of the cartilage matrix. In Section 3.3, we consider a *Mikado* network configuration of straight fibrils, with random alignment and spatial distribution as an alternative, surface-specific network.

3.2 Zigzag Configuration

3.2.1 Materials and Methods

A 2-D model of collagen microstructure (30 by 30 μm) was implemented in C/C++. The scale addressed by this study is below the scale which requires consideration of

inertia and thermodynamics, so each node has no mass and there is no inclusion of thermodynamics in our model.

For simplicity, collagen fibrils were not represented as Euler-Bernoulli filaments; instead each fibril was modelled as a series of one-dimensional (1-D) springs of length approximately 1 μm connected at nodes, via torque-free pin joints. Assuming a fibril diameter of 100 nm and a linear force-strain relationship, the material properties of a fibril were calculated by fitting experimental data from a single fibril tensile test [197] to give a force-strain relationship of 4 μN/unit strain (equivalent to a Young's modulus of around 500 MPa) (Figure 3.1).

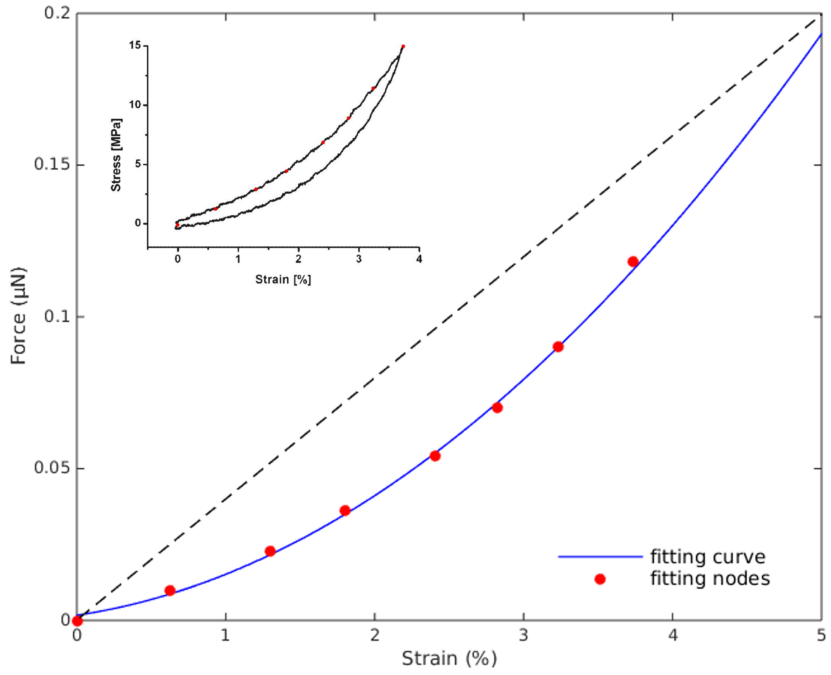


Figure 3.1: The material property of a fibril was calculated by fitting experimental data from a single fibril tensile test [197] (inset figure) to give a linear force-strain relationship of 4 μN/unit strain (the black dashed line). The red dots show the fitting nodes from the stress-strain experimental data after conversion to a force-strain relationship.

Crosslinks were implemented with a linear force-strain relationship on the assumption of small deformation, with parameters chosen *a posteriori* due to a lack of available data. It should be noted that crosslinking in this model refers to inter-fibril connectivity, and does not probe, for example, enzymatic or AGE-related crosslinking [124, 170]. Validation of the fibril implementation was performed using a single fibril of length 20 μm (20 segments) under load in one dimension. Validation of crosslink behaviour was similarly performed by linking two fibrils in series. Each spring had the linear force-strain relationship

$$F = k(\frac{L'-L_0}{L_0}), \tag{3.1}$$

where L' was the displaced length of the spring, L_0 was the resting length of the spring, F was force and k is the spring constant, a material property. The error in the numerical solution, relative to the analytical solution, was considered by calculating the spring length when it reached equilibrium (i.e. all node movement was below a very small tolerance). The accuracy of the numerical solution was better than 99.9% (Table 3.1).

Table 3.1: Numerical spring length error under one-dimensional tensile test load for an isolated spring segment (single spring) and a single, 20-segment spring (single fibril).

	single spring	single fibril		
Spring resting length	1μm	0.5μm	1μm	2μm
Error(%)	-0.006	-0.022	-0.003	-0.003

Thirty collagen meshwork configurations were constructed to simulate the pseudo-random collagen observed in electron micrographs [65, 68, 198], with anisotropy and connectivity forming the Benninghoff arcades [47] at larger scales. A representative structure is given in Figure 3.2. Each node, shown in yellow, is connected to two neighbours on the same fibre by linear springs, shown in green. All structures were based on 30 parallel sets of 24 springs, giving a total fibre length 24 μm, initially aligned with the y-axis and separated by 1 μm in the x direction. Nodes were then randomly displaced in x direction within $\pm$ 1 μm. Crosslinks (shown in red in Figure 3.2) were incorporated based on the proximity of nodes from adjacent fibrils.

Proximity thresholds of 0.3, 0.5 and 0.8 μm were applied to each structure, with a linear stress-strain relationship for the crosslink varying between 2 and 12 μN/unit strain. Once a crosslink formed in the model, it was not allowed to break.

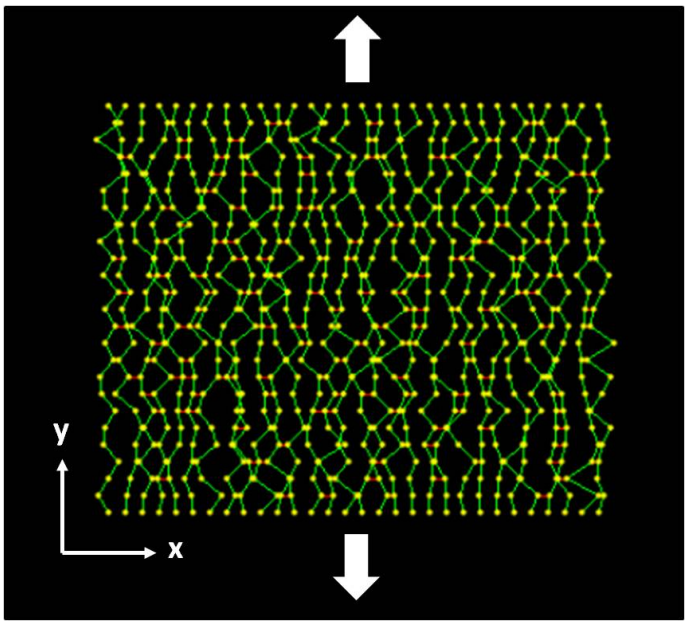


Figure 3.2: Representative collagen network model. Spring segments are shown in green, nodes shown in yellow and crosslinks shown in red.

Uniaxial tensile loading, in the direction of predominant fibril alignment, was applied as an exemplar to simplify the complex stress environment of the tissue while capturing the tensile response of the collagen meshwork to macroscale applied loads [199, 200]. In each simulation, the end nodes of each fibril were fixed in the x-direction and subjected to a constant tensile force of 0.5 μN in the y-direction. Node positions were time-stepped according to a linear overdamping law. When the structure reached equilibrium, the load was released and the structure allowed to recover. Node positions were recorded at original, equilibrium and recovered positions and transferred to MATLAB (2015a) for analysis.

Strains and fibril organisations were calculated for each simulation. Fibril strains in each structure were calculated based on the change in distance between adjacent nodes. Bulk strains were calculated based on the mean distance between the fibril end nodes. Organisation was classified using an anisotropy parameter r_{mean} based on

polarised optical parameters used for cartilage measurements [201–203], providing a means for comparison with experimental results. In particular r_{mean} is defined by

$$r_{mean} = \frac{1}{N} \sum_{i=1}^{N} \frac{\delta Y_i - \delta X_i}{\delta Y_i + 2\delta X_i}, \tag{3.2}$$

where N is the total number of springs, and $\delta X_i = |\delta x_{i+1} - \delta x_i|$, $\delta Y_i = |\delta y_{i+1} - \delta y_i|$ and δx_i and δy_i are the x and y positions of the i^{th} node. Note for instance that when $r_{mean} = 1$, the fibrils are aligned in the direction of loading.

3.2.2 Results

3.2.2.1 Effect of Crosslink Density

A representative model simulation before and after stretching is shown in Figure 3.3.

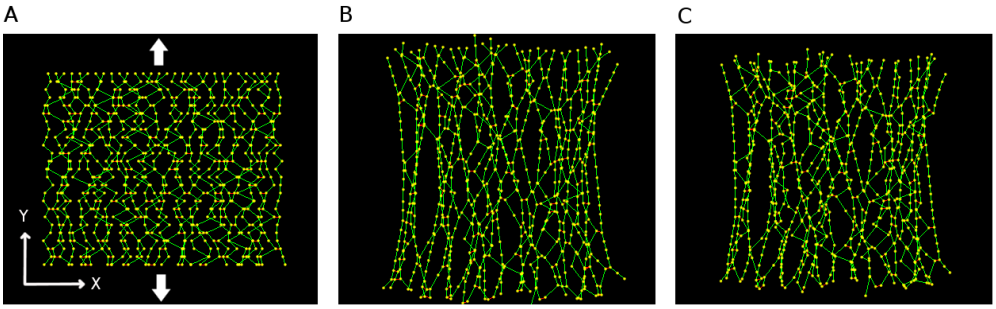


Figure 3.3: A representative structure (A) before stretching, (B) after stretching and (C) after relaxation. White arrows show the force direction. Springs are shown in green, nodes in yellow and crosslinks in red.

Qualitatively, different numbers of crosslinks lead to different configurations after loading. Highly-crosslinked microstructures maintained a 'normal' configuration with loading (Figure 3.4A). On the other hand, microstructures with lower crosslink densities were more aligned with the direction of loading, and formed fibre bundles (Figure 3.4B) which were similar to those observed in electron microscopy of osteoarthritic cartilage (Figure 3.4C [120]).

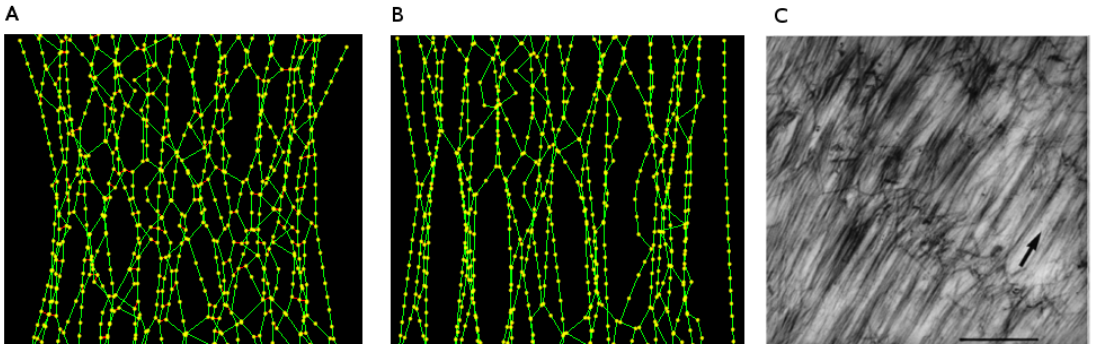


Figure 3.4: Representative structure with (A) 314 crosslinks and (B) with 81 crosslinks after stretching. (C) Transmission electron micrograph of collagen fibril organisation in osteoarthritic cartilage, reproduced from [120]. Scale bar 1.5μm. (permissions to reuse the contents and figures of these papers have been granted by John Wiley and Sons (Appendix B))

For a given structure and crosslinking threshold, the crosslink density was inversely proportional to the anisotropy measure of the pre-loaded meshwork structure (Figure 3.5), with $r^2 > 0.9$ (Pearson's correlation coefficient)).

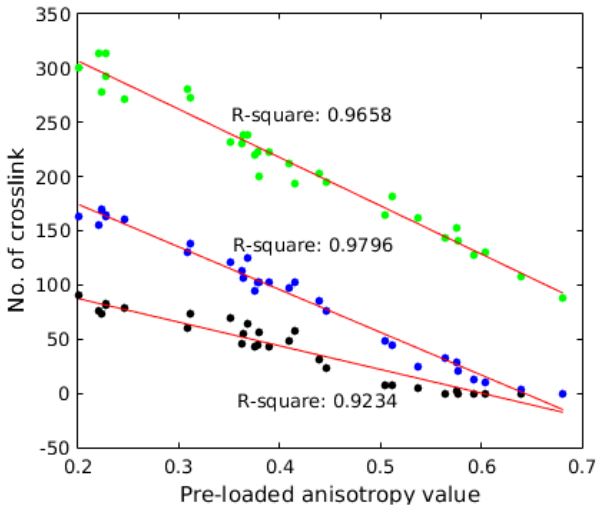


Figure 3.5: Relationship between crosslink density and angular anisotropy (r_{mean}) of the pre-loaded structure. Each line represents data from a single crosslink threshold. Black represents 0.3 μm, blue represents 0.5 μm and green represents 0.8 μm crosslink proximity thresholds.

Quantitative differences due to crosslink density were also observed. Because of the random modification of node positions for each microstructure, threshold distances for crosslinking produced a range of crosslink densities in the structures. The reconfiguration of fibrils under loading, quantified by the above anisotropy parameter r_{mean} (equation 3.2) is presented in Figure 3.6. At low crosslink densities, fibrils aligned with the direction of load, with minimal recovery. At higher crosslink densities, the microstructures resisted realignment (Figure 3.6A) and recovered their isotropy to a greater extent (Figure 3.6C). The maximum recovery of isotropy (% recovered r_{mean} relative to r_{mean} at equilibrium), however, was only 35%.

For a fixed crosslink proximity threshold, bulk strain data clustered into groups. Within these groups (i.e. black, green or blue dots in Figure 3.7), bulk strain increased with increasing crosslink density, both after stretching (Figure 3.7A) and

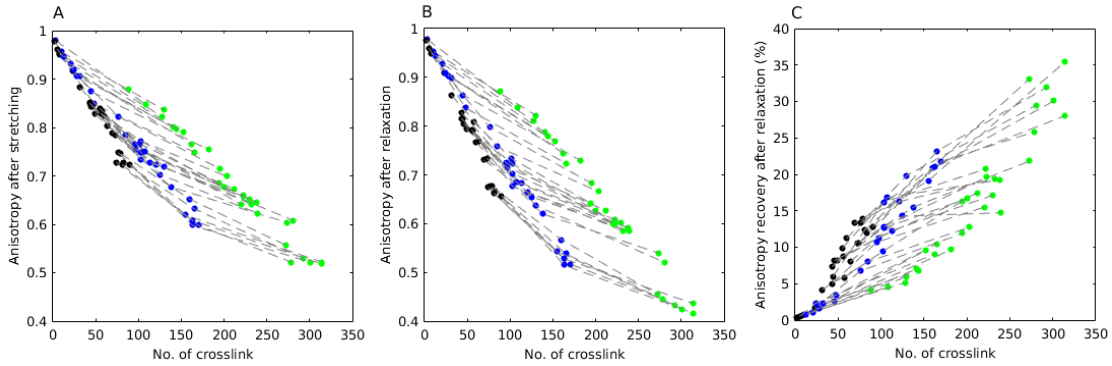


Figure 3.6: Structural anisotropy as defined by r_{mean} under loading and recovery. (A) Greater isotropy was maintained, and (B, C) recovered, in highly-crosslinked microstructures. Dashed lines plot the trends within the same structure at different crosslink thresholds. Different crosslink proximity thresholds are presented in different colours where 0.3 μm is black, 0.5 μm is blue and 0.8 μm is green.

after relaxation (Figure 3.7B). This was likely due to the relationship between crosslink density and angular isotropy in the pre-loaded state (Figure 3.5), and therefore greater structural reconfiguration under load. Within a structural configuration (linked by dashed lines, Figure 3.7), however, increasing crosslink densities consistently reduced bulk strain. In both cases, greater bulk strain was recovered upon relaxation with increasing crosslink density (Figure 3.7C).

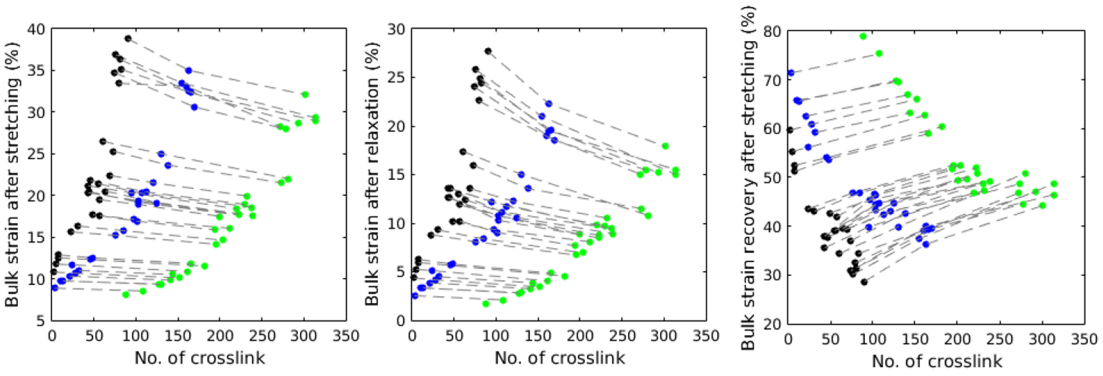


Figure 3.7: Bulk mechanical strain under loading and recovery. (A, B) Bulk strain decreased with increasing crosslink density, (C) with greater recovery in highly crosslinked microstructures. Dashed lines plot the trends within the same structure at different crosslink proximity thresholds. Different crosslink proximity thresholds are presented in different colours where 0.3 μm is black, 0.5 μm is blue and 0.8 μm is green.

Fibril strain (the mean of the distribution of fibril strains) after stretching increased with crosslink density (Figure 3.8). Two exceptions to this trend were

apparent, however, reasons for this are unclear. Recovery of fibril strain after relaxation was near 100%, with mean fibril strain reduced to $0.037 \pm 0.004\%$.

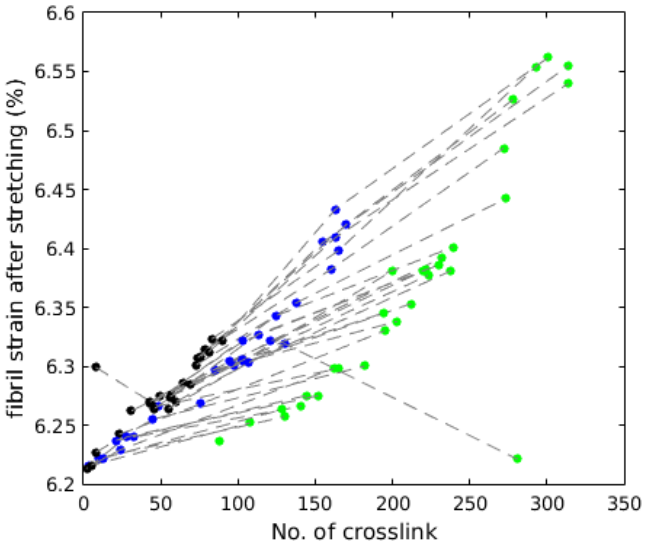


Figure 3.8: Fibril strain at equilibrium at different crosslink densities. Dashed lines link the same structure with different crosslink thresholds. Different crosslink thresholds are shown in different colours where 0.3 μm is black, 0.5 μm is blue and 0.8 μm is green.

3.2.2.2 Effect of Crosslink Stiffness

Six different material properties were assigned to test the effects of crosslink properties on the mechanical behaviour of the microstructure. Output parameters generated for a representative structure are given in Table 3.2. Kruskal-Wallis tests (SPSS Statistics 17.0, IBM) showed no significant differences (all $P > 0.4$) in the structural response to loading for different crosslink stiffnesses.

Table 3.2: Mechanical behaviour of a representative structure (293 crosslinks) with different crosslink stiffness.

Output parameter	Material property of crosslink (Force (μN)/unit strain)					
	2	4	6	8	10	12
fibril strain at equilibrium (%)	6.540	6.554	6.560	6.563	6.565	6.566
bulk strain at equilibrium (%)	28.935	28.654	28.549	28.493	28.459	28.435
anisotropy at equilibrium	0.439	0.433	0.431	0.430	0.429	0.429
fibril strain after relaxation (%)	0.037	0.036	0.036	0.036	0.035	0.035
bulk strain after relaxation (%)	17.306	17.296	17.289	17.283	17.279	17.276
anisotropy after relaxation	0.362	0.362	0.362	0.362	0.362	0.362

3.3 *Mikado* Configuration

A *Mikado* network structure was implemented for comparison with the network geometry above. These networks consist of straight fibrils, randomly orientated and distributed in the 2-D plane, providing an alternative configuration yet similar averaged orientation.

3.3.1 Materials and Methods

The configuration was generated by sequential random deposition of filaments of length 30 μm into a circle with a radius of 15 μm (MATLAB, 2015a). Fifty filaments were placed at random orientations and random spatial distribution inside this circle. Each filament was divided by 10 nodes, creating nine segments of equal length incorporated with a linear force-strain relationship which was 4 μN/unit strain. Crosslinks, shown in red, were incorporated based on the proximity of nodes which were thresholded at 0.5, 0.7, 0.9, 1.1, 1.3 and 1.5 μm from adjacent fibrils in each structure. As in the previous sections, crosslinks were implemented with the same linear force-strain relationship as used for the collagen and once formed, were not allowed to break.

3.3.2 Model Simulation and Analysis

A tensile radial force of 0.5 μN was applied to 30 different structures (Section 3.3.3.1). We further tested 10 structures with anisotropic loading including uniaxial tensile loading (i.e. y-direction) and uneven 2-dimensional tensile force of 0.5 μN in the x-direction and 0.1 μN in the y-direction to observe the difference (Section 3.3.3.2). When the changes in the node positions were below a very small tolerance (equilibrium), the force was released and the structure allowed to recover. The positions of the nodes were recorded at the original, equilibrium and recovered positions and transferred to MATLAB (2015a) for analysis. As in previous sections, strains and fibril organisations were calculated for each simulation. Fibril strains in each structure were calculated based on the change in the distance between adjacent nodes. Instead of measuring bulk strain, the changes in the areas of

each structure before and after stretching and recovery were calculated (MATLAB, 2015a). Calculations were performed by setting the outer boundaries of the structure before and after pulling and after recovery. The outer springs of the structures were discarded from the analysis. Therefore, the positions of second layers of outer springs were applied for boundary detection by MATLAB (2015a). A representative figure of boundary detection is shown in Figure 3.9. The areas enclosed by the boundary were returned during boundary detection and then the differences between these areas before and after pulling and after relaxation were calculated.

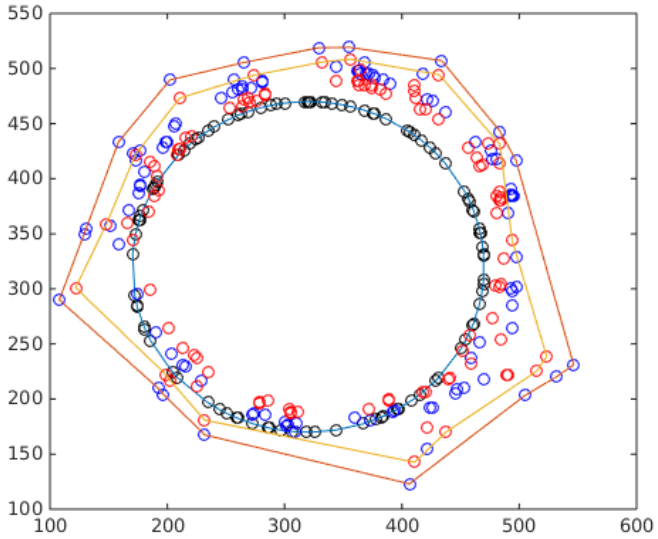


Figure 3.9: Representative boundary detection from one structure with a crosslinking threshold of 0.9 μm. Black dots represent the boundary nodes of the structure before stretching. Blue dots represent the boundary nodes of the structure at equilibrium and red dots show the boundary nodes of the structure after recovery. The boundary of the structure before stretching is shown in blue, after stretching is shown in red and after recovery is shown in yellow.

3.3.3 Results

3.3.3.1 Radial Tensile Force

3.3.3.1.1 Anisotropy, Fibril Strain, Bulk Strain and Area Changes

A representative figure of the *Mikado* collagen meshwork is shown in Figure 3.10A. A 0.5 μN radial force was applied to the outer nodes until equilibrium was reached (Figure 3.10B). The load was then released and the structure considered relaxed when the velocities of nodes were below a very small tolerance (Figure 3.10C).

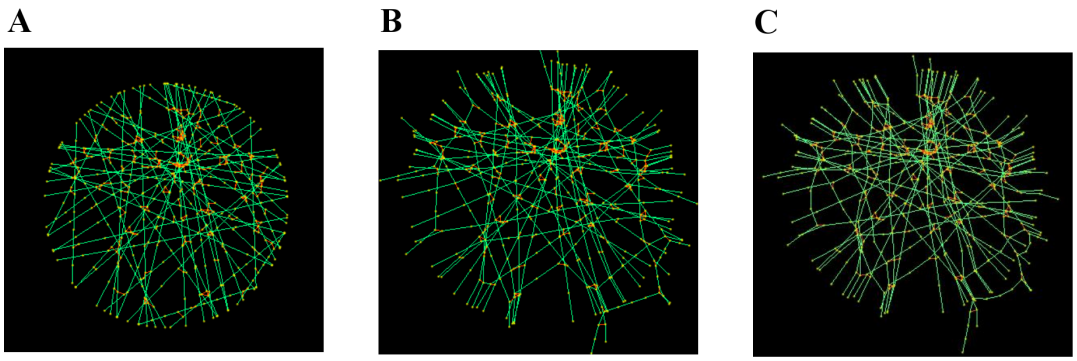


Figure 3.10: Configuration of a representative surface specific simulation with a 0.9 μm crosslink threshold (A) before stretching, (B) after stretching and (C) after relaxation. Fibrils are shown in green, nodes are shown in yellow and crosslinks are shown in red.

Figure 3.11 shows the anisotropy before and after loading. Unlike 'zigzag' configurations under 1-D load, no clear trends in organisation were observed after loading due to the complexity of the structure and uniformity of the applied load.

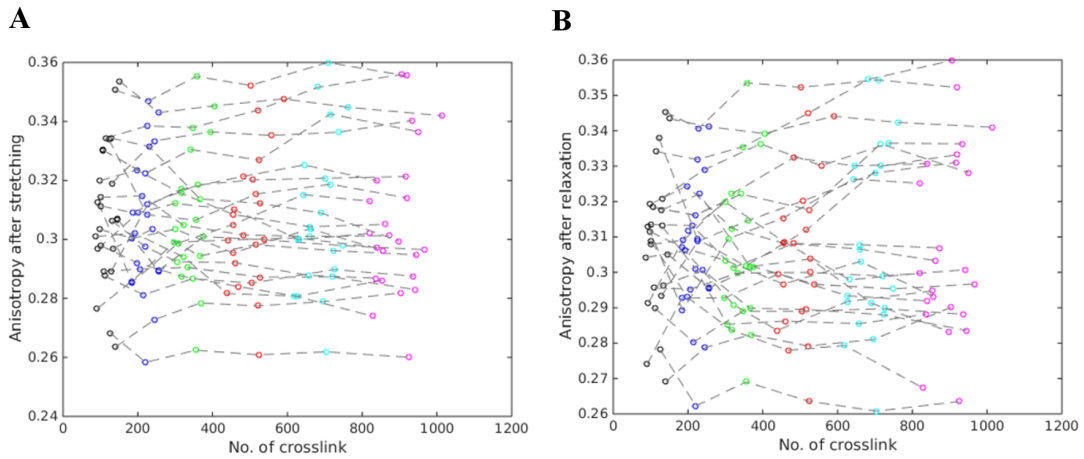


Figure 3.11: Relationship between crosslink density and angular anisotropy (A) at equilibrium and (B) after relaxation. Different crosslink thresholds are shown in different colours where 0.5 μm is black, 0.7 μm is blue, 0.9 μm is green, 1.1 μm is red, 1.3 μm is cyan and 1.5 μm is magenta.

Figure 3.12 shows the changes in the areas of each structure before and after stretching and after recovery. Highly-crosslinked structures showed smaller area changes after stretching (Figure 3.12A) and relaxation (Figure 3.12B), with a higher percentage of recovery (Figure 3.12C).

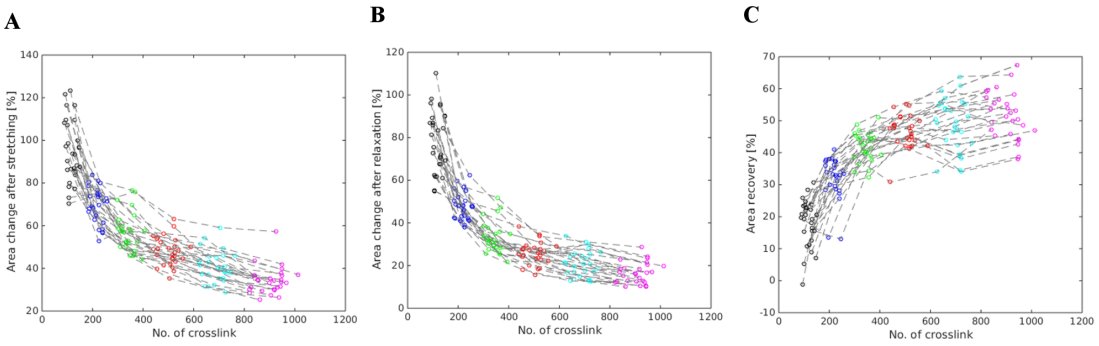


Figure 3.12: Area changes (A) after stretching, (B) after relaxation and (C) recovery. Dashed lines link the same structure with different crosslink thresholds. Different crosslink thresholds are shown in different colours where 0.5 μm is black, 0.7 μm is blue, 0.9 μm is green, 1.1 μm is red, 1.3 μm is cyan and 1.5 μm is magenta.

Virtually no fibril strain was observed after relaxation (data not shown). However, fibril strain at equilibrium (Figure 3.13) revealed a different trend to that observed in our previous 'zigzag' model. Instead of the fibril strain increasing along with the

increase in the number of crosslinks, fibril strain initially increased with crosslinking and then decreased after the number of crosslinks exceeded between 200 and 400.

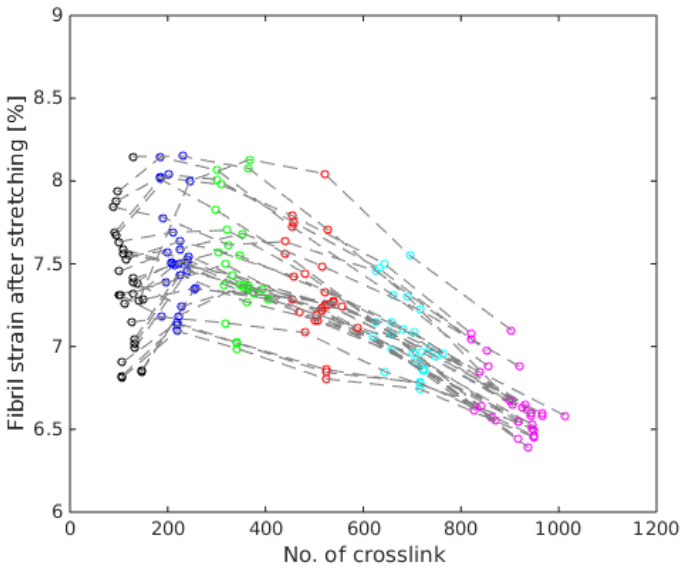


Figure 3.13: Fibril strain at equilibrium at different crosslink densities. Dashed lines link the same structure with different crosslink thresholds. Different crosslink thresholds are shown in different colours where 0.5 μm is black, 0.7 μm is blue, 0.9 μm is green, 1.1 μm is red, 1.3 μm is cyan and 1.5 μm is magenta.

We further plotted the fibrils with strain greater than 7.5% to observe their location in the structure and to better understand the functional difference between lower- and higher- crosslinked structures. Figure 3.14 compares the distribution of fibril strains of over 7.5% (shown in white) between lower crosslinks (Figure 3.14A) and higher crosslinks (Figure 3.14B). We found that decreased fibril strain occurred around clusters of high-density crosslinks (yellow dashed ellipse), forming highly-localised 'protected' regions where fewer fibrils in the greater structure experienced high strains. This is further reflected in the variance in fibril strain observed between different crosslink patterns (Figure 3.15), showing that the lower the number of crosslinks, the higher the variance of fibril strain.

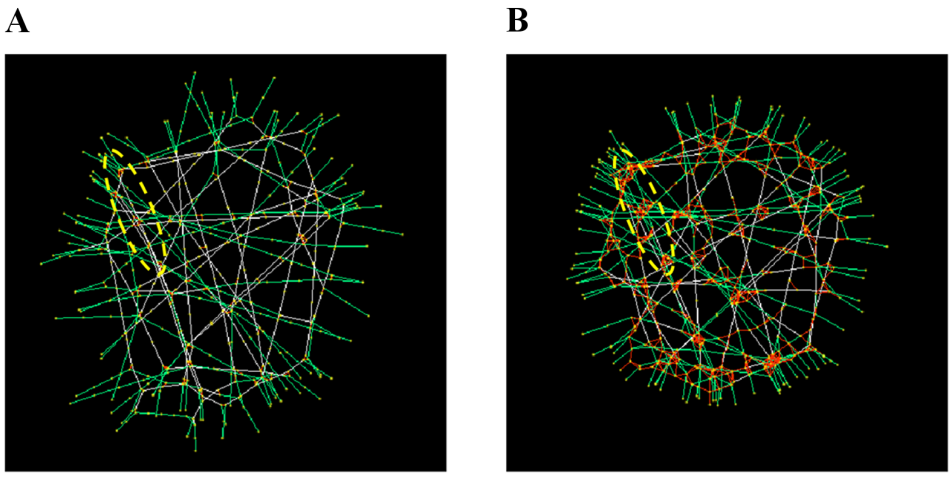


Figure 3.14: A representative structure highlighting fibrils under high strain (over 7.5%) with crosslink thresholds of (A) 7 μm and (B) 15 μm. The fibrils in white indicates those with strain of over 7.5%. The yellow dashed ellipse shows a region of local strain reduction due to the high density of crosslinks.

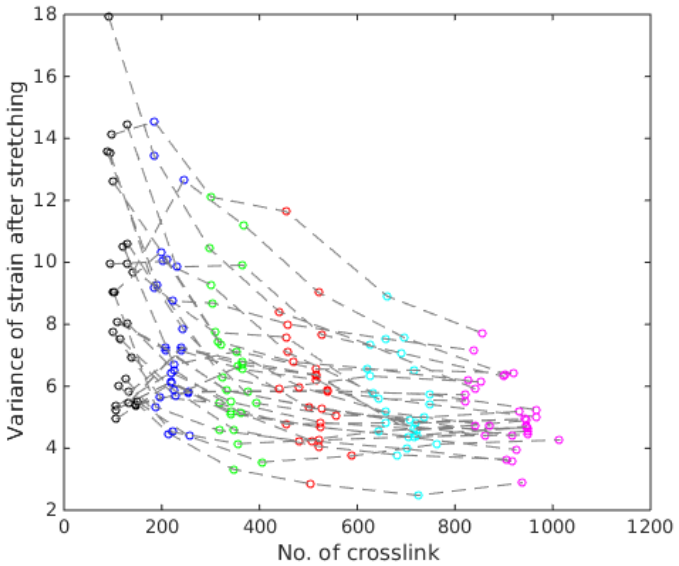


Figure 3.15: Variance of fibril strain at equilibrium at different crosslink densities. Dashed lines link the same structure with different crosslink thresholds. Different crosslink thresholds are shown in different colours where 0.5 μm is black, 0.7 μm is blue, 0.9 μm is green, 1.1 μm is red, 1.3 μm is cyan and 1.5 μm is magenta.

3.3.3.1.2 Redundancy and Crosslink Clustering

Since Figure 3.13 showed a decreasing trend of fibril strain at equilibrium in highly crosslinked structures, the length after stretching was compared with the original length to observe whether there was any compression behaviour. Figure 3.16 shows that when the number of crosslinks increased, more fibrils were placed under compression, indicating increased redundancy in the system and an increasingly complex local loading environment.

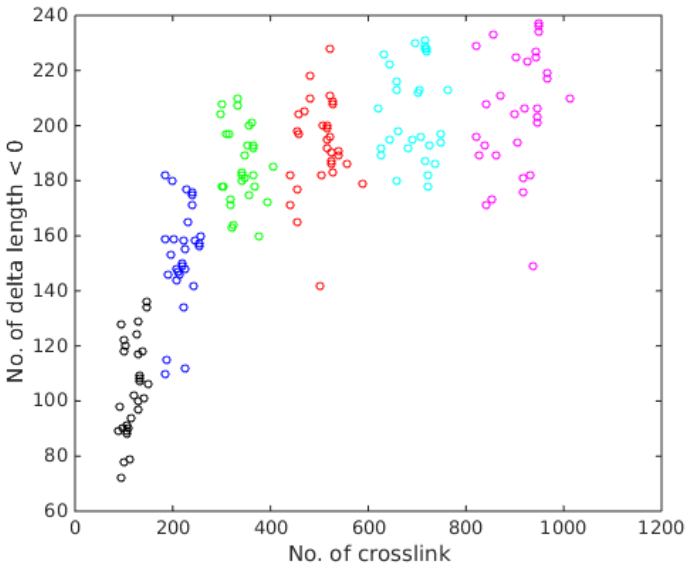


Figure 3.16: Number of lengths shorter than the original lengths after stretching. Different crosslink thresholds are shown by different colour dots where 0.5 μm is black, 0.7 μm is blue, 0.9 μm is green, 1.1 μm is red, 1.3 μm is cyan and 1.5 μm is magenta.

Unlike the microscopically-aligned configuration which is more linear with less opportunity for the clustering of nodes, the microscopically-random configuration contains many intersecting fibrils and thus more opportunity for the crosslinking of more than two fibrils in a single location, or cluster (Figure 3.17A). Hence it is easier for crosslinks to link neighbouring nodes and thus gradually form regions with a higher density of crosslinks. An example is provided in Figure 3.18 (red dotted rectangle), which shows a region in which crosslinks cluster with increasing threshold distance (Figure 3.18, lower half).

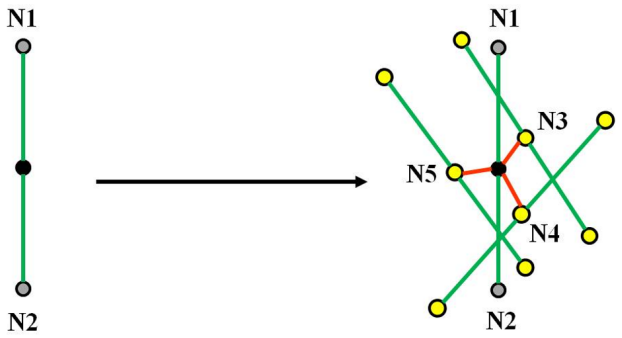


Figure 3.17: Schematic diagram showing crosslinking in the *Mikado* spring structure. (Left) each node (grey circle) except the top and bottom nodes has two neighbours (N1 and N2). (Right) when forming a crosslink (red) with other fibrils, the neighbouring nodes increased.

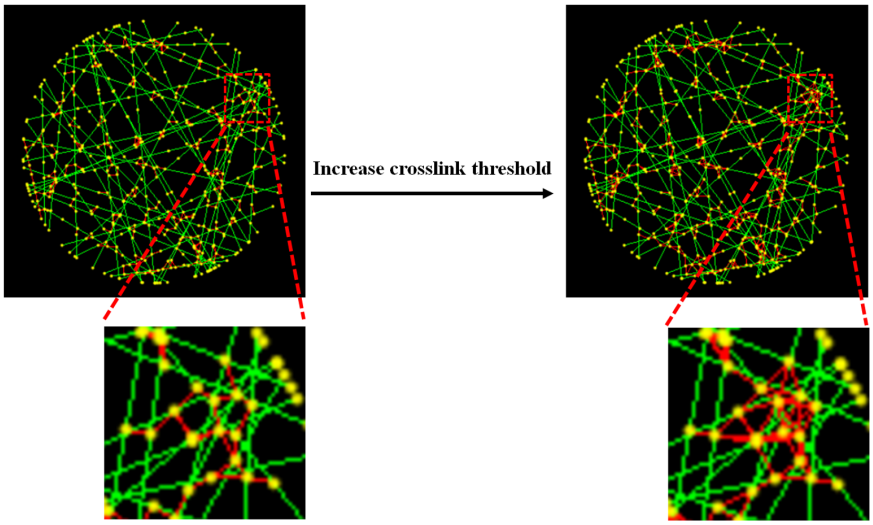


Figure 3.18: Example of the structure showing the high density of crosslinks in a specific area. A structure with a 1.1 μm crosslink threshold (left) and with a 1.3 μm crosslink threshold. The red dotted rectangle indicates the formation of the region with a high density of crosslinks when the crosslink threshold increased. The lower half of the figures shows this formation at higher magnification. Nodes are shown in yellow, springs in green and crosslinks in red.

To further explore cluster formation and related protection, we investigated the distribution of these regions. From visual inspection of the structures, we observe regions formed by a node which has more than four neighbouring nodes (Figure 3.17, right). Figure 3.19 shows that when the number of crosslinks increases, the number of nodes with $\geqslant 4$ neighbouring nodes increases linearly, while the number

of nodes with $\geqslant 2$ neighbours plateaus at higher overall crosslinking densities. It is interesting to note that the greatest difference between the $\geqslant 2$ and $\geqslant 4$ curves was between 200 and 400 crosslinks per structure (threshold of 0.7-0.9 μm), at the same point as the maximum average fibril strain shown in Figure 3.13. This indicates that the crosslinking sites are established at a density of approximately 600 per structure, after which they cluster.

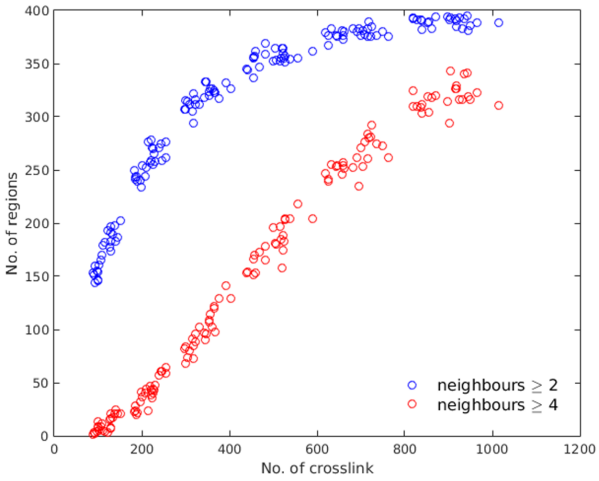


Figure 3.19: The relationship between the number of crosslinks and the number of nodes with $\geqslant 2$ neighbouring nodes (red dots) and with $\geqslant 4$ neighbouring nodes (blue dots).

Based on the initial results for fibril strains and clustering behaviour described above, we chose two thresholds, 0.7 and 1.5 μm, to investigate fibril strains in further detail. Figure 3.20 shows the distribution of fibril strains in 10 representative structures with crosslink thresholds of 0.7 and 1.5 μm. These show a relative skew in distributions, with lower crosslink densities revealing a tendency for isolated (outlier) fibrils under higher strain, in contrast to the predominantly low-strain outliers in highly crosslinked structures. Figure 3.21 shows the lumped distribution of a total of 450 fibril strains from 10 structures with crosslink thresholds of 0.7 and 1.5 μm. Here, the skew in distribution could be more clearly observed, with the related increase in fibrils exposed to high strain (and therefore stress) despite a relatively small change in mean strain.

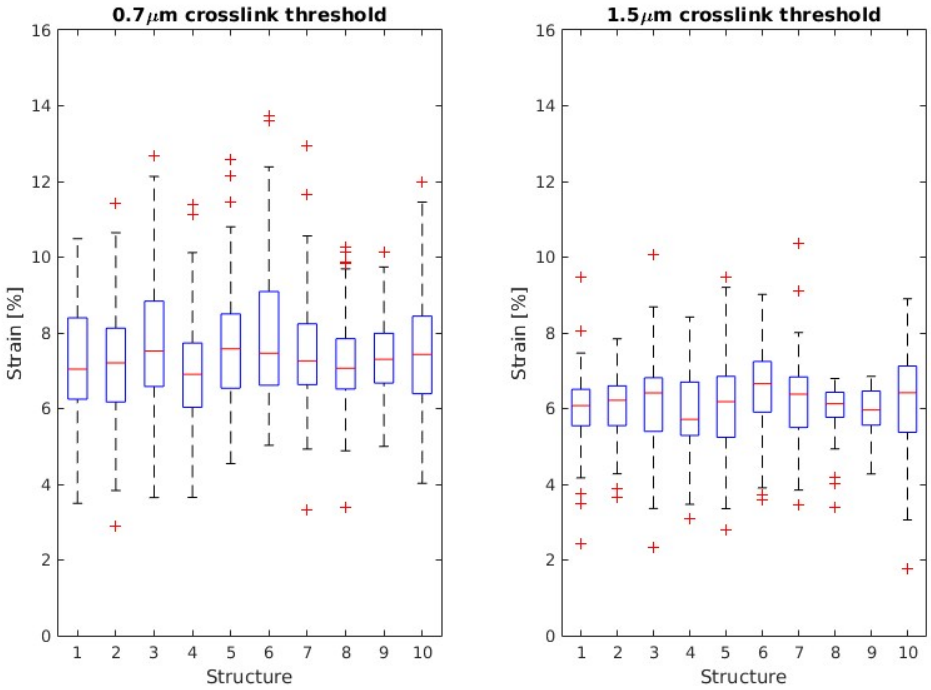


Figure 3.20: Fifty fibril strains of ten representative structures with 0.7 μm and 1.5 μm. Red crosses indicate the outliers (whisker lengths are defined as $\pm$ 2.7σ and 99.3% coverage if data are normally distributed).

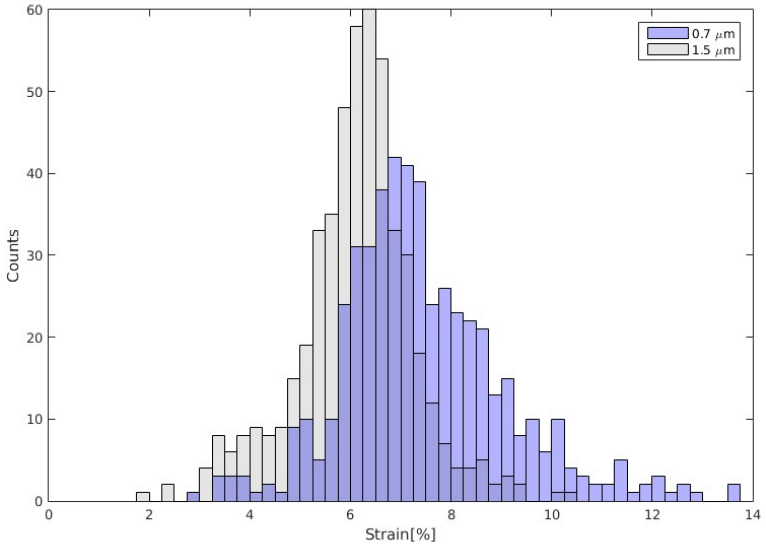


Figure 3.21: Histogram of a total of 500 fibril strains from ten representative structures with crosslink thresholds of 0.7 μm (blue) and 1.5 μm (light grey).

3.3.3.2 Anisotropic Loading

3.3.3.2.1 Uniaxial Tensile Force

To explore the effects of anisotropic loading we used a subset of 10 structures, first considering a uniaxial force in the y-direction (Figure 3.22). A 0.5 μN uniaxial tensile force (y-direction) was applied to the structure to equilibrium (Figure 3.22B). After reaching equilibrium, the force was released and the structure relaxed until the node velocities were below a very small tolerance (Figure 3.22C).

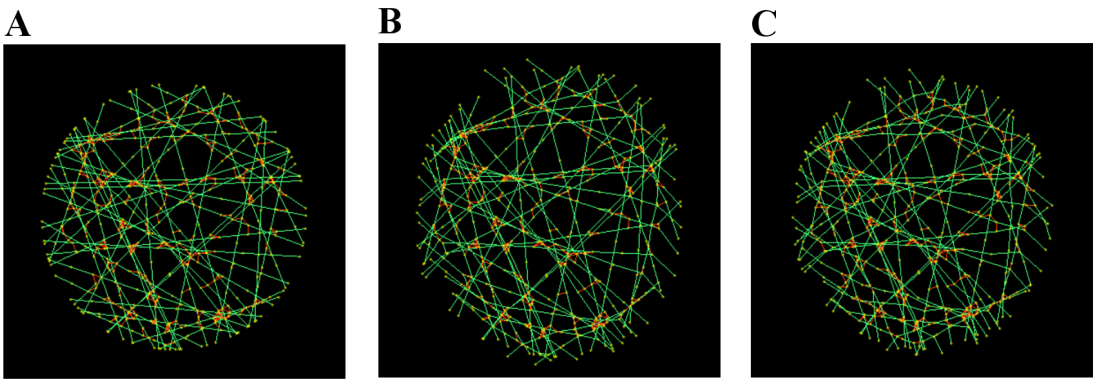


Figure 3.22: A representative surface specific simulation with a 1.1 μm crosslink threshold (A) before stretching, (B) after stretching and (C) after relaxation. Fibrils are shown in green, nodes in yellow and crosslinks in red.

Anisotropy under 1-D loading, shown in Figure 3.23, increases with loading in contrast to the isotropic 2-D loading (radial tension force) of the same structures. Here, fibrils become increasingly aligned up to 400-600 crosslinks per structure, after which anisotropy plateaus. The bulk response (Figure 3.24) follows a similar trend with a pronounced change in behaviour up to 400-600 crosslinks per structure, after which behaviour stabilised. Highly-crosslinked structures expanded less under load (Figure 3.24A) and after relaxation (Figure 3.24B), with a higher percentage of recovery (Figure 3.24C) compared to low crosslink densities.

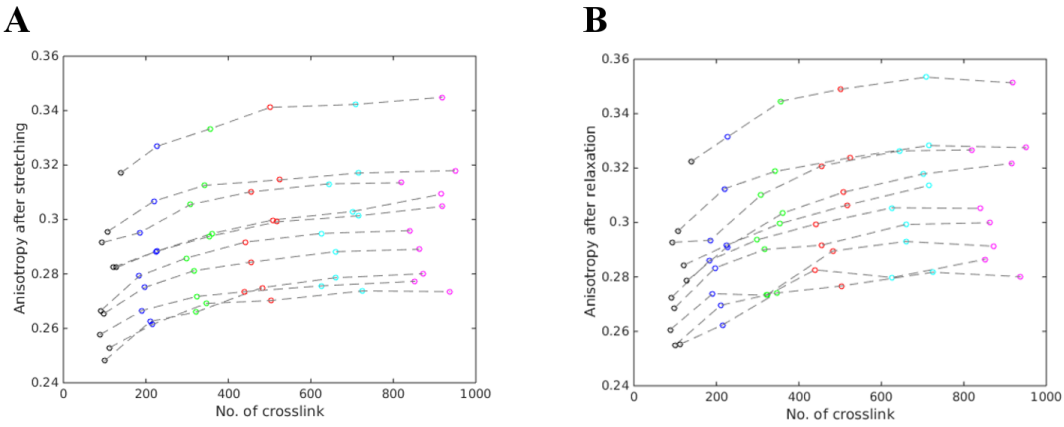


Figure 3.23: Relationship between crosslink density and angular anisotropy at (A) equilibrium and (B) after relaxation. Different crosslink thresholds are shown in different colours where 0.5 μm is black, 0.7 μm is blue, 0.9 μm is green, 1.1 μm is red, 1.3 μm is cyan and 1.5 μm is magenta.

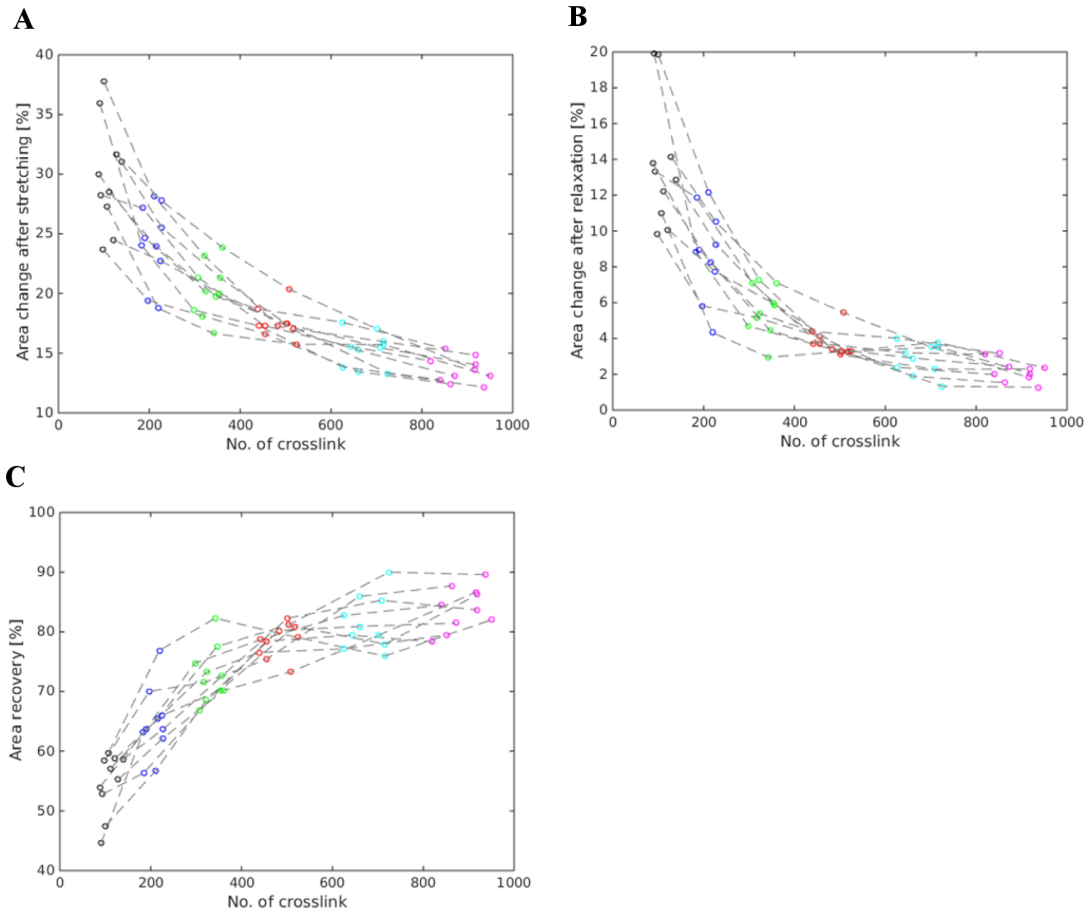


Figure 3.24: Area changes (A) after stretching, (B) after relaxation and (C) after recovery. Dashed lines link the same structure with different crosslink thresholds. Different crosslink thresholds are shown in different colours where 0.5 μm is black, 0.7 μm is blue, 0.9 μm is green, 1.1 μm is red, 1.3 μm is cyan and 1.5 μm is magenta.

Fibril strain at equilibrium (Figure 3.25) decreased linearly with increasing crosslink density. Variance, however, decreased to a minimum at 300-600 crosslinks per structure after which it increased with increasing density (Figure 3.26).

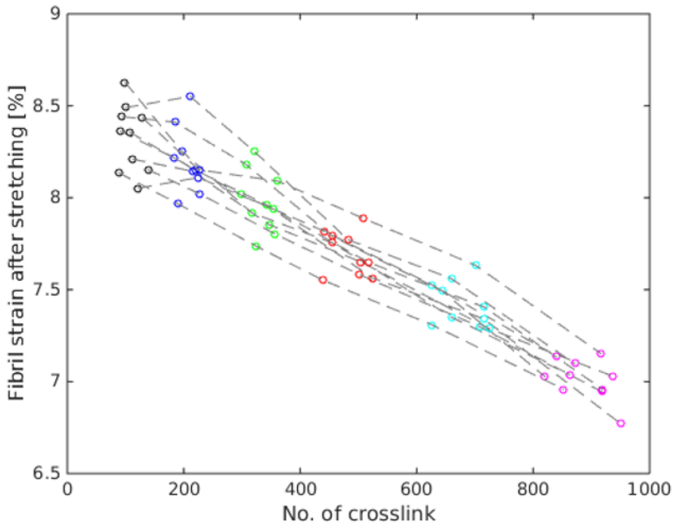


Figure 3.25: Fibril strain at equilibrium at different crosslink densities. Dashed lines link the same structure with different crosslink thresholds. Different crosslink thresholds are shown in different colours where 0.5 μm is black, 0.7 μm is blue, 0.9 μm isgreen, 1.1 μm is red, 1.3 μm is cyan and 1.5 μm is magenta.

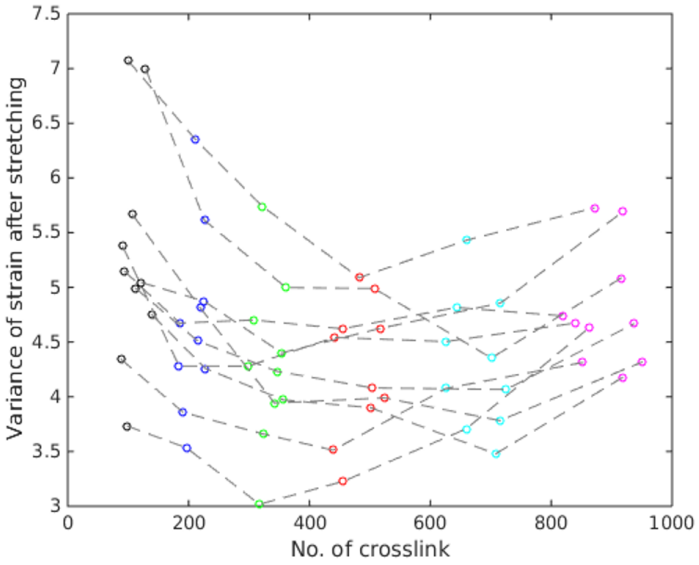


Figure 3.26: Variance of fibril strain at equilibrium at different crosslink densities. Dashed lines link the same structure with different crosslink thresholds. Different crosslink thresholds are shown in different colours where 0.5 μm is shown in black, 0.7 μm in blue, 0.9 μm in green, 1.1 μm in red, 1.3 μm in cyan and 1.5 μm in magenta.

Figures 3.27 and 3.28 show a similar narrowing of distribution at higher crosslink densities to that from isotropic loading. Similar distribution shapes were observed for both crosslinking conditions, yet the large variance and shift towards higher strain produced a similar pattern of stress-exposed fibrils at low crosslinking densities to that under isotropic loading.

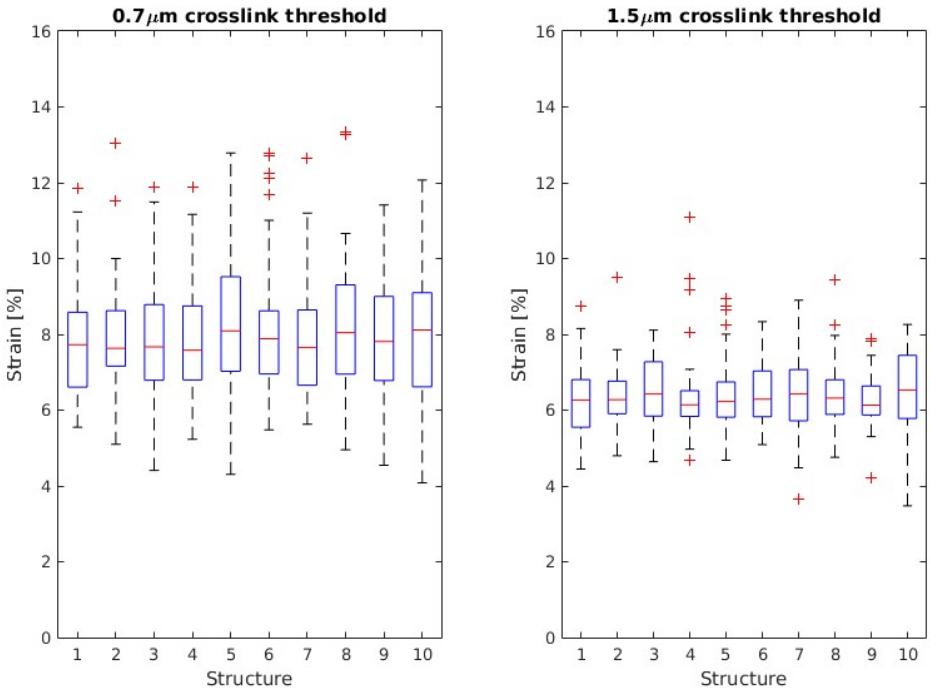


Figure 3.27: Fifty fibril strains of ten representative structures with 0.7 μm and 1.5 μm. Red crosses indicate the outliers (whisker lengths are defined as $\pm$ 2.7σ and 99.3% coverage if data are normally distributed).

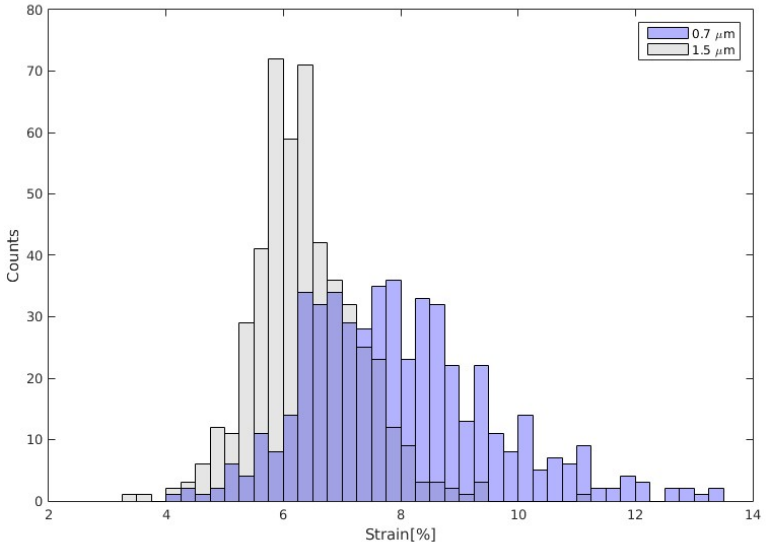


Figure 3.28: Histogram of a total of 500 fibril strains from ten representative structures with crosslink thresholds of 0.7 μm (blue) and 1.5 μm (light grey).

3.3.3.2.2 Uneven 2-D Tensile Force

An anisotropic 2-D load was used to explore the combination between the 1-D and radial 2-D loading situations. A representative structure under this loading condition is shown in Figure 3.29. An uneven force (0.5 μN in the x-direction and 0.1 μN in the y-direction) was applied the structure (Figure 3.29B). After reaching equilibrium, the force was released and the structure relaxed as in previous simulations (Figure 3.29C).

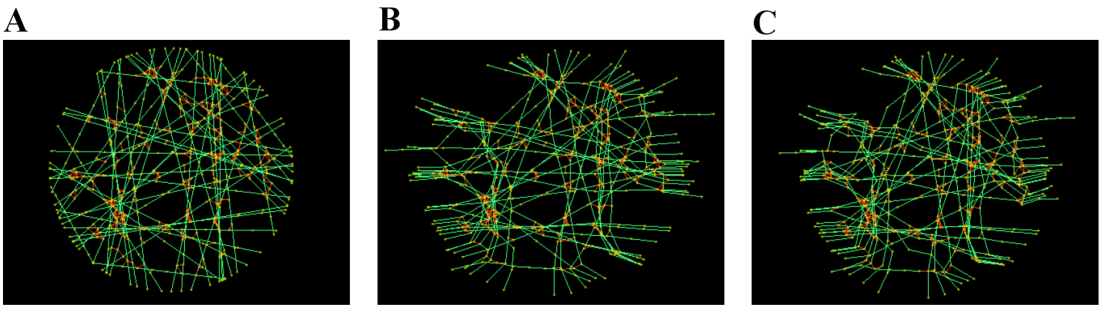


Figure 3.29: A representative anisotropic 2-D simulation with a 1.1 μm crosslink threshold (A) before stretching, (B) after stretching (0.5 μN in the x-direction and 0.1 μN in the y-direction) and (C) after relaxation. Fibrils are shown in green, nodes in yellow and crosslinks in red.

Qualitative differences in the structural response to load were most pronounced under this loading condition. Specifically, structures with low crosslink densities became more aligned with the direction of loading, forming fibre bundles (Figure 3.30B, yellow rectangle, Figure 3.31A and Figure 3.32A) and knots (Figure 3.30B, red rectangle), similar to that observed in diseased tissues (Figure 3.4C). Highly-crosslinked microstructures, however, maintained a 'normal' configuration with loading (Figure 3.31B and Figure 3.32B).

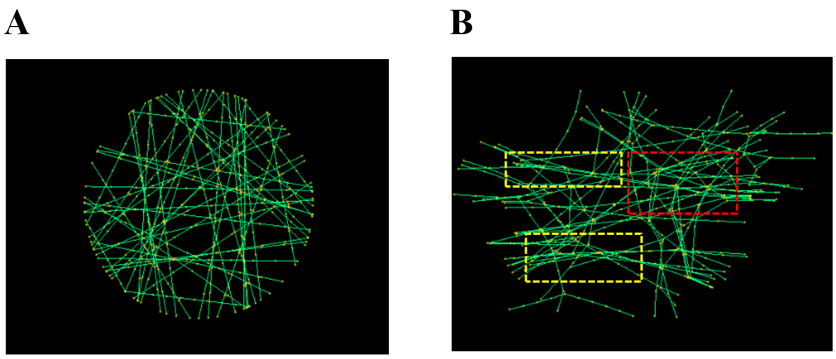


Figure 3.30: A representative structure with 139 crosslinks (A) before and (B) after application of anisotropic force. The red dashed rectangle indicates the knots formed and the yellow dashed rectangle indicates bundle formation.

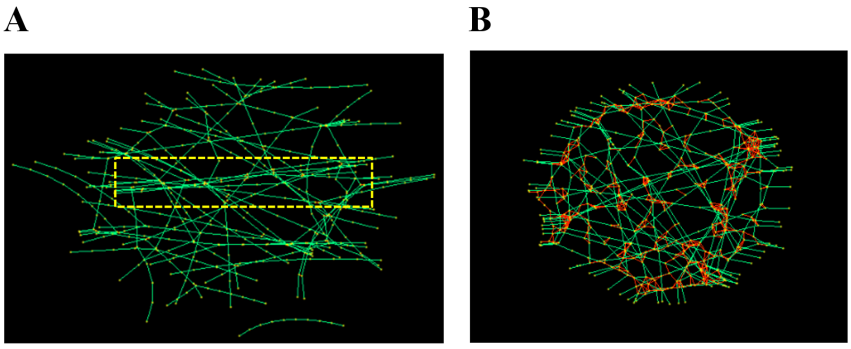


Figure 3.31: A representative structure with (A) 94 crosslinks and (B) 820 crosslinks after loading. Bundle formation is indicated by the yellow rectangle.

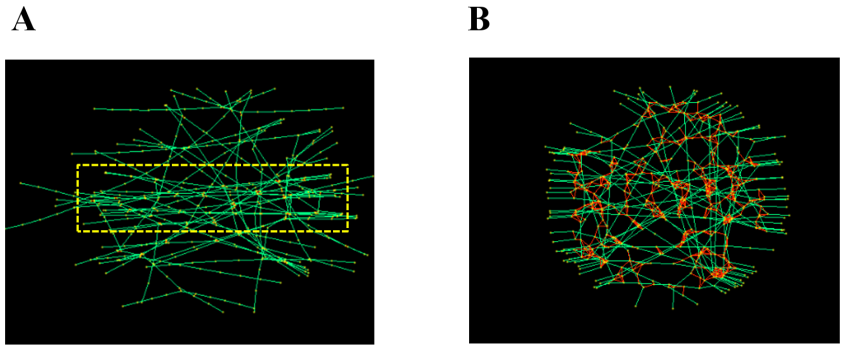


Figure 3.32: A representative structure with (A) 129 crosslinks and (B) 916 crosslinks after loading. Bundle formation is indicated by the yellow rectangle.

Anisotropy initially decreased with increasing crosslinking to a minimum at approximately 300 crosslinks per structure, after which anisotropy increased (Figure 3.33A). Similar to the 1-D loading condition, highly-crosslinked structures were more resistant to bulk deformation (Figure 3.34A, B), with a higher percentage of recovery (Figure 3.34C). The plateau, however, was reached at lower crosslink densities (200-400 per structure).

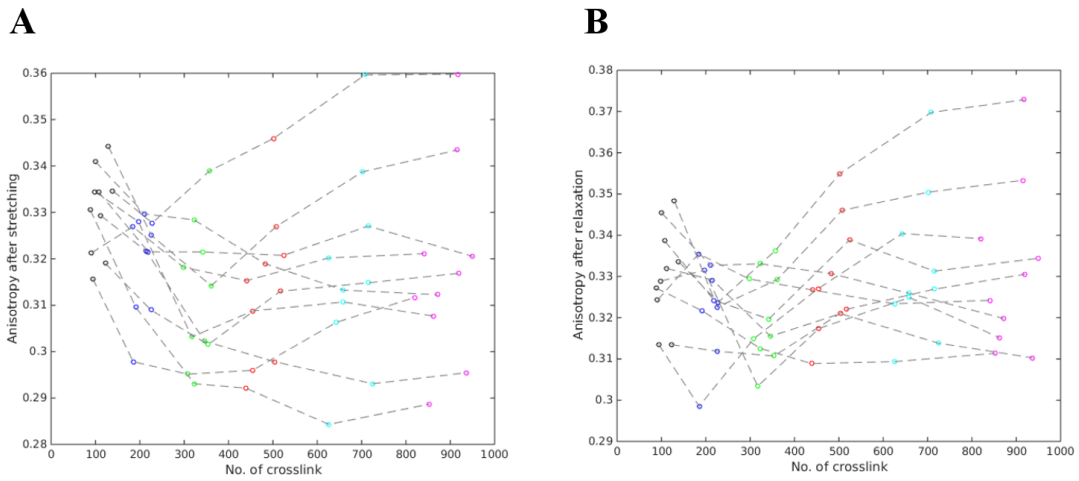


Figure 3.33: Relationship between crosslink density and angular anisotropy at (A) equilibrium and (B) after relaxation. Different crosslink thresholds are shown in different colours where 0.5 μm is shown in black, 0.7 μm in blue, 0.9 μm in green, 1.1 μm in red, 1.3 μm in cyan and 1.5 μm in magenta.

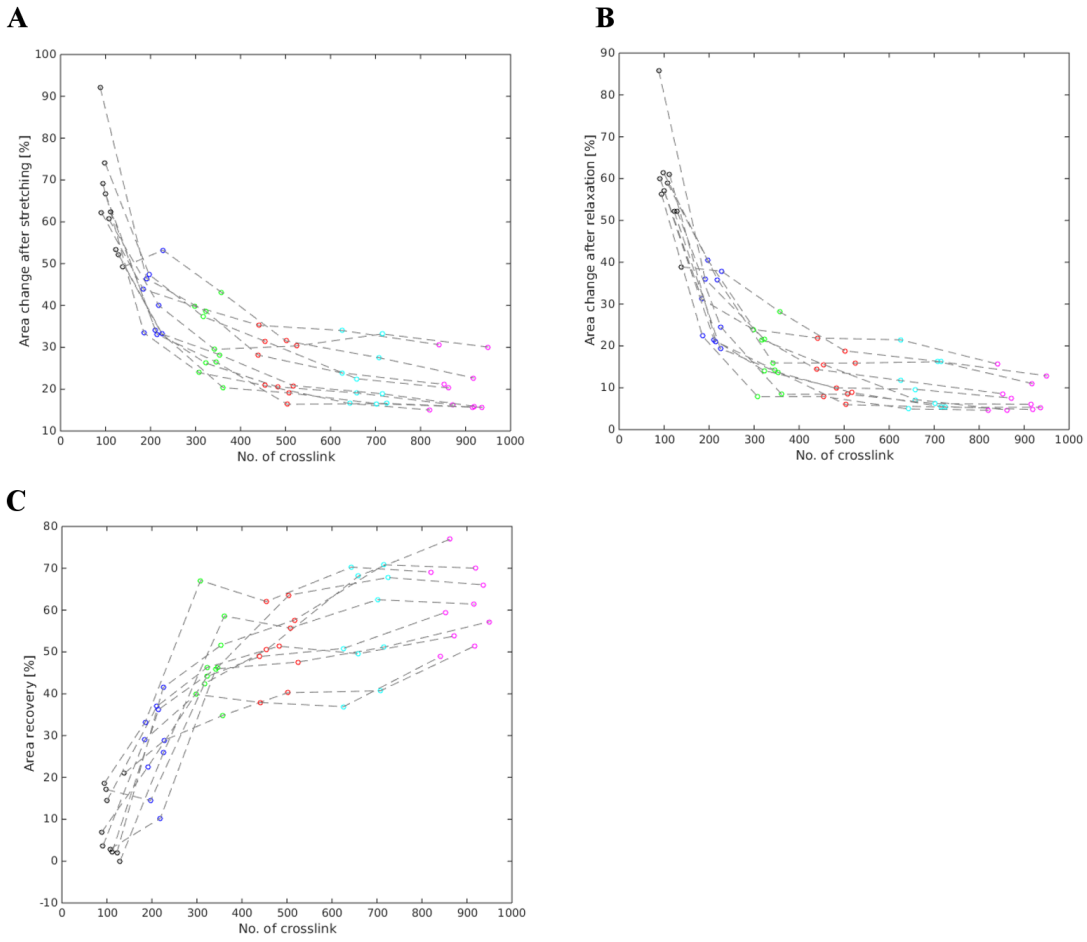


Figure 3.34: Area changes (A) after stretching, (B) after relaxation and (C) after recovery. Dashed lines link the same structure with different crosslink thresholds. Different crosslink thresholds are shown in different colours where 0.5 μm is shown in black, 0.7 μm in blue, 0.9 μm in green, 1.1 μm in red, 1.3 μm in cyan and 1.5 μm in magenta.

Again, fibril strain at equilibrium (Figure 3.35) decreased when the number of crosslinks increased. However, some structures showed a similar trend to that of radial tensile force (Figure 3.13) with a peak strain at around 200 crosslinks per structure. In contrast to 1-D loading, variance was maximised at around 300-400 crosslinks per structure (Figure 3.36).

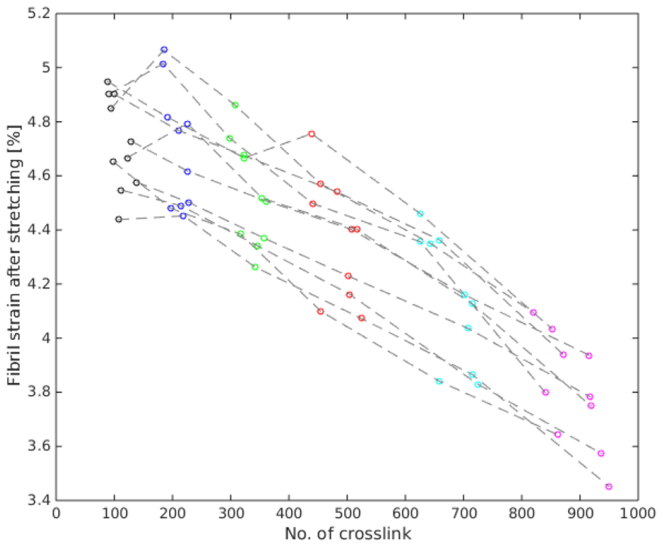


Figure 3.35: Fibril strain at equilibrium at different crosslink densities. Dashed lines link the same structure with different crosslink thresholds. Different crosslink thresholds are shown in different colours where 0.5 μm is shown in black, 0.7 μm in blue, 0.9 μm in green, 1.1 μm in red, 1.3 μm in cyan and 1.5 μm in magenta.

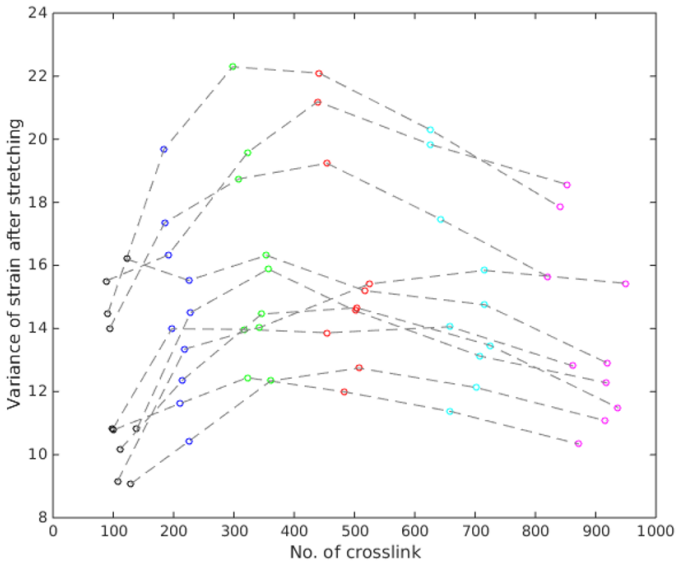


Figure 3.36: Variance of fibril strain at equilibrium at different crosslink densities. Dashed lines link the same structure with different crosslink thresholds. Different crosslink thresholds are shown in different colours where 0.5 μm is shown in black, 0.7 μm is blue, 0.9 μm is green, 1.1 μm is red, 1.3 μm is cyan and 1.5 μm is magenta.

Figures 3.37 and 3.38 show the individual and lumped fibril strains from ten representative structures. Unlike radial and uniaxial loading, fibril strain distributions were remarkably similar for the two crosslinking densities, with only a slight shift to higher strain at low densities.

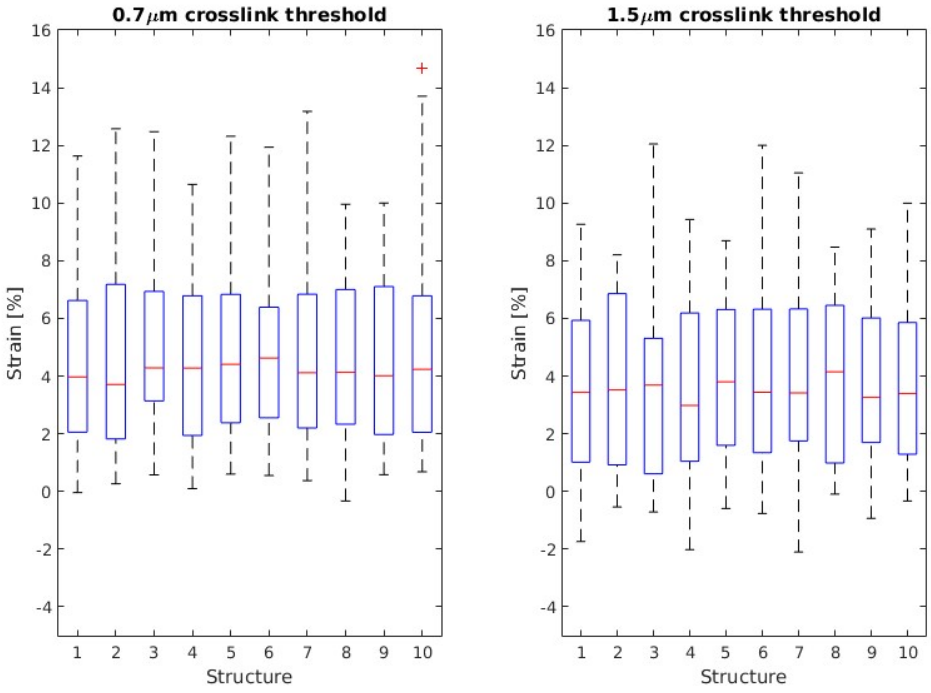


Figure 3.37: Fifty fibril strains of ten representative structures with 0.7 μm and 1.5 μm. Red crosses indicate the outliers (whisker lengths are defined as $\pm$ 2.7σ and 99.3% coverage if data are normally distributed).

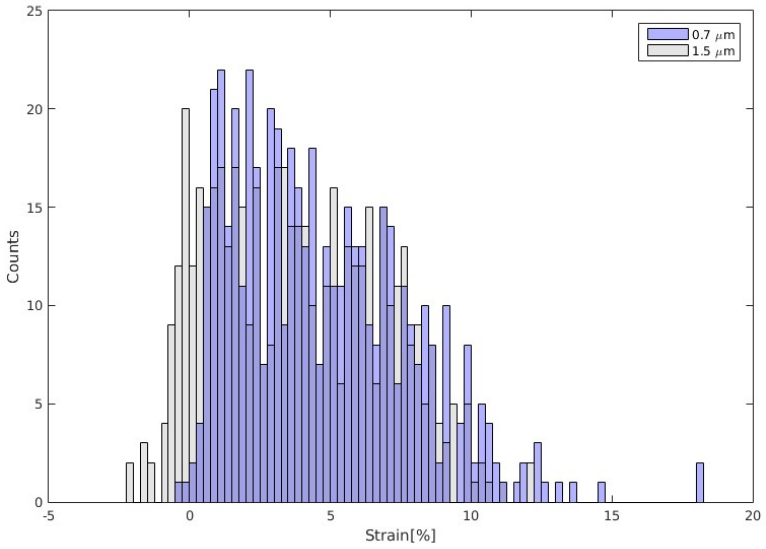


Figure 3.38: Histogram of a total of 500 fibril strains from ten representative structures with crosslink thresholds of 0.7 μm (blue) and 1.5 μm (light grey).

3.3.3.3 Comparison of Loading Conditions

Figures 3.39, 3.40, and 3.41 show combined results for anisotropy, area change and fibril strain at equilibrium and after relaxation under different loading conditions.

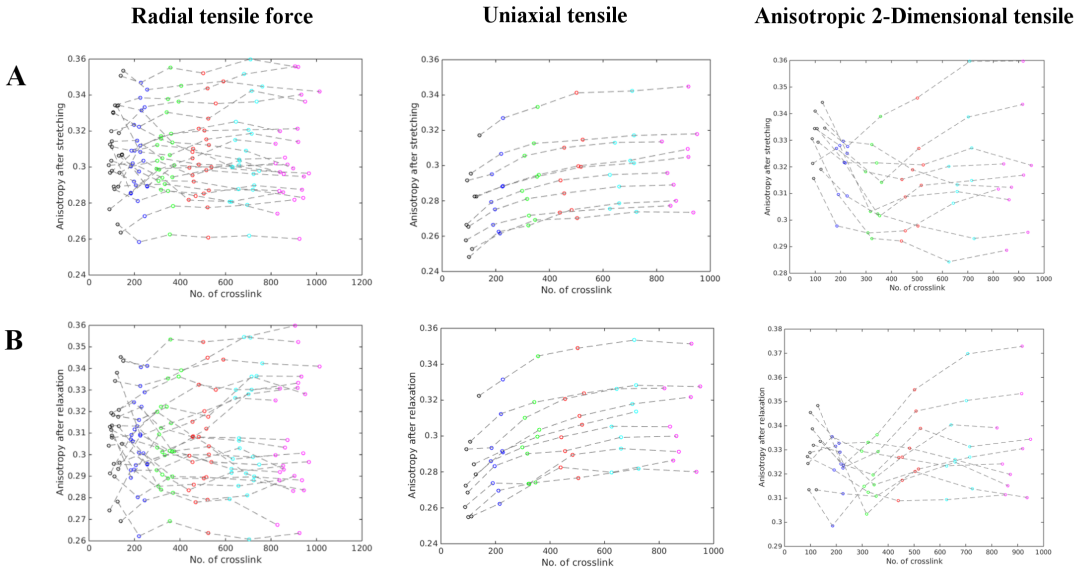


Figure 3.39: Relationship between crosslink density and angular anisotropy at (A) equilibrium and (B) after relaxation with different types of tensile force. Different crosslink thresholds are shown in different colours where 0.5 μm is shown in black, 0.7 μm is blue, 0.9 μm is green, 1.1 μm is red, 1.3 μm is cyan and 1.5 μm is magenta.

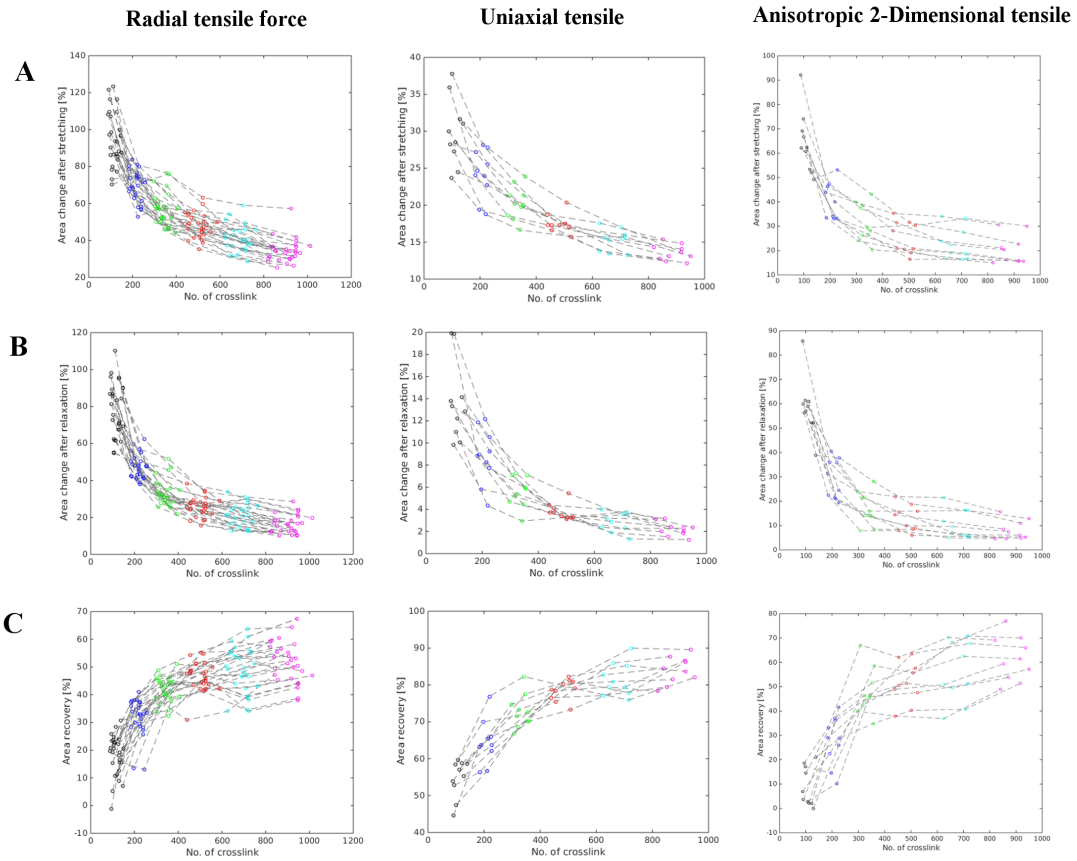


Figure 3.40: Area changes (A) after stretching, (B) after relaxation and (C) after recovery with different types of tensile force. Different crosslink thresholds are shown in different colours where 0.5 μm is shown in black, 0.7 μm is blue, 0.9 μm is green, 1.1 μm is red, 1.3 μm is cyan and 1.5 μm is magenta.

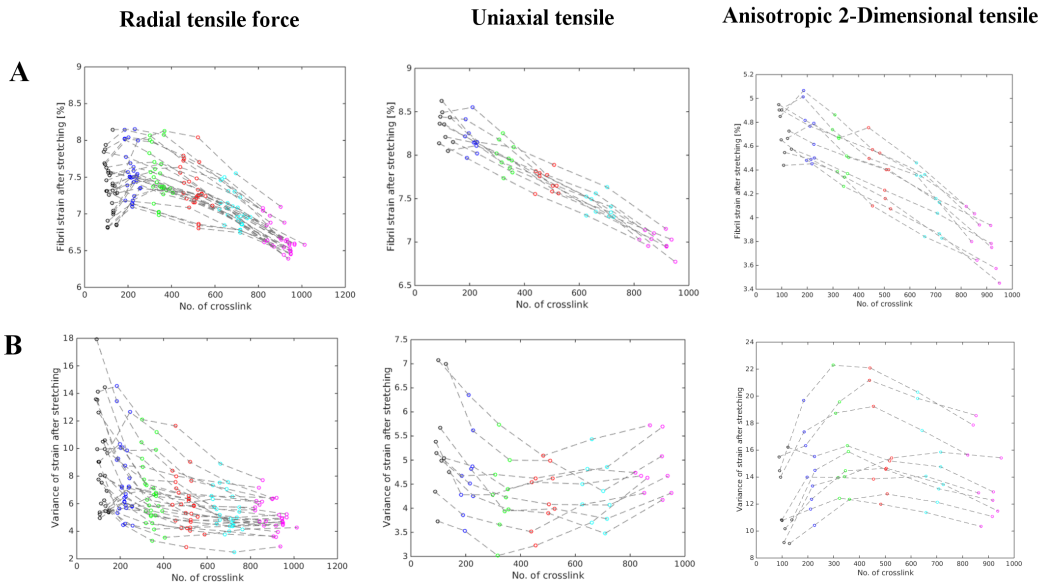


Figure 3.41: Summary of the (A) fibril strain and (B) variance of fibril strain at equilibrium with different types of tensile force. Dashed lines link the same structure with different crosslink thresholds. Different crosslink thresholds are shown in different colours where 0.5 μm is shown in black, 0.7 μm is blue, 0.9 μm is green, 1.1 μm is red, 1.3 μm is cyan and 1.5 μm is magenta.

3.4 Discussion

3.4.1 Zigzag Configuration

Using a bottom-up model of a cartilage-like collagen meshwork, we have demonstrated the effect of fibril interconnectivity, represented by crosslinking, on restructuring under load. Although crosslink stiffness, within the parameter range considered, had no significant effect, the number of crosslinks in each structure consistently altered the structural response to loading. This finding is in agreement with previously published studies, although these were based on entropy-based mechanics [204] in contrast to the elastic dominated regime adopted here for collagen fibrils [170].

Increasing crosslink density in 'zigzag' configuration increased resistance to bulk deformation, and improved the recovery of both bulk deformation (Figure 3.7) and structural isotropy (Figure 3.6). This improved resistance to network reconfiguration under loading, although at the expense of higher stresses for the collagen fibrils themselves (Figure 3.8).

In the context of cartilage and cartilage degradation, this may provide an insight into the mechanisms underpinning the transition from a normal, intact meshwork to the degraded collagen architecture observed in experimental studies [198]. In particular, a highly connected meshwork was predicted to maintain its 'normal' configuration under loading. In Figure 3.4A for example, the highly-crosslinked structure maintained its pseudorandom organisation after loading, also shown by the lower anisotropy at high crosslink densities, shown in Figure 3.6. The same structures with lower connectivity, however, transformed to a 'diseased' configuration (Figure 3.4B). This 'diseased' configuration, as observed experimentally by electron microscopy of osteoarthritic cartilage (e.g. Figure 3.4C [120]), was characterised by bundling of fibrils in the direction of the applied force, and increased anisotropy (Figure 3.6).

Expanding on findings and hypotheses from previous experimentally-driven studies [21, 34, 65] which focussed on structural disease progression rather than initiation, the role of collagen connectivity provides insight into the mechanisms by

which bundle formation and micro-cracking occur. Small regions of fibril alignment, of the size of a few tens of microns for example, have been observed in the deep zone of human cartilage sections prior to changes in histological score, with increasing bundling during progression [34]. While progression can be explained by stress concentrations and critical-size crack formation, the initiation of bundling may be explained by a local loss of connectivity through the breaking/removal of crosslinks with the latter being consistent with the modelling predictions presented here. Specifically, high inter-fibril connectivity appears critical in maintaining the balance between swelling pressure and collagen tension [33] required for cartilage function.

In this context, the same effect would be obtained by either a loss of direct collagen-collagen connectivity or the loss of physical separation of fibrils by aggrecan digestion. Our results suggest, due to the increased stress at the fibril level in highly crosslinked structures (Figure 3.8), that such restructuring is likely to be driven by damage to connecting elements rather than the collagen fibrils themselves. The reduced fibril-level strain observed with reduced connectivity further suggests that recovery from a 'diseased' collagen configuration is energetically unfavourable while loading is maintained.

3.4.2 *Mikado* Configuration

In addition to the mesoscopically-aligned yet locally-random fibrils of the 'zigzag' networks, a series of *Mikado* networks, consisting of microscopically-disordered yet straight fibrils, was implemented to explore the mechano-structural characteristics of an alternative configuration. Based on the results presented in Chapter 2, this may better represent the organisation of collagen in the 'normal' cartilage surface.

The *Mikado* networks showed a number of similarities, yet also key differences in behaviour to that of the 'zigzag' network. Bulk deformation, quantified by changes in area, showed that highly crosslinked structures consistently resist loading better than structures at low crosslink densities and display improved recovery (Figure 3.40). Increased bundling at low crosslink densities was also observed in *Mikado* simulations, particularly under anisotropic 2-D loading (e.g. Figures 3.30, 3.31 and 3.32).

Fibril strain in particular showed different trends in the *Mikado* simulations than for the 'zigzag' fibril configuration (Figure 3.41). Under each loading condition, fibril strain in the *Mikado* network decreased with increasing crosslink density in direct contrast with previous results, indicating that in this configuration, crosslinks may be protective. The interpretation of average fibril strain in this more complex loading environment, however, must be balanced against the distribution of that strain.

Considering first the radial loading simulations, observations of increased redundancy and decreased variance with increasing crosslink density indicate that structures with low crosslink densities place isolated fibrils under very high stress. Unlike the 'zigzag' simulation, these randomly-aligned, straight fibrils are thus prone to rupture as a damage mechanism rather than reorganisation alone (e.g. Figure 3.14). Further, it suggests that some damage in a *Mikado*-like network may be recoverable via increased collagen synthesis.

Related to this magnitude distribution in fibril-level load is the spatial distribution, controlled by the distribution of crosslinks within the structure. Particularly relevant is the formation of crosslink clusters. As crosslink thresholds increased, the overall number of crosslinks increased as expected. Their distributions, however, changed, with a plateau in the number of sites above 400-600 crosslinks, with each site continually growing in size (Figure 3.19). It is difficult to determine quantitatively whether the increased number of sites, or size of those sites, has a stronger protective effect. The formation of protected 'islands' of highly-crosslinked clusters, however, is unlikely to translate to a global protective state, instead redistributing load unevenly to the surrounding matrix.

Within the *Mikado* simulations, loading conditions (radial 2-D; anisotropic 2-D and 1-D) produced different patterns of behaviour. A transition in structural response, however, was observed in each. Bulk strain, measured by area change, consistently decreased with increasing crosslink density. In each case a fast change was observed at low densities, followed by a plateau of minimal change, with the sharpest transition observed under anisotropic 2-D loading.

Increased alignment (given by anisotropy) under 1-D load at higher crosslinking densities was an unexpected result (Figure 3.39A, middle), contrasting directly with the 'zigzag' model. This can be interpreted as a different role for crosslinks in the *Mikado* network. In a network of mesoscopically-aligned collagen, crosslinks act to maintain isotropy where all fibrils are necessarily engaged. In the *Mikado* model, crosslinks allow the recruitment of fibres that are not aligned with the direction of load. Under an anisotropic 2-D load, a combined effect is seen (Figure 3.39A, right). Here, fibrils at very low crosslink densities realign to the direction of maximum load, and at high densities more efficiently recruit fibrils with a transition between behaviours at densities of 300-600 per structure. This interpretation is reflected in the results for fibril level strains for which the transition is matched by a peak in variance under anisotropic 2-D load (Figure 3.41B, right).

In summary, a number of points can be made from the results of this chapter. The behaviour of a cartilage-like collagen network depends on the organisation and number of crosslinks rather than the properties of those crosslinks. In a *Mikado* network, high numbers of crosslinks are protective and allow efficient recruitment of fibrils in response to load, however this protection can be at the expense of neighbouring regions where crosslinks are not evenly distributed. In the mesoscopically-aligned yet locally random 'zigzag' configuration, low numbers of crosslinks conversely reduced fibril level strain. A decrease in crosslink density in this configuration is therefore mechanically irreversible while loading is maintained. Finally, the changes in network behaviour under different applied loads are neither linear nor consistent, indicating that, in addition to crosslink density, structural organisation must be highly optimised to a given loading environment to perform effectively. While the physical changes to the properties of fibrils, described in Chapter 2, may increase potential for local damage initiation, the current chapter shows that it is instead the interactions between fibrils that drives disease.

4

Potential for Intraoperative Assessment of Initiation and Progression of Osteoarthritis

Contents

4.1 Introduction 128
4.2 UV-VIS-NIR Spectroscopy 130
4.2.1 System Set-up 130
4.2.2 Data Collection and Data Analysis 131
4.2.3 Results 133
4.2.3.1 Absorbance Peaks 135
4.2.3.2 Colour 138
4.2.3.3 Slope Between the Wavelengths of 600 and 980 nm 140
4.3 Mie Scattering Model 141
4.3.1 Mie Theory and the Scattering Model 141
4.3.2 Results 142
4.3.2.1 Polar Scattering Profiles 142
4.3.2.2 Cylinder Diameter and 600-980 nm Slope . . . 148
4.4 Discussion 152

4.1 Introduction

The findings of Chapters 2 and 3, and from recent literature [16, 19, 21, 65] highlight the importance of collagen organisation and interactions in the disease process.

Particularly important is the formation of aligned collagen bundles, which was identified as a 'mechanically irreversible' step in disease progression (Section 3.4.1). In early disease (Grade 0 to 1), a change in the interactions between molecules within the fibre, a measure of collagen 'quality' (Section 2.3.3), were also observed as changes to the loss tangent (Section 2.3.2.2) without necessarily including changes at the molecular level. This can be conceptually linked to the embrittlement of the fibrils by predisposing molecular fracture over energy dissipating stick-slip mechanisms (see, for example Buehler [170]), providing a measure of susceptibility to direct fibril damage. There remains however, a question of whether such changes can be identified clinically, and this 'irreversibly damaged' tissue distinguished during keyhole surgery.

An efficient and objective measure of early OA detection is crucial to improve clinical decision-making, improve treatment, and to advance the understanding of disease progression. Modalities such as x-ray and MRI are often used clinically to diagnose OA, however, these techniques can only detect macroscopic damage to the tissue and are thus limited to late stage assessment. More advanced MRI techniques have shown promise as non-invasive methods for detection of OA [205, 206], yet signal changes with disease are too weak to detect against the background of normal variation [207] in the context of the early stages of disease and related treatments that motivate the present work.

For the application of, for example, scaffold- or cell-based techniques the surgeon must intraoperatively distinguish the non-viable tissue to be removed from the viable tissue to be preserved. Currently, decision making is based on the visual and tactile impression of the surgeon at arthroscopy, yet it has been demonstrated that the visually normal tissue in a degraded joint is not always healthy [17, 208].This prompts the necessity of a tool or technique that can aid treatment decisions, and provide feedback on post-treatment tissue healing in both clinical practice and the trials of new treatment methods. Several techniques have been developed to diagnose early OA [85], with a number of arthroscopic assessment tools commercialised. None, however, have become widely used due to limitations such as heavy dependence on operator, image post processing requirements, poor

performance, or technological requirements that cannot be addressed within the size, weight and cost constraints of a useful medical device.

Here, we undertake a pilot study to assess the potential of a new approach to characterise the afore-mentioned changes. This approach aims to utilise the light source and optics available in current arthroscopes, extending them from qualitative to quantitative tools without change to the radiation or instrumentation to which the patient must be subjected. Utilising a similar source and optical path to a standard arthroscope, and constraining input to the range available to a standard detector/camera, we therefore capture and analyse spectral information from the cartilage surface. Specifically, UV-VIS-NIR spectroscopy is applied, and analysed quantitatively in terms of specific electronic absorbance bands, colour, and scattering, again with a focus on the early stages of degradation.

4.2 UV-VIS-NIR Spectroscopy

4.2.1 System Set-up

Figure 4.1A shows the UV-VIS-NIR spectroscopy setup. UV-VIS-NIR spectra were measured with a fibreoptic probe (Ocean Optics, Dunedin, FL, USA). The probe was held in position by a probe holder maintaining a distance of 4 mm between sample and probe. The probe was composed of six illumination fibres and one read fibre, each with a 400 μm diameter core and with a $\pm$ 12.7 °collection angle. Figure 4.1B shows the details of illumination and collection from the probe at the sample. The six-fibre illumination leg was connected to a deuterium-halogen light source (DH-2000, Ocean Optics). Scattered light from the sample was collected by the read fibre and delivered to a highly-sensitive spectrometer (QEPro-Abs, Ocean Optics). The spectrometer had a 2-D arrangement of pixels (1044 horizontal $\times$ 64 vertical) which was responsive from a wavelength of 185 nm up to 1100 nm. The combination of the spectrometer's detector and 16-bit A/D converter delivered a dynamic range of -85000:1 and the signal-to-noise ratio of the spectrometer was approximately 1000:1.

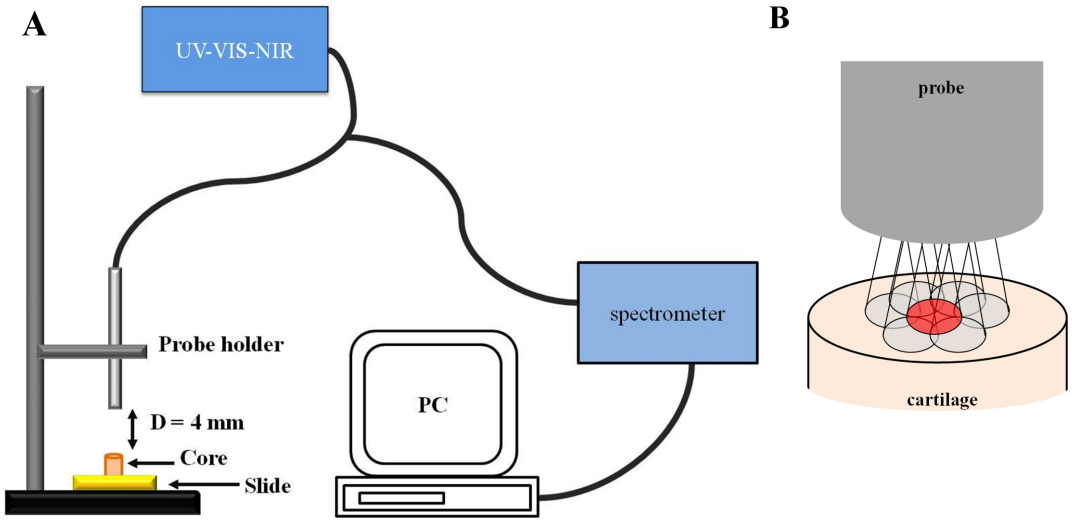


Figure 4.1: Schematic diagram of the (A) UV-VIS-NIR spectroscopy setup and (B) measurement from the probe. (A) Light from the deuterium-halogen light source (UV-VIS-NIR) was delivered to the probe head through six 400 μm optical fibres. The probe was held in a position by a probe holder to maintain the correct distance between sample and probe head. Scattered light from the sample was collected by the probe and delivered to the spectrometer. D: distance from the probe head to the core. (B) Probe is composed of six illumination fibres (light gray circle) around one read fibre (red circle).

4.2.2 Data Collection and Data Analysis

Prior to spectroscopic probing of the tissue, a reference spectrum was acquired from a Teflon^{TM}-based material across the entire wavelength and used as the reference for optical measurements in this study. A background spectrum was acquired prior to each sample scan and the resultant spectrum was then subtracted from each sample spectrum. Measurements were taken from each sample used in Chapter 2, allowing comparison with detailed physical characterisation and histological scoring. Unlike Raman spectroscopy in which five points were measured at 1 mm intervals, the measurement point of UV-VIS-NIR spectroscopy was taken in the middle of the core due to the large area of the measuring point (Figure 4.2, black dotted circle). Each spectrum was acquired at 30 ms integration time, averaging 20 continuous readings. Three of these spectra were then averaged to produce the final UV-VIS-NIR spectrum for each measurement point. Each

sample spectrum was then processed by normalising to the area under the curve between the wavelengths of 250-980 nm.

All statistical analysis used GraphPad Prism (Version 5, GraphPad Software, Inc.), with $P < 0.05$ considered significant. The mean spectral densities, intensities of the spectra and the ratios of the intensities were compared using a one-way ANOVA with Tukey's multiple comparison test. All results are presented as mean ± standard error of the mean unless indicated otherwise.

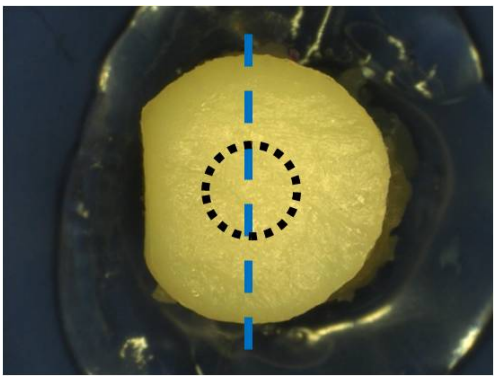


Figure 4.2: The measuring point used for UV-VIS-NIR spectroscopy (black dotted circle). The blue dotted line shows the cutting line after optical measurement. The cut edge shows the mark of disease progression.

4.2.3 Results

Due to failures in some measurements, a total of 33 spectra were analysed in this study (Table 4.1). As visual assessment is sufficient to characterise late stage disease (OARSI grade > 2), this chapter primarily aims to distinguish between grades 0 and 1. The means and standard deviations of spectra at grade 0 and grade 1 are given in Figure 4.3. In addition to differences in peak heights, the slopes of grade 0 and grade 1 after the wavelength of 600 nm show clear qualitative differences. Figure 4.4 shows the mean spectrum for each OARSI grade for comparison.

Table 4.1: Numbers of samples with each histological score.

OARSI score	**0**	**1**	**2**	**3**	**4**
Number of sample	3	4	9	14	13

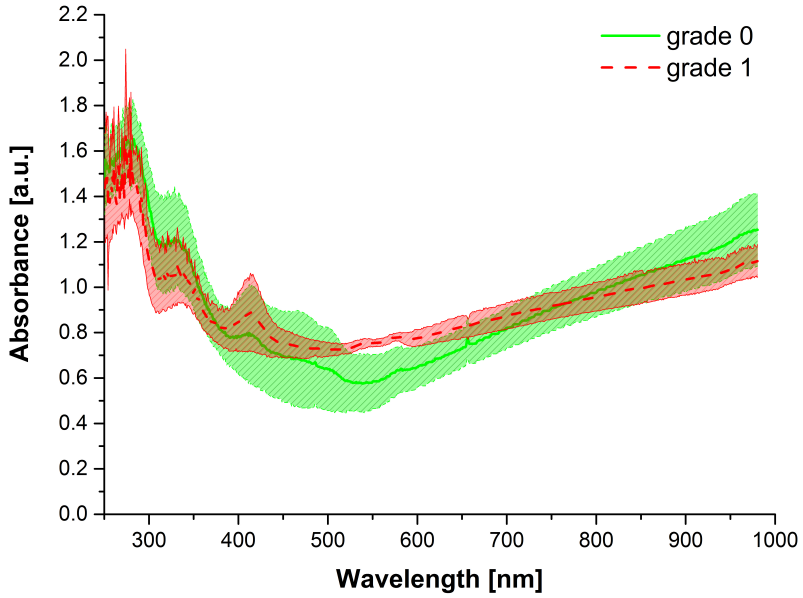


Figure 4.3: The UV-VIS-NIR spectrum between the wavelengths of 250-980 nm at grade 0 and grade 1. Grade 0: green straight line and grade 1: red dashed line. Shaded areas show the standard deviation.

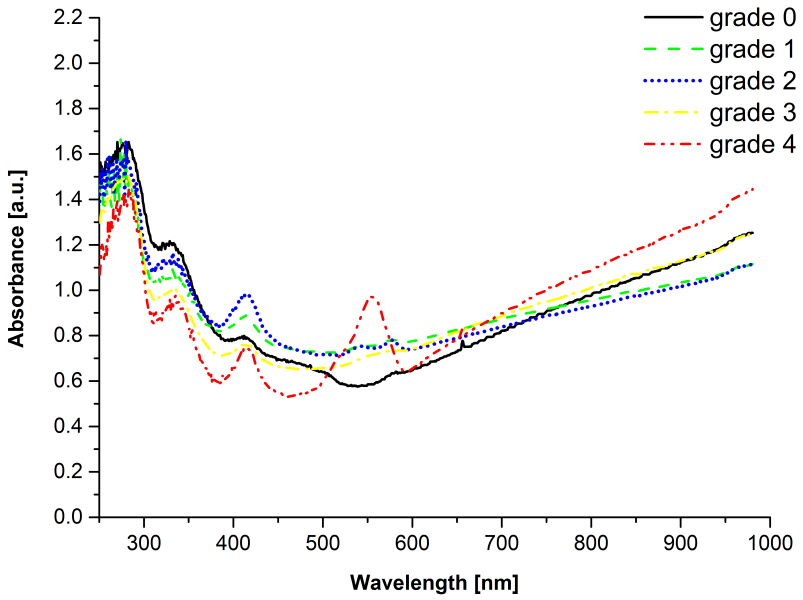


Figure 4.4: The mean UV-VIS-NIR spectrum between the wavelengths of 250-980 nm at different stages of disease. Grade 0: black straight line; grade 1: green dashed line; grade 2: blue short-dotted line; grade 3 line: yellow dash-dotted line and grade 4: red dash-dot-doted line.

A linear fit was applied to the data points between 600 and 980 nm, and the slopes were compared at different disease stages. Five peaks at wavelengths of 320, 405, 455, 531 and 566 nm were also analysed and compared. As peak positions shifted between spectra at different disease stages, instead of peak value, areas under specific ranges were calculated to minimise error (Table 4.2). Data (areas under the peaks and the ratios between these values) were normalised to grade 0 to facilitate comparison with normal cartilage.

Table 4.2: The wavelengths of the peaks and range selection

Wavelength (nm)	Selection of the range of wavelength (nm)
320	303-344
405	373-433
455	435-475
531	510-547
566	539-582

4.2.3.1 Absorbance Peaks

Figure 4.5 shows the five spectral peaks at different disease stages. General patterns in peak area can be observed, mirroring those described by AFM and Raman measurements in Chapter 2. At 320, 531 and 566 nm, a step-change could be observed from grade 0 to grade 1, with peak area remaining relatively stable with disease progression. Peaks at 405 and 455 nm 'pivoted' at grade 2.

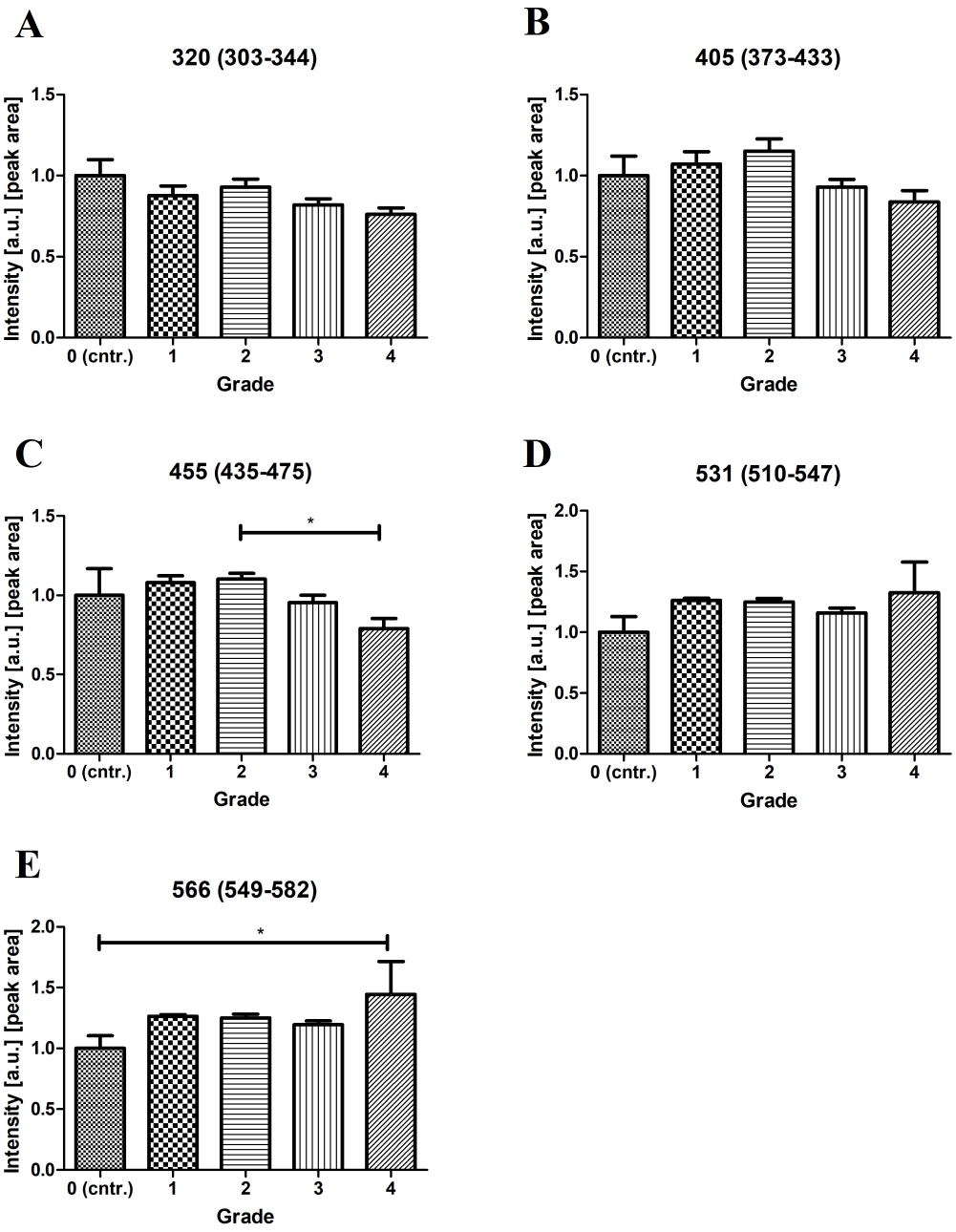


Figure 4.5: Areas under the main peaks at different stages of disease at (A) 320 nm, (B) 405 nm, (D) 455 nm, (E) 531 nm and (F) 566 nm. *:$P < 0.05$. cntr.:control.

Figure 4.6 shows the ratios between these peaks. No significant difference was observed at the early stages (grade 0 to grade 1), however the complementary patterns observed for individual peak areas were magnified. This was particularly prevalent for the 320/531 and 320/566 nm ratios (Figure 4.6A and B), each of

which showed opposing step changes in individual peak areas.

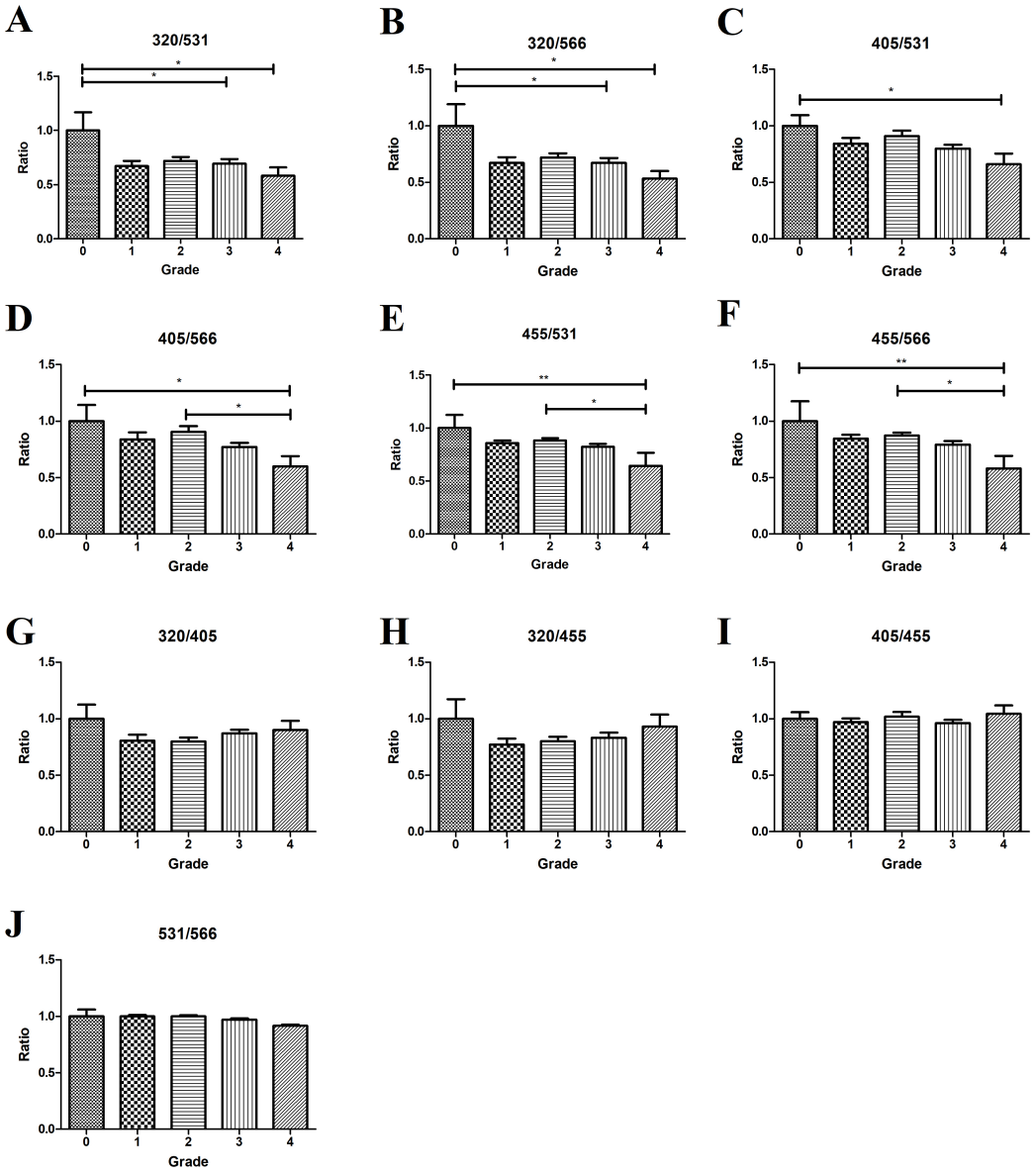


Figure 4.6: Comparison of the under areas of the five peaks at different stages of disease: (A) 320/531, (B) 320/566, (C) 405/531, (D) 405/566, (E) 455/531, (F) 455/566, (G) 320/405, (H) 320/455, (I) 405/455 and (J) 531/566. *:$P < 0.05$ and **:$P < 0.01$.

We further analysed the maximum value of these peaks (i.e. peak height) as a sense check. Patterns and levels of significance remained consistent with area calculations (data not shown). Area calculations were subsequently maintained both to avoid the possibility of missing information due to peak shifts, and to better capture the total contribution of absorbing material at these energy levels.

4.2.3.2 Colour

As mentioned earlier, decision making by the surgeon at arthroscopy is based on the visual and tactile impression. We therefore wonder how camera detected the colour changes with disease progression. We think having this information might provide another way to objectively distinguish disease stages. Reflectance in the 610-650 nm, 520-570 nm, and 420-510 nm ranges were calculated to give red, green and blue (RGB) values respectively as detected by a CCD camera, based on the RGB profile of a generic detector [209] (Figure 4.7)). Calculated colours at different disease stages are given in Figure 4.8A, with 95% confidence intervals indicated for each. Data from each region (areas under the curve) were normalised to grade 0 to facilitate comparison with normal cartilage. Then, intensities of blue and green region were then normalised to red at each stage to maximise colour contrast in a visual comparison. Red was chosen as this wavelength range is expected to be equally reflected by both cartilage and bone [117]. The resulting artificial colour profile with disease is shown in Figure 4.8B. The colour became increasingly red-dominated with the change from grade 0 to grades 1 and 2, with blue-dominated changes most apparent at later stages. The decrease in the relative intensity of green with disease can be further observed in the strong magenta hue at grade 4. No significant differences, however, were observed at different disease stages.

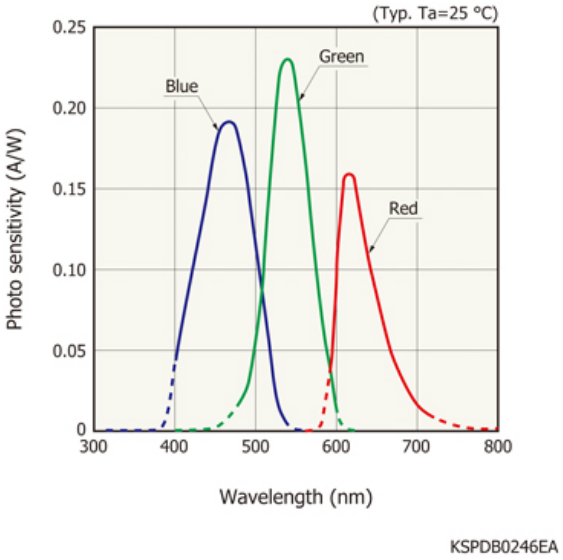


Figure 4.7: RGB profile of a generic detector [209].

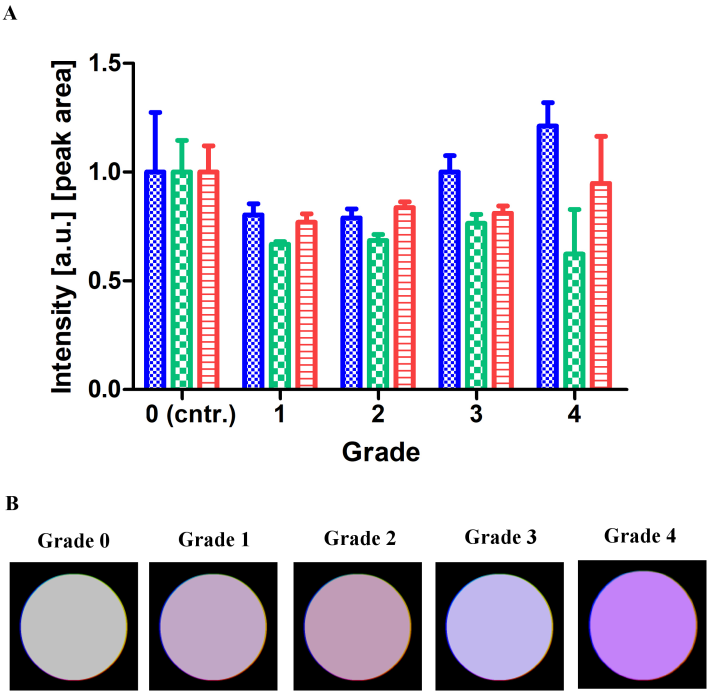


Figure 4.8: The intensity of RGB reflectance at different disease stages: (A) changes in RGB profile and (B) resulting artificial colour. cntr.:control.

4.2.3.3 Slope Between the Wavelengths of 600 and 980 nm

The slopes between the wavelengths of 600 and 980 nm at different stages of disease (all $r^2 > 0.97$) are shown in Figure 4.9. The slope decreases markedly from grade 0 to grade 1, after which it increases with disease progression. Despite this large change in mean slope, differences are not statistically significant for early OA.

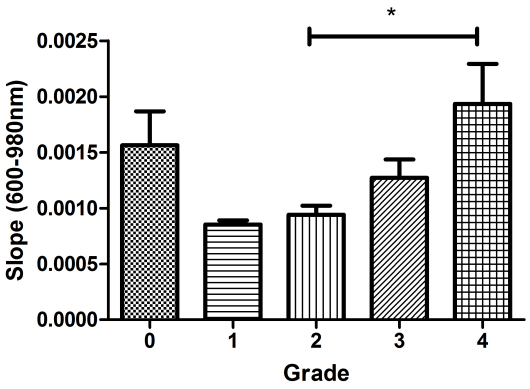


Figure 4.9: Slopes of UV-VIS-NIR absorbance spectra between the wavelengths of 600 and 980 nm at different stages of disease. *:$P < 0.05$.

4.3 Mie Scattering Model

The appearance of peaks in the UV-VIS-NIR spectrum is related to the absorbance of light due to electron excitations. The slope of the spectrum between 600 and 980 nm, however, is related to scattering. We speculated that the change of scattering profile observed in Section 4.2.3.3 could be related to changes in effective fibril diameter, from either a direct increase in fibril size or the bundling of fibrils into larger structures. This bundling may then be related to the disease process defined in previous chapters. We therefore used a Mie scattering model to investigate the relationship between scattering profile and fibril (or bundle) diameter, and interpreted in terms of the scattering profile at different disease stages. Section 4.3.1 briefly introduces Mie scattering, the developed model and its related parameters that were used in this study, with model outputs described below.

4.3.1 Mie Theory and the Scattering Model

When an electromagnetic (EM) wave (i.e. incident light ray) with frequency ν_0 encounters an obstacle, the electron's orbit within the obstacle's constituent molecules is set in oscillation at the same frequency as the electric field of the incident wave.This oscillation is manifested as a source of EM radiation, thereby resulting in scattered light. Light scattering theory can be generally categorised into the Rayleigh theory [210] and Mie theory [211]. Rayleigh scattering primarily refers to the scattered light from particles whose diameter is smaller than the wavelength of the incident ray, typically by an order of ten. However, in the theory of Mie scattering [211] that encompasses the general spherical scattering without a particular bound on particle size. Therefore, Mie scattering theory has no size limitations and converges to the limit of geometric optics for larger particle which may be used for describing most scattering systems, including Rayleigh scattering. For normal fibril diameters of around 80 to 100 nm, and disease-related bundles (at micro level), Mie theory was seemed most appropriate to describe this scattering.

A perviously-developed scattering model [212–216] was used to explore the relationship between fibril diameter and scattering angles at different wavelengths.

The differential scattering cross-section was calculated to quantify the intrinsic rate at which the scattered light can be detected at a given angle (Figure 4.10). That is, the higher the differential scattering implied by the cross section, the greater the opportunity for the scattered light to be collected from the spectrometer at any given angle.

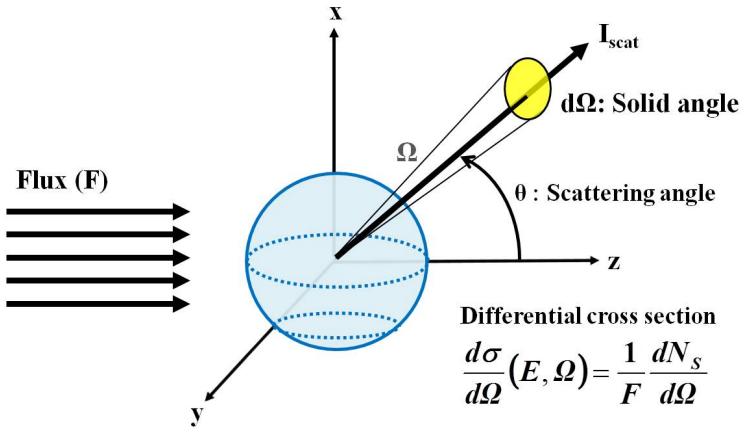


Figure 4.10: Angular scattering intensity. σ: cross section; N_s: number of scattering particles.

In this study, a collagen fibril is assumed to be a cylinder irradiated by a far field light with a 0 degree incident angle. Several parameters are required for the Mie simulation including the cylinder diameter(s), and the refractive indices of collagen and the surrounding medium. The refractive index of collagen has been reported to be 1.46-1.55 [217]; therefore, we used a refractive index of 1.5 for the cylinder in this simulation. Water is the main component of articular cartilage extracellular matrix, so the refractive index of the surrounding medium was taken to be 1.33.

4.3.2 Results

4.3.2.1 Polar Scattering Profiles

Scattering profiles were considered for a range of cylinder diameters (5-400 nm) at wavelengths between 600 and 980 nm (Figure 4.11). Although this range extends beyond the 80-100 nm diameter range observed by AFM, the extended parameter space was chosen to clarify patterns of change. As the diameter of the cylinder increased, the scattering profile shifts markedly forwards (towards a 0

degree scattering angle). Shorter wavelengths scattered more strongly than larger wavelengths, though it is interesting to note that for the 200 nm diameter cylinder, this trend was revered in the backwards direction.

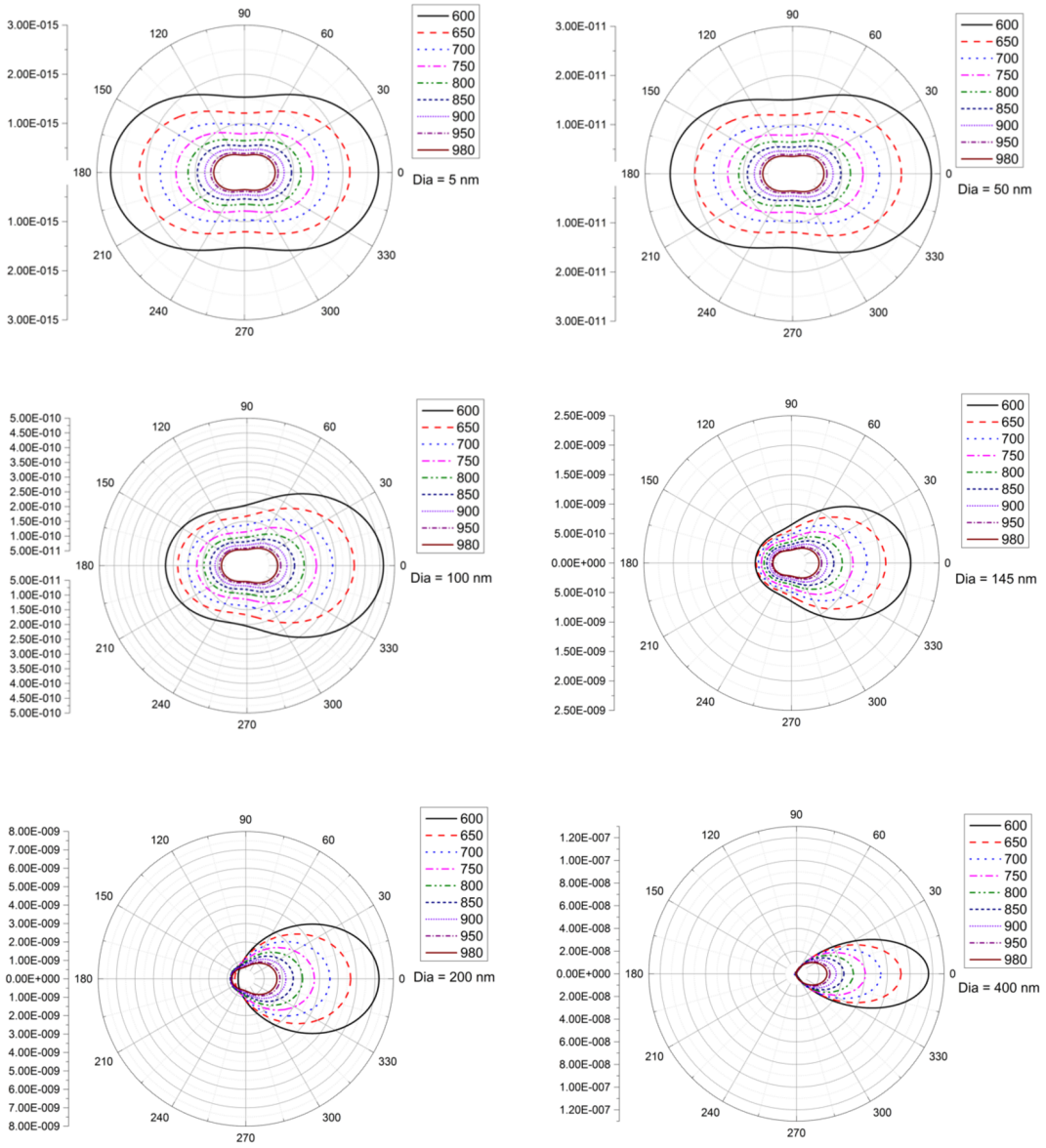


Figure 4.11: Calculated scattering profiles with different diameters of cylinders (5-400 nm) at wavelengths of 600, 650, 700, 750, 800, 850, 900, 950 and 980 nm. Dia.:diameter.

Figure 4.12 shows the scattering profiles for diameters ranging from 200-1600 nm, approximating fibril bundling. Here the trend of forwards-dominated scattering for larger diameters was continued. Scattering profiles in the these larger cylinders were

more complex due to constructive and destructive interference. Hence scattering profiles at 50-310 degrees were plotted separately in the lower half of each part of Figure 4.12, showing the formation of lobes.

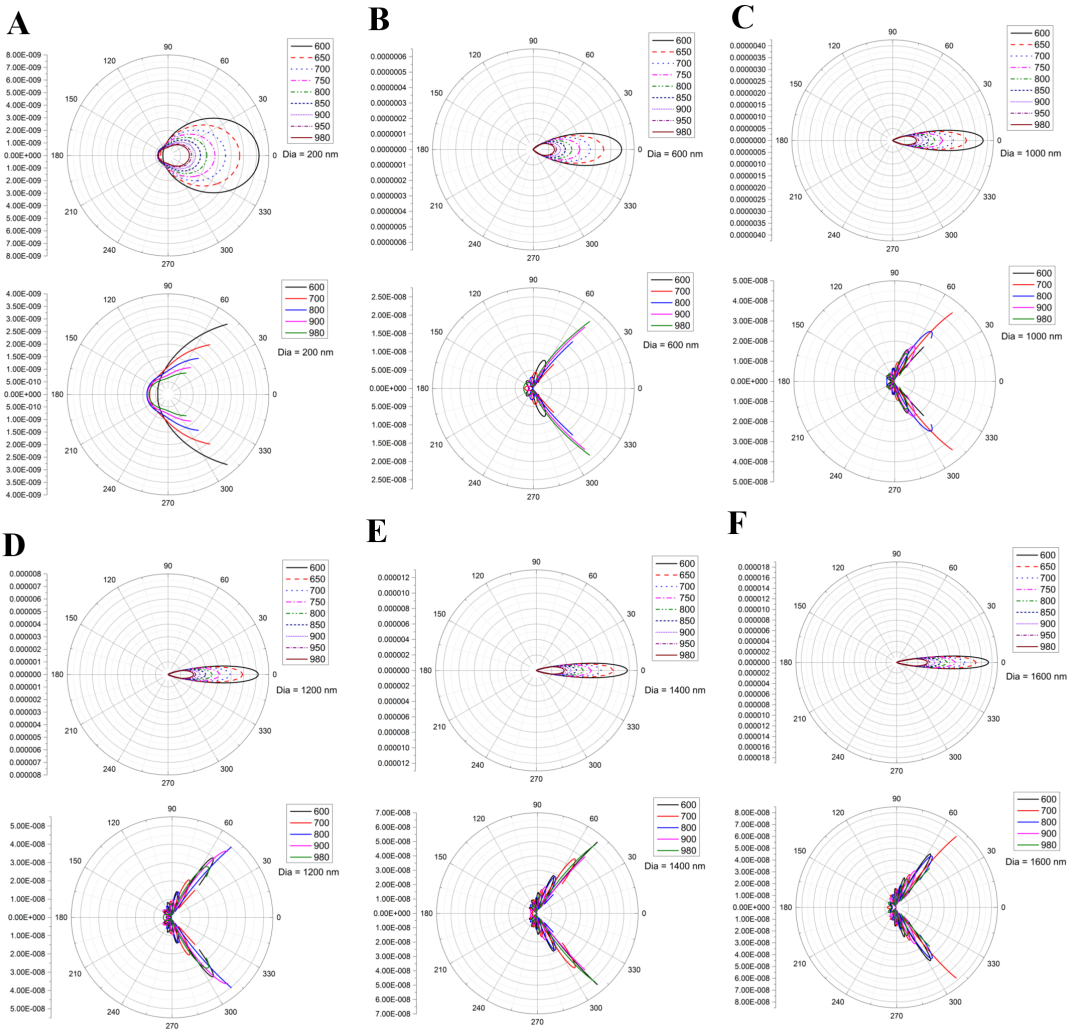


Figure 4.12: Calculated scattering profiles with different diameters of cylinders (200-1600 nm) at 600-980 nm. Profiles for 50-310 degree scattering angles are included below each figure. Cylinder diameters were (A) 200 nm, (B) 600 nm, (C) 1000 nm, (D) 1200 nm, (E) 1400 nm, and (F) 1600 nm. Dia.:diameter.

To better elucidate the angular scattering patterns, results from a subset of cylinders irradiated at 600 and 980 nm are given in Figures 4.13 and 4.14. In addition to the increased scattering at 0 degrees with increasing cylinder diameter, the increasingly complex interference patterns can be observed. With local peaks and troughs differing by a factor of 10 in differential scattering cross section, and with the fast change in peak position with increasing cylinder diameter, this makes interpretation of diameter effects challenging.

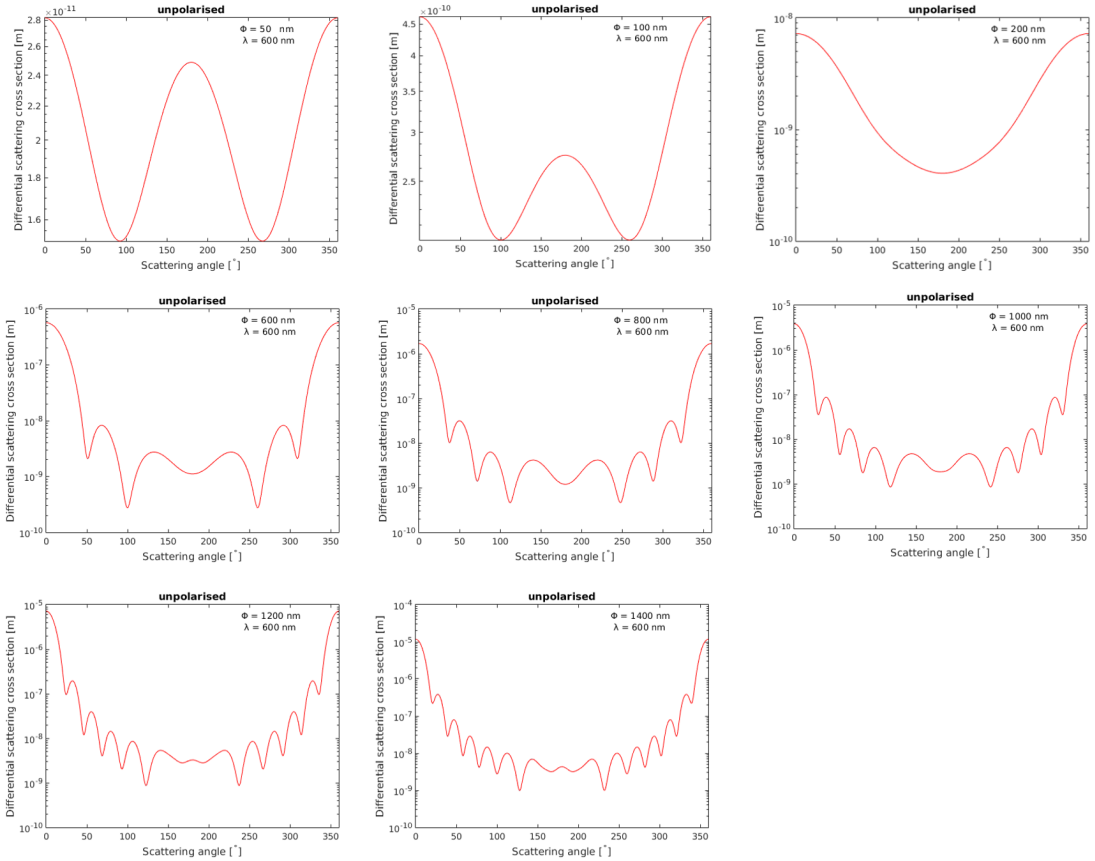


Figure 4.13: Differential scattering cross-sections as a function of scattering angle with different diameters of cylinders at a wavelength of 600 nm.

It was unclear, however, whether the interference patterns would persist in the context of multiple fibrils. Simulations were therefore re-run and differential scattering cross-section calculated for multiple cylinders. Twenty cylinders were randomly located in a 10×10 μm cross section without overlapping. A comparison of single versus multiple cylinder scattering is given in Figure 4.15. The use of multiple

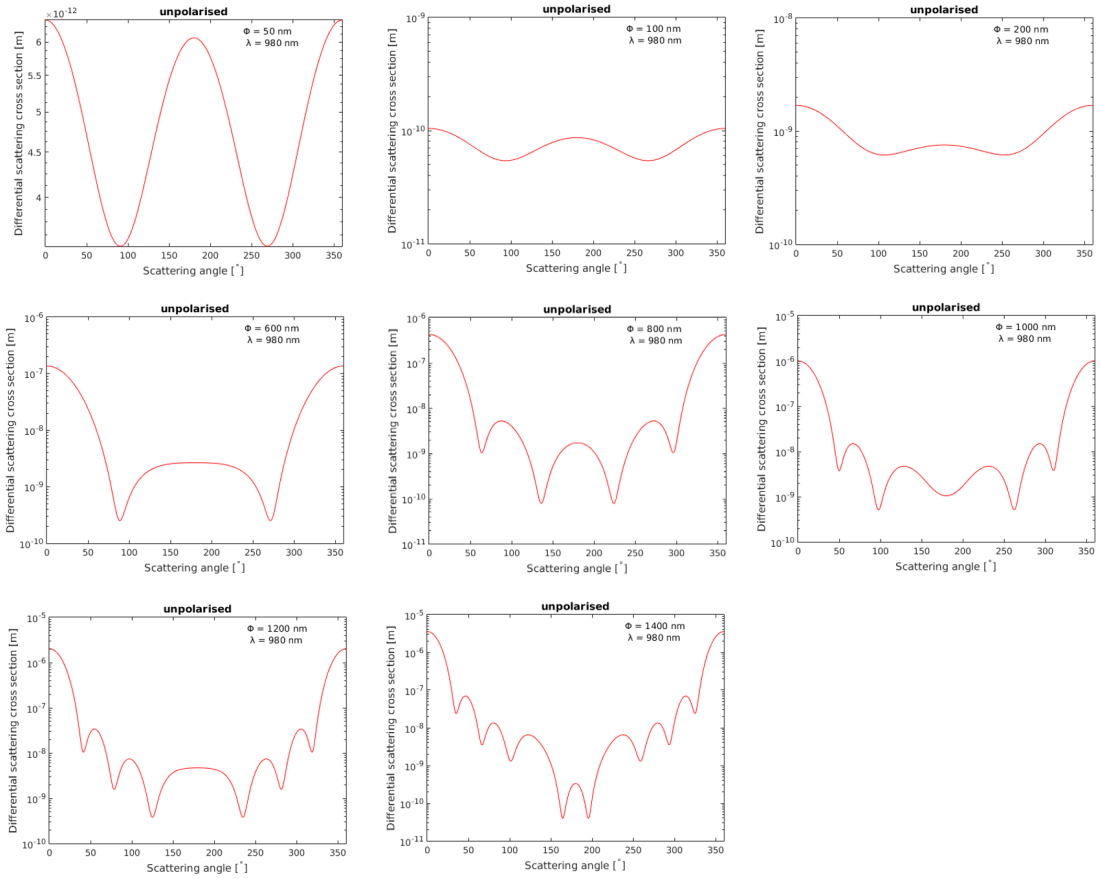


Figure 4.14: Differential scattering cross-sections as a function of scattering angle with different diameters of cylinder at a wavelength of 980 nm.

cylinders of equal diameter added noise to the system, in many cases extending over two orders of magnitude, without a substantial effect on lobe formation. Interpretation of results was therefore based on single cylinder simulations.

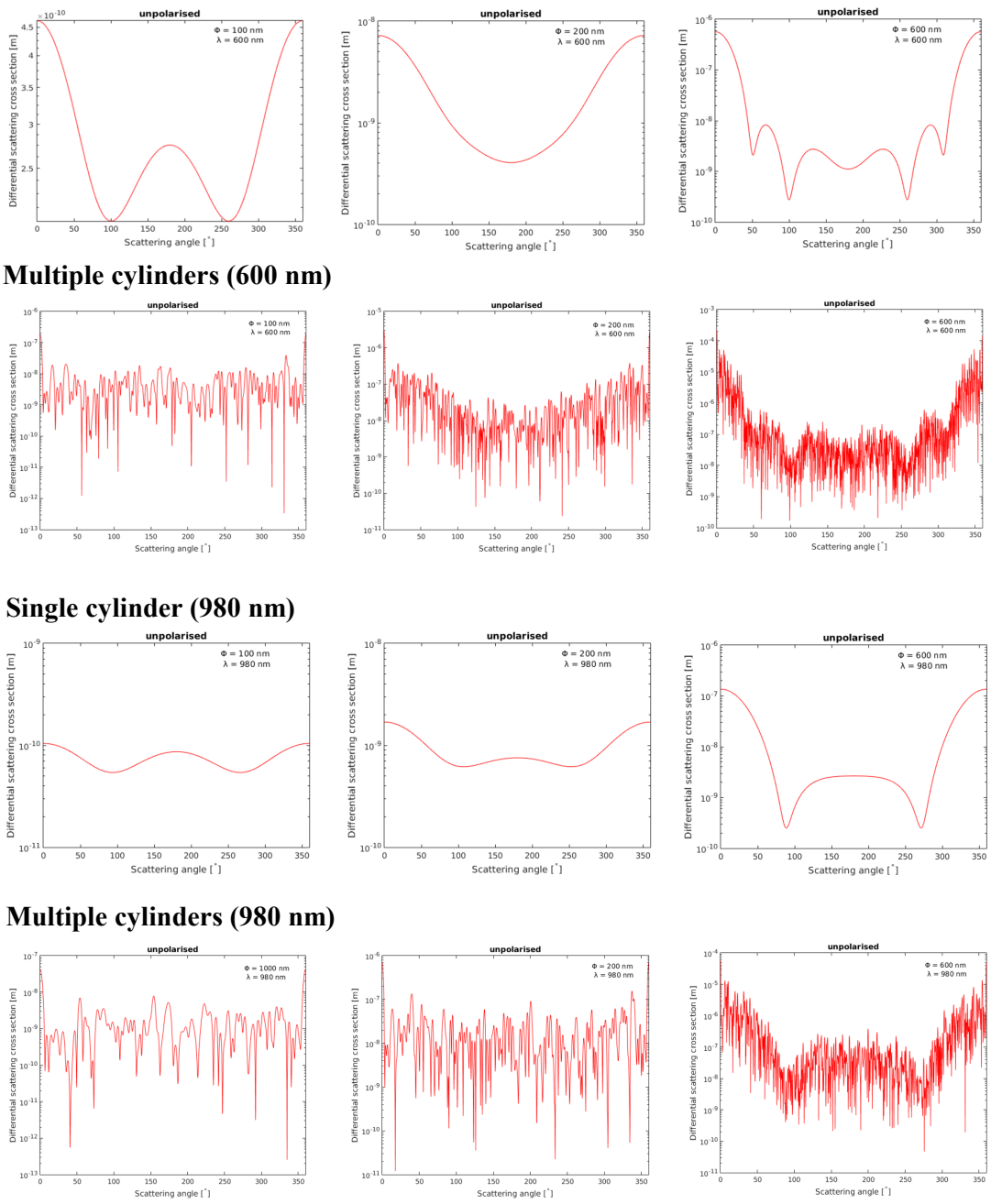


Figure 4.15: Differential scattering cross-section of single and multiple cylinders at wavelengths of 600 and 980 nm. The diameters of cylinders were 100, 200 and 600 nm. Scattering profiles showed more noisy from multiple cylinders.

4.3.2.2 Cylinder Diameter and 600-980 nm Slope

As can be seen in Figures 4.11 and 4.12, a greater proportion of light at a given wavelength is scattered forwards (0 degree) with increasing cylinder diameter. More formally, this can be stated as a greater proportion of forward scattering with an increasing size parameter χ, which is defined as

$$\chi = \frac{2\pi aN}{\lambda} \tag{4.1}$$

where a is the cylinder radius, N is the refractive index of the surrounding medium and λ is the incident wavelength. That is, as the ratio of diameter to wavelength increases, so does the proportion of forward scattering. This relationship may then be used to extract information on the cylinder diameter by comparing the scattering of short and long wavelengths.

As the measured light is backscattered, the proportion of non-forward scattered light is of interest. This includes primary scattering (i.e. single scattering event at or near 180 degrees) as well as secondary backscattered light (i.e. multiple scattering events, at any angle away from 0 degree). Figure 4.16 and Figure 4.17 show the differential scattering cross-sections at 0, 0 $\pm$ 90, 180, 180 $\pm$ 90, and total scattering (integration of all angles) at wavelengths of 600 and 980 nm. Scattering at 180 degrees was strongly influenced by interference patterns, resulting in a large 'noise' signal. This also affected results for the integrated scattering angles. In all cases, however, a general trend of increased scattering cross section was observed with increasing cylinder diameter.

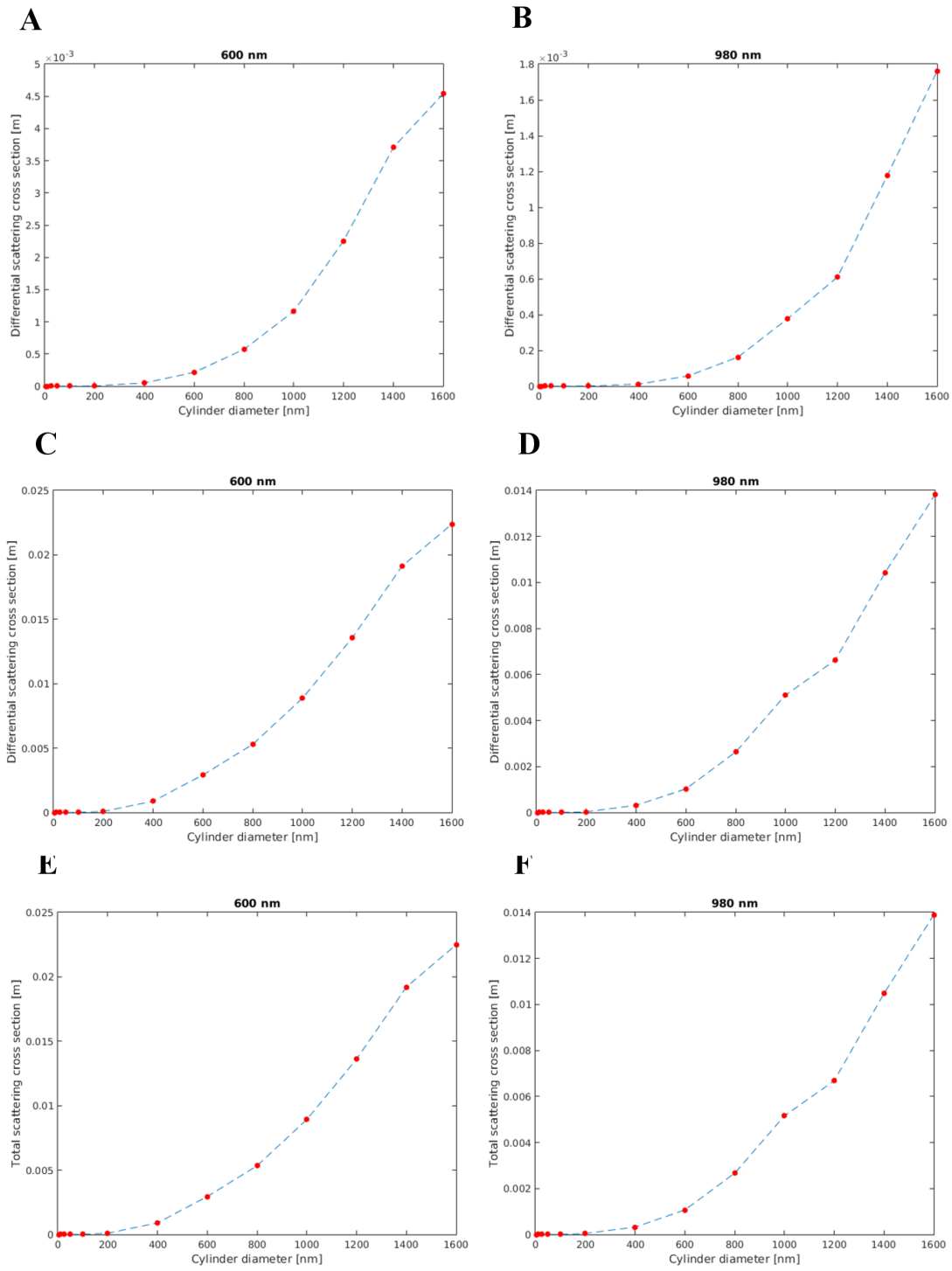


Figure 4.16: Differential scattering cross sections at (A and B) a 0 degree scattering angle, (C and D) between 0 ± 90 degree scattering angles and (E and F) total cross-sections with different diameters of cylinder at wavelengths of 600 and 980 nm from Mie simulation.

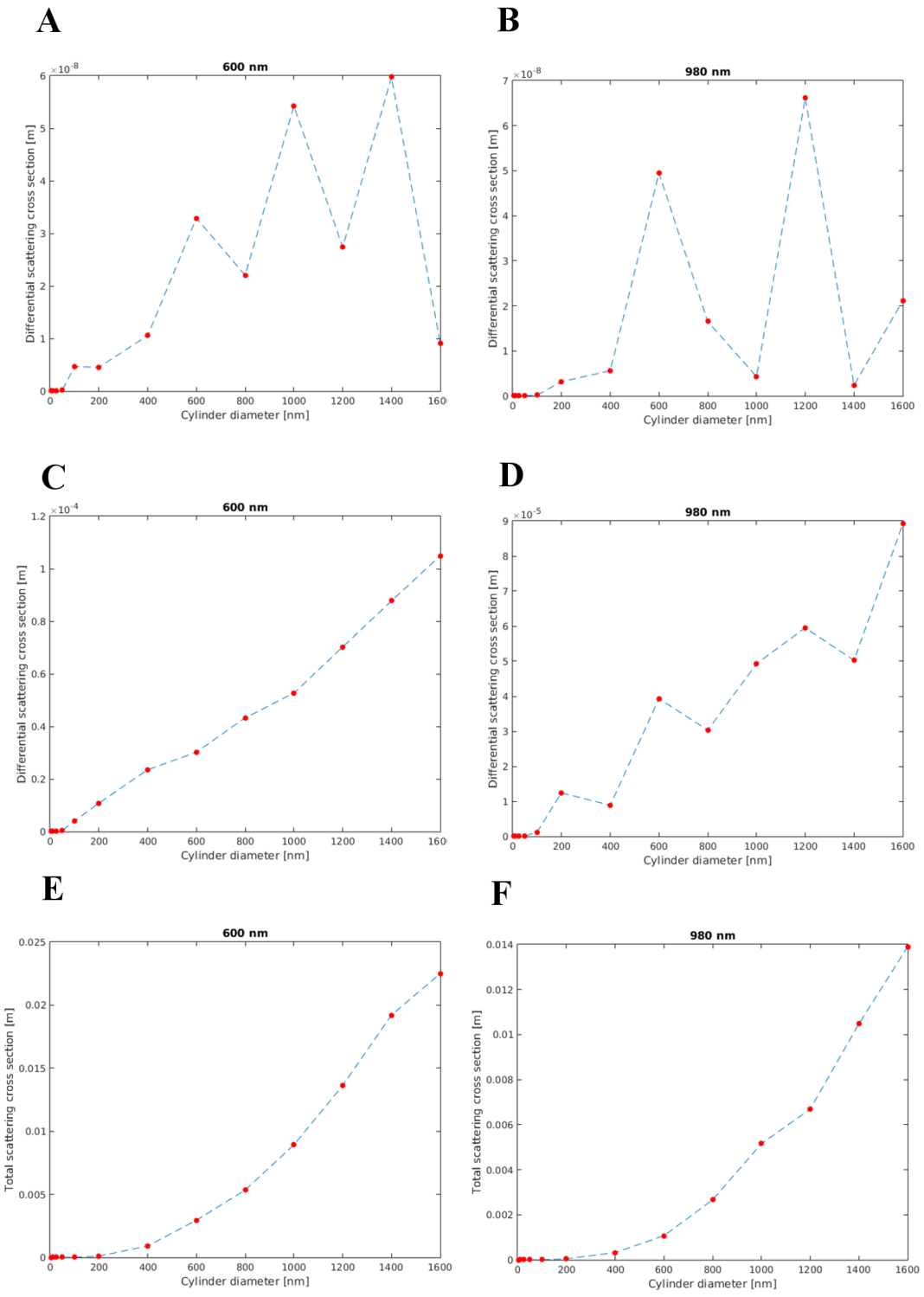


Figure 4.17: Differential scattering cross sections at (A and B) a 180 degree scattering angle, (C and D) between 90-270 degree scattering angles and (E and F) total cross-sections with different diameters of cylinder at wavelengths of 600 and 980 nm from Mie simulation.

The wavelength dependence of this backscattered light is of particular interest for understanding and interpreting the experimental measurements. This dependence was explored by fitting power law relationships (all $r^2 > 0.95$) to the 0 degree and total scattering cross sections at each wavelength, as the ratios retain their power law form and can be compared without magnifying noise contributions. Figure 4.18A shows the ratio of proportional backscattering at 980 and 600 nm can thus be calculated and the inset figure shows the broader diameter effect ranging from 5-1600 nm. To aid interpretation and allow comparison, experimental results were replotted for the same ratio (Figure 4.18B). Note that the experimental data above are plotted in reflectance ($\log_{10} \frac{1}{R}$, where R is reflectance), hence trends are reversed with respect to absorbance data in Figure 4.9. As shown in Figure 4.18, wavelength dependence is strong at relatively small cylinder diameters, as the scattering behaviour transfers from the Rayleigh regime to the Mie regime. At larger diameters, above 400-500 nm, this dependence is weaker.

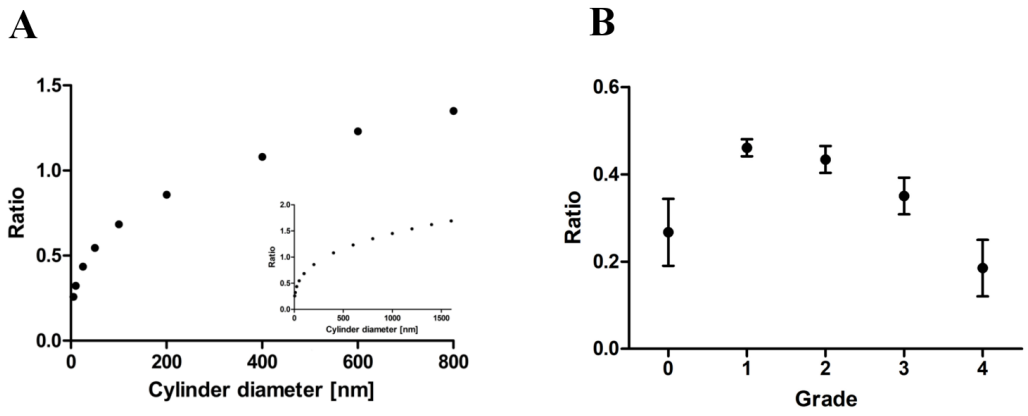


Figure 4.18: The ratio of 980 and 600 nm comparison from Mie scattering model and experimental data. (A) Ratio of the proportional backscattering between 980 and 600 nm with cylinder diameter ranging from 5-800 nm (inset figure shows the slope of proportional backscattering between 980 and 600 nmwith cylinder diameter ranging from 5-1600nm. (B) Slope changes from experimental data (reflectance).

4.4 Discussion

UV-VIS-NIR spectroscopy was applied to explore the potential of three approaches for detecting disease-related changes to the cartilage surface within the constraints of the arthroscopic light source and path. These approaches were based on electronic absorbance peaks, a scattering interpretation of the slope in the 600 to 980 nm region, and colour analysis. It should be noted that this is a pilot study: due to the very low numbers of samples, it aims to explore the potential of a spectral measurement approach in preparation for a future assessment of efficacy.

When sample molecules are exposed to light which has an energy matching a potential electron transition within that molecule, some of the energy will be absorbed and then the electron will be excited to a higher energy orbital. The absorbance is determined by the structure of the molecules comprising the object. It is particularly sensitive to the degree of conjugation, which determines the energy difference between ground and excited state: high levels of conjugation give rise to low energy transitions. In this study, we found five apparent absorbance peaks which were at 320, 405, 455, 531 and 566 nm. Areas under these five peaks and the ratios of them were analysed at different disease stages (Figure 4.5 and 4.6). Patterns of absorbance peaks with OARSI grade were similar at 405 and 455 nm, and at 531 and 566 nm, with inverse patterns for the 320 nm and >500 nm peaks. Little previous work has been performed in this area. One previous study found that above 510 nm, the absorbance of weight-bearing cartilage is significantly higher than that of nonweight-bearing cartilage [218]. Our results showed similar effects with disease progression (Figure 4.5D and E). It may further be possible to take advantage of the inverse patterns of the 320 nm and >500 nm peaks, taking a ratio of the two to enhance the potential to discriminate between normal and diseased tissue. This can be observed in Figure 4.5A and B.

Despite the potential of this approach, we were unable to determine the source of the absorbance peaks of interest. Theoretical calculation of UV-VIS absorbance peak assignments reveal no obvious source of the absorbance peaks, and are generally used in the analysis of smaller conjugations (i.e. higher energy,

shorter wavelength) than observed here. An experimental approach, systematically removing proteoglycans or lipids, or digesting collagen, did not remove absorbance peaks. Further analysis is therefore required to quantitatively link the absorbance results to specific disease processes.

Closely related to the absorbance peaks is colour. Colour change, from pristine white cartilage to diseased yellow/red cartilage, is anecdotally associated with OA progression and is used in qualitative assessment. Based on the spectral range of a standard RGB sensor, we therefore incorporated three broad peaks (Figure 4.8) at 610-650 nm, 520-570 nm, and 420-510 nm which combines contributions from both scattering and absorbance from electronic transitions. Quantifying this change, we observed a red-dominated (with reduced green reflectance) change at early stages and a blue-dominated change at later stages (Figure 4.8), although it should be reiterated that the colouring in Figure 4.8B is the product of normalisation and calculations to highlight colour related change and should not to be taken as an approximation to the true colour of cartilage.

Finally, we examined the VIS-NIR slope, with an interpretation based on scattering. Experimental measures of the slopes between the wavelengths of 600 and 980 nm differed at different stages of disease, with a ≈50% decrease from grade 0 to grade 1, followed by an increase in slope with further disease progression (Figure 4.9). Given the 80-100 nm diameter of collagen fibrils observed in Chapter 2, the bundling of fibrils to form structures of a larger effective diameter will therefore transition from a Rayleigh scattering regime to a Mie scattering regime. A Mie scattering model was applied to investigate the relationship between the slope and this change of effective fibril size with disease, representing fibrils as cylinders oriented perpendicular to the light path.

Analysis was complicated by a number of features of Mie scattering, and also of the samples themselves. First is the roughness of the surface, and its change with disease. The interpretation of scattering based on cylinder size assumes, and requires, that the surface is intact. The presence of cracks/fissures in later-stage diseased tissue (summarised in Figure 4.19) therefore produces complications to the

specular reflectance profile, with related interference due to the complex geometry, and further exposes deeper layers of cartilage within which fibrils are no longer perpendicular to the surface [47]. Fibril bundling is further difficult to detect due to the natural change in fibril diameters with depth [219, 220].



Figure 4.19: Safranin-O stained sections at different stages of disease: (A) grade 1, (B) grade 2 and (C) grade 3. Cracks/fissures from the surface of the cartilage appeared at grade 2 and grade 3 (magnification 10×).

Second, the formation of lobes at around 50-310 scattering degrees due to constructive and destructive interference of scattering events in different regions of the cylinder (Figure 4.13 and 4.14).Compounding this is interference of scattering from adjacent cylinders. The wavelength and cylinder diameter dependence of backwards scattered light was therefore approximated by summing light that was not forward scattered. This includes directly backscattered light, and that which undergoes multiple scattering events away from 180 degrees to reach the detector as diffuse reflectance. Taking the ratio of total scattered light to forward scattered light at each wavelength, we were thus able to capture the distinct proportional back scattered light (Figure 4.12) when transitioning from the Rayleigh to Mie regimes in a way that best approximates the light measured via the fibreoptic probe (Figure 4.1B).

As the transition is a function of both the wavelength and diameter, an upper bound of cylinder size exists, above which both wavelengths are in the Mie regime and the technique becomes insensitive. This sensitivity is highlighted in Figure 4.18A, showing a flattening of the curve above cylinder diameters of 400 nm, corresponding to a bundle of ≈12 fibrils, substantially smaller than the bundles of tens to hundreds of fibrils observed in SHG studies of cartilage [21].

In summary, due to the spot size of the probe allowing only single measurements per core, and the resultant low sample numbers, this Chapter was pursued as a pilot study to explore the potential of spectral measurements rather than test efficacy. From our limited results, we found that the absorbance peaks and their ratios change with disease progression, implying that the conjugated system of molecular structure changed with disease progression, although we were unable to define the responsible molecular structures for this change. A simplified, yet related analysis RGB changes revealed red/blue-dominated changes at early stages and blue-dominated changes at late disease stages. These related changes detected by the camera may provide a simple and easily tested objective reference to the surgeon to distinguish the disease stages. Finally, slope changes between 600-980 nm were applied to explore the relationship between the structural changes explored in earlier chapters and spectra available to the arthroscopic camera. By comparing the computational Mie scattering model and experimental data, we found that the slope changes could be related to the bundle size, with sensitivity restricted to bundle sizes below 400-500 nm. These findings, and the different sensitivity of each method suggest a combined spectral approach will provide the most robust results. Further analyses are required but we conclude that a UV-VIS-NIR spectroscopy approach has good potential for application as an integrated arthroscopic assessment tool.

5
Discussion and Future Work

Contents

5.1 Limitations 157
5.2 Discussion and Conclusion 159
5.3 Future Work and Future Directions 167
5.3.1 Opportunities to Improve Current Work 167
5.3.2 Future Directions 169

Having established collagen as a central factor in the function and dysfunction of articular cartilage, this thesis has sought both to improve our understanding of the physical processes in disease and to explore new approaches to detecting the key features of irreversible damage. Focussing on the articular cartilage surface, Chapter 2 examines physical changes within the collagen fibrils, Chapter 3 examines interactions between collagen fibrils when placed in a cartilage-like network, and Chapter 4 explores a potential diagnostic/assessment method to probe them. Before any general conclusions can be reached from this work, however, a number of limitations must be discussed.

5.1 Limitations

The main limitation in this study was the low number of samples: tibial plateaus of 10 patients (35 cores) were available to the project. Particularly important was the small numbers of grade 0 samples available to the study, limiting statistical power when examining changes with early stage disease. Although the use of animal tissues may address this deficiency, human samples, even at low numbers, is argued to provide better insight into the disease states of interest and at a minimum allows power calculations required to examine our preliminary findings in further detail.

The second major limitation relates to our ability to define the articular surface in later stages of disease. As shown in Figure 5.1, OARSI grades 3 and above are characterised by large scale fissuring or complete loss of the surface layer. Comparison of surface characteristics may therefore only be valid for grades 0 to 1, or grade 2, as later measurements from later stages of disease are likely to probe the exposed deeper layers of the tissue.

A number of specific experimental limitations further affect our ability to draw conclusions. First, by taking measurements from cores, we were unable to examine the continuous transition from the histologically normal to diseased cartilage surface. Therefore, some detailed spectral changes, topography and mechanical changes of collagen fibrils along disease progression may be missed. Second, we were unable to perform experiments in an aqueous solution, which is closer to the physiological environment, although the of effect on results is unclear. Finally, our inability to develop a satisfactory polarised Raman system within the time and budget constraints of the project, limited our investigation of collagen organisation at different stages of disease. Consequently a direct experimental link between fibril properties (Chapter 2) and fibril organisation (Chapter 3) could not be made, the conceptual link between Chapters instead relying on previous findings in the literature.

The ability to draw conclusions from our model may be limited by three factors. First, it does not consider non-collagenous components such as aggrecan and fluid. Although very little aggrecan is present in the surface zone, and is unlikely to

contribute mechanically, fluid flow through the surface is prevalent. At the level of scale examined in this model, and considering the overdamped nature of the collagen network, inertial effects are unlikely to be large. By considering only the equilibrium behaviour, the need for inclusion of highly complicated fluid effects are minimised. The consequent inability to examine dynamic behaviour of the network, and its role in disease progression should be highlighted as an important limitation of this work.

The second factor was the simplification of collagen load carriage to ignore compressive behaviour. This may be an important oversight, based on our observation of fibril-level compression in the *Mikado* model (Figure 3.16). As the bending and rotation characteristics of the collagen fibrils, however small, are overlooked, interpretations of fibril stresses in the *Mikado* models may be incomplete.

The third limitation is a lack of precise information on the structure and loading environment in the surface layers. Our simulations therefore explore a number of different structures under different applied loads, comparing findings with observations from experimental data. Although we argue that the structure and environment is within the variation tested in Chapter 3, its true nature is unclear.

5.2 Discussion and Conclusion

Figure 5.1 summarises the main experimental outputs from the characterisation of cartilage by AFM and Raman spectroscopy (Chapter 2) and the exploration of UV-VIS-NIR spectroscopy for detecting structural features associated with OA (Chapter 4).

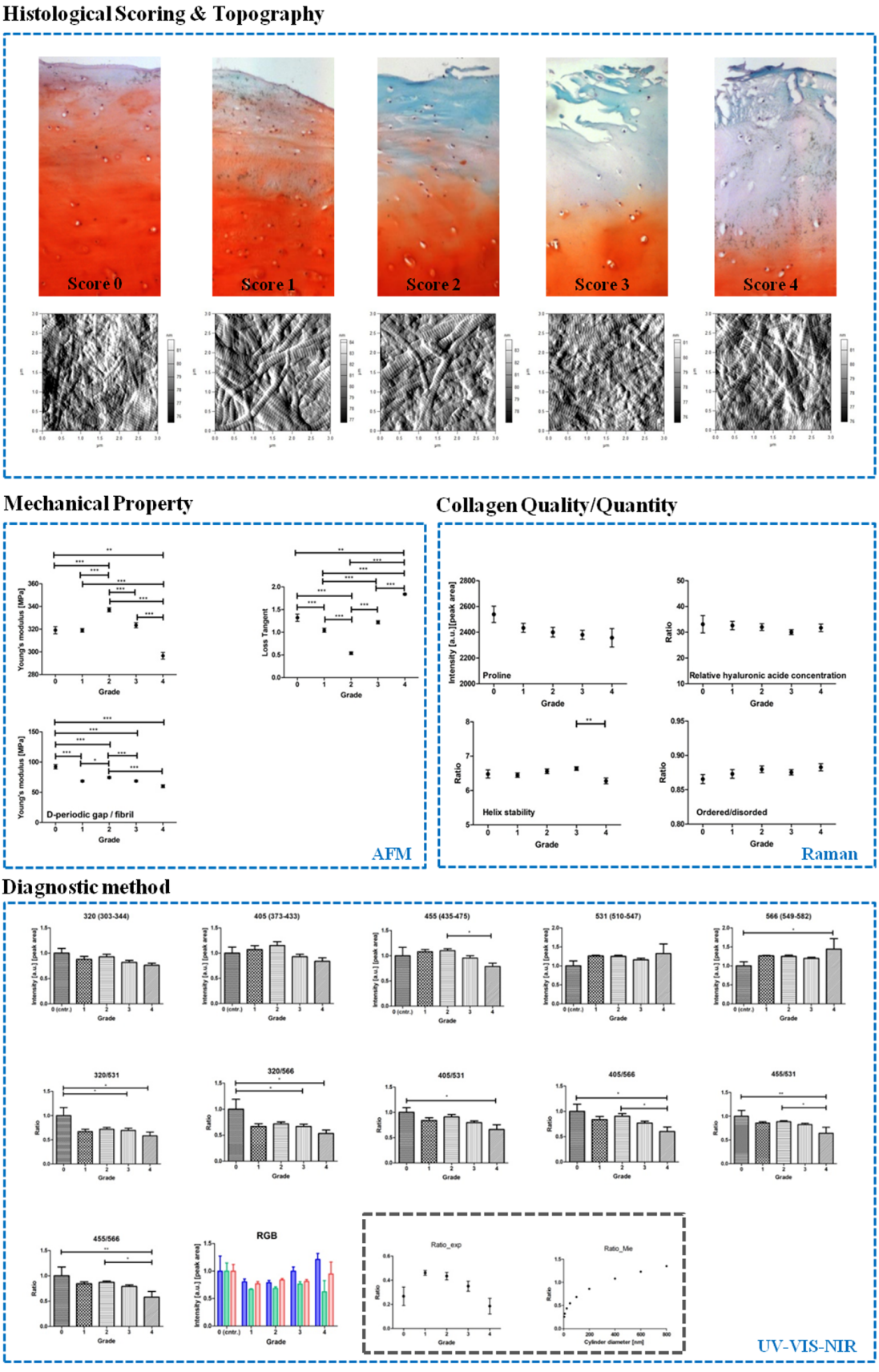


Figure 5.1: Summary of the characterisation of OA progression and potential methods for detection of OA structural features.

Three main questions are addressed in this study. As collagen plays an important role in the functioning of the tissue and also in disease, the first question we asked was: *What physical changes occur in collagen during early disease progression?*

Raman spectroscopy and AFM were used to characterise collagen at different stages of OA. Raman spectroscopy indicated that the quality and quantity of collagen, and the relative concentration of hyaluronic acid, decreased with disease progression at early stages (grade 0 to grade 1), though changes were not statistically significant against the large variations within each group, particularly for 'normal' samples. This variation may result from the combined synthesis [221] and degradation [222] processes characteristic of early disease. The level of order in the tropocollagen molecule (Figure 2.40) appeared to decrease with disease progression. Helix stability (Figure 2.39), however, was maintained up to grade 3. More important for interpretation is the magnitude of changes between groups: the small differences observed between disease states indicates that the central changes in early OA are not at the level of the collagen molecules' secondary structure, but rather at a higher hierarchical level.

This finding is reinforced by mechanical results. Young's modulus increased up to grade 2, accompanied by a marked decrease in loss tangent (Figure 2.33A and B, Figure 5.1). After grade 2, trends were reversed. Relative Young's moduli along the fibre, measured as the difference between the gap region and the inter-gap region decreased with the onset of grade 1 OA and remained stable thereafter (Figure 2.36, Figure 5.1).

Coupled with a lack of correlation between mechanical and Raman results (all $r^2 << 0.5$), these findings demonstrate that the central changes are at the level of tropocollagen interactions, potentially via AGEs, and act to embrittle the collagen fibril. By strengthening interactions at this level, energy dissipation through the generation of slip pulses is nullified, forcing fracture of the tropocollagen molecule itself and release of stored elastic energy causing catastrophic failure.

Topographical changes were also observed at different stages of disease. A number of granules were observed on collagen fibrils, similar to those reported

by some studies [167, 223, 224], however their origin and potential role in disease remains unclear. A reorganisation of collagen into bundle and knot formations was also observed in a number of late OA samples. In early OA samples, regions of aligned fibrils, and a number of isolated, thin fibrils were found (Figure 2.29). It is uncertain whether the thin fibrils were a sign of new fibril formation, or alternatively whether they were a different type of collagen. Insufficient fibril exposure may also have been a factor.

Interestingly, during sample preparation we found that, after enzyme treatment, collagen fibrils were most easily exposed at late disease stages. In normal samples, and at early stages of degradation, an adhesive 'ground substance' remained attached to collagen. This ground substance, which could not be removed by targeted enzymatic treatment or isopropanol is thus likely to modulate interactions between fibrils, and therefore the behaviour of the collagen network.

The findings of Chapter 2 indicate a crucial role for for network behaviour, and warrant investigation at the tens of micron level of scale. From the above results, and findings of collagen network restructuring at the earliest stages of OA [21], we speculated that the inter-fibril interactions may be critical as a physical disease progression mechanism. This raises the second question of the thesis: *how physical changes relate mechanistically to osteoarthritic progression mechanically?*

2-D cartilage-like collagen network models, based on two different configurations, were developed to investigate the role of inter-fibril connectivity in the cartilage surface. These models included a mesoscopically-aligned yet locally-random 'zigzag' network, and the randomly-oriented and distributed, straight-fibrilled *Mikado* network. Beginning with the *Mikado* network which, based on Chapter 2 results, may best represent the collagen in the cartilage surface, increasing crosslink density acts to resist load at the network level, and improve recovery of the network when load is removed (Figure 3.40). Highly-crosslinked networks also reduce the strain carried by individual fibrils as stress is more effectively distributed across the network and more fibrils are engaged to carry an applied load. With a loss of

connectivity, isolated fibrils are placed under increasing stress (Figure 3.21, and 3.41), and fibrils are observed to form aligned and bundled structures, particularly under anisotropic applied loads (Figure 3.30). Coupled with the embrittlement of fibrils observed in Chapter 2, the increased stress on isolated fibrils may act as a trigger for catastrophic damage.

With increased mesoscale alignment, and maintaining local disorder, such a network will transition to a state better approximated by the 'zigzag' model. Here, crosslink density had a similar effect on the network level resistance to, and recovery from, applied loads, and better maintained its organisation (Figure 3.8 and 3.7). With decreasing crosslink density, however, fibrils carried less stress as they could more freely realign in the direction of applied loads (Figure 3.6). Thus, a qualitatively 'normal' structure, with low crosslink density is transformed to a disease-like structure, fitting experimental observations by electron microscopy [120]. From this lower energy state, given by the strain energy stored per fibril, it is energetically unfavourable to revert to the normal network configuration, and the disease process may be argued to have reached a mechanically irreversible state.

Building on the findings that the intra- and, perhaps more importantly, inter-fibril interactions are critical to maintaining the collagen structural and functional integrity, we finally ask *whether we can detect these early, irreversible changes to cartilage intraoperatively to facilitate treatment?*

Attempting to utilise the light source and optics available in current arthroscopes, and without change to the radiation or instrumentation to which the patient must be subjected, we examined opportunities for the quantitative analysis of reflected light. Utilising a similar source and optical path to a standard arthroscope, and constraining input to the range available to a standard detector/camera, we therefore analysed the spectral properties of reflected light in the UV-VIS-NIR range. This included analysis of UV-VIS absorbance peaks from electronic transitions, the colour properties, and the slope from 600 to 980 nm, which we examine in the context of scattering. This work in particular was limited by sample numbers, as the

experimental setup of the UV-VIS-NIR probe allowed only a single measurement per core. Chapter 4 should therefore be considered a pilot study, exploring the potential of different approaches rather than establishing their efficacy. It should also be noted that an assessment tool need not be sensitive to disease progression beyond OARSI grade 2, as the large scale fissuring and fibrillation in the surface is easily visible to the naked eye. From this consideration, and from the limitations discussed above, analysis therefore focussed on the change from grade 0 to grade 1.

Results from the analysis of five absorbance peaks revealed similar patterns in absorbance with disease progression at 405 and 455 nm, and at 531 and 566 nm, with inverse patterns for the 320 nm and >500 nm peaks (Figure 5.1, UV-VIS-NIR). Taking advantage of this inverse relationship with disease progression, the ratio of the 320 nm and >500 nm absorbances produced a more distinct change from the normal to diseased states, which may have potential as an assessment tool. Further analysis, however, is required to quantitatively link the absorbance results to specific compounds and disease processes.

Spectra were then analysed to quantify the colour of the cartilage surface. This used the relative intensity of the RGB components of the reflectance spectra at each stage, based on a standard RGB sensor configuration. RGB colour ratios of cartilage were increasingly unbalanced towards late stage, matching anecdotal observation. Absolute intensities of the reflected light of all colours decreased with the onset of disease, with later-stage changes primarily driven by changes to the blue component. The relationship between red and green intensities may provide the most useful indication of early stage disease, and may capture some aspects of both the absorbance peak changes and the slope changes with disease (Figure 5.1). From the current results, however, the use of RGB appears to have lowest potential of the three approaches when assessed as a quantitative diagnostic tool.

Using a scattering interpretation of the slope between wavelengths of 600 and 980 nm, we finally explored the transition from the Rayleigh to Mie scattering regimes at different diameters of cylinder, representative of either single of bundled fibrils. Capturing the edge of the transition, and utilising the marked forward shift

of scattering from larger structures (i.e. in the Mie regime), we found that diameter-dependent scattering at these wavelengths could be sensitive up to approximately 400 nm bundles (Figure 5.1). This equates to a bundle of approximately 12 fibrils, above which the method is largely insensitive. Relative to findings from nonlinear optical techniques [34] this scale of bundling represents an extremely early stage of disease. This sensitivity window could be considered as a strength, where such an analysis is coupled with an approach that maintains sensitivity beyond this disease state. If not, it should be considered a limitation.

To conclude, the physical changes to collagen with osteoarthritis are multifaceted and dynamic. With disease progression, the impact of intra-fibrillar changes appears to be lower than that of inter-fibrillar changes. Intra-fibrillar changes, however, may be more closely linked with disease initiation, and an increased susceptibility to mechanical damage. The significant changes to the loss tangent, with minimal changes to the tropocollagen molecules themselves, indicates that with the onset of disease, collagen fibrils change from a dissipative, ductile deformation and fracture mechanism to one which is brittle. The loss of dissipative slip pulse mechanisms substantially increases stored energy during deformation, which is released upon fracture, thus undermining the controlled fracture propagation.

Coupled with the findings of the 2-D network models, the combination of this embrittlement and a decrease in fibril interaction will instigate and progress damage as high levels of stress are carried by individual fibrils. We argue that the inter-fibril interaction is key for driving disease. The restructuring of the collagen network, via this loss of connectivity appears energetically irreversible while loading is maintained. This may form a 'tipping point' beyond which damage is irreversible while loading is maintained. The precise structural changes that would constitute such a tipping point, however, require substantial further investigation.

It may further be possible to detect the onset of the above physical/structural changes by quantitative analysis of the light available via arthroscopy to aid intraoperative decision making and the application of localised treatments such

as tissue engineered replacement or cell implantation. Assessing specific UV-VIS absorbance bands, the related RGB colour profile, and the VIS-NIR scattering behaviour, we conclude that significant potential exists to detect early physical, and importantly irreversible, changes to the cartilage surface with OA. This raises the possibility of advancing arthroscopy from a qualitative to quantitative tool, without requiring modification of either the radiation (the light source and path) or instrumentation (the arthroscope itself) delivered to the patient, thus allowing a low-cost yet potentially high-value technology.

5.3 Future Work and Future Directions

5.3.1 Opportunities to Improve Current Work

Considering the limitations outlined in Section 5.1, several improvements could be made to expand this work in future. First, and the main limitation of the thesis, relates to the number of samples. This can be overcome given more time to gather more human samples of an appropriate disease state so as to allow examination of the full spectrum of disease. Samples from amputees would provide normal and early-stage OA tissue.

Second, the lack of a continuous tracking function with disease progression may be overcome with a modified experimental set-up. For AFM measurement, scanning over the entire region of interest instead of measuring random spots within specific regions would improve coverage. Mounting motorised stages to the sample holder for both Raman and UV-VIS-NIR spectroscopy would allow continuous tracking at a smaller scale with disease progression, but maintaining the precise focal point on the cartilage surface is of concern when using such an approach. To compensate for the focus effect, mounting a camera with a focal point conjugated to the objective may help to precisely adjust the focal point of the laser light onto the cartilage surface by allowing the operator to observe the clear image from the camera. Where continuous tracking could be achieved, another issue that needs to be overcome to improve UV-VIS-NIR spectroscopy is the large spot size. A reduction in spot size could be achieved by using a different type of probe, coupling the light source and the spectrometer to a scanning microscopy system, or by using hyperspectral imaging. With these improvements, the continuous transition with disease progression could be examined in greater detail.

The third limitation is the inability to directly compare the organisation of collagen with the scattering profile. This could be overcome by improving the beam shape by replacing the laser and optical fibre to maintain polarisation throughout the beam path. This modification would need to be coupled to an objective with a long working distance and high NA that would provide a tighter focus to minimise

the effect of turgidity in the sample. Increasing the precision of the focal point would necessitate a strategy to maintain its position in the sample, using a compensation method such as that outlined above.

5.3.2 Future Directions

In addition to the above improvements in experimental set-up, there are also opportunities to expand the analysis, and offer new directions for the work. First, further study of the slope changes within different regions of the UV-VIS-NIR spectra is needed. As the scattering sensitivity of the wavelengths is different, analysing different slope changes from other regions may provide more information and potentially broaden the window of sensitivity.

Potential also exists to investigate the D-periodic gaps of the fibrils at different disease stages. It has been shown that the population distribution of D-periodic gaps of Type I collagen can be changed by altering the protein structure, although the average spacing was unchanged [225]. The D-periodic gap distribution has also been found to change in age-dependent diseases such as oestrogen-depletion-related osteoporosis [226, 227]. A recent study found that the stiffness of the overlap regions of the D-periodic gaps increased with OA progression [74] but no significant difference in D-periodic gap patterns was found between collagen fibrils from intact and osteoarthritic cartilage. A decrease in the D-periodic length in aged tissue has also been observed [128]. Therefore, we believe that further study of the D-periodic gaps of collagen fibrils, such as the material properties of overlap regions and distribution of D-periodic gaps at different disease stages, may provide more information on the collagen structure with disease progression, and provide insight into the related mechanics. The accumulation of more spectra and data on mechanical properties from continuous sampling of disease progression will allow deeper exploration of the relationships between properties. Future work could explore the use of these relationships as predictive tools.

Our future model would be in a 3-D environment and includes dynamics which requires data on aspects including fluid, bending and rotation of collagen. This allow us to investigate damage feedback, the dynamic transition from normal to disease states, and the sensitivity of this process to phenomena such as embrittlement, connectivity and loading environment. Having created a more sophisticated model, we would be able to develop key structural markers of functionality or

defunctionalisation and investigate the 'tipping point' at which collagen structural change becomes irreversible after loading.

Future application of the model could be based on this 'tipping point'. Before the 'tipping point', our model would be applied to study the pharmaceutics for early treatment. Targeted drug delivery, retention of drug in the targeted tissue and morphology of the drug are important in medical therapy. In combination with pharmacodynamic parameters, the model would improve understanding of the interactions between drug and tissue, aiding pharmaceutic drug design. Since collagen is an important component of connective tissues, this could also be expanded to other tissues such as skin or tendon. For application to other tissues, the mechanical properties and the organisation of different types of collagen from different tissues would be investigated and incorporated into our model.

After the 'tipping point' where structural changes become irreversible, tissue engineering would be necessary for this mid-late and late disease treatment. Articular cartilage tissue engineering has evoked massive interest in recent decades and has been shown to hold great potential for improving articular cartilage therapy [27, 228, 229]. In addition to cell sources, biocompatible materials, growth factors and mechanical stimuli, recreating the native scaffold and function of the tissue is important in tissue engineering. There is no doubt that it is better to use a biomaterial with characteristics closer to the native collagen fibrils. The use of AFM allows comparison of the mechanical properties of a biomaterial with those of native collagen fibrils. A good design of scaffold which can support the growth and expansion of cells while retaining the characteristics of native cartilage is also important. The use of a well-developed collagen model will enable simulation of the mechanical performance of different structures with different material properties under different mechanical stimuli or investigation of the interaction between native and artificial collagen under loading to optimise scaffold designs.

Appendices

A
Publications

1. V. Klika, E. A. Gaffney, **Y.-C. Chen**, and C. P. Brown, "An overview of multiphase cartilage mechanical modelling and its role in understanding function and pathology," Journal of the mechanical behavior of biomedical materials, vol. 62, pp. 139–157, 2016.

2. **Y.-c. Chen**, M. Chen, E. A. Gaffney, and C. P. Brown, "Effect of crosslinking in cartilage-like collagen microstructures," Journal of the Mechanical Behavior of Biomedical Materials, vol. 66, pp. 138–143, 2017.

JOURNAL OF THE MECHANICAL BEHAVIOR OF BIOMEDICAL MATERIALS 62 (2016) 139–157

Available online at www.sciencedirect.com

ScienceDirect

www.elsevier.com/locate/jmbbm



Review Article

An overview of multiphase cartilage mechanical modelling and its role in understanding function and pathology

Václav Klika[a,1,*], Eamonn A. Gaffney[b,1], Ying-Chun Chen[c], Cameron P. Brown[c]

[a]Department of Mathematics, FNSPE, Czech Technical University in Prague, Prague, Czech Republic
[b]Wolfson Centre for Mathematical Biology, Mathematical Institute, University of Oxford, Oxford, UK
[c]Nuffield Department of Orthopaedics, Rheumatology and Musculoskeletal Sciences, University of Oxford, Oxford, UK

ARTICLE INFO

Article history:
Received 22 December 2015
Received in revised form
15 April 2016
Accepted 25 April 2016
Available online 11 May 2016

Keywords:
Cartilage
Multiphase
Modelling
Structure
Function
Pathology

ABSTRACT

There is a long history of mathematical and computational modelling with the objective of understanding the mechanisms governing cartilage's remarkable mechanical performance. Nonetheless, despite sophisticated modelling development, simulations of cartilage have consistently lagged behind structural knowledge and thus the relationship between structure and function in cartilage is not fully understood. However, in the most recent generation of studies, there is an emerging confluence between our structural knowledge and the structure represented in cartilage modelling. This raises the prospect of further refinement in our understanding of cartilage function and also the initiation of an engineering-level understanding for how structural degradation and ageing relates to cartilage dysfunction and pathology, as well as informing the potential design of prospective interventions. Aimed at researchers entering the field of cartilage modelling, we thus review the basic principles of cartilage models, discussing the underlying physics and assumptions in relatively simple settings, whilst presenting the derivation of relatively parsimonious multiphase cartilage models consistent with our discussions. We proceed to consider modern developments that start aligning the structure captured in the models with observed complexities. This emphasises the challenges associated with constitutive relations, boundary conditions, parameter estimation and validation in cartilage modelling programmes. Consequently, we further detail how both experimental interrogations and modelling developments can be utilised to investigate and reduce such difficulties before summarising how cartilage modelling initiatives may improve our understanding of cartilage ageing, pathology and intervention.

© 2016 The Authors. Published by Elsevier Ltd. This is an open access article under the CC BY license (http://creativecommons.org/licenses/by/4.0/).

*Corresponding author.
E-mail addresses: vaclav.klika@fjfi.cvut.cz (V. Klika), gaffney@maths.ox.ac.uk (E.A. Gaffney), cameron.brown@ndorms.ox.ac.uk (C.P. Brown).
[1]These authors contributed equally.

http://dx.doi.org/10.1016/j.jmbbm.2016.04.032
1751-6161/© 2016 The Authors. Published by Elsevier Ltd. This is an open access article under the CC BY license (http://creativecommons.org/licenses/by/4.0/).

Journal of the mechanical behavior of biomedical materials 66 (2017) 138–143

Contents lists available at ScienceDirect

Journal of the Mechanical Behavior of Biomedical Materials

journal homepage: www.elsevier.com/locate/jmbbm

Effect of crosslinking in cartilage-like collagen microstructures

Ying-chun Chen[a], Minsi Chen[b], Eamonn A. Gaffney[c], Cameron P. Brown[a,*]

[a] Botnar Research Centre, NDORMS, University of Oxford, UK
[b] Department of Computing and Mathematics, University of Derby, UK
[c] Wolfson Centre for Mathematical Biology, Mathematical Institute, University of Oxford, UK

ARTICLE INFO

Keywords:
Articular cartilage
Cartilage model
Osteoarthritis
Ultrastructure
Collagen network model

ABSTRACT

The mechanical performance of biological tissues is underpinned by a complex and finely balanced structure. Central to this is collagen, the most abundant protein in our bodies, which plays a dominant role in the functioning of tissues, and also in disease. Based on the collagen meshwork of articular cartilage, we have developed a bottom-up spring-node model of collagen and examined the effect of fibril connectivity, implemented by crosslinking, on mechanical behaviour. Although changing individual crosslink stiffness within an order of magnitude had no significant effect on modelling predictions, the density of crosslinks in a meshwork had a substantial impact on its behaviour. Highly crosslinked meshworks maintained a 'normal' configuration under loading, with stronger resistance to deformation and improved recovery relative to sparsely crosslinked meshwork. Stress on individual fibrils, however, was higher in highly crosslinked meshworks. Meshworks with low numbers of crosslinks reconfigured to disease-like states upon deformation and recovery. The importance of collagen interconnectivity may provide insight into the role of ultrastructure and its mechanics in the initiation, and early stages, of diseases such as osteoarthritis.

1. Introduction

Articular cartilage performs an impressive mechanical function, which is underpinned by a hierarchical structural configuration of type II collagen, proteoglycans, and interstitial fluid (Huber et al., 2000). As one of the main determinants of function in the tissue, changes to the collagen meshwork are central to disease processes (Hwang et al., 1992; Hunziker, 1999; Brown et al., 2012; Stolz et al., 2009). Collagen-collagen interactions dominate the cohesive strength of the matrix (Broom and Silyn-Roberts, 1990) and therefore the resistance to mechanical damage progression.

The breakdown from the intermeshed, pseudo-random collagen configuration at the micrometer scale to form aligned fibre bundles has been identified as a mechanically irreversible step in the damage process (Brown et al., 2012) and has long been associated with abnormal cartilage softening (Broom, 1982). A recent study has further found localised regions of collagen meshwork disruption and reconfiguration at early stages of disease before the appearance of histological changes (Brown et al., 2014). An improved understanding of the mechanics of the collagen meshwork, and the implications of its properties and connectivity, is therefore of interest for osteoarthritis pathogenesis, diagnostics and the design of regenerative medicine strategies.

Computational modelling provides an ideal platform from which to explore mechano-structural changes. In recent years, increasingly sophisticated constitutive models have been developed to represent tissue-level cartilage mechanics (Wilson et al., 2006; Pierce et al., 2013; Ateshian et al., 2009; Wilson et al., 2005; Deneweth et al., 2013; Wilson et al., 2007). With this sophistication has come an improved representation of structure. Wilson et al., for example, integrated the relation between permeability and tissue composition with a viscoelastic constitutive relation within a fibril-reinforced model for predicting the equilibrium and transient response of articular cartilage during compression, indentation and swelling tests (Wilson et al., 2006). Ateshian et al. applied continuous fibre angular distributions to model the solid matrix of cartilage and successfully predicted experimental observations of the tissue's equilibrium response to mechanical and osmotic loading (Ateshian et al., 2009).

However, such models do not incorporate details from individual fibres but instead consider the impact of average fibril orientations on the scale of continuum. In particular, while there have been advances in the theoretical mechanics of upscaling (e.g. Quintard and Whitaker, 1994; Cushman et al., 2002; Davit et al., 2013), whereby material properties at the sub-continuum scale are systematically incorporated into the constitutive relation of continuum models with controlled accuracy, such approaches are generally not tractable for collagen

* Corresponding author.
E-mail address: cameron.brown@ndorms.ox.ac.uk (C.P. Brown).

http://dx.doi.org/10.1016/j.jmbbm.2016.10.006
Received 2 June 2016; Received in revised form 3 October 2016; Accepted 14 October 2016
Available online 15 October 2016
1751-6161/ © 2016 Elsevier Ltd. All rights reserved.

B

Copyright Clearance

ELSEVIER LICENSE TERMS AND CONDITIONS

Mar 21, 2017

This Agreement between Yingchun Chen ("You") and Elsevier ("Elsevier") consists of your license details and the terms and conditions provided by Elsevier and Copyright Clearance Center.

License Number	4063721374257
License date	Mar 07, 2017
Licensed Content Publisher	Elsevier
Licensed Content Publication	Journal of the Mechanical Behavior of Biomedical Materials
Licensed Content Title	Effect of crosslinking in cartilage-like collagen microstructures
Licensed Content Author	Ying-chun Chen,Minsi Chen,Eamonn A. Gaffney,Cameron P. Brown
Licensed Content Date	February 2017
Licensed Content Volume	66
Licensed Content Issue	n/a
Licensed Content Pages	6
Start Page	138
End Page	143
Type of Use	reuse in a thesis/dissertation
Portion	full article
Format	both print and electronic
Are you the author of this Elsevier article?	Yes
Will you be translating?	No
Order reference number	
Title of your thesis/dissertation	Exploring Mechano-structural Processes in Osteoarthritis
Expected completion date	May 2017
Estimated size (number of pages)	180
Elsevier VAT number	GB 494 6272 12
Requestor Location	[redacted]
Total	**0.00 GBP**
Terms and Conditions	

INTRODUCTION

1. The publisher for this copyrighted material is Elsevier. By clicking "accept" in connection with completing this licensing transaction, you agree that the following terms and conditions apply to this transaction (along with the

ELSEVIER LICENSE
TERMS AND CONDITIONS

Jun 05, 2017

This Agreement between Yingchun Chen ("You") and Elsevier ("Elsevier") consists of your license details and the terms and conditions provided by Elsevier and Copyright Clearance Center.

License Number	4122321032477
License date	Jun 05, 2017
Licensed Content Publisher	Elsevier
Licensed Content Publication	Journal of the Mechanical Behavior of Biomedical Materials
Licensed Content Title	Damage initiation and progression in the cartilage surface probed by nonlinear optical microscopy
Licensed Content Author	C.P. Brown,M.-A. Houle,M. Chen,A.J. Price,F. Légaré,H.S. Gill
Licensed Content Date	Jan 1, 2012
Licensed Content Volume	5
Licensed Content Issue	1
Licensed Content Pages	9
Start Page	62
End Page	70
Type of Use	reuse in a thesis/dissertation
Intended publisher of new work	other
Portion	figures/tables/illustrations
Number of figures/tables/illustrations	4
Format	both print and electronic
Are you the author of this Elsevier article?	No
Will you be translating?	No
Order reference number	
Original figure numbers	figure 3, 4, 6 and 7
Title of your thesis/dissertation	Exploring Mechano-structural Processes in Osteoarthritis
Expected completion date	May 2017
Estimated size (number of pages)	180
Elsevier VAT number	GB 494 6272 12
Requestor Location	Yingchun Chen 
Publisher Tax ID	GB 494 6272 12

SPRINGER LICENSE
TERMS AND CONDITIONS

Jun 06, 2017

This Agreement between Yingchun Chen ("You") and Springer ("Springer") consists of your license details and the terms and conditions provided by Springer and Copyright Clearance Center.

License Number	4122940644651
License date	Jun 06, 2017
Licensed Content Publisher	Springer
Licensed Content Publication	Tribology Letters
Licensed Content Title	Imaging of the Surface of Human and Bovine Articular Cartilage with ESEM and AFM
Licensed Content Author	R. Crockett
Licensed Content Date	Jan 1, 2005
Licensed Content Volume	19
Licensed Content Issue	4
Type of Use	Thesis/Dissertation
Portion	Figures/tables/illustrations
Number of figures/tables/illustrations	1
Author of this Springer article	No
Order reference number	
Original figure numbers	Figure 3
Title of your thesis / dissertation	Exploring Mechano-structural Processes in Osteoarthritis
Expected completion date	May 2017
Estimated size(pages)	180
Requestor Location	Yingchun Chen [redacted]
Billing Type	Invoice
Billing Address	Yingchun Chen [redacted]
Total	0.00 GBP
Terms and Conditions	

JOHN WILEY AND SONS LICENSE TERMS AND CONDITIONS

Jun 05, 2017

This Agreement between Yingchun Chen ("You") and John Wiley and Sons ("John Wiley and Sons") consists of your license details and the terms and conditions provided by John Wiley and Sons and Copyright Clearance Center.

License Number	4122331326107
License date	Jun 05, 2017
Licensed Content Publisher	John Wiley and Sons
Licensed Content Publication	Journal of Anatomy
Licensed Content Title	On the ultrastructure of softened cartilage: a possible model for structural transformation
Licensed Content Author	MIN-HUEY CHEN,NEIL BROOM
Licensed Content Date	Apr 1, 1998
Licensed Content Pages	13
Type of use	Dissertation/Thesis
Requestor type	University/Academic
Format	Print and electronic
Portion	Figure/table
Number of figures/tables	1
Original Wiley figure/table number(s)	Figure 6
Will you be translating?	No
Title of your thesis / dissertation	Exploring Mechano-structural Processes in Osteoarthritis
Expected completion date	May 2017
Expected size (number of pages)	180
Requestor Location	Yingchun Chen [redacted]
Publisher Tax ID	EU826007151
Billing Type	Invoice
Billing Address	Yingchun Chen [redacted]
Total	0.00 GBP
Terms and Conditions	

TERMS AND CONDITIONS

C

Safranin-O Staining Protocol for Cartilage

1. Deparaffinize in 2 changes of xylene (Thermo Fisher Scientific, Waltham, MA, USA) for 5 minutes.
2. Hydrate through graded series of ethanol (Thermo Fisher Scientific) from high (100%) to low concentration (70%) (2 minutes each).
3. Wash gently in running water for 1 minute.
4. Immerse in distilled water for 1 minute.
5. Stain with hematoxylin (Vector Laboratories Ltd, Burlingame, CA, USA) for 1 minute.
6. Wash gently in running water for 10 minutes.
7. Stain with 0.05% fast green (Sigma-Aldrich, St Louis, MO, USA) solution for 10 minutes.
8. Rinse quickly with 1% acetic acid solution (Sigma-Aldrich) for 1-2 seconds.
9. Stain with 1% safranin-O solution (Sigma-Aldrich) for 5 minutes.
10. Dehydrate with 2 changes of 95% ethanol and 2 changes of absolute ethanol (30 seconds each time).
11. Clear the slides in 2 changes of xylene for 5 minutes each.
12. Mount using mounting medium (DePex, BDH Chemicals Ltd, Poole, UK).

D
Training and Skills

Presentation Skills, Language Skills

1. Jul. 2014 Attending CUDA programming course run by Oxford e-Research Centre, Oxford University Mathematical Institute.

2. Jul. 2015 Presenting my modelling research work at the 25th Congress of International Society of Biomechanics.

3. Dec. 2015 Becoming a member of Oxford Solid Mechanics Junior Committee.

4. Feb. 2016 Presenting the researches in NDORMS at Oxford Solid Mechanics Workshop.

5. 2014-2016 Presenting my research project in Postgraduate Seminar (PGS).

Writing Skills and Other Skills

1. 2014-2015 Attending academic writing course in Oxford university language centre.

2. Oct. 2015 Attending scientific writing course run by Prof. Alan Silman at Botnar Research Centre.

3. Apr. 2016 Attending statistics course - Statistics: Designing clinical research and biostatistics run by IT learning Centre.

4. 2015-2017 Assisting Oxford Solid Mechanics workshops at Department of Engineering Sciences.



Dear Ms Ying-Chun Chen,

Thank you for your abstract submission for the XXV Congress of the International Society of Biomechanics in Glasgow, UK from 12th to 16th July 2015.

We have great pleasure to inform you that your abstract

ISB 2015-1477

BOTTOM-UP MECHANO-STRUCTURAL MODELING OF THE CARTILAGE MATRIX

has been accepted as an **Oral presentation.**

Your abstract has been renumbered and your final oral presentation number is:

AS-0008

Please note the important information below relating to your oral presentation:

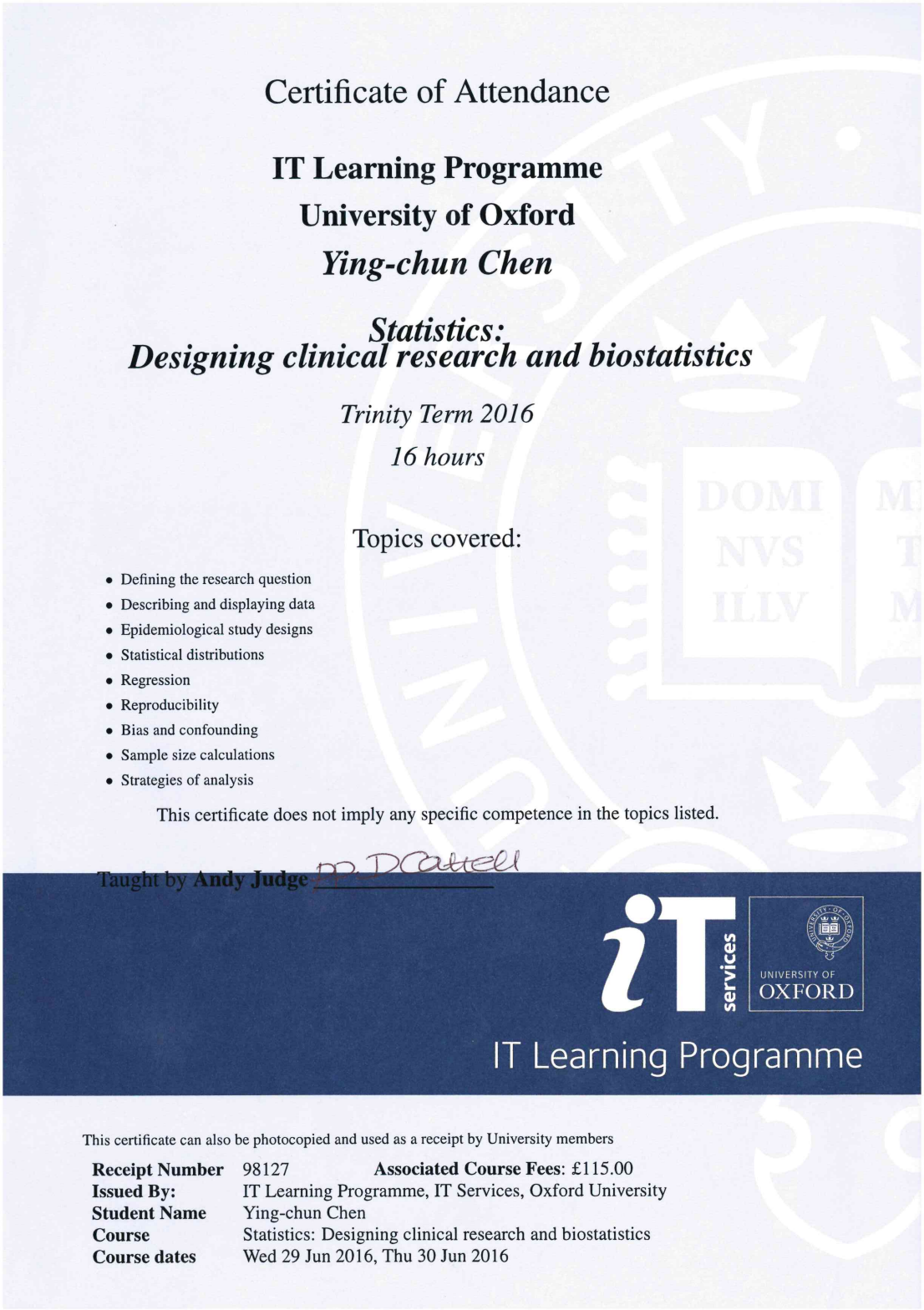
Session Title:	**Abstract Session - Modelling & Computer Simulation 1**
Session Date and Time:	**13.07.2015 08:20**
Session Room:	**Gala**
Time allocated to your Presentation:	**7 + 2 minutes** **1 minute transition**
Presentation order in session	**2**
Presentation start time	**13.07.2015 08:30**
Presentation end time	**13.07.2015 08:40**
Presenting Author	**Ying-Chun Chen**
Speaker Instructions	**Instructions are available on http://www.isbglasgow.com/index.php/scientific-information/abstract-submission-and-guidelines on the abstract page of the meeting website**

You will not be required to produce a poster of your abstract as it will be presented within an oral session.

If you are presenting in a special session, the special session organiser may contact you prior to the meeting.

Oral presentations should focus on the presentation and discussion of scientific data and not be used for marketing or advertising purposes. Any financial support by commercial companies and any ties to commercial companies such as employment and honoraria must be transparently disclosed at the beginning of the presentation. The name of companies linked to the research should be disclosed but company logos should be avoided. The use of brand names of commercial products


ISB
2015
GLASGOW
XXV
CONGRESS OF THE
INTERNATIONAL
SOCIETY OF
BIOMECHANICS
Certificate of Attendance
This certifies that
YING-CHUN CHEN
has attended the
XXV Congress of the International Society of Biomechanics
12th – 16th July 2015
Scottish Exhibition and Conference Centre
Professor Philip Rowe
Chair of the Local Organising Committee



Certificate of Attendance

IT Learning Programme
University of Oxford
Ying-chun Chen

Statistics:
Designing clinical research and biostatistics

Trinity Term 2016
16 hours

Topics covered:

- Defining the research question
- Describing and displaying data
- Epidemiological study designs
- Statistical distributions
- Regression
- Reproducibility
- Bias and confounding
- Sample size calculations
- Strategies of analysis

This certificate does not imply any specific competence in the topics listed.

Taught by **Andy Judge** PP DCattell

iT services
UNIVERSITY OF OXFORD
IT Learning Programme

This certificate can also be photocopied and used as a receipt by University members

Receipt Number	98127	**Associated Course Fees**:	£115.00
Issued By:	IT Learning Programme, IT Services, Oxford University		
Student Name	Ying-chun Chen		
Course	Statistics: Designing clinical research and biostatistics		
Course dates	Wed 29 Jun 2016, Thu 30 Jun 2016		

References

[1] A. R. UK, "Osteoarthritis in general practice: data and perspectives," p. 36, 2013.

[2] C. J. Murray, M. A. Richards, J. N. Newton, K. A. Fenton, H. R. Anderson, C. Atkinson, D. Bennett, E. Bernabé, H. Blencowe, R. Bourne, *et al.*, "Uk health performance: findings of the global burden of disease study 2010," *The lancet*, vol. 381, no. 9871, pp. 997–1020, 2013.

[3] P. Connelly, "The management of chronic pain in older persons," *Journal of the American Geriatrics Society*, vol. 46, no. 5, pp. 635–651, 1998.

[4] M. M. Rahman, J. A. Kopec, J. Cibere, C. H. Goldsmith, and A. H. Anis, "The relationship between osteoarthritis and cardiovascular disease in a population health survey: a cross-sectional study," *BMJ open*, vol. 3, no. 5, p. e002624, 2013.

[5] Y. Y. Leung, Y. H. Pua, and J. Thumboo, "A perpective on osteoarthritis reserach in singapore," *Proceedings of Singapore Healthcare*, vol. 22, no. 1, pp. 31–39, 2013.

[6] A. D. Pearle, R. F. Warren, and S. A. Rodeo, "Basic science of articular cartilage and osteoarthritis," *Clinics in sports medicine*, vol. 24, no. 1, pp. 1–12, 2005.

[7] K. D. Brandt, M. Doherty, and S. Lohmander, *The concept of osteoarthritis as failure of the diarthrodial joint*. Osteoarthritis, Oxford University Press, 2003.

[8] S. Klug and G. Weseloh, *Osteoarthritis: Fundamentals and Strategies for Joint-Preserving Treatment*, ch. Clinical Picture of Osteoarthrosis, pp. 9–22. Springer-Verlag: Berlin, 2000.

[9] K. D. Brandt, P. Dieppe, and E. L. Radin, "Etiopathogenesis of osteoarthritis," *Rheum Dis Clin North Am*, vol. 34, no. 3, pp. 531–59, 2008.

[10] N. J. London, L. E. Miller, and J. E. Block, "Clinical and economic consequences of the treatment gap in knee osteoarthritis management," *Medical hypotheses*, vol. 76, no. 6, pp. 887–892, 2011.

[11] J. Chard and P. Dieppe, "Update: treatment of osteoarthritis," *Arthritis Care & Research*, vol. 47, no. 6, pp. 686–690, 2002.

[12] K. A. Yang, D. Saris, W. Dhert, and A. Verbout, "Osteoarthritis of the knee: current treatment options and future directions," *Current Orthopaedics*, vol. 18, no. 4, pp. 311–320, 2004.

[13] A. P. Newman, "Articular cartilage repair," *The American journal of sports medicine*, vol. 26, no. 2, pp. 309–324, 1998.

[14] K. Messner and J. Gillquist, "Cartilage repair. a critical review," *Acta Orthop Scand*, vol. 67, no. 5, pp. 523–9, 1996.

[15] E. B. Hunziker, "Articular cartilage repair: are the intrinsic biological constraints undermining this process insuperable?," *Osteoarthritis Cartilage*, vol. 7, no. 1, pp. 15–28, 1999.

[16] E. B. Hunziker, "Articular cartilage repair: basic science and clinical progress. a review of the current status and prospects," *Osteoarthritis Cartilage*, vol. 10, no. 6, pp. 432–63, 2002.

[17] J. M. Bert and J. Leverone, "Histologic appearance of "pristine" articular cartilage in knees with unicompartmental osteoarthritis," *The journal of knee surgery*, vol. 20, no. 01, pp. 15–19, 2007.

[18] D. Heinegård, M. Bayliss, and P. Lorenzo, *Biochemistry and Metabolism of Normal and Osteoarthritic Cartilage*, pp. 73–73. Osteoarthritis, 2nd ed, Oxford University Press, 2003.

[19] N. D. Broom, T. Ngo, and E. Tham, "Traversing the intact/fibrillated joint surface: a biomechanical interpretation," *J Anat*, vol. 206, no. 1, pp. 55–67, 2005.

[20] B. Brismar, T. Wredmark, T. Movin, J. Leandersson, and O. Svensson, "Observer reliability in the arthroscopic classification of osteoarthritis of the knee," *Bone & Joint Journal*, vol. 84, no. 1, pp. 42–47, 2002.

[21] C. P. Brown, M. A. Houle, M. Chen, A. J. Price, F. Legare, and H. S. Gill, "Damage initiation and progression in the cartilage surface probed by nonlinear optical microscopy," *J Mech Behav Biomed Mater*, vol. 5, no. 1, pp. 62–70, 2012.

[22] D. Eyre, "Articular cartilage and changes in arthritis: collagen of articular cartilage," *Arthritis Research & Therapy*, vol. 4, no. 1, p. 30, 2001.

[23] V. Klika, E. A. Gaffney, Y.-C. Chen, and C. P. Brown, "An overview of multiphase cartilage mechanical modelling and its role in understanding function and pathology," *Journal of the mechanical behavior of biomedical materials*, vol. 62, pp. 139–157, 2016.

[24] K. A. Athanasiou, E. M. Darling, J. C. Hu, G. D. DuRaine, and A. H. Reddi, *Articular cartilage*. CRC Press, 2013.

[25] L. A. Setton, D. M. Elliott, and V. C. Mow, "Altered mechanics of cartilage with osteoarthritis: human osteoarthritis and an experimental model of joint degeneration," *Osteoarthritis and Cartilage*, vol. 7, no. 1, pp. 2–14, 1999.

[26] A. P. Hollander, I. Pidoux, A. Reiner, C. Rorabeck, R. Bourne, and A. R. Poole, "Damage to type ii collagen in aging and osteoarthritis starts at the articular surface, originates around chondrocytes, and extends into the cartilage with progressive degeneration.," *Journal of Clinical Investigation*, vol. 96, no. 6, p. 2859, 1995.

[27] L. Zhang, J. Hu, and K. A. Athanasiou, "The role of tissue engineering in articular cartilage repair and regeneration," *Critical Reviews™ in Biomedical Engineering*, vol. 37, no. 1-2, 2009.

[28] G. Ofek and K. Athanasiou, "Micromechanical properties of chondrocytes and chondrons: relevance to articular cartilage tissue engineering," *Journal of Mechanics of Materials and Structures*, vol. 2, no. 6, pp. 1059–1086, 2007.

[29] H. Muir, "The chondrocyte, architect of cartilage. biomechanics, structure, function and molecular biology of cartilage matrix macromolecules," *Bioessays*, vol. 17, no. 12, pp. 1039–1048, 1995.

[30] M. Venn and A. Maroudas, "Chemical composition and swelling of normal and osteoarthrotic femoral head cartilage. i. chemical composition.," *Annals of the Rheumatic Diseases*, vol. 36, no. 2, pp. 121–129, 1977.

[31] D. J. Responte, R. M. Natoli, and K. A. Athanasiou, "Collagens of articular cartilage: structure, function, and importance in tissue engineering," *Critical Reviews™ in Biomedical Engineering*, vol. 35, no. 5, 2007.

[32] D. R. Eyre, M. A. Weis, and J.-J. Wu, "Articular cartilage collagen: an irreplaceable framework," *Eur Cell Mater*, vol. 12, no. 1, pp. 57–63, 2006.

[33] A. Maroudas, "Balance between swelling pressure and collagen tension in normal and degenerate cartilage," *Nature*, vol. 260, no. 5554, pp. 808–809, 1976.

[34] C. P. Brown, M. Houle, K. Popov, M. Nicklaus, C. Couture, M. Laliberté, T. Brabec, A. Ruediger, A. Carr, A. J. Price, H. S. Gill, L. Ramunno, and F. Légaré, "Imaging and modeling collagen architecture from the nano to micro scale," *Biomedical Oprics Express*, vol. 5, no. 233-43, 2014.

[35] N. Broom and A. Oloyede, "Experimental determination of the subchondral stress-reducing role of articular cartilage under static and dynamic compression," *Clinical Biomechanics*, vol. 8, no. 2, pp. 102–108, 1993.

[36] E. R. Myers and V. C. Mow, "Biomechanics ofcartilage and its response to biomechanical stimuli," *Hall B, ed. Cartilage, structure, Junction, and biochemistry*, pp. 313–37, 2012.

[37] N. D. Broom and H. Silyn-Roberts, "Collagen-collagen versus collagen-proteoglycan interactions in the determination of cartilage strength," *Arthritis Rheum*, vol. 33, no. 10, pp. 1512–7, 1990.

[38] F. Guilak, A. Ratcliffe, N. Lane, M. P. Rosenwasser, and V. C. Mow, "Mechanical and biochemical changes in the superficial zone of articular cartilage in canine experimental osteoarthritis," *Journal of Orthopaedic Research*, vol. 12, no. 4, pp. 474–484, 1994.

[39] A. Aspberg, "The different roles of aggrecan interaction domains," *Journal of Histochemistry & Cytochemistry*, vol. 60, no. 12, pp. 987–996, 2012.

[40] C. B. Knudson and W. Knudson, "Cartilage proteoglycans," vol. 12, no. 2, pp. 69–78, 2001.

[41] C. Kiani, L. Chen, Y. J. Wu, A. J. Yee, and B. B. Yang, "Structure and function of aggrecan," *Cell Res*, vol. 12, no. 1, pp. 19–32, 2002.

[42] A. M. Bhosale and J. B. Richardson, "Articular cartilage: structure, injuries and review of management," *British medical bulletin*, vol. 87, no. 1, pp. 77–95, 2008.

[43] J. Buckwalter, E. Hunziker, L. Rosenberg, R. Coutts, M. Adams, and D. Eyre, *Injury and Repair of the Musculoskeletal Soft Tissues*, ch. Articular cartilage: composition and structure., pp. 405–425. Park Ridge: American Academy of Orthopaedic Surgeons, 1991.

[44] M. Wong, P. Wuethrich, P. Eggli, and E. Hunziker, "Zone-specific cell biosynthetic activity in mature bovine articular cartilage: A new method using confocal microscopic stereology and quantitative autoradiography," *Journal of Orthopaedic Research*, vol. 14, no. 3, pp. 424–432, 1996.

[45] H. Akkiraju and A. Nohe, "Role of chondrocytes in cartilage formation, progression of osteoarthritis and cartilage regeneration," *Journal of Developmental Biology*, vol. 3, no. 4, pp. 177–192, 2015.

[46] J. Hu, *Chondrocyte self-assembly and culture in bioreactors*. PhD thesis, Houston: Rice University, 2005.

[47] A. Benninghoff, "Form und bau der gelenkknorpel in ihren beziehungen zur funktion," *Zeitschrift für Anatomie und Entwicklungsgeschichte*, vol. 76, no. 1-3, pp. 43–63, 1925.

[48] I. Clarke, "Articular cartilage: a review and scanning electron microscope study. ii. the territorial fibrillar architecture.," *Journal of anatomy*, vol. 118, no. Pt 2, p. 261, 1974.

[49] G. Meachim, D. Denham, I. Emery, and P. Wilkinson, "Collagen alignments and artificial splits at the surface of human articular cartilage.," *Journal of anatomy*, vol. 118, no. Pt 1, p. 101, 1974.

[50] R. Minns and F. Steven, "The collagen fibril organization in human articular cartilage.," *Journal of anatomy*, vol. 123, no. Pt 2, p. 437, 1977.

[51] K. Halonen, M. Mononen, J. Jurvelin, J. Töyräs, and R. Korhonen, "Importance of depth-wise distribution of collagen and proteoglycans in articular cartilage—a 3d finite element study of stresses and strains in human knee joint," *Journal of biomechanics*, vol. 46, no. 6, pp. 1184–1192, 2013.

[52] J. Martel-Pelletier, C. Boileau, J.-P. Pelletier, and P. J. Roughley, "Cartilage in normal and osteoarthritis conditions," *Best Practice & Research Clinical Rheumatology*, vol. 22, no. 2, pp. 351–384, 2008.

[53] S. Akizuki, V. C. Mow, F. Müller, J. C. Pita, D. S. Howell, and D. H. Manicourt, "Tensile properties of human knee joint cartilage: I. influence of ionic conditions, weight bearing, and fibrillation on the tensile modulus," *Journal of Orthopaedic Research*, vol. 4, no. 4, pp. 379–392, 1986.

[54] G. Kempson, H. Muir, C. Pollard, and M. Tuke, "The tensile properties of the cartilage of human femoral condyles related to the content of collagen and glycosaminoglycans," *Biochimica et Biophysica Acta (BBA)-General Subjects*, vol. 297, no. 2, pp. 456–472, 1973.

[55] A. P. Hollander, T. F. Heathfield, C. Webber, Y. Iwata, R. Bourne, C. Rorabeck, and A. R. Poole, "Increased damage to type ii collagen in osteoarthritic articular cartilage detected by a new immunoassay.," *Journal of Clinical Investigation*, vol. 93, no. 4, p. 1722, 1994.

[56] A. R. Poole, L. C. Rosenberg, A. Reiner, M. Ionescu, E. Bogoch, and P. J. Roughley, "Contents and distributions of the proteoglycans decorin and biglycan in normal and osteoarthritic human articular cartilage," *Journal of Orthopaedic Research*, vol. 14, no. 5, pp. 681–689, 1996.

[57] J. Bertrand, C. Cromme, D. Umlauf, S. Frank, and T. Pap, "Molecular mechanisms of cartilage remodelling in osteoarthritis," *The international journal of biochemistry & cell biology*, vol. 42, no. 10, pp. 1594–1601, 2010.

[58] R. F. Loeser, "Aging and osteoarthritis: the role of chondrocyte senescence and aging changes in the cartilage matrix," *Osteoarthritis Cartilage*, vol. 17, no. 8, pp. 971–9, 2009.

[59] H. E. Panula, M. M. Hyttinen, J. P. Arokoski, T. K. Långsjö, A. Pelttari, I. Kiviranta, and H. J. Helminen, "Articular cartilage superficial zone collagen birefringence reduced and cartilage thickness increased before surface fibrillation in experimental osteoarthritis," *Annals of the Rheumatic Diseases*, vol. 57, no. 4, pp. 237–245, 1998.

[60] W. Wilson, J. M. Huyghe, and C. C. van Donkelaar, "A composition-based cartilage model for the assessment of compositional changes during cartilage damage and adaptation," *Osteoarthritis Cartilage*, vol. 14, no. 6, pp. 554–60, 2006.

[61] F. Richard, M. Villars, and S. Thibaud, "Viscoelastic modeling and quantitative experimental characterization of normal and osteoarthritic human articular cartilage using indentation," *J Mech Behav Biomed Mater*, vol. 24, pp. 41–52, 2013.

[62] P. Julkunen, W. Wilson, J. S. Jurvelin, and R. K. Korhonen, "Composition of the pericellular matrix modulates the deformation behaviour of chondrocytes in articular cartilage under static loading," *Med Biol Eng Comput*, vol. 47, no. 12, pp. 1281–90, 2009.

[63] C. Orford, D. Gardner, and P. O'Connor, "Ultrastructural changes in dog femoral condylar cartilage following anterior cruciate ligament section.," *Journal of anatomy*, vol. 137, no. Pt 4, p. 653, 1983.

[64] M. Adams, "Cartilage hypertrophy following canine anterior cruciate ligament transection differs among different areas of the joint.," *The Journal of rheumatology*, vol. 16, no. 6, pp. 818–824, 1989.

[65] N. Broom, M. H. Chen, and A. Hardy, "A degeneration-based hypothesis for interpreting fibrillar changes in the osteoarthritic cartilage matrix," *J Anat*, vol. 199, no. Pt 6, pp. 683–98, 2001.

[66] S. Lin and L. Gu, "Influence of crosslink density and stiffness on mechanical properties of type i collagen gel," *Materials*, vol. 8, no. 2, pp. 551–560, 2015.

[67] W. Hwang, B. Li, L. Jin, K. Ngo, N. Schachar, and G. Hughes, "Collagen fibril structure of normal, aging, and osteoarthritic cartilage," *The Journal of pathology*, vol. 167, no. 4, pp. 425–433, 1992.

[68] M. Stolz, R. Gottardi, R. Raiteri, S. Miot, I. Martin, R. Imer, U. Staufer, A. Raducanu, M. Duggelin, W. Baschong, A. U. Daniels, N. F. Friederich, A. Aszodi, and U. Aebi, "Early detection of aging cartilage and osteoarthritis in mice and patient samples using atomic force microscopy," *Nat Nanotechnol*, vol. 4, no. 3, pp. 186–92, 2009.

[69] J. Arokoski, M. M. Hyttinen, T. Lapveteläinen, P. Takács, B. Kosztáczky, L. Módis, V. Kovanen, and H. Helminen, "Decreased birefringence of the superficial zone collagen network in the canine knee (stifle) articular cartilage after long distance running training, detected by quantitative polarised light microscopy.," *Annals of the rheumatic diseases*, vol. 55, no. 4, pp. 253–264, 1996.

[70] Y.-c. Chen, M. Chen, E. A. Gaffney, and C. P. Brown, "Effect of crosslinking in cartilage-like collagen microstructures," *Journal of the Mechanical Behavior of Biomedical Materials*, vol. 66, pp. 138–143, 2017.

[71] T. Aigner, N. Schmitz, and J. Haag, "Nanomedicine: Afm tackles osteoarthritis," *Nature nanotechnology*, vol. 4, no. 3, pp. 144–145, 2009.

[72] S. Chan, C. Neu, G. DuRaine, K. Komvopoulos, and A. H. Reddi, "Atomic force microscope investigation of the boundary-lubricant layer in articular cartilage," *Osteoarthritis and Cartilage*, vol. 18, no. 7, pp. 956–963, 2010.

[73] M. Stolz, R. Raiteri, A. Daniels, M. R. VanLandingham, W. Baschong, and U. Aebi, "Dynamic elastic modulus of porcine articular cartilage determined at two different levels of tissue organization by indentation-type atomic force microscopy," *Biophysical journal*, vol. 86, no. 5, pp. 3269–3283, 2004.

[74] C.-Y. Wen, C.-B. Wu, B. Tang, T. Wang, C.-H. Yan, W. Lu, H. Pan, Y. Hu, and K.-Y. Chiu, "Collagen fibril stiffening in osteoarthritic cartilage of human beings revealed by atomic force microscopy," *Osteoarthritis and Cartilage*, vol. 20, no. 8, pp. 916–922, 2012.

[75] B. Tang, M. K. Fong, C. Y. Wen, C. H. Yan, D. Chan, A. H. W. Ngan, K. Y. Chiu, and W. W. Lu, "Nanostiffness of collagen fibrils extracted from osteoarthritic cartilage characterized with afm nanoindentation," *Soft Materials*, vol. 12, no. 3, pp. 253–261, 2014.

[76] J. M. Wallace, B. G. Orr, J. C. Marini, and M. M. B. Holl, "Nanoscale morphology of type i collagen is altered in the brtl mouse model of osteogenesis imperfecta," *Journal of structural biology*, vol. 173, no. 1, pp. 146–152, 2011.

[77] C. R. Chu, A. Williams, D. Tolliver, C. K. Kwoh, S. Bruno, and J. J. Irrgang, "Clinical optical coherence tomography of early articular cartilage degeneration in patients with degenerative meniscal tears," *Arthritis & Rheumatism*, vol. 62, no. 5, pp. 1412–1420, 2010.

[78] M. Laasanen, J. Töyräs, J. Hirvonen, S. Saarakkala, R. Korhonen, M. Nieminen, I. Kiviranta, and J. Jurvelin, "Novel mechano-acoustic technique and instrument for diagnosis of cartilage degeneration," *Physiological measurement*, vol. 23, no. 3, p. 491, 2002.

[79] P. West, M. Bostrom, P. Torzilli, and N. Camacho, "Fourier transform infrared spectral analysis of degenerative cartilage: an infrared fiber optic probe and imaging study," *Applied spectroscopy*, vol. 58, no. 4, pp. 376–381, 2004.

[80] Y. Pan, Z. Li, T. Xie, and C. R. Chu, "Hand-held arthroscopic optical coherence tomography for in vivo high-resolution imaging of articular cartilage," *Journal of biomedical optics*, vol. 8, no. 4, pp. 648–654, 2003.

[81] C. R. Chu, N. J. Izzo, J. J. Irrgang, M. Ferretti, and R. K. Studer, "Clinical diagnosis of potentially treatable early articular cartilage degeneration using optical coherence tomography," *Journal of biomedical optics*, vol. 12, no. 5, pp. 051703–051703, 2007.

[82] C. R. Chu, D. Lin, J. L. Geisler, C. T. Chu, F. H. Fu, and Y. Pan, "Arthroscopic microscopy of articular cartilage using optical coherence tomography," *The American journal of sports medicine*, vol. 32, no. 3, pp. 699–709, 2004.

[83] J. Herrmann, C. Pitris, B. Bouma, S. Boppart, C. Jesser, D. Stamper, J. Fujimoto, and M. Brezinski, "High resolution imaging of normal and osteoarthritic cartilage with optical coherence tomography.," *The Journal of rheumatology*, vol. 26, no. 3, pp. 627–635, 1999.

[84] W. Drexler, D. Stamper, C. Jesser, X. Li, C. Pitris, K. Saunders, S. Martin, M. B. Lodge, J. G. Fujimoto, and M. E. Brezinski, "Correlation of collagen organization with polarization sensitive imaging of in vitro cartilage: implications for osteoarthritis.," *The Journal of rheumatology*, vol. 28, no. 6, pp. 1311–1318, 2001.

[85] H. J. Braun and G. E. Gold, "Diagnosis of osteoarthritis: imaging," *Bone*, vol. 51, no. 2, pp. 278–288, 2012.

[86] B. He, J. P. Wu, T. B. Kirk, J. A. Carrino, C. Xiang, and J. Xu, "High-resolution measurements of the multilayer ultra-structure of articular cartilage and their translational potential," *Arthritis research & therapy*, vol. 16, no. 2, p. 205, 2014.

[87] R. Kumar, K. M. Gronhaug, C. L. Davies, J. O. Drogset, and M. B. Lilledahl, "Nonlinear optical microscopy of early stage (icrs grade-i) osteoarthritic human cartilage," *Biomed Opt Express*, vol. 6, no. 5, pp. 1895–903, 2015.

[88] G. Cox, E. Kable, A. Jones, I. Fraser, F. Manconi, and M. D. Gorrell, "3-dimensional imaging of collagen using second harmonic generation," *Journal of structural biology*, vol. 141, no. 1, pp. 53–62, 2003.

[89] P.-J. Su, W.-L. Chen, T.-H. Li, C.-K. Chou, T.-H. Chen, Y.-Y. Ho, C.-H. Huang, S.-J. Chang, Y.-Y. Huang, H.-S. Lee, *et al.*, "The discrimination of type i and type ii collagen and the label-free imaging of engineered cartilage tissue," *Biomaterials*, vol. 31, no. 36, pp. 9415–9421, 2010.

[90] F. Faris, M. Thorniley, Y. Wickramasinghe, R. Houston, P. Rolfe, N. Livera, and A. Spencer, "Non-invasive in vivo near-infrared optical measurement of the penetration depth in the neonatal head," *Clinical Physics and Physiological Measurement*, vol. 12, no. 4, p. 353, 1991.

[91] I. Afara, I. Prasadam, R. Crawford, Y. Xiao, and A. Oloyede, "Non-destructive evaluation of articular cartilage defects using near-infrared (nir) spectroscopy in osteoarthritic rat models and its direct relation to mankin score," *Osteoarthritis Cartilage*, vol. 20, no. 11, pp. 1367–73, 2012.

[92] I. Afara, S. Singh, and A. Oloyede, "Application of near infrared (nir) spectroscopy for determining the thickness of articular cartilage," *Med Eng Phys*, vol. 35, no. 1, pp. 88–95, 2013.

[93] I. O. Afara, S. Singh, and A. Oloyede, "Load-unloading response of intact and artificially degraded articular cartilage correlated with near infrared (nir) absorption spectra," *J Mech Behav Biomed Mater*, vol. 20, pp. 249–58, 2013.

[94] D. Baykal, O. Irrechukwu, P.-C. Lin, K. Fritton, R. G. Spencer, and N. Pleshko, "Nondestructive assessment of engineered cartilage constructs using near-infrared spectroscopy," *Applied spectroscopy*, vol. 64, no. 10, pp. 1160–1166, 2010.

[95] C. P. Brown, J. Bowden, L. Rintoul, R. Meder, A. Oloyede, and R. W. Crawford, "Diffuse reflectance near infrared spectroscopy can distinguish normal from enzymatically digested cartilage," *Physics in medicine and biology*, vol. 54, no. 18, p. 5579, 2009.

[96] G. Spahn, H. Plettenberg, E. Kahl, H. M. Klinger, T. Mückley, and G. O. Hofmann, "Near-infrared (nir) spectroscopy. a new method for arthroscopic evaluation of low grade degenerated cartilage lesions. results of a pilot study," *BMC musculoskeletal disorders*, vol. 8, no. 1, p. 47, 2007.

[97] G. Spahn, H. Plettenberg, H. Nagel, E. Kahl, H. M. Klinger, T. Mückley, M. Günther, G. O. Hofmann, and J. A. Mollenhauer, "Evaluation of cartilage defects with near-infrared spectroscopy (nir): an ex vivo study," *Medical engineering & physics*, vol. 30, no. 3, pp. 285–292, 2008.

[98] C. P. Brown, A. Oloyede, R. W. Crawford, G. E. Thomas, A. J. Price, and H. S. Gill, "Acoustic, mechanical and near-infrared profiling of osteoarthritic progression in bovine joints," *Phys Med Biol*, vol. 57, no. 2, pp. 547–59, 2012.

[99] C. P. Brown, C. Jayadev, S. Glyn-Jones, A. J. Carr, D. W. Murray, A. J. Price, and H. S. Gill, "Characterization of early stage cartilage degradation using diffuse reflectance near infrared spectroscopy," *Physics in Medicine and Biology*, vol. 56, no. 7, pp. 2299–2307, 2011.

[100] G. O. Hofmann, J. Marticke, R. Grossstück, M. Hoffmann, M. Lange, H. K. Plettenberg, R. Braunschweig, O. Schilling, I. Kaden, and G. Spahn, "Detection and evaluation of initial cartilage pathology in man: a comparison between mrt, arthroscopy and near-infrared spectroscopy (nir) in their relation to initial knee pain," *Pathophysiology*, vol. 17, no. 1, pp. 1–8, 2010.

[101] G. Spahn, G. Felmet, and G. O. Hofmann, "Traumatic and degenerative cartilage lesions: arthroscopic differentiation using near-infrared spectroscopy (nirs)," *Archives of orthopaedic and trauma surgery*, vol. 133, no. 7, pp. 997–1002, 2013.

[102] U. P. Palukuru, C. M. McGoverin, and N. Pleshko, "Assessment of hyaline cartilage matrix composition using near infrared spectroscopy," *Matrix Biol*, vol. 38, pp. 3–11, 2014.

[103] C. P. Brown and M. Chen, "A constituent-based preprocessing approach for characterising cartilage using nir absorbance measurements," *Biomedical Physics & Engineering Express*, vol. 2, no. 1, p. 017002, 2016.

[104] D. Chenery and H. Bowring, "Infrared and raman spectroscopic imaging in biosciences," *Spectroscopy Europe*, vol. 14, pp. 8–14, 2003.

[105] Y. Takahashi, N. Sugano, M. Takao, T. Sakai, T. Nishii, and G. Pezzotti, "Raman spectroscopy investigation of load-assisted microstructural alterations in human knee cartilage: Preliminary study into diagnostic potential for osteoarthritis," *J Mech Behav Biomed Mater*, vol. 31, pp. 77–85, 2014.

[106] R. A. de Souza, M. Xavier, N. M. Mangueira, A. P. Santos, A. L. Pinheiro, A. B. Villaverde, and J. Silveira, L., "Raman spectroscopy detection of molecular changes associated with two experimental models of osteoarthritis in rats," *Lasers Med Sci*, vol. 29, no. 2, pp. 797–804, 2014.

[107] A. Kunstar, J. Leijten, S. van Leuveren, J. Hilderink, C. Otto, C. A. van Blitterswijk, M. Karperien, and A. A. van Apeldoorn, "Recognizing different tissues in human fetal femur cartilage by label-free raman microspectroscopy," *J Biomed Opt*, vol. 17, no. 11, p. 116012, 2012.

[108] Y.-N. Wang, C. Galiotis, and D. Bader, "Determination of molecular changes in soft tissues under strain using laser raman microscopy," *Journal of biomechanics*, vol. 33, no. 4, pp. 483–486, 2000.

[109] K. A. Esmonde-White, F. W. Esmonde-White, M. D. Morris, and B. J. Roessler, "Fiber-optic raman spectroscopy of joint tissues," *Analyst*, vol. 136, no. 8, pp. 1675–1685, 2011.

[110] A. J. Makowski, C. A. Patil, A. Mahadevan-Jansen, and J. S. Nyman, "Polarization control of raman spectroscopy optimizes the assessment of bone tissue," *J Biomed Opt*, vol. 18, no. 5, p. 55005, 2013.

[111] P. Xu, G. Cox, J. A. M. Ramshaw, P. Lukins, and C. Sheppard, "Polarization effects in shg of collagen," *Multiphoton Microscopy in the Biomedical Sciences Iv*, vol. 5323, pp. 343–352, 2004.

[112] N. S. Lim, Z. Hamed, C. H. Yeow, C. Chan, and Z. Huang, "Early detection of biomolecular changes in disrupted porcine cartilage using polarized raman spectroscopy," *J Biomed Opt*, vol. 16, no. 1, p. 017003, 2011.

[113] A. Bonifacio and V. Sergo, "Effects of sample orientation in raman microspectroscopy of collagen fibers and their impact on the interpretation of the amide iii band," *Vibrational Spectroscopy*, vol. 53, no. 2, pp. 314–317, 2010.

[114] L. Galvis, J. W. Dunlop, G. Duda, P. Fratzl, and A. Masic, "Polarized raman anisotropic response of collagen in tendon: towards 3d orientation mapping of collagen in tissues," *PloS one*, vol. 8, no. 5, p. e63518, 2013.

[115] M. Janko, P. Davydovskaya, M. Bauer, A. Zink, and R. W. Stark, "Anisotropic raman scattering in collagen bundles," *Optics letters*, vol. 35, no. 16, pp. 2765–2767, 2010.

[116] J. Kinnunen, J. S. Jurvelin, J. Mäkitalo, M. Hauta-Kasari, P. Vahimaa, and S. Saarakkala, "Optical spectral imaging of degeneration of articular cartilage," *Journal of biomedical optics*, vol. 15, no. 4, pp. 046024–046024, 2010.

[117] P. Öberg, T. Sundqvist, and A. Johansson, "Assessment of cartilage thickness utilising reflectance spectroscopy," *Medical and Biological Engineering and Computing*, vol. 42, no. 1, pp. 3–8, 2004.

[118] A. Johansson, T. Sundqvist, J. Kuiper, and P. Å. Öberg, "A spectroscopic approach to imaging and quantification of cartilage lesions in human knee joints," *Physics in medicine and biology*, vol. 56, no. 6, p. 1865, 2011.

[119] I. O. Afara, M. Hauta-Kasari, J. S. Jurvelin, A. Oloyede, and J. Töyräs, "Optical absorption spectra of human articular cartilage correlate with biomechanical properties, histological score and biochemical composition," *Physiological measurement*, vol. 36, no. 9, p. 1913, 2015.

[120] M. H. Chen and N. Broom, "On the ultrastructure of softened cartilage: a possible model for structural transformation," *J Anat*, vol. 192 (Pt 3), pp. 329–41, 1998.

[121] J. DeGroot, N. Verzijl, M. J. Wenting-Van Wijk, R. A. Bank, F. P. Lafeber, J. W. Bijlsma, and J. M. TeKoppele, "Age-related decrease in susceptibility of human articular cartilage to matrix metalloproteinase-mediated degradation: the role of advanced glycation end products," *Arthritis Rheum*, vol. 44, no. 11, pp. 2562–71, 2001.

[122] D. R. Eyre, I. R. Dickson, and K. Van Ness, "Collagen cross-linking in human bone and articular cartilage. age-related changes in the content of mature hydroxypyridinium residues," *Biochem J*, vol. 252, no. 2, pp. 495–500, 1988.

[123] N. Verzijl, J. DeGroot, Z. C. Ben, O. Brau-Benjamin, A. Maroudas, R. A. Bank, J. Mizrahi, C. G. Schalkwijk, S. R. Thorpe, J. W. Baynes, J. W. Bijlsma, F. P. Lafeber, and J. M. TeKoppele, "Crosslinking by advanced glycation end products increases the stiffness of the collagen network in human articular cartilage: a possible mechanism through which age is a risk factor for osteoarthritis," *Arthritis Rheum*, vol. 46, no. 1, pp. 114–23, 2002.

[124] A. C. Chen, M. M. Temple, D. M. Ng, N. Verzijl, J. DeGroot, J. M. TeKoppele, and R. L. Sah, "Induction of advanced glycation end products and alterations of the tensile properties of articular cartilage," *Arthritis Rheum*, vol. 46, no. 12, pp. 3212–7, 2002.

[125] A. Gautieri, S. Vesentini, A. Redaelli, and R. Ballarini, "Modeling and measuring visco-elastic properties: From collagen molecules to collagen fibrils," *International Journal of Non-Linear Mechanics*, vol. 56, pp. 25–33, 2013.

[126] A. K. Nair, A. Gautieri, and M. J. Buehler, "Role of intrafibrillar collagen mineralization in defining the compressive properties of nascent bone," *Biomacromolecules*, vol. 15, no. 7, pp. 2494–2500, 2014.

[127] R. B. Svensson, H. Mulder, V. Kovanen, and S. P. Magnusson, "Fracture mechanics of collagen fibrils: influence of natural cross-links," *Biophysical journal*, vol. 104, no. 11, pp. 2476–2484, 2013.

[128] A. Gautieri, F. S. Passini, U. Silván, M. Guizar-Sicairos, G. Carimati, P. Volpi, M. Moretti, H. Schoenhuber, A. Redaelli, M. Berli, *et al.*, "Advanced glycation end-products: Mechanics of aged collagen from molecule to tissue," *Matrix Biology*, 2016.

[129] M. T. Bayliss, F. P. Lafeber, A. Maroudas, J. M. Tekoppele, *et al.*, "Ageing and zonal variation in post-translational modification of collagen in normal human articular cartilage: the age-related increase in non-enzymatic glycation affects biomechanical properties of cartilage," *Biochemical Journal*, vol. 330, no. 1, pp. 345–351, 1998.

[130] A. E. Peters, E. J. Comerford, S. Macaulay, K. T. Bates, and R. Akhtar, "Micromechanical properties of canine femoral articular cartilage following multiple freeze-thaw cycles," *Journal of the Mechanical Behavior of Biomedical Materials*, vol. 71, pp. 114–121, 2017.

[131] E. Kennedy, D. Tordonado, and S. Duma, "Effects of freezing on the mechanical properties of articular cartilage.," *Biomedical sciences instrumentation*, vol. 43, pp. 342–347, 2006.

[132] M. Plodinec, M. Loparic, and U. Aebi, "Imaging articular cartilage tissue using atomic force microscopy (afm)," *Cold Spring Harbor Protocols*, vol. 2010, no. 10, pp. pdb–prot5499, 2010.

[133] B. Rolauffs, J. M. Williams, A. J. Grodzinsky, K. E. Kuettner, and A. A. Cole, "Distinct horizontal patterns in the spatial organization of superficial zone chondrocytes of human joints," *Journal of structural biology*, vol. 162, no. 2, pp. 335–344, 2008.

[134] Y. Xia, K. I. Momot, Z. Chen, C. T. Chen, D. Kahn, and F. Badar, "Introduction to cartilage," 2016.

[135] A. Asanbaeva, K. Masuda, E. J. Thonar, S. M. Klisch, and R. L. Sah, "Mechanisms of cartilage growth: modulation of balance between proteoglycan and collagen in vitro using chondroitinase abc," *Arthritis & Rheumatism*, vol. 56, no. 1, pp. 188–198, 2007.

[136] H. T. Nia, I. S. Bozchalooi, Y. Li, L. Han, H. H. Hung, E. Frank, K. Youcef-Toumi, C. Ortiz, and A. Grodzinsky, "High-bandwidth afm-based rheology reveals that cartilage is most sensitive to high loading rates at early stages of impairment," *Biophys J*, vol. 104, no. 7, pp. 1529–37, 2013.

[137] F. P. Rojas, M. A. Batista, C. A. Lindburg, D. Dean, A. J. Grodzinsky, C. Ortiz, and L. Han, "Molecular adhesion between cartilage extracellular matrix macromolecules," *Biomacromolecules*, vol. 15, no. 3, pp. 772–780, 2014.

[138] R. C. Billinghurst, W. Wu, M. Ionescu, A. Reiner, L. Dahlberg, J. Chen, H. Van Wart, and A. R. Poole, "Comparison of the degradation of type ii collagen and proteoglycan in nasal and articular cartilages induced by interleukin-1 and the selective inhibition of type ii collagen cleavage by collagenase," *Arthritis & Rheumatism*, vol. 43, no. 3, p. 664, 2000.

[139] A. L. da Cunha, L. G. de Oliveira, L. F. Maia, L. F. C. de Oliveira, Y. M. Michelacci, and J. A. K. de Aguiar, "Pharmaceutical grade chondroitin sulfate: Structural analysis and identification of contaminants in different commercial preparations," *Carbohydrate polymers*, vol. 134, pp. 300–308, 2015.

[140] I. Cukrowski, L. Popović, W. Barnard, S. O. Paul, P. H. van Rooyen, and D. C. Liles, "Modeling and spectroscopic studies of bisphosphonate–bone interactions. the raman, nmr and crystallographic investigations of ca–hedp complexes," *Bone*, vol. 41, no. 4, pp. 668–678, 2007.

[141] W. Richardson, D. Wilkinson, L. Wu, F. Petrigliano, B. Dunn, and D. Evseenko, "Ensemble multivariate analysis to improve identification of articular cartilage disease in noisy raman spectra," *Journal of biophotonics*, vol. 8, no. 7, pp. 555–566, 2015.

[142] M. Raghavan, N. D. Sahar, R. H. Wilson, M.-A. Mycek, N. Pleshko, D. H. Kohn, and M. D. Morris, "Quantitative polarized raman spectroscopy in highly turbid bone tissue," *Journal of biomedical optics*, vol. 15, no. 3, pp. 037001–037001, 2010.

[143] Q. Zhong, D. Inniss, K. Kjoller, and V. Elings, "Fractured polymer/silica fiber surface studied by tapping mode atomic force microscopy," *Surface science*, vol. 290, no. 1-2, pp. L688–L692, 1993.

[144] R. Proksch and R. Callahan, "Material property measurements using multiple frequency atomic fore microscopy," Oct. 15 2013. US Patent 8,555,711.

[145] R. Proksch and D. G. Yablon, "Loss tangent imaging: Theory and simulations of repulsive-mode tapping atomic force microscopy," *Applied Physics Letters*, vol. 100, no. 7, p. 073106, 2012.

[146] F. J. Giessibl, "Forces and frequency shifts in atomic-resolution dynamic-force microscopy," *Physical Review B*, vol. 56, no. 24, p. 16010, 1997.

[147] I. N. Sneddon, "The relation between load and penetration in the axisymmetric boussinesq problem for a punch of arbitrary profile," *International journal of engineering science*, vol. 3, no. 1, pp. 47–57, 1965.

[148] H. Hertz, "On the contact of elastic solids," *J. Reine Angew Math.*, vol. 92, pp. 156–171, 1881.

[149] J. Cleveland, B. Anczykowski, A. Schmid, and V. Elings, "Energy dissipation in tapping-mode atomic force microscopy," *Applied Physics Letters*, vol. 72, no. 20, pp. 2613–2615, 1998.

[150] R. García García, F. J. Tamayo de Miguel, and Á. San Paulo, "Phase contrast and surface energy hysteresis in tapping mode scanning force microscopy," 1999.

[151] R. Fraser, T. MacRae, A. Miller, and E. Suzuki, "Molecular conformation and packing in collagen fibrils," *Journal of molecular biology*, vol. 167, no. 2, pp. 497–521, 1983.

[152] A. Hodge and J. Petruska, *Aspects of Protein Structure*, ch. Recent Studies with the Electron Microscope on Ordered Aggregates of the Tropocollagen Molecule, p. p289. New York:Academic Press, 1963.

[153] J. P. Orgel, A. Miller, T. C. Irving, R. F. Fischetti, A. P. Hammersley, and T. J. Wess, "The in situ supermolecular structure of type i collagen," *Structure*, vol. 9, no. 11, pp. 1061–1069, 2001.

[154] M. Fang, E. L. Goldstein, A. S. Turner, C. M. Les, B. G. Orr, G. J. Fisher, K. B. Welch, E. D. Rothman, and M. M. B. Holl, "Type i collagen d-spacing in fibril bundles of dermis, tendon and bone: bridging between nano-and micro-level tissue hierarchy," *ACS nano*, vol. 6, no. 11, p. 9503, 2012.

[155] A. Mahadevan-Jansen, M. F. Mitchell, N. Ramanujam, A. Malpica, S. Thomsen, U. Utzinger, and R. Richards-Kortum, "Near-infrared raman spectroscopy for in vitro detection of cervical precancers," *Photochem Photobiol*, vol. 68, no. 1, pp. 123–32, 1998.

[156] M. D. Shoulders and R. T. Raines, "Collagen structure and stability," *Annual review of biochemistry*, vol. 78, pp. 929–958, 2009.

[157] B. Erickson, M. Fang, J. M. Wallace, B. G. Orr, C. M. Les, and M. M. Banaszak Holl, "Nanoscale structure of type i collagen fibrils: quantitative measurement of d-spacing," *Biotechnology journal*, vol. 8, no. 1, pp. 117–126, 2013.

[158] J. Bella, M. Eaton, B. Brodsky, and H. M. Berman, "Crystal and molecular structure of a collagen-like peptide at 1.9 angstrom resolution," *Science*, vol. 266, no. 5182, pp. 75–82, 1994.

[159] K. A. Dehring, A. R. Smukler, B. J. Roessler, and M. D. Morris, "Correlating changes in collagen secondary structure with aging and defective type ii collagen by raman spectroscopy," *Applied spectroscopy*, vol. 60, no. 4, pp. 366–372, 2006.

[160] Z. Movasaghi, S. Rehman, and I. U. Rehman, "Raman spectroscopy of biological tissues," *Applied Spectroscopy Reviews*, vol. 42, no. 5, pp. 493–541, 2007.

[161] K. A. Esmonde-White, *Raman spectroscopy detection of molecular changes associated with osteoarthritis*. PhD thesis, The University of Michigan, 2009.

[162] M. Rutgers, M. J. van Pelt, W. J. Dhert, L. B. Creemers, and D. B. Saris, "Evaluation of histological scoring systems for tissue-engineered, repaired and osteoarthritic cartilage," *Osteoarthritis Cartilage*, vol. 18, no. 1, pp. 12–23, 2010.

[163] K. P. Pritzker, S. Gay, S. A. Jimenez, K. Ostergaard, J. P. Pelletier, P. A. Revell, D. Salter, and W. B. van den Berg, "Osteoarthritis cartilage histopathology: grading and staging," *Osteoarthritis Cartilage*, vol. 14, no. 1, pp. 13–29, 2006.

[164] R. Outerbridge and J. Dunlop, "The problem of chondromalacia patellae.," *Clinical orthopaedics and related research*, vol. 110, pp. 177–196, 1975.

[165] R. W. Wright, M. Group, *et al.*, "Osteoarthritis classification scales: interobserver reliability and arthroscopic correlation," *J Bone Joint Surg Am*, vol. 96, no. 14, pp. 1145–1151, 2014.

[166] W. W. Curl, J. Krome, E. S. Gordon, J. Rushing, B. P. Smith, and G. G. Poehling, "Cartilage injuries: a review of 31,516 knee arthroscopies," *Arthroscopy: The Journal of Arthroscopic & Related Surgery*, vol. 13, no. 4, pp. 456–460, 1997.

[167] R. Crockett, S. Roos, P. Rossbach, C. Dora, W. Born, and H. Troxler, "Imaging of the surface of human and bovine articular cartilage with esem and afm," *Tribology Letters*, vol. 19, no. 4, pp. 311–317, 2005.

[168] R. Kumar, K. M. Grønhaug, N. K. Afseth, V. Isaksen, C. de Lange Davies, J. O. Drogset, and M. B. Lilledahl, "Optical investigation of osteoarthritic human cartilage (icrs grade) by confocal raman spectroscopy: a pilot study," *Analytical and bioanalytical chemistry*, vol. 407, no. 26, pp. 8067–8077, 2015.

[169] W. B. Fischer and H. H. Eysel, "Polarized raman spectra and intensities of aromatic amino acids phenylalanine, tyrosine and tryptophan," *Spectrochimica Acta Part A: Molecular Spectroscopy*, vol. 48, no. 5, pp. 725–732, 1992.

[170] M. J. Buehler, "Nature designs tough collagen: explaining the nanostructure of collagen fibrils," *Proceedings of the National Academy of Sciences*, vol. 103, no. 33, pp. 12285–12290, 2006.

[171] M. J. Buehler, "Nanomechanics of collagen fibrils under varying cross-link densities: atomistic and continuum studies," *Journal of the mechanical behavior of biomedical materials*, vol. 1, no. 1, pp. 59–67, 2008.

[172] M. C. Chang and J. Tanaka, "Ft-ir study for hydroxyapatite/collagen nanocomposite cross-linked by glutaraldehyde," *Biomaterials*, vol. 23, no. 24, pp. 4811–4818, 2002.

[173] J. Muyonga, C. Cole, and K. Duodu, "Fourier transform infrared (ftir) spectroscopic study of acid soluble collagen and gelatin from skins and bones

of young and adult nile perch (lates niloticus)," *Food Chemistry*, vol. 86, no. 3, pp. 325–332, 2004.

[174] M. Kazemi, Y. Dabiri, and L. P. Li, "Recent advances in computational mechanics of the human knee joint," *Comput Math Methods Med*, vol. 2013, p. 718423, 2013.

[175] G. Kempson, M. Freeman, and S. Swanson, "The determination of a creep modulus for articular cartilage from indentation tests on the human femoral head," *Journal of biomechanics*, vol. 4, no. 4, pp. 239–250, 1971.

[176] W. Hayes, L. Keer, G. Herrmann, and L. Mockros, "A mathematical analysis for indentation tests of articular cartilage," *Journal of biomechanics*, vol. 5, no. 5, pp. 541–551, 1972.

[177] W. Hayes and L. Mockros, "Viscoelastic properties of human articular cartilage.," *Journal of applied physiology*, vol. 31, no. 4, pp. 562–568, 1971.

[178] J. Parsons and J. Black, "The viscoelastic shear behavior of normal rabbit articular cartilage," *Journal of Biomechanics*, vol. 10, no. 1, pp. 21–29, 1977.

[179] M. A. Biot, "General theory of three-dimensional consolidation," *Journal of applied physics*, vol. 12, no. 2, pp. 155–164, 1941.

[180] V. C. Mow, S. Kuei, W. M. Lai, C. G. Armstrong, *et al.*, "Biphasic creep and stress relaxation of articular cartilage in compression: theory and experiments," *J Biomech Eng*, vol. 102, no. 1, pp. 73–84, 1980.

[181] V. C. Mow, M. Gibbs, W. M. Lai, W. Zhu, and K. A. Athanasiou, "Biphasic indentation of articular cartilage—ii. a numerical algorithm and an experimental study," *Journal of biomechanics*, vol. 22, no. 8-9, pp. 853–861, 1989.

[182] V. Mow and V. Roth, "Effects of nonlinear strain-dependent permeability and rate of compression on the stress behavior of articular cartilage," *Journal of biomechanical engineering*, vol. 103, p. 61, 1981.

[183] J.-K. Suh, R. Spilker, and M. Holmes, "A penalty finite element analysis for nonlinear mechanics of biphasic hydrated soft tissue under large deformation," *International journal for numerical methods in engineering*, vol. 32, no. 7, pp. 1411–1439, 1991.

[184] L. Li, J. Soulhat, M. Buschmann, and A. Shirazi-Adl, "Nonlinear analysis of cartilage in unconfined ramp compression using a fibril reinforced poroelastic model," *Clinical Biomechanics*, vol. 14, no. 9, pp. 673–682, 1999.

[185] J. Soulhat, M. Buschmann, and A. Shirazi-Adl, "A fibril-network-reinforced biphasic model of cartilage in unconfined compression.," *Journal of biomechanical engineering*, vol. 121, no. 3, pp. 340–347, 1999.

[186] L. Li, M. Buschmann, and A. Shirazi-Adl, "Strain-rate dependent stiffness of articular cartilage in unconfined compression," *Journal of biomechanical engineering*, vol. 125, no. 2, pp. 161–168, 2003.

[187] G. A. Ateshian, V. Rajan, N. O. Chahine, C. E. Canal, and C. T. Hung, "Modeling the matrix of articular cartilage using a continuous fiber angular distribution predicts many observed phenomena," *J Biomech Eng*, vol. 131, no. 6, p. 061003, 2009.

[188] W. M. Lai, J. S. Hou, and V. C. Mow, "A triphasic theory for the swelling and deformation behaviors of articular cartilage," *J Biomech Eng*, vol. 113, no. 3, pp. 245–58, 1991.

[189] G. A. Ateshian, N. O. Chahine, I. M. Basalo, and C. T. Hung, "The correspondence between equilibrium biphasic and triphasic material properties in mixture models of articular cartilage," *Journal of biomechanics*, vol. 37, no. 3, pp. 391–400, 2004.

[190] W. Y. Gu, W. M. Lai, and V. C. Mow, "A mixture theory for charged-hydrated soft tissues containing multi-electrolytes: Passive transport and swelling behaviors," *J Biomech Eng*, vol. 120, no. 2, pp. 169–80, 1998.

[191] J. M. Huyghe and J. Janssen, "Quadriphasic mechanics of swelling incompressible porous media," *International Journal of Engineering Science*, vol. 35, no. 8, pp. 793–802, 1997.

[192] M. Quintard and S. Whitaker, "Transport in ordered and disordered porous media i: The cellular average and the use of weighting functions," *Transport in Porous Media*, vol. 14, no. 2, pp. 163–177, 1994.

[193] J. H. Cushman, L. S. Bennethum, and B. X. Hu, "A primer on upscaling tools for porous media," *Advances in Water Resources*, vol. 25, no. 8, pp. 1043–1067, 2002.

[194] Y. Davit, C. G. Bell, H. M. Byrne, L. A. Chapman, L. S. Kimpton, G. E. Lang, K. H. Leonard, J. M. Oliver, N. C. Pearson, R. J. Shipley, *et al.*, "Homogenization via formal multiscale asymptotics and volume averaging: How do the two techniques compare?," *Advances in Water Resources*, vol. 62, pp. 178–206, 2013.

[195] B. Lee, X. Zhou, K. Riching, K. W. Eliceiri, P. J. Keely, S. A. Guelcher, A. M. Weaver, and Y. Jiang, "A three-dimensional computational model of collagen network mechanics," *PLoS One*, vol. 9, no. 11, p. e111896, 2014.

[196] N. D. Broom, "Abnormal softening in articular cartilage: its relationship to the collagen framework," *Arthritis Rheum*, vol. 25, no. 10, pp. 1209–16, 1982.

[197] J. A. van der Rijt, K. O. van der Werf, M. L. Bennink, P. J. Dijkstra, and J. Feijen, "Micromechanical testing of individual collagen fibrils," *Macromol Biosci*, vol. 6, no. 9, pp. 697–702, 2006.

[198] R. Teshima, T. Otsuka, N. Takasu, N. Yamagata, and K. Yamamoto, "Structure of the most superficial layer of articular cartilage," *Journal of Bone & Joint Surgery, British Volume*, vol. 77-B, no. 3, pp. 460–464, 1995.

[199] W. Wilson, C. van Donkelaar, B. van Rietbergen, K. Ito, and R. Huiskes, "Stresses in the local collagen network of articular cartilage: a poroviscoelastic fibril-reinforced finite element study," *Journal of Biomechanics*, vol. 37, no. 3, pp. 357 – 366, 2004.

[200] A. Thambyah and N. Broom, "Micro-anatomical response of cartilage-on-bone to compression: mechanisms of deformation within and beyond the directly loaded matrix," *J Anat*, vol. 209, no. 5, pp. 611–22, 2006.

[201] M.-A. Houle, C.-A. Couture, S. Bancelin, J. Kolk, E. Auger, C. Brown, K. Popov, L. Ramunno, and F. Légaré, "Analysis of forward and backward second harmonic generation images to probe the nanoscale structure of collagen within bone and cartilage," *Journal of biophotonics*, vol. 8, no. 11-12, pp. 993–1001, 2015.

[202] C.-A. Couture, S. Bancelin, J. Van der Kolk, K. Popov, M. Rivard, K. Légaré, G. Martel, H. Richard, C. Brown, S. Laverty, *et al.*, "The impact of collagen fibril polarity on second harmonic generation microscopy," *Biophysical journal*, vol. 109, no. 12, pp. 2501–2510, 2015.

[203] P. J. Campagnola and L. M. Loew, "Second-harmonic imaging microscopy for visualizing biomolecular arrays in cells, tissues and organisms," *Nat Biotech*, vol. 21, no. 11, pp. 1356–1360, 2003.

[204] Y. Jin and T. Wang, "Three-dimensional numerical modeling of the damage mechanism of amorphous polymer network," *Computational Materials Science*, vol. 46, no. 3, pp. 632 – 638, 2009.

[205] D. Burstein and M. Gray, "Is mri fulfilling its promise for molecular imaging of cartilage in arthritis?," 2006.

[206] X. Li, C. B. Ma, T. M. Link, D.-D. Castillo, G. Blumenkrantz, J. Lozano, J. Carballido-Gamio, M. Ries, and S. Majumdar, "In vivo t 1ρ and t 2 mapping of articular cartilage in osteoarthritis of the knee using 3t mri," *Osteoarthritis and cartilage*, vol. 15, no. 7, pp. 789–797, 2007.

[207] P. Glover and P. Mansfield, "Limits to magnetic resonance microscopy," *Reports on progress in physics*, vol. 65, no. 10, p. 1489, 2002.

[208] D. Heinegård, M. Bayliss, and P. Lorenzo, *Biochemistry and Metabolism of Normal and Osteoarthritic Cartilage*, pp. 73–73. Osteoarthritis, 2nd ed, Oxford University Press, 2003.

[209] Hamamatsu, "RGB Color Sensor." `https://www.hamamatsu.com/eu/en/product/alpha/R/4153/S9032-02/index.html`. Accessed: 2017-06-21.

[210] J. W. Strutt, "Lviii. on the scattering of light by small particles," *The London, Edinburgh, and Dublin Philosophical Magazine and Journal of Science*, vol. 41, no. 275, pp. 447–454, 1871.

[211] G. Mie, "Beiträge zur optik trüber medien, speziell kolloidaler metallösungen," *Annalen der physik*, vol. 330, no. 3, pp. 377–445, 1908.

[212] M. Kerker, "The scattering of light and other electromagnetic radiation," *Academic Press*, 1969.

[213] S. C. Lee, "Dependent scattering of an obliquely incident plane-wave by a collection of parallel cylinders," *Journal of Applied Physics*, vol. 68, no. 10, pp. 4952–4957, 1990.

[214] R. H. Picard, "Absorption and scattering of light by small particles - bohren,c, huffman,d," *Optical Engineering*, vol. 23, no. 2, pp. Sr48–Sr48, 1984.

[215] J. Schäfer, S.-C. Lee, and A. Kienle, "Calculation of the near fields for the scattering of electromagnetic waves by multiple infinite cylinders at perpendicular incidence," *J. Quant. Spectrosc. Radiat. Trans.*, vol. 113, no. 16, 2012.

[216] J.-P. Schäfer, *Implementierung und Anwendung analytischer und numerischer Verfahren zur Lösung der Maxwellgleichungen für die Untersuchung der Lichtausbreitung in biologischem Gewebe*. PhD thesis, Universität Ulm, 2011.

[217] Y. Yarker, R. Aspden, and D. Hukins, "Birefringence of articular cartilage and the distribution of collagen fibril orientations," *Connective tissue research*, vol. 11, no. 2-3, pp. 207–213, 1983.

[218] D. W. Ebert, C. Roberts, S. K. Farrar, W. M. Johnston, A. S. Litsky, and A. L. Bertone, "Articular cartilage optical properties in the spectral range 300-850 nm," *Journal of biomedical optics*, vol. 3, no. 3, pp. 326–333, 1998.

[219] E. J. Miller and S. Gay, "[1] the collagens: An overview and update," *Methods in enzymology*, vol. 144, pp. 3–41, 1987.

[220] J. M. Lane and C. Weiss, "Review of articular cartilage collagen research," *Arthritis & Rheumatism*, vol. 18, no. 6, pp. 553–562, 1975.

[221] R. C. Billinghurst, L. Dahlberg, M. Ionescu, A. Reiner, R. Bourne, C. Rorabeck, P. Mitchell, J. Hambor, O. Diekmann, H. Tschesche, *et al.*, "Enhanced cleavage of type ii collagen by collagenases in osteoarthritic articular cartilage.," *Journal of Clinical Investigation*, vol. 99, no. 7, p. 1534, 1997.

[222] A. R. Poole, M. Ionescu, M. Fitzcharles, and R. C. Billinghursta, "The assessment of cartilage degradation in vivo: development of an immunoassay for the measurement in body fluids of type ii collagen cleaved by collagenases," *Journal of immunological methods*, vol. 294, no. 1, pp. 145–153, 2004.

[223] J. Jurvelin, D. Müller, M. Wong, D. Studer, A. Engel, and E. Hunziker, "Surface and subsurface morphology of bovine humeral articular cartilage as assessed by atomic force and transmission electron microscopy," *Journal of structural biology*, vol. 117, no. 1, pp. 45–54, 1996.

[224] C. Orford and D. Gardner, "Ultrastructural histochemistry of the surface lamina of normal articular cartilage," *The Histochemical Journal*, vol. 17, no. 2, pp. 223–233, 1985.

[225] M. Minary-Jolandan and M.-F. Yu, "Nanomechanical heterogeneity in the gap and overlap regions of type i collagen fibrils with implications for bone heterogeneity," *Biomacromolecules*, vol. 10, no. 9, pp. 2565–2570, 2009.

[226] J. M. Wallace, B. Erickson, C. M. Les, B. G. Orr, and M. M. B. Holl, "Distribution of type i collagen morphologies in bone: relation to estrogen depletion," *Bone*, vol. 46, no. 5, pp. 1349–1354, 2010.

[227] M. Fang, K. G. Liroff, A. S. Turner, C. M. Les, B. G. Orr, and M. M. B. Holl, "Estrogen depletion results in nanoscale morphology changes in dermal collagen," *Journal of Investigative Dermatology*, vol. 132, no. 7, pp. 1791–1797, 2012.

[228] M. W. Kessler and D. A. Grande, "Tissue engineering and cartilage," *Organogenesis*, vol. 4, no. 1, pp. 28–32, 2008.

[229] E. A. Makris, A. H. Gomoll, K. N. Malizos, J. C. Hu, and K. A. Athanasiou, "Repair and tissue engineering techniques for articular cartilage," *Nature Reviews Rheumatology*, vol. 11, no. 1, pp. 21–34, 2015.